



City Research Online

City, University of London Institutional Repository

Citation: Ghosh, S. (2018). Design and optimisation of integrated photonic waveguides and sensors. (Unpublished Doctoral thesis, City, University of London)

This is the accepted version of the paper.

This version of the publication may differ from the final published version.

Permanent repository link: <https://openaccess.city.ac.uk/id/eprint/20954/>

Link to published version:

Copyright: City Research Online aims to make research outputs of City, University of London available to a wider audience. Copyright and Moral Rights remain with the author(s) and/or copyright holders. URLs from City Research Online may be freely distributed and linked to.

Reuse: Copies of full items can be used for personal research or study, educational, or not-for-profit purposes without prior permission or charge. Provided that the authors, title and full bibliographic details are credited, a hyperlink and/or URL is given for the original metadata page and the content is not changed in any way.

Design and Optimisation of Integrated Photonic Waveguides and Sensors

By

SOUVIK GHOSH

Thesis Submitted for the Degree of
Doctor of Philosophy



School of Mathematics, Computer Science and Engineering

CITY, UNIVERSITY OF LONDON

2018

I would like to dedicate this thesis to my father Mr. Samir Kumar Ghosh and mother Mrs. Sumita Ghosh.

Declaration

I do solemnly and sincerely declare that I am the sole author of this dissertation and the work in this dissertation was carried out in accordance with the requirements of the regulations by City, University of London, UK. Any use of textbooks, theses, and published works in which copyright exists are cited and title of the work and its authors have been carefully acknowledged. The contents of the dissertation are original and have not been submitted in whole or in part for consideration for any academic or professional degree or award.

I grant the power of discretion to the Librarian at City, University of London to allow the thesis to be copied partially or entirely without further reference to the author. This permission covers only single copies made for study purposes, subject to normal conditions of acknowledgement.

Souvik Ghosh

June 2018

Acknowledgements

This dissertation would not have been accomplished without the abundant assistance, guidance, suggestions, and encouragement from my supervisor Prof. Dr. B. M. Azizur Rahman during the preparation and completion of the study. I am also grateful to my co-supervisor Prof. Dr. Kenneth Grattan for his guidance and support throughout the work.

I would like to thank the Erasmus Mundus AREAS+ scholarship program from the European Commission and Optics and Photonics Education Scholarship by SPIE, for providing the financial assistance, and also to the School of Mathematics, Computer Science, and Engineering (SMCSE) of City, University of London for the facilities provided. Special thanks go to the City Graduate School and the Worshipful Company of Tin Plate Workers alias Wire Workers for funding me to attend conferences.

I would like to thank every member and alumni of the Photonics Modelling Research group for all the technical and moral support. I express my thanks to the all academics and administrative staff of the City, University of London for immense assistance during my progress.

Additionally, I am thankful to all my teachers and mentors especially, Dr. Rajib Chakraborty and Dr. Kallol Bhattacharya from the University of Calcutta, India for always being supportive and motivating me during my study.

Finally and most importantly, I wish to thank my parents, my wife Subhasri, sister Shreyasi, brother Satyaban and my beloved friends Pradip and Shirsendu for unremittingly supporting and encouraging me. Without them, this thesis would never have been possible.

Abstract

The study in this dissertation aimed to develop novel slot waveguide and resonator based compact integrated photonic sensors. Using guided photons as the probe for detection and measurement, and finally converting the signal magnitude from any domain to an electronic signal is one of the most effective approaches of sensing. Novel and efficient designs of hybrid and composite plasmonic horizontal slot waveguides and dielectric straight slot resonators are proposed and optimised to detect a small refractive index change. Practically, the concentrations of chemical liquid and gas or vapour are often expressed in terms of ‘grams per litre (g/l)’ and ‘parts per million (ppm)’, respectively. Thus, device sensitivities related to the detection of those substances may be expressed in amplitude or wavelength shift of the output optical signal per unit g/l or ppm. However, changes in the concentration and the chemical property of any liquid, gas, and chemical vapour result in refractive index variation of those substances. Therefore, we emphasised the detection of the refractive index change which, on the other hand, represents the concentration and/or chemical property change in the testing sample.

Design, optimisations, and performance analyses of those waveguides are carried out by a direct divergence modified full-vectorial two-dimensional (2D) finite element method (FV-FEM). It provides an accurate spurious free better characterisation approach to handle all types of waveguides especially, the plasmonic and hybrid plasmonic waveguides where the guided mode is a complex mixture of the dielectric waveguide mode and surface plasmon polaritons (SPPs). Additionally, a full-vectorial three-dimensional (3D) FV-FEM dedicated to solve the 3D resonator problems is also developed and implemented.

As an application of the 2D FV-FEM, first a metal nano-wire with identical and non-identical cladding conditions are considered and modal evolutions of its plasmonic fundamentals and complex supermodes are studied which also work as a benchmark of the direct divergence modified 2D FV-FEM code. Different mode effective area definitions

are incorporated with this newly modified code and the low and high index contrast and hybrid plasmonic complex waveguides are simulated to determine the appropriateness of different effective area approaches for various waveguiding structures. Following this, the 2D FV-FEM is implemented in designing complex plasmonic slot based sensing waveguides. A horizontal slot composite plasmonic waveguide structure with a low index porous ZnO (P-ZnO) layer as slot material is reported and also incorporated in a compact symmetric Mach-Zehnder interferometer (MZI) to detect the presence of ethanol vapour in the environment. The waveguide is optimised to obtain a maximum slot confinement (41%) and overall a high phase sensitivity of the MZI device. A similar hybrid plasmonic horizontal slot waveguide is designed and optimised for detection of small refractive index change in the bio-layers (ssDNA and dsDNA) during DNA hybridisation. Next, a metal strip loaded horizontal slot hybrid plasmonic waveguide is designed for a high slot confinement and lower modal loss. The waveguide structure contains a suspended Si slab on top of an optimised thin metal layer (silver) to obtain a lower modal attenuation. It shows an enhanced 60% and 82% power confinement in the slot and sensing (slot+clad) sections, respectively with a small modal attenuation value of $0.036 \text{ dB}/\mu\text{m}$. This waveguide is incorporated in an asymmetric Mach-Zehnder interferometer with an asymmetric power splitting scheme which results in an improved interferometric fringe visibility. This compact device exhibits a high temperature and chemical concentration sensitivity of $244 \text{ pm}/^\circ\text{C}$ and $437.5 \text{ nm}/\text{RIU}$, respectively. Beside these waveguides, a silicon-on-insulator (SOI) based vertically slotted straight resonator is also reported in this thesis. Due to its easy and straight structural design it is free from the bending losses and its fabrication steps are much easier compared to other complex devices such as ring, disk resonators, and grating based sensors. The slot cross-section is first optimised and then its length is calculated with those optimised parameters. The 3D straight resonator as a whole is then considered for bulk and surface sensing. Complete performance analyses and the resonating wavelength shift of the device due to small refractive index change during bulk and surface sensing applications are determined by using the newly developed 3D FV-FEM code. This straight resonator exhibits a 5.2 nm resonating wavelength shift for a 5 nm ultra-thin bio-layer and high bulk sensitivities of $820 \text{ nm}/\text{RIU}$ and $683 \text{ nm}/\text{RIU}$ for filled and empty slot conditions, respectively.

TABLE OF CONTENTS

	Page
List of Symbols and Acronyms	ix
List of Tables	xi
List of Figures	xii
List of Publications	xxiv
1 Introduction	1
1.1 Objectives and Motivations	1
1.2 Thesis Outline	4
2 Overview of Photonic Sensors and its Modelling	6
2.1 Introduction	6
2.2 Principles of Optical Sensing Technology	6
2.2.1 Fluorescence-based Sensing	7
2.2.2 Frequency Comb-based Sensing	9
2.2.3 Terahertz (THz) Sensing Technology	10
2.2.4 Plasmonic Sensors	11
2.2.5 Photonic Crystal Fibre-based Sensors	13
2.2.6 Integrated Waveguide-based Sensors	14
2.3 Numerical Methods as Modelling Tools	20
2.3.1 Frequency Domain Methods	20
2.3.2 Time Domain Methods	22
2.4 Waveguide Fabrication Technologies	23
2.4.1 Wafer Fabrication	23
2.4.2 Hybrid Plasmonic Waveguide Fabrication	24
2.5 Summary	25
3 Finite Element Based Frequency Domain Analyses	26
3.1 Introduction	26
3.2 Full Vectorial Finite Element Method (FV-FEM)	27
3.2.1 2D and 3D Computational Domain Discretisation	28

3.2.2	Set-up Interpolation Equations	29
3.2.3	Vectorial Variational Formulation for Electromagnetism	35
3.3	Two Dimensional FV-FEM	36
3.3.1	Spurious Solutions: Direct Divergence Modified Approach	40
3.4	Three Dimensional FV-FEM	41
3.5	Boundary Conditions	48
3.6	Least Squares Boundary Residual (LSBR) Method	50
3.7	Perturbation Analysis for Waveguide Modal Loss	53
3.8	Summary	54
4	Modal Analyses of Integrated Photonic Waveguides	55
4.1	Introduction	55
4.2	Modal Evolution of Metal Nano-wire by the Divergence Modified FV-FEM Approach	56
4.2.1	Metal Nano-wire with Identical Cladding	59
4.2.2	Metal Nano-wire with Non-identical Cladding	65
4.3	Studies of Waveguide Mode Effective Area (A_{eff})	75
4.3.1	Different Definitions of A_{eff}	75
4.3.2	Waveguide Modal Effective Area Analyses	79
4.4	Summary	103
5	Horizontal Slot Composite Plasmonic Waveguide (HSCPW) for Detection of Ethanol Vapour and DNA Hybridisation	105
5.1	Introduction	105
5.2	Ethanol Vapour Sensing by HSCPW	106
5.2.1	Porous ZnO (P-ZnO) Capillary Condensation	107
5.2.2	Horizontal Slotted Composite Plasmonic Waveguide (HSCPW) . .	109
5.2.3	Optimisation of Design Parameters and Waveguide Performance as a Sensor	115
5.2.4	Waveguide Sensitivity	119
5.2.5	Mach-Zehnder Interferometer (MZI) using HSCPW	122
5.2.6	Fabrication Tolerance	126
5.3	Detection of DNA Hybridisation by SOI Based HSCPW	127
5.3.1	DNA Hybridisation	128
5.3.2	Horizontal Slot Composite Plasmonic Waveguide (HSCPW) and its Mode Analyses	130
5.3.3	Optimisation and Performance Analysis of HSCPW Bio-sensor . .	131
5.4	Summary	138
6	Metal Strip Loaded Hybrid Plasmonic Waveguide as a Temperature and Liquid Concentration Sensor	140
6.1	Introduction	140

6.2	Optical Properties of the Waveguide Materials	143
6.2.1	Silicon (Si), Silica (SiO_2), and Isopropanol(C_3H_8O) Solution	143
6.2.2	Metal - Silver (Ag)	147
6.3	Hybrid Plasmonic Waveguide Incorporated Mach-Zehnder Interferometer	148
6.3.1	Metal Strip Loaded Horizontal Slot Hybrid Plasmonic Waveguide (MSLHSHPW)	150
6.3.2	Design and Optimisation of Waveguides	152
6.3.3	MZI design with MSLHSHPW and DHS waveguides	159
6.4	MZI Transducer: Performance Evaluation	164
6.4.1	Temperature Sensing	167
6.4.2	Chemical Sensing	170
6.5	Fabrication Tolerance	172
6.6	Summary	173
7	Vertical Slotted Straight Resonator as a Biochemical Sensor	175
7.1	Introduction	175
7.2	Vertical Slotted Straight Resonator	178
7.2.1	Design and Optimisation of Device Parameters	179
7.3	Device Performance as a Sensor	187
7.3.1	Surface Sensing	188
7.3.2	Bulk Refractometric Sensing	189
7.4	Fabrication Tolerance	192
7.5	Summary	193
8	Conclusions and Future Work	195
8.1	Conclusions	195
8.2	Future Work	200
Appendices		
A	2D FV-FEM: Calculations of Matrix Elements	201
A.1	Evaluation of $[Q]$ Matrix	201
A.2	Evaluation of $[A]_e$ and $[B]_e$ Matrix	203
B	3D FV-FEM: Calculations of Matrix Elements	206
B.1	Evaluation of $[A]_e$ and $[B]_e$ Matrices	206
C	Validation of 3D FV-FEM	212
C.1	Empty Rectangular Cavity: Analytical Solutions	212
C.2	Empty Rectangular Cavity: Numerical Computation by 3D FV-FEM . . .	214
Bibliography		220

LIST OF SYMBOLS AND ACRONYMS

Symbols

c	Light velocity in free-space
λ	Wavelength
n_{eff}	Effective refractive index
n_{eq}	Equivalent refractive index
k_0	Wavenumber
α	Attenuation constant
β	Phase constant
L_p	Propagation length
A_{eff}	Mode effective area
ϵ_r	Relative permittivity
μ_r	Relative permeability
ω	Angular frequency
Γ	Power confinement
L_c	Coupling length
\vec{E}	Electric field vector
\vec{H}	Magnetic field vector
\vec{D}	Electric flux density
\vec{B}	Magnetic flux density
S_z	z-component of Poynting vector
p	Penalty term
Si	Silicon
SiO_2	Silicon dioxide
Si_3N_4	Silicon nitride

ZnO Zinc oxide

Au Gold

Ag Silver

Acronyms

RI Refractive index

SMF Single mode fibre

PCF Photonic crystal fibre

SOI Silicon-on-insulator

SON Silicon-on-nitride

P-ZnO Porous zinc oxide

FV-FEM Full-vectorial finite element method

LSBR Least squares boundary residual

FDM Finite difference method

FDTD Finite difference time domain method

PEW Perfect electric wall

PMW Perfect magnetic wall

SP Surface plasmon

SPP Surface plasmon polariton

SPZ Spot-size

HSCPW Horizontal slot composite plasmonic waveguide

MSLHSPW Metal strip loaded horizontal slot hybrid plasmonic waveguide

MZI Mach-Zehnder interferometer

FSR Frequency spectral shift

TE Transverse electric

TM Transverse magnetic

ssDNA Single stranded deoxyribonucleic acid

dsDNA Double stranded deoxyribonucleic acid

DI water Deionised water

BSA Bovine serum albumin

LIST OF TABLES

TABLE	Page
2.1 Published works on dielectric and hybrid plasmonic slot waveguide based photonic sensors.	17
6.1 Different sections of the MZI arms for calibrations of FSR	166
C.1 Analytical results of resonating wavelength (λ_{res}), wavenumber (k_0), and k_0a of different resonating modes of the empty rectangular cavity.	213
C.2 Analytical and 3D FV-FEM simulated wavenumber of the TE_{101} mode.	218
C.3 Analytical and 3D FV-FEM simulated wavenumber of the TE_{110} mode.	218
C.4 Analytical and 3D FV-FEM simulated wavenumber of degenerated TE_{111} and TM_{111} mode.	218

LIST OF FIGURES

FIGURE	Page
2.1 Different fluorescence sensing mechanism spectra. Figures from left to right define the sensing schemes depending on intensities (a), intensity ratio (b), anisotropies (c), time-dependent lifetimes (d), and phase-modulation measurements. Reproduced from [Lakowicz, 2006]	8
3.1 Pascal triangle exhibits the relationship in between element node number and term number in the shape function (N_i^e).	29
3.2 (a) and (b) represent linear triangular and tetrahedral element for two-dimensional and three-dimensional domain discretisation. The Q point is taken as any arbitrary point inside the element of coordinate (x,y) for 2D and (x,y,z) for 3D.	30
3.3 Linear and quadratic elements with its node numbering scheme depending on the element order. (a) and (b) depict the 2D triangular elements with linear and quadratic configuration. (c) and (d) are the first and second order tetrahedral elements.	33
3.4 Schematic diagram to show waveguide discontinuity at a junction.	51
4.1 Real effective index (n_{eff}) variation of the fundamental plasmonic ss^0 mode in an identical clad metal nano-wire ($W = 1000$ nm, $t = 100$ nm) with the FV-FEM mesh size. The orange solid and purple dashed lines indicate the n_{eff} determined by the new divergence modified FV-FEM and earlier penalty method, respectively. The insets (a), (c) and (b), (d) show the 1D-line plot of the H_x field along y-axis of the ss^0 mode (magnified to the metal-dielectric interfaces) for a lower 300×300 (180,000 elements) and a higher 1000×1000 (2,000,000 elements) FV-FEM meshes, respectively.	57
4.2 Schematic diagram of dielectric clad metal nano-wire and its plasmonic mode field profiles simulated by FV-FEM at 1550 nm. (a) Schematic diagram of a silver (Ag) wire, (b)-(e) are the H_x field distributions of four plasmonic modes, ss^0 , as^0 , sa^0 , and aa^0 , respectively and (f) is a higher order mode (sa^1) guided the metal waveguide. Ag nano-wire of width, $W = 1000$ nm and thickness, $t = 100$ nm are considered.	58
4.3 Dispersions of different plasmonic modes with the operating wavelength (λ) ranging from 633 nm to 1550 nm.	60

4.4	Normalised effective indices variations of plasmonic modes with the surrounding identical material. The solid and dotted lines indicate the variations for $W = 1000$ and 500 nm, respectively when t is fixed at 100 nm. The operating wavelength (λ) is fixed at 1550 nm.	60
4.5	n_{eff} variations of plasmonic modes with metal width (W). The solid and dashed lines indicate the variations for two different thickness, $t = 100$ and 40 nm, respectively.	63
4.6	The main and inset figures show the mode propagation length (L_p) of different SPP modes with metal width (W) for different thickness, $t = 100$ and 40 nm, respectively.	64
4.7	Plasmonic modal characteristics with metal nano-wire thickness (t) for a fixed width, $W = 1000$ nm. The main plot shows the n_{eff} variations of all fundamental higher order modes and the inset shows the corresponding modal propagation length (L_p) variations against t	66
4.8	SPP modal characteristics its evolutions with metal thickness (t) for a metal nano-wire with a small index-difference ($n_{substrate} = 3.5$ and $n_{superstrate} = 3.3$) in the cladding. The main and inset of (a) show the n_{eff} and L_p variations of long range supermode, sa^0 and aa^0 modes for fixed $W = 1000$ nm and 600 nm shown by the solid and dashed-dotted lines, respectively. The solid blue and dashed-dotted lines in (b) depict the modal effective area (MEA) of supermodes for $W = 1000$ and 600 nm, respectively.	67
4.9	(a), (b), and (c) denote the H_x field evolution of the long range plasmonic supermode (PSM) for three different metal thickness, $t = 100, 60$, and 20 nm, respectively. W is fixed at 1000 nm. The operating wavelength is kept fixed at 1550 nm.	68
4.10	Normalised H_x 1D field plot of the long range supermode for three different thickness, $t = 100, 40$, and 20 nm, shown by the solid green, red, and blue lines, respectively. Corresponding mode effective area (MEA) are shown in (b). The metal nano-wire width (W) is fixed at 600 nm. The top ($n_{superstrate} = 3.3$) and bottom ($n_{substrate} = 3.5$) interfaces field distributions are shown in sub-figures (a) and (b), respectively.	71
4.11	Variations of plasmonic supermode (PSM) parameters in non-identical clad metal nano-wire with core metal width (W) for different fixed thickness, $t = 20, 40, 60$, and 80 nm shown by the black, blue, red, and green lines, respectively. Variation of n_{eff} and corresponding L_p variations with W are shown in sub-figures (a) and (b), respectively.	72

4.12	n_{eff} and L_p variations of different plasmonic modes with superstrate refractive index (S-RI) shown by the main and the inset plots, respectively. The solid black, red, blue, and purple lines indicate the PSM ($s_L^1 a s_U^0$), sa^0 , aa^0 , and sa^1 variations with S-RI, respectively for waveguide dimension, $W = 1000$ nm and $t = 100$ nm. The dashed black, red, blue, and green lines and pink star denote the guided PSM, sa^0 , aa^0 , aa^2 , and ss^0 modal characteristics with S-RI for dimension, $W = 1000$ nm and $t = 20$ nm.	73
4.13	The H_x field distribution of different plasmonic modes of non-identical clad plasmonic waveguide simulated by FV-FEM, (a) and (b) depict the sa^0 and aa^0 field distributions for large index difference in the background ($n_{superstrate} = 1.0$ and $n_{substrate} = 3.5$) for metal thickness, $t = 100$ nm, (c) and (d) show the field distributions of $s_L^1 a s_U^0$ PSM and aa^2 when $n_{superstrate} = 3.0$ and $n_{substrate} = 3.5$ for metal thickness, $t = 100$ and 20 nm, respectively. Metal width (W) is fixed at 1000 nm.	74
4.14	Schematic cross-section of the step index circular optical fibre.	79
4.15	Mode effective area (A_{eff}) and effective index (n_{eff}) variations with fibre core radius (R).	80
4.16	(a), (b), and (c) depicts the H_y field profile of the quasi-TE mode and its Gaussian fitting profile shown by solid blue and dashed red lines, respectively. Insets are showing the fundamental 2D mode field distributions.	81
4.17	(a) and (b) show the schematic cross-section of the rectangular silicon (Si) ridge waveguide and its refractive index profile, respectively. (c) and (d) represent the FV-FEM simulated quasi-TE E_y and S_z field profiles, respectively.	82
4.18	Quasi-TE H_y , E_x , and S_z profiles of the Si ridge ($W_{Si} = 400$ nm, $H_{Si} = 220$ nm) waveguide along x and y axes passing through the centre of the waveguide. (a), (c), and (e) present the fields along x-axis; (b), (d), and (f) present the fields along y-axis.	83
4.19	Effective index (n_{eff}) variation of the Si ridge waveguide with Si core width (W_{Si}) and height (H_{Si}), shown by the red and black solid lines, respectively. For W_{Si} and H_{Si} variation the H_{Si} and W_{Si} was kept fixed at 220 and 350 nm, respectively.	83
4.20	(a) and (b) depict the different A_{eff} variations with W_{Si} . Si ridge height (H_{Si}) is kept fixed at 220 nm.	84
4.21	(a) and (b) depict the different A_{eff} variations with H_{Si} . Si ridge width (W_{Si}) is kept fixed at 550 nm.	84
4.22	(a) and (b) show the schematic cross-section of a SOI based vertical slot waveguide and its refractive index profile, respectively. (c) and (d) represent the FV-FEM simulated quasi-TE E_x and S_z field profiles, respectively.	87

4.23	Quasi-TE H_y , E_x fields and S_z intensity distribution of a SOI based vertical slot waveguide ($W_{Si} = 210$ nm, $H_{Si} = 220$ nm, and $W_{slot} = 100$ nm) along x and y axes passing through the centre of the waveguide. (a), (c), and (e) show the distributions along x-axis; (b), (d), and (f) show the distributions along y-axis.	88
4.24	SOI based vertical slot effective index (n_{eff}) variation with Si slab width (W_{Si}) for a fixed Si slab height (H_{Si}) and slot width (W_{slot}) of 220 and 100 nm, respectively.	89
4.25	(a) and (b) depict the mode effective area variations by different approaches such as $A_{eff}^{H_t}$, $A_{eff}^{H_y}$, $A_{eff}^{E_t}$, $A_{eff}^{E_x}$, $A_{eff}^{S_z}$, $A_{eff}^{S_z max}$, A_{eff}^U , and $A_{eff}^{U_{max}}$ against W_{Si} . The H_{Si} and W_{slot} are kept fixed at 220 and 100 nm, respectively.	90
4.26	SOI based vertical slot effective index (n_{eff}) variation with slot width (W_{slot}) for a fixed Si slab height (H_{Si}) and width (W_{Si}) of 220 and 200 nm, respectively.	90
4.27	(a) and (b) depict the mode effective area variations by different approaches such as $A_{eff}^{H_t}$, $A_{eff}^{H_y}$, $A_{eff}^{E_t}$, $A_{eff}^{E_x}$, $A_{eff}^{S_z}$, $A_{eff}^{S_z max}$, A_{eff}^U , and $A_{eff}^{U_{max}}$ against W_{slot} . The H_{Si} and W_{Si} are kept fixed at 220 and 200 nm, respectively.	91
4.28	(a) shows the schematic cross-sectional digram of a SOI based horizontal slot waveguide. (b) and (c) depict the FV-FEM simulated E_y and S_z field distributions of the fundamental quasi-TM mode.	92
4.29	Quasi-TM H_x , E_y fields, and S_z intensity distributions of the SOI based horizontal slot waveguide along x and y axes passing through the centre of the waveguide. (a), (c), and (e) present the distributions along x-axis and (b), (d), and (f) present the same but along y-axis.	93
4.30	Fundamental quasi-TM mode effective index (n_{eff}) variation with Si slab width (W_{Si}) for a fixed Si slab height (H_{Si}) and slot height (H_{slot}) of 220 and 100 nm, respectively.	94
4.31	(a) and (b) show the mode effective area variations by different approaches such as $A_{eff}^{H_t}$, $A_{eff}^{H_x}$, $A_{eff}^{E_t}$, $A_{eff}^{E_y}$, $A_{eff}^{S_z}$, $A_{eff}^{S_z max}$, A_{eff}^U , and $A_{eff}^{U_{max}}$ against Si slab width W_{Si} . The H_{Si} and H_{slot} are kept fixed at 220 and 100 nm, respectively.	95
4.32	Fundamental quasi-TM mode effective index (n_{eff}) variation with Si slab height (H_{Si}) for a fixed Si slab width (W_{Si}) and slot height (H_{slot}) of 300 and 50 nm, respectively.	96
4.33	(a) and (b) show the mode effective area variations by different approaches such as $A_{eff}^{H_t}$, $A_{eff}^{H_x}$, $A_{eff}^{E_t}$, $A_{eff}^{E_y}$, $A_{eff}^{S_z}$, $A_{eff}^{S_z max}$, A_{eff}^U , and $A_{eff}^{U_{max}}$ against Si slab height H_{Si} . The W_{Si} and H_{slot} are kept fixed at 300 and 50 nm, respectively.	96
4.34	(a) and (b) depict a schematic cross-section of horizontal slot hybrid plasmonic waveguide and its refractive index profile along y-axis, respectively.	97

4.35	In-house 2D FV-FEM simulated field distribution of horizontal slot hybrid plasmonic waveguide. (a), (b), and (c) represent the quasi-TM H_x , E_y fields, and S_z intensity distributions, respectively when Si slab height (H_{Si}) is considered as 220 nm. (d) and (e) depict the quasi-TM E_y and S_z profiles for 180 nm Si slab height (H_{Si}). The circular highlighted sections present the sub-wavelength field confinement at the corners of the metal layer. Other parameters are considered as $W_{core} = 350$ nm, $H_{slot} = 100$ nm, and $H_{Ag} = 200$ nm.	98
4.36	Effective index ($Re(n_{eff})$) and mode propagation length (L_p) variation of the HPW as a function of Si slab height (H_{Si}). Waveguide core (W_{core}), slot height (H_{slot}), and Ag height (H_{Ag}) are considered to be fixed as 350, 100, and 200 nm, respectively.	100
4.37	(a) and (b) show the evaluation of mode effective area A_{eff} of the HPW by different definitions as a function of H_{Si} . Other design parameters are considered as $W_{core} = 350$ nm, $H_{slot} = 100$ nm, and $H_{Ag} = 200$ nm.	100
4.38	Effective index ($Re(n_{eff})$) and mode propagation length (L_p) variation of the HPW as a function of slot height (H_{slot}). Waveguide core (W_{core}), Si slab height (H_{Si}), and Ag height (H_{Ag}) are considered to be fixed as 350, 220, and 200 nm, respectively.	102
4.39	(a) and (b) show the evaluation of mode effective area A_{eff} of the HPW by different definitions as a function of H_{slot} . Other design parameters are considered as $W_{core} = 350$ nm, $H_{Si} = 220$ nm, and $H_{Ag} = 200$ nm.	102
5.1	Refractive index variation with porosity (P) and change of equivalent refractive index of P-ZnO with volume fraction (V) of capillary condensed ethanol. . . .	108
5.2	Schematic diagram of a horizontal slotted composite plasmonic waveguide (HSCPW). (a) shows the geometrical cross-section of the proposed HSCPW where P-ZnO is used as low index medium sandwiched between high index silicon (Si) and lossy metal (Ag). The black bordered region depicts the one folded computational domain. (b) depicts the symmetrical arm Mach-Zehnder interferometer (MZI) where the HSCPW is used.	110
5.3	Simulated field profile of the dominated quasi-TM mode of the HSCPW. (a) and (b) illustrate the H_x and E_y field distributions, respectively.	112
5.4	1D line plot of fundamental mode E_y and H_x field along the symmetry line (y-axis). The red solid curve shows E_y field enhancement in the low index horizontal slot region, effective for sensing applications. The blue dashed-dotted line shows light guidance by the dielectric Si core.	113
5.5	Simulated H_y field profile of quasi-TE mode; (a) and (b) illustrate the H_y field distributions along x and y axes, respectively.	113

- 5.6 Real effective index ($Re(n_{eff})$) variation with the slot thickness (t_{slot}). Fundamental quasi-TE (H_y^{11}) and TM (H_x^{11}) modal real effective indices with t_{slot} variations are shown by green, red and blue dashed-dotted and solid lines for three different core widths (W_{core}) 350, 450, and 550 nm, respectively. The orange dotted line denotes the $Re(n_{eff})$ of the quasi-TM mode simulated by our code for benchmarking with [Alam *et al.*, 2011] shown by purple triangular markers. 115
- 5.7 Variation of the mode propagation length (L_p) with the t_{slot} . Quasi-TE modes (dashed-dotted lines) show higher L_p than quasi-TM mode (solid lines), shown by dashed-dotted and solid lines, respectively. 350, 450 and 550 nm W_{core} are represented by green, red and blue lines, respectively. The orange dotted line denotes the L_p of the quasi-TM mode simulated by our code for benchmarking with [Alam *et al.*, 2011] shown by purple triangular markers. 116
- 5.8 Quasi-TM and TE slot confinement variations with t_{slot} . The TM slot confinement ($\Gamma_{TM\ slot}$) and TE slot confinement ($\Gamma_{TE\ slot}$) variations for three different $W_{core} = 350, 450, \text{ and } 550$ nm are indicated by solid and dashed-dotted green, red and blue lines, respectively. $W_{core} = 450$ nm shows maximum $\Gamma_{TM\ slot}$ at $t_{slot} = 70$ nm. 117
- 5.9 (a) and (b) illustrates the normalised 1D-line plot of the dominant fundamental quasi-TM (E_y and H_x) field variations along y-axis for three different slot heights, $t_{slot} = 70, 100, \text{ and } 150$ nm. The field distribution along y-axis is taken at the left or right side of the HSCPW. Other parameters are kept fixed as, $W_{core} = 450$ nm, $t_{Ag} = 100$ nm, and $t_{Si} = 220$ nm. 119
- 5.10 The $\Gamma_{TM\ slot}$ variations with HSCPW core width (W_{core}) for two different t_{slots} . The red and green solid lines depict the same variations for $t_{slot} = 70$ and 100 nm, respectively. An over 41% power confinement is observed for $W_{core} = 450$ nm at $t_{slot} = 70$ and 100 nm. 120
- 5.11 Real part of the effective index ($Re(n_{eff})$) variations of the quasi-TE and TM modes against W_{core} for fixed values of $t_{slot} = 70$ and 100 nm. The solid and dashed-dotted lines depict the TM and TE modes, respectively. Other parameters, such as t_{Si}, t_{Ag} were kept fixed at 220 and 100 nm, respectively. 120
- 5.12 Variation of effective index change ($\Delta Re(n_{eff})$) of quasi-TM mode against volume fraction of ethanol into P-ZnO layer. Quasi-TE changes are shown as inset. The black, red, blue and cyan solid and dashed lines in main and inset plot depict the TM and TE modal $\Delta Re(n_{eff})$ changes due to different volume fraction of ethanol into 30%, 40%, 50%, and 60% porous ZnO layers, respectively. 121

5.13	(a) and (b) represent the HSCPW quasi-TM real effective index sensitivity ($S_{Re(TM)}$) and normalised attenuation sensitivity ($S_{Im(TM)}$) variations with volume fraction of ethanol into horizontal slotted P-ZnO layer, respectively. The black star, red ball, blue triangle, and cyan diamond markers on both figures illustrate the sensitivity variation with absorbed ethanol vapour into P-ZnO slot having porosity, $P = 30\%$, 40% , 50% , and 60% , respectively.	123
5.14	Normalised output power (P_{norm}) and phase sensitivity $ (\partial P_{norm})/(\partial(\Delta\phi)) $ variations against volume fraction of ethanol into P-ZnO. Blue diamond, red star, black square, and green triangle markers with dashed lines denote sinusoidal $ (\partial P_{norm})/(\partial(\Delta\phi)) $ variations for different porosity, $P = 30\%$, 40% , 50% , and 60% , respectively. The solid blue, red, black, and green lines indicate cosine natured P_{norm} variations for all four P-ZnO layers.	125
5.15	DNA hybridisation process in the horizontal slot region. A poly-L-lysine bio-linker layer is used to attach the target ssDNA.	128
5.16	(a) Schematic cross-section of the SOI based HSCPW to detect DNA hybridisation. (b) Quasi-TM E_y field profile of half symmetric HSCPW, (c) depicts the variation of the E_y field along the y-axis symmetry line and (d) denotes the light confinement variations due to presence of ssDNA and dsDNA.	129
5.17	shows the H_x field of the quasi-TM mode. One-fold waveguide symmetry is used for FV-FEM simulation.	130
5.18	Variation of the power confinement in the DNA bio-layer ($\Gamma_{Bio-layer}$) with Si core height (h_{Si}) for three different waveguide core widths, $W_{core} = 350$, 550 , and 750 nm. Other parameters such as thickness of top SiO_2 layer h_{SiO_2} , Au layer (h_{Au}), and slot height (h_{slot}) are kept fixed at 100 nm. The variation $\Gamma_{Bio-layer}$ for ssDNA and dsDNA are shown by the dashed-dotted and solid lines, respectively.	132
5.19	Variation of the power confinement in the DNA bio-layer ($\Gamma_{Bio-layer}$) with slot height (h_{slot}) for three different waveguide core width and height combinations, such as $W_{core} = 350$ and $h_{Si} = 210$ nm, $W_{core} = 550$ and $h_{Si} = 190$ nm, and $W_{core} = 750$ nm and $h_{Si} = 180$ nm. Other parameters such as h_{SiO_2} and h_{Au} are kept fixed at 100 nm. The variation $\Gamma_{Bio-layer}$ for ssDNA and dsDNA are shown by the dashed-dotted and solid lines, respectively.	133
5.20	Variation of real part of the effective index ($Re(n_{eff})$) of the sensitive quasi-TM mode and effective index change (Δn_{eff}) of the same mode due to DNA hybridisation against Si core height (h_{Si}) for three fixed core widths, $W_{core} = 350$, 550 , and 750 nm. A 100 nm h_{slot} is considered. The variation of $Re(n_{eff})$ for ssDNA and dsDNA are shown by dashed-dotted and solid lines, respectively.	134

5.21	Variation of real part of the effective index ($Re(n_{eff})$) of the sensitive quasi-TM mode and effective index change (Δn_{eff}) of the same mode due to DNA hybridisation against Si core height (h_{Si}) for three fixed core widths, $W_{core} = 350, 550, \text{ and } 750 \text{ nm}$. A 100 nm h_{slot} is considered. The variation of $Re(n_{eff})$ for ssDNA and dsDNA are shown by dashed-dotted and solid lines, respectively.	135
5.22	Variation of quasi-TM effective index change ($\Delta Re(n_{eff})$) against horizontal slot height (h_{slot}) for optimised W_{core} and h_{Si} combinations. The red, green, and blue solid lines indicate the $\Delta Re(n_{eff})$ variation for $W_{core} = 350, 550, \text{ and } 750$, and $h_{Si} = 210, 190, \text{ and } 180 \text{ nm}$, respectively.	135
5.23	Variation of quasi-TM effective index change ($\Delta Re(n_{eff})$) with bio-layer thickness (h_{bio}).	136
5.24	Variation of waveguide surface sensitivity ($S_{surface}$) with bio-layer thickness (h_{bio}) for $80 \text{ and } 100 \text{ nm}$ slot heights (h_{slot}).	136
5.25	Variation of waveguide bulk sensitivity (S_{bulk}) against sucrose solution concentrations for two different slot heights, $h_{slot} = 80 \text{ and } 100 \text{ nm}$.	137
6.1	Si refractive index variations with wavelength (λ) and temperature (T).	144
6.2	SiO_2 refractive index variations with wavelength (λ) and temperature (T).	145
6.3	Isopropanol (C_3H_8O) refractive index variations with wavelength (λ) and temperature (T).	146
6.4	Equivalent refractive index (n_{eq}) and index difference (Δn) of the isopropanol-water solution depending on the volume fraction (V%) of isopropanol (C_3H_8O) and water (H_2O) at the temperature, $T = 20^\circ\text{C}$. Isopropanol and water concentrations are highlighted in red and blue, respectively along the x-axis.	147
6.5	Dispersion of real and imaginary dielectric constants (ϵ_r and ϵ_i , respectively) of silver (Ag) at the room temperature ($T = 25^\circ\text{C}$).	148
6.6	Optical characterisation set-up (a) and schematic top view (b) of the metal strip loaded hybrid plasmonic waveguide (MSLHSPW) incorporated MZI. The MSLHSPW is butt-coupled with SiO_2 clad dielectric horizontal slot (DHS) waveguide at both ends in the sensing arm of length, $L_{Ref} = 2L(DHS) + L_{MSLHSPW}$. Only DHS is employed in the reference arm having four bending sections of radius, $R_B = 5 \mu\text{m}$ and three straight sections, $L_{R1}, L_{R2}, \text{ and } L_{R3}$. Thus, total length of the reference arm is $L_{Ref} = 2\pi R_B + L_{R1} + L_{R2} + L_{R3}$.	149
6.7	3D schematic diagram of the hybrid plasmonic waveguide assisted sensing arm section. The metal strip loaded horizontal slot hybrid plasmonic waveguide (MSLHSPW) acts as an active sensing region. The MSLHSPW is butt-coupled with the SiO_2 clad dielectric horizontal slot (DHS) waveguide at both ends. The inset figure shows a cross-section of the MSLHSPW.	150
6.8	(a) and (b) show the FV-FEM simulated quasi-TM H_x and E_y -field distributions of MSLHSPW, respectively.	153

6.9	shows the FV-FEM simulated quasi-TM E_y field distributions of the $Si/SiO_2/Si$ dielectric horizontal slot (DHS) waveguide.	153
6.10	The blue solid and red dashed lines represent the (a) E_y and (b) H_x field line plots along y-axis of the MSLHSHPW and DHS, respectively. Maximum quasi-TM E_y field confines in the slot which is highly sensitive to a small refractive index change in that region.	154
6.11	Effective index (n_{eff}), mode power attenuation (α') and slot confinement (Γ_{slot}) variations with the thickness (H_{Ag}) of silver metal film deposited on the SiO_2 buffer layer. The inset figure shows the confinement (Γ_{Ag}) variation of the Ag layer against H_{Ag} . Other parameters such as, Si slab width (W_{Si}), height (H_{Si}) and slot height (H_{slot}) are kept fixed at 700, 150 and 100 nm, respectively.	155
6.12	The contour plots in (a), (b), and (c) show the variations of n_{eff} , α' (dB/ μ m), and Γ_{slot} as a function of W_{Si} and H_{slot} . The H_{slot} and H_{Ag} are kept fixed at 100 and 150 nm, respectively. An abrupt variation of Γ_{slot} is observed due to the other higher order quasi-TE mode in a close proximity of the quasi-TM fundamental mode.	156
6.13	Variations of power confinement in slot (Γ_{slot}), clad (Γ_{clad}) and sensing region ($\Gamma_{slot+clad}$) with W_{Si} are shown in the figure. The solid black, red dashed and blue dashed-dotted curves represent the Γ_{slot} , Γ_{clad} , and $\Gamma_{slot+clad}$ variations, respectively. H_{slot} and $H_{Si} = H_{Ag}$ are kept fixed at 100 and 150 nm, respectively.	158
6.14	Variations of power confinement in slot (Γ_{slot}), clad (Γ_{clad}) and sensing region ($\Gamma_{slot+clad}$) with H_{Si} are shown in the figure. The solid black, red dashed, and blue dashed-dotted curves represent the Γ_{slot} , Γ_{clad} , and $\Gamma_{slot+clad}$ variations, respectively. W_{Si} , H_{slot} , and H_{Ag} are kept fixed at 740, 100, and 150 nm, respectively.	158
6.15	(a) and (b) show the power confinement (Γ) variations in the horizontal slot, clad and sensing region (slot + clad) of the quasi-TM and TE modes against slot height (H_{slot}). W_{Si} and $H_{Si} = H_{Ag}$ are kept fixed at 740 and 150 nm, respectively.	159
6.16	Variation of the coupling length (L_c) with gap or separation of the dielectric horizontal slot (DHS) based coupler. Inset shows the cross-section of the $Si/SiO_2/Si$ DHS waveguide coupler whose dimensions are taken as, $W_{Si} = 740$ nm, $H_{Si} = 150$ nm, and $H_{slot} = 100$ nm.	162
6.17	(a) depicts the input power requirements in the sensing (P_{in-Sen}) and the reference arms (P_{in-Ref}) depending on the MSLHSHPW length ($L_{MSLHSHPW}$) in the MZI sensing arm. (b) shows the desired coupling section (L_x) variations of the input directional coupler as a function of MSLHSHPW length ($L_{MSLHSHPW}$) and gap.	163
6.18	shows the fringe visibility (V , V') of the MZI interference output with equal and unequal power splitting. For the 50:50 equal and unequal power splitting, the V-parameters are calculated using Eq. 6.16 and 6.18, respectively.	165

6.19	illustrates the variation of the MZI FSR as a function of L_{Ref} for fixed length of MSLHSHPW.	166
6.20	illustrates the variation of the MZI FSR as a function of L_{Ref} for fixed length of MSLHSHPW.	167
6.21	(a) - (f) MZI transmitted output power for the temperature sensing of 100% isopropanol liquid. The figures (a), (b), and (c) on the left column indicate the transmission spectra with the FSR value of 10 nm. The right-sided figures (d), (e), and (f) indicate the same with the $FSR = 15$ nm. Figures in each row (a, d), (b, e) and (c, f) depict the output responses of the MZI with 20, 30, and 40 μm long $L_{MSLHSHPW}$, respectively.	168
6.22	(a) and (b) represents the wavelength shift ($\Delta\lambda_T$) variations with the changing temperature of isopropanol for 10 and 15 nm FSR values, respectively. Slope of each curve represent the MZI sensitivity (S_T) as a temperature sensor. . .	169
6.23	(a) - (f) indicate the MZI transmitted spectra for the volume concentration sensing of the isopropanol/water solution at a fixed temperature of 20°C. The figures (a), (b), and (c) on the left column indicate the output transmission spectra with the FSR value of 10 nm. The right-sided figures (d), (e), and (f) indicate the same with the $FSR = 15$ nm. Figures in each row (a, d), (b, e) and (c, f) depict the output responses of the MZI with 20, 30, and 40 μm long $L_{MSLHSHPW}$, respectively.	170
6.24	(a) and (b) represents the linear variations of wavelength shift ($\Delta\lambda_C$) with the volume concentration of isopropanol for 10 and 15 nm FSR values, respectively. Slope of each curve represent the MZI sensitivity (S_C) as a chemical concentration sensor.	171
7.1	3D schematic diagram of the single vertically-slotted straight SOI based resonator. Red dashed box is showing the computational domain. Insets are showing the mid-sliced plane with dominant E_x field profile along x-axis shown by black lines.	177
7.2	Cross-section of the 3D vertically slotted straight resonator. The x-y plane cross-sectional geometry of the device is similar to the vertically slotted waveguide. . .	179
7.3	Optimisation of Si core width (W) depending on confinement factor (Γ). Total slot confinement ($\Gamma_{slot-total}$) and confinement of 5 nm sensing layer into slot versus Si core width (W) for a fixed Si core/slot height (H) of 220 and 324 nm. Slot width (W_s) is kept fixed at 100 nm. The cover medium, slot region, and sensing layer into slot are filled with water.	180
7.4	Left side scale shows the power confinement ($\Gamma\%$) variation of different regions, such as sensing layer into slot, Si core, and cover medium with Si core or slot height (H). Right side scale shows the effective index (n_{eff}) variation with H . The Si core width (W) and slot width (W_s) are fixed at 190 and 100 nm. A 5 nm ultra-thin bio-layer is considered for surface sensing.	181

7.5	Si core or slot height (H) optimisation depending on confinement factor (Γ), normalised power density (NPD) and Δn_{eff} . The green dashed-dotted, blue dashed, and red solid lines depicts the variation of total slot confinement ($\Gamma_{slot-total}$), Δn_{eff} , and normalised power density (NPD), respectively with slot height (H). The Si core width (W) and slot width (W_s) are kept fixed at 190 and 100 nm, respectively. The cover medium, slot region, and the sensing layer into slot are filled with water.	182
7.6	Optimisation of slot width (W_s). The solid lines (red, green, and blue) illustrates the variation of $\Gamma_{slot-total}$, $\Gamma_{slot\ sensing\ layer}$, and Δn_{eff} with W_s for $W = 170$ nm and $H = 500$ nm and the dashed-dotted lines (red, green, and blue) depicts the same for 190 nm Si strip width (W) and 500 nm height (H).	183
7.7	Enhanced E_x field into slot region for optimised structural dimensions: Si strip width (W) = 170 nm, height (H) = 500 nm, and slot width (W_s) = 130 nm. Full-vectorial 2D FV-FEM code is used for simulation.	184
7.8	(a) and (b) illustrate the 1D line plot of the normalised E_x field of the vertically slotted quasi-TE mode along x and y-axes, respectively. Field plots are generated by 2D FV-FEM simulations.	185
7.9	Resonating wavelength (λ_{res}) variation with the number of nodes in the three dimensional mesh distributions. A non-uniform, unstructured tetrahedral elements have been used for the 3D domain discretisation.	187
7.10	Surface sensing of the proposed device with optimised design parameters. The red line depicts a linear resonance wavelength shift ($\Delta\lambda_{res}$) for different bio-layer thickness of refractive index 1.45. The blue stars denote the surface sensitivity ($S_{surface}$) variation with bio-layer thickness ranging from 5 to 50 nm.	188
7.11	Bulk refractometric sensitivity (S) analysis of vertically single slotted waveguide with optimised design parameters at 1550 nm. The slope of the curve denotes the sensitivity of the slot waveguide while the cover medium is filled with sucrose solution.	190
7.12	Bulk sensitivity (S_{bulk}) analysis of the proposed device. Resonating wavelength shift versus refractive index variation ($\Delta n_{sucrose}$) of sucrose solution at ambient temperature (20°C). The solid lines illustrate the resonating wavelength shift when the perfect electric walls (PEW) are touching the end faces of Si core. The dashed lines present the same when the PEWs are 300 nm away from both end faces of the Si core. The slope of each linear curve represents the sensitivity (S_{bulk}) for the filled and empty conditions.	191

7.13	The dominant E_x field (2D and 3D) confined into straight single slotted resonator with optimised design parameters at the telecommunication wavelength. Field profiles are generated by post-processing of eigenvectors of resonating wavelength (λ_{res} being an eigenvalue), (a) shows the E_x field profile of slot resonator on an x-z sliced plane and (b) depicts the 3D iso-surface profile of E_x field. The PEWs are considered at both end faces of the Si cores. (c) 3D iso-surface profile of confined E_x field when the boundary PEWs are 300 and 500 nm away from both end faces and side faces of Si strips, respectively. A full-vectorial 3D FV-FEM code is used for complete resonating structure simulation.	193
C.1	Schematic diagram of a 3D air filled rectangular cavity with dimensions $a = 5$ cm, $b = 4$ cm, and $c = 10$ cm along x, y, and z directions. The cavity is considered to be enclosed with perfect electric walls (PEW).	213
C.2	Variation of computed TE_{101} wavenumber (k_0) of the empty rectangular cavity (Fig. C.1) against penalty term (p). The physical solution varies very slowly and its wavenumber(k_0) for each p are connected by a black dashed line. Other scattered points represent the non-physical spurious modes.	215
C.3	H_x (top row) and H_z (bottom row) field distributions of TE_{101} mode with penalty term, $p = 0, 0.1$, and 0.5	215
C.4	(a) shows the wavenumber (k_0) variation of different modes such as TE_{101} , TE_{011} , TE_{102} , TM_{110} , degenerated TE_{111} and TM_{111} , and TM_{210} with penalty term (p); (b) illustrates the variation of numerical %error of those modes against penalty term. A 3D unstructured mesh with 18076 nodes is used for domain discretisation.	216
C.5	Schematic diagram of a 3D air filled rectangular cavity of dimensions $a = 5$ cm, $b =$ cm, and $c = 10$ cm along x, y, and z directions. The cavity is considered to be enclosed with perfect electric walls (PEW).	217
C.6	Schematic diagram of a 3D air filled rectangular cavity of dimensions $a = 5$ cm, $b =$ cm, and $c = 10$ cm along x, y, and z directions, respectively. The cavity is considered to be enclosed with perfect electric walls (PEW).	219

LIST OF PUBLICATIONS

Published Journal Articles

1. **Ghosh, S.** and Rahman, B. M. A., [2017], ‘An innovative straight resonator incorporating a vertical slot as an efficient bio-chemical sensor’, *IEEE Journal of Selected Topics in Quantum Electronics*, **23**(2), pp. 132 – 139.
2. **Ghosh, S.** and Rahman, B. M. A., [2017], ‘A compact Mach-Zehnder interferometer using composite plasmonic waveguide for ethanol vapor sensing’, *Journal of Lightwave Technology*, **35**(14), pp. 3003 – 3011.
3. **Ghosh, S.** and Rahman, B. M. A., [2018], ‘Evolution of plasmonic modes in a metal nano-wire studied by a modified finite element method’, *Journal of Lightwave Technology*, **36**(3), pp. 809 – 818.
4. **Ghosh, S.** and Rahman, B. M. A., [2018], ‘Design of on-chip hybrid plasmonic Mach-Zehnder interferometer for temperature and concentration detection of chemical solution’, *Sensors and Actuators B: Chemical*, **279**, pp. 490 – 502.
5. Gulistan, A., **Ghosh, S.**, Ramachandran, S. and Rahman, B. M. A., [2017], ‘Efficient strategy to increase higher order inter-modal stability of a step index multimode fiber’, *Optics Express*, **25**(24), pp. 29714 – 29723. **(Not a part of this thesis)**
6. Karim, M. R., Ahmad, H., **Ghosh, S.**, and Rahman, B. M. A., [2018], ‘Design of dispersion-engineered As₂Se₃ channel waveguide for mid-infrared region supercontinuum generation’, *Journal of Applied Physics*, **123**(21), pp. 213101-1–6. **(Not a part of this thesis)**

Papers Presented at Conferences

1. **Ghosh, S.** and Rahman, B. M. A., [2016], December, 'Full vectorial finite element modelling: a composite plasmonic horizontal slot waveguide as a bio-sensor', *International Conference on Fibre Optics and Photonics, OSA*, (pp. Tu5C-3), IIT-Kanpur, India. (**Best paper award**)
2. **Ghosh, S.**, Pan, C. and Rahman, B. M. A., [2017], August, 'Cross-slot waveguide and compact straight slotted resonator based bio-chemical sensors', *IEEE 14th International Conference on Group IV Photonics (GFP)*, (pp. 75-76), Berlin, Germany.
3. **Ghosh, S.** and Rahman, B. M. A., [2018], February, 'Design of ultra-compact composite plasmonic Mach-Zehnder Interferometer for chemical vapor sensing', *Integrated Optics: Devices, Materials, and Technologies XXII, SPIE. Photonics West*, (vol. 10535, pp. 1053505), California, USA.
4. Dhingra, N., Song, J., **Ghosh, S.**, Zhou, L. and Rahman, B. M. A., [2018], February. 'Design of phase change $\text{Ge}_2\text{Sb}_2\text{Te}_5$ based on-off electro-optic switch',. *Silicon Photonics XIII, SPIE. Photonics West* (Vol. 10537, pp. 105370Z). California, USA. (**Not a part of this thesis**)

Book Chapter

1. **Ghosh, S.**, Dar, T., Viphavakit, C., Pan, C., Kejalakshmy, N., and Rahman, B. M. A., [2018], 'Compact Photonic SOI Sensors', in 'Computational Photonic Sensors', (pp. 343–383), *Springer, Cham*.
2. Atia, K. S., **Ghosh, S.**, Heikal, A. M., Hameed, M. F. O., Rahman, B. M. A., and Obayya, S. S. A., [2018], 'Finite Element Method for Sensing Applications', in 'Computational Photonic Sensors' (pp. 109–151), *Springer, Cham*.

INTRODUCTION

1.1 Objectives and Motivations

Advancement of photonic technology not only shows its maturity in telecommunications but also shows a great potential in diverse field of applications such as optical trapping [Ashkin *et al.*, 1987; Neuman and Block, 2004], tweezing [Curtis *et al.*, 2002], quantum computations [Kok *et al.*, 2007; O’Brien, 2007], and sensing [Narayanaswamy and Wolfbeis, 2013]. Among them, photonic sensors have a close relation with daily human life from environmental monitoring to medical diagnoses where light science and technologies are used for detection and measurements. In a photonic sensor, the measurand modulates the guided light and that can be analysed to interpret the physical or chemical changes in the measurand. A positive growth in Photonic sensors can be observed after the development of optical fibre. Giallorenzi *et al.* [1982] and Grattan and Sun [2000] have shown the contributions of the optical fibre sensors in temperature, pressure, strain, chemical, magnetic, and acoustic by means of different transducer technologies such as Mach-Zehnder, Michelson, Fabry-Perot, Sagnac interferometers. Photosensitivity of the optical fibre helps to inscribe the Bragg gratings [Meltz *et al.*, 1989] and long period gratings [Bhatia and Vengsarkar, 1996] in fibre core. Since its development grating based fibre sensors became key technology for sensing. Innovation of photonic crystal fibre [Birks *et al.*, 1995; Knight *et al.*, 1996] and special

type fibres made a remarkable progress in optical sensing.

Billions of dollars have already been invested and a positive market growth can be observed due to increasing demands of photonic sensors in smart-phones, chemical, food, and pharmaceutical industries. A report published by Market Research Future, a technology forecast consultancy company, states that the optical sensing market is expected to grow nearly about 3.10 Billion USD by 2023 with a compound annual growth rate (CAGR) of $\sim 14.3\%$ between 2017 and 2023 [Future, 2018]. This positive growth rate in photonic sensing industry impose a considerable amount of responsibility on scientists and researchers. These increased legislative requirements motivate one to apply novel phenomena in the development of integrated, compact, and nano dimensioned photonic devices mainly for accurate measurement of chemical, physical and biological parameters, such as humidity, temperature, hazardous gases, stress, strain, pressure, displacements, surface roughness, microscopic living substance, DNA hybridisations etc.

Integrated photonic sensors can easily be designed with pure dielectric materials, noble metals, and in combination of both. Dielectric optical sensors are loss less and can easily be developed by the well-known CMOS fabrication technology. However, dielectric materials in combination with metals forms a novel type of waveguide where the guided light mode is a combination of dielectric guided wave and excited surface plasmon polaritons (SPPs). It can be termed as hybrid or composite plasmonic waveguide. This allows a sub-wavelength light confinement which can be used for an enhanced light-matter interactions. Although, presence of lossy material introduces modal losses, however, a greater sensitivity could be obtained with a smaller device footprint.

Compared to other commercially available electrical and electronic sensors, the photonic sensors are more reliable to use in hazardous atmosphere where other conventional sensors are unsafe due to fire, electrical short-circuit, high temperature, corrosive environment, radiation risk, and high electromagnetic interferences. On the other hand, for real-time medical and bio-chemical sensing, the sensor should be light weight, compact, and portable along with high precision and sensitivity. Dielectric material and noble metal-based optical waveguides and resonators would serve those purposes for both invasive and non-invasive measurements. Although, most commercially available sensors are mainly fibre based, the state-of-the-art fabrication technology leads researchers to

work on innovative high index contrast and composite material based integrated on-chip sensors.

Design of a complete photonic system often requires individual component assessment to evaluate its performance for the specially dedicated purpose. Analytical, semi-analytical and numerical modelling are often considered for an accurate and optimised device design. Thus, advanced photonics modellings are helpful to predict and understand the complex sensor characteristics before expensive production and experimental validations. A complete sensing device comprises of many distributed complex optical waveguides and supportive components. Understanding of fundamental light guiding phenomenon and wave propagation characteristics through the optical components are necessary for their effective use. Several modelling methods have already available based on analytical and semi-analytical approaches. However, a pure analytical and semi-analytical method exhibits its inefficiency for the solution of today's practical waveguides where the power confines in a transverse plane. Analytical approach only can solve the planar waveguide by analysing the transcendental equations by taking field continuity at the material interfaces. In 1969 and 1970 Marcatili [1969], Goell [1969], and Knox and Toullos [1970] have introduced semi-analytical methods which can only handle simple waveguide problems but inadequate to solve complex waveguide geometries containing inhomogeneous and anisotropic materials. Over last 40 years, several methods have been developed such as the matrix methods [Sharma *et al.*, 1983], mode matching method [Dagli and Fonstad, 1985], finite difference method [Bierwirth *et al.*, 1986], method of lines [Rogge and Pregla, 1991], and the spectral index method [Stern *et al.*, 1990]. Beside these approximated approaches, the full-vectorial finite element method (FV-FEM) shows its high efficiency for design, optimisations, and performance analysis of complex structured waveguides and resonators [Rahman and Davies, 1984*a,b*, 1988]. Any arbitrarily shaped waveguide geometry with isotropic and anisotropic multi-layered materials can easily be handled by this powerful numerical tool. Simple mathematical formulations and clever use of memory management algorithm for sparse matrices can make this method suitable for readily available computer workstations.

1.2 Thesis Outline

This thesis comprises eight chapters, including the current introduction chapter and three appendices. The chapter contents are briefly described as follows:

Chapter 2 presents the review of different photonic sensing technologies. Integrated photonic sensing method is emphasised and relevant works are reviewed and presented in a table form. Different widely-used time and frequency domain numerical methods, useful for rigorous design and optimisation of photonic integrated sensors and their advantages and disadvantages are also reviewed in this chapter.

Chapter 3 consists of the numerical approaches used for design, optimisation, and performance analyses of the waveguides and resonators used in this research work. The two-dimensional full-vectorial method (FV-FEM) is redeveloped with a direct divergence modified approach especially for an accurate modal analysis of plasmonic and complex hybrid plasmonic waveguides. In the next section, a three-dimensional FV-FEM, useful for resonator problems, is developed and its mathematical steps are described in detail. Appendices A and B contain the calculation of global matrix elements used for the 2D and 3D FV-FEM, respectively. Benchmarking and validation of the 3D FV-FEM code has been demonstrated in Appendix C. To study the waveguide junctions and modal losses the least squares boundary residual (LSBR) method and perturbation formulation are used.

Chapter 4 focuses on the modal analyses of different waveguides such as metal nano-wire, low index contrast optical fibre, high index contrast silicon-on-insulator (SOI) based ridge, vertical and horizontal slot waveguides, and hybrid plasmonic slot waveguide with the newly modified 2D FV-FEM. A metal nano-wire with identical and non-identical cladding conditions are considered and corresponding plasmonic modal evolutions with different design parameters are studied rigorously. In the next section, a comparative investigation is carried out on different mode effective area (MEA) formulations and their applicability to determine the effective area (A_{eff}) of the low and high index contrast and hybrid plasmonic waveguides.

Chapter 5 presents two different designs of the horizontal composite plasmonic waveguide (HSCPW) and its applications in chemical vapour and bio-chemical surface sensing. In the first section, a porous ZnO (P-ZnO) layer of different porosity is considered

to be sandwiched in between metal (silver) and high index dielectric silicon (Si) to form a horizontal slot waveguide and it is incorporated to design a compact Mach-Zehnder interferometer (MZI). Maximum light confines into P-ZnO slot region ($\sim 41\%$). The refractive index change due to capillary condensation of the absorbed ethanol vapour into ZnO mesopores of different porosities are obtained in terms of MZI phase sensitivity. In the second section, a metal layer (gold) is suspended on top of Si to form a horizontal slot. The waveguide design is optimised based on the power confinement in the bio-layers (ssDNA and dsDNA), useful for a surface sensing mechanism. A considerably high power confinement ($\sim 8\%$) is obtained which results in the waveguide surface sensitivities of 0.0025 and 0.0019 RIU/nm for 80 and 100 nm slot height, respectively.

Chapter 6 presents a design of a metal strip loaded horizontal slot hybrid plasmonic waveguide (MSLHSPW) and its applications in temperature and liquid concentration sensing. A horizontal slot is formed in between deposited metal (silver) layer on silica (SiO_2) and a suspended Si layer. The waveguide design is optimised for maximum slot confinement ($\sim 60\%$) which gives a maximum waveguide sensitivity of 1.13. This MSLHSPW is then incorporated in an asymmetric Mach-Zehnder interferometer (MZI) to detect the temperature and concentration change of the isopropanol solution. Asymmetric power splitting scheme is adapted to enhance the MZI fringe visibility to the ideal value (≈ 1). This single on-chip sensor design provides a considerable high temperature and chemical concentration sensitivity of 243.9 pm/ $^{\circ}C$ and 437.3 nm/RIU, respectively.

Chapter 7 describes a design of silicon-on-insulator (SOI) based vertical slotted straight resonator which is free from the bending losses like ring resonator. The slot design parameters are optimised for maximum light confinement for both bulk and surface sensing applications. The resonator length is then calculated with the optimised design parameters. Finally, the resonator performance is evaluated by using the newly developed 3D FV-FEM. A sucrose solution and an ultra-thin bio-layer (refractive index 1.45) are considered for bulk and surface sensing, respectively. This straight resonator provides a 5.2 nm resonating shift for surface sensing and high bulk sensitivity of 820 nm/RIU.

This thesis concludes with the **Chapter 8** which summarises all the findings and explores the possible directions of future research work.

OVERVIEW OF PHOTONIC SENSORS AND ITS MODELLING

2.1 Introduction

This chapter provides a comprehensive review of photonic devices and its application in sensing technologies. The study starts with the concepts of different light guiding mechanisms with detailed description of various optical waveguide and resonator designs. It proceeds with a discussion of different numerical methods suitable for modelling those photonic devices. Finally, we have summarised some of the most recent and relevant works on dielectric and hybrid plasmonic slot waveguide based integrated optical sensors.

2.2 Principles of Optical Sensing Technology

A sensor transform a measurable physical parameter into an electrical or electronic signal which can be manipulated or measured easily to quantify the measurand parameter. A photonic sensor follows the same definition but here the measurable parameters can be encountered by means of a bunch of guided photons i.e. light. Nowadays, utilisation of light probe for optical sensing is considered as one of the most efficient approach. Optical sensing technology gained its maturity after 1960, the invention and demonstration of laser. Photonic sensors can be classified as intrinsic and extrinsic depending on its

application choice. If a waveguide itself acts as a sensor probe, an intrinsic sensor is formed, however, in an extrinsic sensor, the waveguide only guides the light from a sensing element to another optical element for light-matter interaction. Photonic sensors can also be classified into two sections such as labelled and label-free sensors. Apart from this broad classification, the photonic sensors can also be categorised by the way of their sensing mechanisms for different applications. All these mechanisms have been discussed in following sections.

2.2.1 Fluorescence-based Sensing

One of the widely used labelled sensing mechanism is fluorescence sensing which shows a change in spectral property in response to the analyte. Florescence refers to the emission of light of different wavelength by a substance after it absorbs light. It happens when an orbital electron of a molecule moves to the ground state from an excited state by emitting a photon. In most cases, the emitted photon has lower energy, thus a higher wavelength of the electromagnetic wave associated with it, than the absorbed radiation. It can be explained as:

$$\text{Excitation:} \quad E_0 + h\nu_{excite} \rightarrow E_1 \quad (2.1)$$

$$\text{Emission:} \quad E_1 \rightarrow E_0 + h\nu_{emission} + \text{heat} \quad (2.2)$$

where E_0 , E_1 are the ground and excited energy states. h is the Planck's constant. ν_{excite} and $\nu_{emission}$ are the frequency of the excited and emitted light, respectively.

The change in spectral property can be obtained in the intensity, emission spectrum, anisotropy, or the lifetime of the fluorophore [Lakowicz, 2006]. The most common approach is when the fluorescence intensity varies due to analyte properties, shown in Fig. 2.1(a). However, this scheme is often inconvenient to use because the fluorescence intensity may vary due to many reasons. The fluorophore concentration is not easy to control in sample locations. Also the local fluorophore concentration changes in a random fashion due to diffusion or photo-bleaching. This limitation can be overcome by following the measurement which is independent of fluorophore concentration. An intensity ratio could be considered where spectral shifts occur in the emission or absorption spectra due to binding of analyte, shown in Fig. 2.1(b). In reverse analysis, the analyte

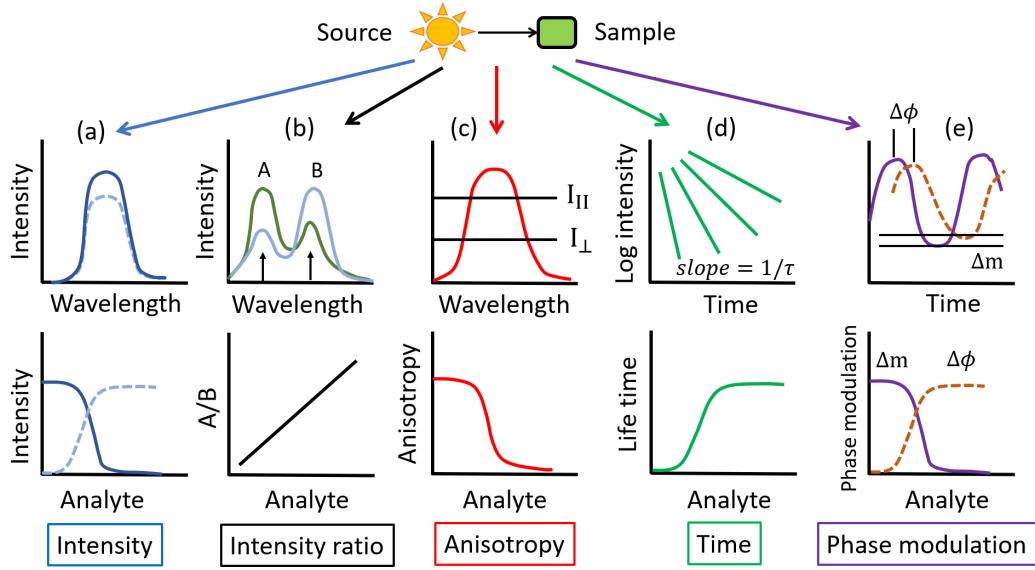


Figure 2.1: Different fluorescence sensing mechanism spectra. Figures from left to right define the sensing schemes depending on intensities (a), intensity ratio (b), anisotropies (c), time-dependent lifetimes (d), and phase-modulation measurements. Reproduced from [Lakowicz, 2006]

concentration can be calculated by taking ratio of spectral intensities measured at two excitation and emission wavelengths. Additionally, another ratio-based measurement depends on fluorescence polarisations or anisotropy where the sample analyte causes the change in the anisotropy [Canet *et al.*, 2001]. Anisotropy value can be obtained by taking ratio of polarised intensities. Anisotropic fluorescence measurements are independent of fluorescence material concentrations until the measurements are influenced by autofluorescence or poor signal-to-noise of the measurement devices. Fluorescence lifetime is also an useful parameter for sensing measurements where the intensity based measurements are inadequate to produce reliable results. The lifetime can be measured either by using time-domain (shown in Fig. 2.1(d)) [Szmecinski and Lakowicz, 2002, 1995] or by frequency-domain (shown in Fig. 2.1(e)) methods [Szmecinski and Lakowicz, 1993; Lakowicz and Maliwal, 1993; Harms *et al.*, 1999]. In the time domain measurements, an intensity slope i.e. decay which is free from the signal attenuation, can be used. If the lifetime is determined by either phase or amplitude modulations then the values are free from intensity measurements.

Although, this technique can accurately sense a small fractional change in target analyte, however, a fluorescence sensor also offers some disadvantages which makes it

difficult to implement it outside of a testing laboratory. These disadvantages can be listed as:

1. A foreign body such as fluorophore may damage the sensor and its performance.
2. Fluorescence sensing may face observation difficulties due the photo-bleaching. It is a photochemical alteration of a fluorophore molecule or dye due to change in covalent bonding or some reactions between fluorophore and sample analyte. It can damage the dye permanently to fluoresce.
3. Dye or fluorophore response may get affected by local pH and/or oxygen.
4. Reaction between dye and analyte may damage the living substances in the sample under observations.
5. This process requires expensive, dedicated optical devices for interrogations.

2.2.2 Frequency Comb-based Sensing

Frequency comb-based measurement was first introduced in late 1990s that has reformed the precise measurements of time and frequency by directly linking microwave and optical frequencies [Ferreira *et al.*, 2017]. A frequency comb can be defined as an optical spectrum consisting of phase coherence equidistant narrow lines. A femtosecond mode-locked laser can generate millions of laser modes as lines with an equidistant gap. It can be used as an optical ruler in frequency space if the comb frequencies are known. A separation between different optical frequencies can easily be determined with that. Nowadays, researchers have applied laser optical combs for distance [Schuhler *et al.*, 2006; Salvadé *et al.*, 2008], strain [Minamikawa *et al.*, 2018; Zhang, Lu, Chen, Huang, Liu and Jiang, 2012], optical coherence tomography [Bajraszewski *et al.*, 2008], and also for atomic and molecular spectroscopy [Hasegawa and Sasada, 2017; Gatti *et al.*, 2012; Mandon *et al.*, 2009]. The broadband frequency comb spectroscopic sensing have already been demonstrated in mid-IR region that can detect ppb level of molecular concentrations with hundreds of MHz resolution in less than a minute acquisition time [Foltynowicz *et al.*, 2011].

Frequency comb-based sensing is in its early stage of development. Current research and continuous progress could lead this technology to the next generation molecular sensing beyond spectroscopic limits.

2.2.3 Terahertz (THz) Sensing Technology

Terahertz (THz) band refers to the electromagnetic spectrum that lies between microwaves and infrareds with wavelengths and frequencies between 10 mm and 30 μm , and 30 GHz and 10 THz, respectively. This frequency region was untouched until the development of ultra-fast mode lock laser and semiconductor based photo-conductive emitters and detectors. This gives rise to the time-domain terahertz spectroscopy [Cheung and Auston, 1986]. It has a great potential for label-free characterisations of DNA and RNA topology. The spectroscopic analysis shows a unique complex refractive index in the THz frequency domain as a function of the binding state of the analysed DNA sequence. Therefore, by analysing the THz spectra one can infer the binding state of the oligo- and polynucleotides [Brucherseifer *et al.*, 2000; Bolívar *et al.*, 2004]. In addition to THz spectroscopy, THz imaging also has a great potential for non-destructive, non-contact sensing, especially for security applications. As non-metallic and many non-polar materials are transparent to the THz radiation, thus, it can easily detect hidden weapons. Many target explosives, bio-chemicals, and illegal drugs have characteristic THz spectra that can be used to identify the hidden chemical compounds. Moreover, THz radiation has minimal health risk on human body [Federici *et al.*, 2005] thus, THz based sensors and imaging systems have a wide applications in defence and securities. Many explosives such as C-4, HMX, TNT, and RDX and illegal drugs have unique fingerprints in the THz range. Therefore, any hidden suspicious materials could easily be detected by analysing either the reflective or transmissive spectra.

Apart from THz spectroscopy and imaging based technologies, there has been an extensive research on other types of THz sensors and detectors. For instance GaAs/AlGaAs-based quantum well infrared photo-detector at a wavelength of 84 μm [Graf *et al.*, 2004]. Graphene and semiconductor nano-wire assisted field effect transistors (FET) act as THz detectors [Vicarelli *et al.*, 2012; Vitiello *et al.*, 2011]. A FET channel acts as a resonator of plasma waves. Nonlinear properties of that electron plasma waves in a commercial

GaAs/AlGaAs and in a double quantum well FET channel can be used for detection and mixing of THz frequencies [Teppe *et al.*, 2005; Knap *et al.*, 2009]. THz radiation can also be useful for detection of water content biological pathogens [Castro-Camus *et al.*, 2013], complex dynamics and structures of proteins [Falconer and Markelz, 2012], food inspection [Yan *et al.*, 2006] and as a probing tool for various industrial applications.

Recent researches on the THz-based sensors have shown its enormous potential as an inspection tool for various applications. However, the relatively expensive components of the sensing probe make this technology remain away from the normal commercial uses.

2.2.4 Plasmonic Sensors

Surface plasmon based sensing is one of the label-free matured method of photonic sensing technology where a surface plasmon resonance (SPR) is used to detect a small refractometric change in local and bulk sensing material. The SPR occurs at the interface of metal and dielectric having dielectric constants of opposite signs. The evanescent field of the guided wave by the dielectric medium excites the free electrons at the metal surface. These results in electron charge density oscillations and forms a surface plasmon wave (SPW). Often the TM-polarised SPW undergoes a phase change if the SPW comes in contact with the target analyte. This phase change can be measured and correlated with the change in analyte. Here, the phase matching condition between dielectric waveguide guided core mode and a plasmonic mode which is directly influenced by the adjacent sensing analyte is exploited. When the phase matching condition is satisfied, the power from the guided mode couples to the highly lossy plasmonic mode. Therefore, sensitivity of the SPR-based devices can be derived from the change in power loss of the guided mode. The SPR phenomenon was first proposed by Kretschmann and Otto in late 1960s [Kretschmann and Raether, 1968; Otto, 1968]. In Otto configuration, evanescent light wave from the prism wall interact and excites the plasma wave on the inward surface of a closely placed thin metal film. Besides, in the Kretschmann configuration, a thin metal film is evaporated onto the prism wall. Thus, evanescent wave penetrates the metal film and excites the surface plasmon wave. This SPW excitation happens at a certain incident angle (θ), also known as SPR angle, of illumination that can be obtained as a dip in the intensity distribution of the reflected light. Thus, a minor change in the nearest dielectric

media may shift the SPR angle results in a shift in the intensity dip. This scheme has much potential in the field of real-time optical sensing.

Later on, an extensive research has been done on plasmonic based waveguides and devices to obtain highly sensitive and compact sensors. In most cases, multimode fibres were widely used to exploit the long range surface plasmon polariton (LRSP) with lower attenuation which is useful to enhance the device sensitivity due to its much longer length of light-matter interaction [Trouillet *et al.*, 1996; Sharma *et al.*, 2007; Jorgenson and Yee, 1993]. Single mode fibre can also be used to excite the SPW by polishing one side of the fibre (D-shaped) and deposit a thin metal layer over the polished region [Slavik *et al.*, 1999; Piliarik *et al.*, 2003]. In this case, the fundamental guided mode excites the plasmon mode at the interface between metal and sensing medium and corresponding resonance occurs if these two dielectric and the plasmonic modes are closely phased matched. Thus, a small refractive index change adjacent to metal surface due to receptor molecule and target analyte interaction can be determined by means of resonant wavelength shift. A metal coated complete circular single mode fibre without a D-shaped side-polished profile can also be used for surface plasmon excitation [Sharma and Gupta, 2005]. Chen *et al.* [2014] have shown a low-index polymer (CYTOP) and metal coated circular single mode fibre (SMF-28) sensor where the fibre cladding modes couple to LRSPs on the metal-analyte interface, useful for bulk and surface sensing. Besides, a metal coated tapered fibre sensing probe also has a great impact as a SPR based sensor [Verma *et al.*, 2008, 2007]. It has been shown that the increasing taper ratio helps to increase the penetration depth of the evanescent field of the guided mode which, therefore, enhance the device sensitivity. However, tapering of the fibre core makes the fibre probe more fragile. Additionally, a U-shaped SPR-based fibre sensor have been proposed by [Verma and Gupta, 2008] where an optimum bending radius can be obtained to achieve a maximum probe sensitivity, even better than the tapered fibre. The U-bent fibre covered with gold (Au) [Satija *et al.*, 2014] and silver (Ag) [Dutta *et al.*, 2011] nano-particles also have been exploited for the SPR based fibre optic sensing applications.

2.2.5 Photonic Crystal Fibre-based Sensors

Optical fibre-based sensors is a well-developed technology and can be used in different types of sensing devices and transducers. Since 1980s, many researchers developed SPR-based single mode and multimode side-polished, U-shaped, tapered fibre probes for sensing applications that have already been discussed in the previous section (Section 2.2.4). On the other hand, after introduction of photonic crystal fibre (PCF) by [Birks *et al.*, 1995; Knight *et al.*, 1996], a new concept of fibre-based sensing came under researcher's interest. PCF is a special type of optical fibre with periodic micro-structured air-holes in the transverse cladding plane [Russell, 2003]. This fibre is fabricated with a single material, typically silica, and different structured air-hole arrays along the fibre length. PCF allows to confine light in small solid core via modified total internal reflections. This type of fibre shows high nonlinear coefficients [Dudley and Taylor, 2009], controllable dispersion, and mode shape properties [Knight *et al.*, 1998] which is useful for supercontinuum generation over a wide wavelength range [Wadsworth *et al.*, 2002] with relatively low energy pump pulses. It makes this fibre useful for optical coherence tomography (OCT) [Wang *et al.*, 2003; Aguirre *et al.*, 2006] and low cost compact sized spectroscopic systems [Kano and Hamaguchi, 2004; Okaba *et al.*, 2014]. Besides, presence of air-holes in close vicinity of the fibre core makes it possible to exploit the PCF modal properties by filling the air-holes with measurand materials. Chemical, biological liquid or gaseous sample can be accommodated inside the air-holes leads to a strong light-matter interaction. These channels can also be fictionalised with selective bio-linker layer that can enhance the binding of target molecules. Due to the micron sized air-holes, a very small amount of the fluid or chemical sample can be used for detection. These properties make the PCF useful for chemicals, protein and DNA hybridisation recognitions [Skorobogatiy, 2009; Monro *et al.*, 2010; Ruan *et al.*, 2008]. Real-time detection of gas emission and diffusion have wide applications in chemical, pharmaceutical, food, petroleum, and defence industries. Therefore, the sensing devices need to be fast, selective, accurate, and most obviously not susceptible to any chemical hazards. Several works have been carried out on different PCF-based strategies for the detection of acetylene [Hoo *et al.*, 2002; Pickrell *et al.*, 2004; Hoo *et al.*, 2005; Austin *et al.*, 2009; Henningsen *et al.*, 2005], methane [Kornaszewski

et al., 2007], ethane [Buric *et al.*, 2008], propane [Buric *et al.*, 2008], hydrogen [Minkovich *et al.*, 2006], carbon dioxide [Ding *et al.*, 2011], hydrogen cyanide [Henningsen *et al.*, 2005; Ritari *et al.*, 2004], and ammonia [Ritari *et al.*, 2004] gases. Even more, oxygen, nitrogen, and quantitative measurement of gas mixtures have been done with the help of spontaneous Raman backscattering in PCF [Buric *et al.*, 2009] and in-line hollow core photonic bandgap fibre (PBF) [Lehmann *et al.*, 2011], respectively. The large mode area PCF-based interferometric sensor proposed by [Mathew *et al.*, 2010] can easily detect the environmental humidity without any hygroscopic material. Hollow and solid core PCFs can also be used for simultaneous measurements of temperature and strain. A germanium-doped PCF based distributed Brillouin sensing system, high birefringence PCF-based polarimetry, hybrid Fabry-Perot cavity splicing at the end of a SMF, Sagnac loop using an elliptical hollow-core PBF, and modal interferometer by using hollow core PCF in between two SMFs and two tapers in a boron-doped high birefringence PCF can simultaneously measure strain and temperature with high sensitivity and resolution [Zou *et al.*, 2004; Han *et al.*, 2009; Frazao *et al.*, 2009; Andre *et al.*, 2010; Kim *et al.*, 2009; Aref *et al.*, 2009; Statkiewicz-Barabach *et al.*, 2011]. It is also noticeable that gratings can be inscribed into the PCFs with germanium-doped core [Eggleton *et al.*, 1999; Kakarantzas *et al.*, 2002]. Long period gratings (LPG) incorporated PCFs have a great potential to the detection and measurement of pressure, temperature, humidity and bio-chemicals [Bock *et al.*, 2007; Hu *et al.*, 2012; Zheng *et al.*, 2013; Rindorf *et al.*, 2006; Dobb *et al.*, 2004; He *et al.*, 2008]. Apart from the sensing technologies discussed above, the PCF is also useful for the detection of flying particles trapped inside hollow cores [Bykov *et al.*, 2015], electrical and magnetic fields [Mathews *et al.*, 2011; Chamorovski *et al.*, 2009], bend/curvature [Gong *et al.*, 2010], twist [Fu *et al.*, 2010], and vibration [Thakur *et al.*, 2011]. The development of the hollow and solid core PCFs not only improve the sensor performance but also exploits the novel sensing concepts that are impossible to achieve with the conventional fibres.

2.2.6 Integrated Waveguide-based Sensors

Optical waveguides, initially developed and used for telecommunications, is also useful for sensing process due to its tunable light-matter interaction, precise measurement,

and flexible design. So far, a detailed discussion has been placed in previous sections on the advancement of various photonic sensing technologies and its incorporation with recently developed optical optical fibres, waveguides and other devices. Optical fibre is a well-established light-guiding method that has already been used with different sensing platforms. However, light guiding can also be possible in a chip-level by means of nano-dimensioned rib, channel, ridge, hollow-core, and slot waveguides. Both the labelling and label-free sensing processes can be exploited by these exotic waveguiding designs. A CMOS compatible standard lithographic technique can be used in fabrication of low-cost mass production of these waveguides on a single chip. Compared to the low index contrast optical fibres, a high index contrast silicon-on-insulator (SOI) based waveguides are more efficient for light confinement in the core region. It also provides smaller bending radius which makes it possible to accommodate a large number of components on a single chip. The rib, channel, ridge, and strip waveguides provide a tight confinement in the core and a modest evanescent tail may interact with the surrounding sensing analyte in the form of clad. Another exotic design, a hollow-core waveguide is much useful and advantageous for bio-chemical liquid and gas sensing, reported by [Saito *et al.*, 1993; Bernini *et al.*, 2002]. It works as an absorption cell and its performance is highly wavelength dependent. One of the main drawback is its waveguide length which is much larger (few centimetres) compared to the integrated SOI-based waveguides (few microns) thus not suitable for on-chip fabrication.

Another revolutionised concept of optical light guiding is the slot waveguide first proposed by [Almeida *et al.*, 2004] where light is mainly guided by the low index slot region. A nano-dimension slot or a gap can be formed by placing two high index dielectrics, metals, or dielectric and metal strips. Therefore, the guided electric field normal to the high and low index material interfaces show a large discontinuity. This unique feature of light guiding mechanism results in a large field enhancement in the nano-dimensioned gap accessible to the outer cladding materials. Depending on the slot orientations, the waveguide can be termed as vertical [Almeida *et al.*, 2004], horizontal [Sun *et al.*, 2007], and a combination of both vertical and horizontal, forming a cross-slot waveguide [Khanna *et al.*, 2009; Pan and Rahman, 2017]. In cases of both the vertical and horizontal slots, the dominant electric field components (E_x and E_y) of the quasi-TE and TM modes,

respectively have the discontinuities at the high and low index material interfaces, therefore, enhance the light confinement inside the gap. Thus, instead of an evanescent field tail which is a small fraction of the guided mode of the conventional waveguides, a dedicated large field of the slot waveguide is now available for sensing. This helps in a strong light-matter interaction which makes this exotic waveguide design more attractive for label-based, label-free sensors and opto-mechanical tweezers [Yang, Moore, Schmidt, Klug, Lipson and Erickson, 2009; Yang, Lerdsuchatawanich and Erickson, 2009]. Most often, the main aim of the optical waveguide sensor has been to detect the refractive index changes of the surrounding environment and correlate it with its physical changes. For accurate measurement of these refractometric changes, the designed and optimised slot waveguides can be incorporated into suitable transducers such as Bragg gratings [Wang *et al.*, 2013a], conventional photonic crystals [Lai *et al.*, 2011], interferometers and resonators. Several interferometric configurations e.g. Mach-Zehnder (MZ), Young, Sagnac, and coupler interferometers can be used as transducers. Waveguide modal shift due to light-matter interaction introduces a phase change and that can be detected by measuring the interferometric fringe shift at the output. A very small refractive index change can be monitored by these transducers. On the other hand, ring, disk, and whispering gallery based resonating devices can also detect the changes in measurand analyte by means of wavelength shift of the resonating spectra. Several research articles can be found based on slot waveguide sensors. Different slot waveguide structures can be formed based on pure dielectrics, metals and by combining dielectric and metal. Metal and dielectric combination forms a hybrid slot which not only excites the surface plasmon polaritons (SPPs) at the metal-dielectric surface but also carries a hybrid plasmonic mode, a mixture of SPPs and dielectric guided wave. It has a significant advantage as it enhance the slot power confinement compared to a pure dielectric waveguide. Several research works on dielectric and hybrid plasmonic slot waveguide based integrated photonic sensors have been reported and an overview of those published results are listed the Table 2.1. In this thesis, our work is mainly focused on the design and optimisation of slot waveguide based integrated photonic sensors for detection of bio-chemicals, DNA hybridisation, gas, chemical vapour, and temperature.

Table 2.1: Published works on dielectric and hybrid plasmonic slot waveguide based photonic sensors.

Sensing device	Target analyte	Sensitivity (S) and/or detection limit (DL)	Operating wavelength	Evaluation method and reference
Si_3N_4 - SiO_2 -based micro-ring resonator	DI water-ethanol solution, RI: 1.33 - 1.42	S = 212 nm/RIU DL = 2×10^{-4} RIU	$\sim 1.3 \mu\text{m}$	Experimental [Barrios <i>et al.</i> , 2007a]
Si_3N_4 - SiO_2 -based micro-ring resonator	Label-free bio-sensing: Bovine serum albumin (BSA) and anti-BSA	BSA: S = 3.2 nm/(ng/mm ²) DL = 16 pg/mm ² Anti-BSA: S = 1.8 nm/(ng/mm ²) DL = 28 pg/mm ²	$\sim 1.3 \mu\text{m}$	Experimental [Barrios <i>et al.</i> , 2008]
Si_3N_4 - SiO_2 -based triple slot waveguide	Bulk sensing: RI: 1.45 - 1.46	>20% waveguide sensitivity than single slot ¹	1.3 μm	Simulation and experimental [Vivien <i>et al.</i> , 2008]
Si_3N_4 slot waveguide ring resonator	Bulk sensing: DI water - NaCl Surface sensing: bilayer (poly-4-tyrenesulfonate/ poly-allylamine hydrochloride)	Bulk sensing: S = $1730(2\pi)$ /RIU DL = 1.29×10^{-5} RIU Surface sensing: S = 60 nm/(ng/mm ²) DL = 0.155 pg/mm ²	$\sim 1.55 \mu\text{m}$	Simulation and experimental [Tu <i>et al.</i> , 2012]
SOI-based slot waveguide	Bulk sensing: RI: 1.333 - 1.335 Surface sensing: Bio-layer, RI: 1.45	waveguide sensitivities ¹	$\sim 1.55 \mu\text{m}$	Simulation [Dell'Olio and Passaro, 2007]
SOI-based coupled slot waveguide	Glucose-water solution	S = 0.1 g/L DL = 10^{-5} RIU	1.55 μm	Theory and simulation [Passaro <i>et al.</i> , 2009]
SOI-based multi-channel directional coupler	Glucose-water solution Ethanol-DI water solution	S = -172 /RIU (glucose-water) S = 155 /RIU (ethanol-water)	1.55 μm	Theory and simulation [McCosker and Town, 2010]

¹ Waveguide sensitivity may have different values depending on the design parameters. Consult respective article for sensitivity values.

Table 2.1: Published works on dielectric and hybrid plasmonic slot waveguide based photonic sensors. (continued)

Sensing device	Target analyte	Sensitivity (S) and/or detection limit (DL)	Operating wavelength	Evaluation method and reference
Si single and double slot micro-ring	Bulk sensing: water	waveguide sensitivity ¹	1.55 μm	Simulation [Kargar and Chao, 2011]
SOI multiple slot ring resonator	Bulk sensing: water	S = 912 nm/RIU	$\sim 1.55 \mu\text{m}$	Simulation [Khodadad <i>et al.</i> , 2014]
SOI vertical slot ring resonator	Bulk sensing: NaCl-water solution	S = 298 nm/RIU DL = 4.2×10^{-5} RIU	$\sim 1.55 \mu\text{m}$	Simulation and experimental [Claes <i>et al.</i> , 2009]
Loop mirror based slot waveguide	Bulk sensing: air, water	S = 6×10^3 nm/RIU	$\sim 1.55 \mu\text{m}$	Simulation [Kou <i>et al.</i> , 2012]
Si_3N_4 slot based MZI	Bulk sensing: Streptavidin solution	S = 1864π /RIU DL = 1 pg/ml	$\sim 1.55 \mu\text{m}$	Simulation and experimental [Liu <i>et al.</i> , 2013b]
Grating assisted Si_3N_4 strip and slot waveguide coupler	Bulk sensing: water solution	S = 10^5 nm/RIU	$\sim 1.55 \mu\text{m}$	Simulation [Liu <i>et al.</i> , 2013a]
SOI phase-shifted Bragg grating in slot waveguide	Bulk sensing: salt solution	S = 340 nm/RIU DL = 3×10^{-4} RIU	$\sim 1.55 \mu\text{m}$	Experimental [Wang <i>et al.</i> , 2013a]
Au based plasmonic vertical slot cavity	Bulk sensing: water, acetone	S = 600 nm/RIU	$\sim 1.55 \mu\text{m}$	Simulation [Osowiecki <i>et al.</i> , 2014]
Double slot hybrid plasmonic MZI	Bulk sensing: isopropanol solution	S = 1061 nm/RIU	$\sim 1.55 \mu\text{m}$	Simulation and experimental [Sun <i>et al.</i> , 2015a]
Double slot plasmonic ring resonator	Bulk sensing: isopropanol solution	S = 687.5 nm/RIU DL = 5.37×10^{-6} RIU	$\sim 1.55 \mu\text{m}$	Simulation and experimental [Sun <i>et al.</i> , 2015b]

¹ Waveguide sensitivity may have different values depending on the design parameters. Consult respective article for sensitivity values.

Table 2.1: Published works on dielectric and hybrid plasmonic slot waveguide based photonic sensors. (continued)

Sensing device	Target analyte	Sensitivity (S) and/or detection limit (DL)	Operating wavelength	Evaluation method and reference
Horizontal slot hybrid plasmonic MZI	Bulk sensing: isopropanol solution	waveguide sensitivity = 0.8 S = 245 nm/RIU DL = 2.8×10^{-6} RIU	1.530-1.550 μm	Simulation and experimental [Sun <i>et al.</i> , 2017]
SOI based suspended slot waveguide	Bulk sensing	waveguide sensitivity = 1.123	2.25 μm	Simulation and experimental [Zhou <i>et al.</i> , 2017]
Au/Si hybrid plasmonic micro-ring resonator	Bulk sensing: water solution	S = 580 nm/RIU	$\sim 1.55 \mu\text{m}$	Simulation [Zhou <i>et al.</i> , 2011]
SOI slot with side-wall Bragg gratings	Bulk sensing: multi-analyte	S = 291.93 nm/RIU DL = 10^{-6} RIU	$\sim 1.55 \mu\text{m}$	Simulation [Wang and Madsen, 2014]
SOI micro-ring resonator	Acetylene gas	S = 490 nm/RIU DL = 10^{-4} RIU	Near-IR	Simulation and experimental [Robinson <i>et al.</i> , 2008]
Silicon-on-nitride (SON) vertical slot waveguide	Ammonia (NH_3) gas	DL = 5 ppm	Mid-IR	Simulation [Kumari <i>et al.</i> , 2016]
Si rid slot waveguide	Gases: N_2O , CO, and CH_4	DL = 0.2 ppm (N_2O) DL = 0.44 ppm (CO) DL = 36 ppm (CH_4)	Mid-IR	Simulation [Kumari <i>et al.</i> , 2018]
SOI vertical slot ring resonator	DNA hybridisation	S = 856 nm/RIU DL = 1.43×10^{-6} RIU	$\sim 1.55 \mu\text{m}$	Simulation [Dar <i>et al.</i> , 2012]
SOI horizontal slot ring resonator	DNA hybridisation	S = 893.5 nm/RIU	$\sim 1.55 \mu\text{m}$	Simulation [Viphavakit <i>et al.</i> , 2015]
SOI cross-slot waveguide	Surface sensing: Bio-layer of RI 1.45	S = 0.012 /nm	1.55 μm	Simulation [Pan and Rahman, 2017]

N.B.: Published works related to this thesis are not included in this table.

2.3 Numerical Methods as Modelling Tools

Commercial production of photonic waveguides and devices require design, fabrication, characterisation, and possible redesign for performance optimisation. These cyclic development process of micro and nano-dimensioned photonic device is highly expensive and also time-consuming. The computerised numerical modelling is an effective way to cut-down those expensive steps before final production. Chip-level individual waveguides, sensors, and also a complete sensor array can be designed and optimised for its best performance. Simulation also helps to investigate the novel phenomenon that may be hindered with current experimental facilities. Previously, an analytical, semi-analytical, and closed-form solutions were used for simple device modelling. As the progress in technology demands complex devices, the applicability of those analytical methods became limited. Therefore, with the advancement of low-cost computer technologies, it has become possible to study those exotic waveguides and devices using computerised codes based on different numerical simulation tools.

2.3.1 Frequency Domain Methods

The first step to design a waveguide is to study its modal properties such as mode effective index, propagation constant, effective area, dispersion, modal loss, and confinement factor and finally the full-vectorial \vec{E} and \vec{H} field profiles. A simple scalar approach is sufficient to solve the circularly symmetric low index contrast waveguides. However, for high index contrast silicon-on-insulator (SOI) and silicon-on-nitride (SON) based waveguides, complex shaped photonic crystal fibres with non-linear and anisotropic materials require a rigorous full-vectorial approach. Most of the commercially available mode solvers are based on transfer matrix method, finite difference method (FDM), method of lines (MoL), and finite element method (FEM). Among them, the finite element based approach is much effective in terms of sufficient accuracy with less computational resources and handling of complex waveguide design with multiple layers of different materials. Main advantages of the finite element based approaches can be listed as:

- FEM has ability to discretise the computational domain with arbitrarily curved and/or slanted boundaries using the curvilinear and/or irregular mesh elements.

- Easy implementation of the electromagnetic boundary conditions to make the field continuous across the material interfaces.
- A higher accuracy could be obtained by considering element interpolation functions for different types (triangles and quadrilaterals for 2D and tetrahedrons, bricks, prisms, and pyramids for 3D) and orders of mesh elements.
- Easy to set-up scalar and vectorial formulation in a single package whenever necessary.
- Ability to tie-up with other analysis such as perturbation, least squares boundary residual for various applications.
- Its repetitive calculation steps make it suitable for computerised implementation for any large problem domains.

The finite element method for electromagnetic problems can be implemented by two alternative approaches such as the variational approach and the Galerkin method [Rahman and Agrawal, 2013]. In this thesis, a \vec{H} field based full-vectorial variational approach has been followed for the development of two-dimensional and three-dimensional finite element method (described in detail in Chapter 3). Most of the dielectric material based sensing waveguides have real effective index unless the modal loss has been introduced due to bending or by some external means which results in a small imaginary term in the effective index. On the other hand, metal assisted waveguide modelling needs to handle a large imaginary refractive index along with the real one. In recent plasmonic based photonic sensors, a hybrid plasmonic modal investigation with accurate determination of the modal loss is highly recommended and that can easily be performed by the frequency domain finite element analysis.

In some optical waveguide sensors, the cross-section may vary abruptly or continuously, where the beam propagation method (BPM) is more useful for analyses rather than multiple modal solutions at different waveguide cross-sections. Most of the commercially available BPM packages are based on the finite difference method (FDM). However, a FEM based BPM (FE-BPM) developed by [Obayya *et al.*, 2000] is more computationally efficient than the FDM based approach and can be useful for low and high index

contrast bent waveguides and optical fibres. Besides, a conformal transformation can also be applied for bent waveguide analyses proposed by Heiblum and Harris in 1975 [Heiblum and Harris, 1975]. In some cases, a complete photonic sensor design may have a discontinuity between two waveguiding sections where the tangential component of the electric and magnetic fields must be continuous at the interfaces. This disruption causes reflection, scattering, and reduced transmission of the propagating wave at the junction. A simple overlap integral can be used to analyse this discontinuity. However, a full-vectorial least squares boundary residual (LSBR) method developed by [Rahman and Davies, 1988] would be more rigorous to determine the reflection, transmission, and scattering coefficients at the interface.

2.3.2 Time Domain Methods

Several photonic devices require numerical methods that can simulate the field evolutions as a function of time. Some problems include modelling of time dependent transient phenomenon and simultaneous characterisations at various frequencies of the broadband spectra. Several time domain approaches such as finite difference time domain (FDTD) and finite element time domain (FETD) can be used to solve those time dependent problems. FDTD is one of the widely used method in photonics community. It solves the approximate solutions of the differential equations associated with the system and can handle a wide frequency range in a single run. Its formulation steps follow the leapfrog pattern [Yee, 1966] where the electric and magnetic field are located at different spatial grid points and are evaluated at different time steps. The physical significance of the curl operator in the Maxwell's equations is to rotate the $\vec{H}(\vec{E})$ field with the time change in $\vec{E}(\vec{H})$ field. Therefore, this method cannot solve the \vec{E} and \vec{H} field components at the same location at the same instant of time. Thus, a small time step need to consider for an accurate solution which on the other hand demands high computational resources and time. It is also notable that the FDTD only uses rectangular grids for domain discretisation [Taflöv, 1980]. Therefore, it is difficult to handle some arbitrarily and circularly shaped structures with curved boundaries.

2.4 Waveguide Fabrication Technologies

2.4.1 Wafer Fabrication

Recent progress in modern fabrication technologies makes it possible to develop silicon-on-insulator (SOI) and silicon-on-nitride (SON)-based complex waveguides with lower insertion loss, compact integration, low cost, and multi-functional on-chip photonic devices. Si is a centrosymmetric material with indirect bandgap. Therefore, integration with other materials requires additional material processes, wafer bonding, epitaxy, deposition, and others. Development of SOI wafer is a common process of high-index contrast waveguide fabrication. The most favourable choices of SOI wafer fabrication processes are bond and etch-back silicon-on-insulator (BESOI), separation by implantation of oxygen (SIMOX), epitaxial layer transfer (ELTRAN), Smart Cut, and seed method.

The bond and etch-back silicon-on-insulator (BESOI) method follows a direct bonding between silicon wafers with chemically deposited, or thermally grown oxidised surfaces [Iyer, 2002]. The wafer surfaces need to be cleaned before bonding. A controlled high temperature annealing process is followed to strengthen the adhesion after bonding. Next, different waveguide structures can be formed by wet or dry etching or lift-off techniques.

The separation by implantation of oxygen (SIMOX) technology uses ion implantation process in which the oxygen ions are accelerated into solid substrate at low temperature. The oxygen ions combine with the Si atoms to form buried silicon oxide layer. After ion implantation, the wafer follows an annealing process at high temperature ($>1300\text{ }^{\circ}\text{C}$) to form a stable buried oxide (SiO_2) layer in a Si wafer [Ogura, 1999].

The epitaxial layer transfer (ELTRAN) technique was first developed by the Canon Inc., Japan in 1990. This fabrication method involves the BESOI process with epitaxial growth on porous Si. It can be etched selectively by hydrogen annealing. The main advantage of this technique is that the bonded wafer can be split into two wafers at the porous Si layer by using water jet. One part develops the ELTRAN processed wafer and another part can be reused for further processing which on the other hand reduces the wafer manufacturing costs. Here the hydrogen annealing process uses for wafer surface smoothing whose thickness uniformity much greater than the chemical mechanical polishing (CMP) method. The special feature of this process is highly controllable epitaxial

layer growth with thickness from few nanometres to several micrometers.

The Smart Cut is a process of SOI wafer formation which can transfer and develop a very thin layer of crystalline Si from one wafer to another wafer. It involves two technologies such as bonding of two wafers and ion implantation which induces an in-depth splitting of the implanted wafer [Bruel *et al.*, 1997]. The SOI wafer forms by means of hydrophilic conditions to bond the implanted oxidised wafer to the silicon handle substrate. This process requires a special cleaning treatment before bonding because the implantation process manipulates the oxide surface in terms of particle and organic contaminations. After bonding, the splitting step can be followed at the weakened zone of the thick wafer layer in order to grow thin crystalline Si layer. The other separated part can be reused for further SOI wafer fabrication. This Smart Cut process is advantageous because of the thickness flexibility of both the buried oxide layer and Si layers. The buried oxide layer is thermally grown thus its thickness can be tunable. The Si upper layer is formed due to splitting at the depth of maximum hydrogen concentration. Due to controllable ion energy, the Smart Cut process also results in a homogeneous thickened layer after splitting.

The seed method involves direct growing of Si layer on top of insulator. It requires a template for uniform deposition of Si epitaxy onto the insulator by proper orientation or specific chemical treatment of the insulator.

2.4.2 Hybrid Plasmonic Waveguide Fabrication

Fabrication of photonic ICs with customised micro and nano patterns could be obtained with the help of lithographic process. Currently, photolithography is a widely used fabrication technique to print micro-fabrication patterns on thin film for electronic and photonic devices. In this process, light passes through a user defined photomask to a light sensitive chemical photoresist on the substrate. Then the custom geometrical pattern could be formed by either engraving the exposure pattern or depositing another material in that pattern. The photolithography resolution (R) can be written from the Rayleigh equation as, $R = \frac{k\lambda}{NA}$. The resolution depends on the wavelength (λ) of the light source, resolution factor (k) depends on photoresist, and numerical aperture of the lithographic lens system. A high resolution results in a minimum feature size. The smallest feature size of 50 nm

could be achieved by using an Argon Fluoride Excimer laser with $\lambda = 193$ nm. However, for sub-wavelength hybrid plasmonic waveguide design photolithography is not suitable. The electron beam lithography (EBL) is much powerful compared to photolithography for printing nano-structures. This process has very high resolution and it can achieve a minimum feature size of a few nanometres. Here the smaller aperture size of the lens system results in a higher resolution. This technique involves scanning a focused electron beam to write an user defined custom shape on a sample covered with electron-sensitive chemical resist. The electron beam exposure changes the solubility of the resist film. Next, the resist layer can be developed in a suitable solvent to selectively dissolve either the e-beam exposed or unexposed regions.

This thesis comprises SOI-based nanometre scaled dielectric and complex hybrid plasmonic slot waveguides. All these sophisticated waveguide structures could be realised with aforementioned SOI wafer fabrication processes and the electron beam lithography technique.

2.5 Summary

This chapter provides a detailed overview of the current trends in photonic sensing technology. Among them, the integrated waveguide and resonator based photonic sensors have been emphasised and highlighted as the work presented in this thesis is based on the slot based on-chip devices and resonators. All the significant slot based photonic sensors and their important sensing properties, relevant to this work are tabulated in a simplified fashion. The frequency and time domain numerical methods which can be used for rigorous design, optimisation and characterisation of those integrated slot based photonic devices have been briefly discussed and most relevant works have been reviewed which finally helps to modify and develop the two-dimensional divergence modified FEM and three-dimensional FEM, respectively discussed in detail in next chapter.

FINITE ELEMENT BASED FREQUENCY DOMAIN ANALYSES

3.1 Introduction

Design, fabrication, characterisation, error analysis, and possible redesign are the time consuming steps in the development of photonic devices. Here, the numerical simulations play an important role to analyse the devices by reducing the development time and cost. Previously, closed form solutions and analytical methods were used for device modelling. In recent years, due to progressive complications of the nano-scale devices and limitations of analytical solutions, the numerical methods are widely used to simulate the highly complicated single or multi-layered photonic devices with composite materials. Various numerical methods such as transfer matrix method, finite difference method, finite element method, integral-equation method, transfer line matrix method, and stochastic Monte Carlo method are already available for modelling micro and nano-dimensioned photonic devices suitable for user's needs. All these methods solve the Maxwell's electromagnetic equations at some point with their own signature approaches. These methods can be classified in terms of accuracy, efficiency, and complexity. However, Chiang [Chiang, 1994] has shown that every method must have some sort of compromises and assumptions. Thus, not a single method can be claimed as superior to others in all the points. Users should choose the method wisely depending on the problem such that it can provide an acceptable accuracy with minimum implementation effort

and computational resources. Among them, the finite element based frequency domain approach could be considered as dominant and arguably most powerful method due to its versatility and ability to produce robust and accurate results of complex problems in many branches of science and engineering.

In this chapter, the finite element method (FEM) has been described in detail and later on is implemented in two-dimensional and three-dimensional waveguide and resonator modal solutions, respectively. This FEM can easily handle an arbitrarily shaped waveguide and is also efficient for multilayer structures with anisotropic and nonlinear materials. Mathematically, the FEM solves the boundary-value problem with the help of either the variation formulation or the Galerkin method which is also a form of the weighted residual method. The variation formulation is useful where a single parameter such as mode effective index, resonant frequency or loss is evaluated. It is easy to implement and coupling with the perturbation analysis and least squares boundary residual (LSBR) method are also possible. The matrices in variational approach are always symmetric which provides a significant reduction of computational complexities. Additionally, it is easy to set-up the boundary conditions for different variational formulations. The natural boundary condition for \vec{E} and \vec{H} -field based formulations are perfect magnetic and electric wall, respectively. For \vec{E} -field formulation, the natural boundary condition i.e. perfect magnetic wall (PMW) needs to set-up whereas, the boundaries associated with \vec{H} -field based variational formulation are by default perfect electric wall (PEW). Therefore, the arbitrary boundaries can be left free. On the other hand, the Galerkin method may not easily satisfy the natural boundary conditions which demands a tedious computational effort. Therefore, the variational formulation is more advantageous to solve a wide range of electromagnetic problems. In this thesis, the 2D and 3D FEM have been derived and implemented by using the vector variational formulation.

3.2 Full Vectorial Finite Element Method (FV-FEM)

The full-vectorial finite element method (FV-FEM) emerged as an efficient numerical computation approach for solving varieties of complex waveguide and resonator problems ranging from microwave to optical frequency. The fundamental steps to build up the

analysis of any photonic model using FV-FEM can be listed as,

- Discretisation of computational domain of one's interest into many smaller elements.
- Set-up an interpolating equation at each elemental nodes or boundaries to determine unknown parameter. It may be field or potential depending on the problem.
- Assembling the individual equation of discretised elements to form a global eigenvalue equation.
- Finally, post-processing of the eigenvalues and corresponding eigenvectors to obtain desired unknown parameters.

3.2.1 2D and 3D Computational Domain Discretisation

The defined domain over which the FV-FEM can be applied needs to be discretised into a large number of small sections, called elements. These elements can be chosen in such a way that its shape and size matches closely with the geometry and the boundary curvatures of the computational domain of interest. These small elements altogether form a mesh that could be either regular or irregular. Compared to the regular mesh distribution, the irregular mesh is more efficient in domain discretisation. Finer elements can be accommodated in the regions of particular interest and coarse elements elsewhere. Thus, irregular meshing provides greater accuracy over regular meshing. For photonics computations, smaller mesh elements should be considered in the thin, narrow and pointed regions where the electromagnetic fields vary rapidly. Whereas, in the areas where the fields show a nearly constant distribution, a few elements might be sufficient for computations. It is also very important to select the shape and size of the boundary elements carefully so that those can match the complete boundary shape as far as possible. Several elemental geometries can be followed such as straight edge elements, iso-parametric elements, infinite elements, and edge elements. The straight edge elements include the triangles, rectangular, and quadrilaterals for 2D domain and tetrahedrals, prisms, bricks, and pyramids for 3D domains. These are mostly useful for the domains with less curved boundaries. The iso-parametric or curvilinear elements have curvatures on the edges and its nodal positional coordinates are defined by the transformation of

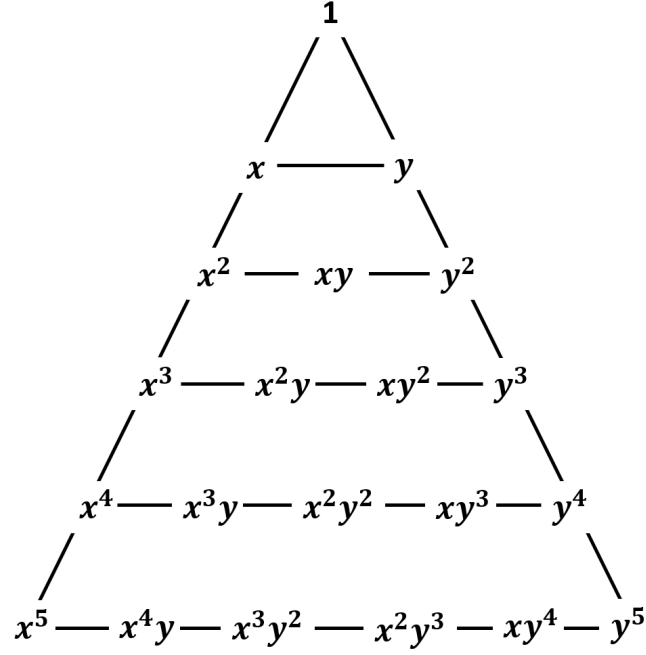


Figure 3.1: Pascal triangle exhibits the relationship in between element node number and term number in the shape function (N_i^e).

the local Cartesian coordinate to the global curvilinear coordinates. These are useful for the geometries with curved boundaries. Higher order elements are also applicable for these types of element family. For an open space or unbounded photonics problem, the infinite mesh elements can be very useful. The shape function for the infinite elements decays exponentially in the directions where the field extends to the infinity [Rahman and Davies, 1984a,b]. The edge elements precisely enforce the field continuity along the element edge rather the nodes. Thus, these elements can successfully eliminate the unwanted spurious solutions.

3.2.2 Set-up Interpolation Equations

Once the domain has been accurately discretised with suitable number of elements, it is necessary to represent the element shape function in terms of the variational unknown parameters. With the help of polynomial interpolation function also known as shape function, any continuous function over the computational domain can be approximated. The chosen function should have continuity within and across the boundaries of each element. Without the continuity, the functions are not eligible for variational formulation

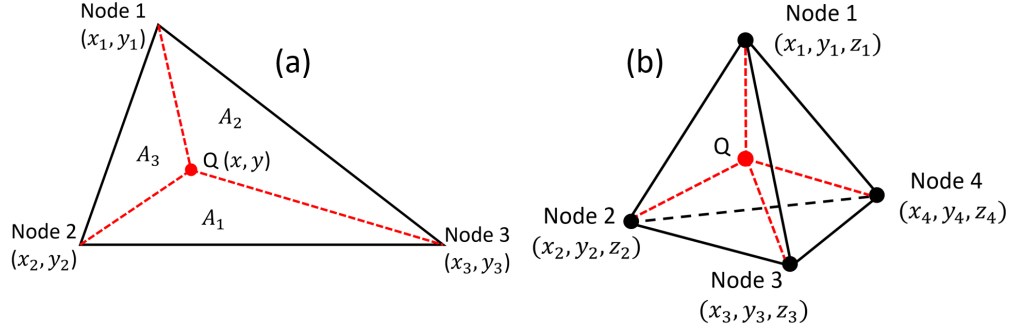


Figure 3.2: (a) and (b) represent linear triangular and tetrahedral element for two-dimensional and three-dimensional domain discretisation. The Q point is taken as any arbitrary point inside the element of coordinate (x, y) for 2D and (x, y, z) for 3D.

and the electromagnetic field or potential cannot be calculated by summing up the individual contribution of elements. For an unique shape function of a specific element, the number of terms must be equal to the number of nodes in the element. The Pascal triangular structure in Fig. 3.1 exhibits a nice graphical representation of the relation in between the element node number and the number of terms in the polynomial for a 2D domain discretisation.

Lagrange interpolation polynomials (L_i^e) are introduced to construct shape functions for the elements of different types. For a linear triangular (for 2D) and tetrahedral (for 3D) element these Lagrange polynomials are given by

$$L_i^e = \frac{1}{2A^e} [a_i^e + b_i^e x + c_i^e y] \quad (\text{for 2D}) \quad (3.1)$$

$$L_i^e = \frac{1}{6V^e} [a_i^e + b_i^e x + c_i^e y + d_i^e z] \quad (\text{for 3D}) \quad (3.2)$$

where A^e and V^e are the area and volume of each of the 2D triangular and 3D tetrahedral element, respectively. The subscript i denotes the element number and a_i^e , b_i^e , c_i^e , and d_i^e are the constant coefficients.

If we consider an arbitrary point Q inside a discretised element, as shown in Fig. 3.2, we can get sub-elements (sub-triangles from triangular and sub-tetrahedral from tetrahedral element) from each element. Now, the area and volume of those sub-regions can be expressed as follows,

The area defined by the point Q and nodes 2 and 3 is

$$\begin{aligned}
 A_1 &= \frac{1}{2} \begin{vmatrix} 1 & x & y \\ 1 & x_2 & y_2 \\ 1 & x_3 & y_3 \end{vmatrix} \\
 &= \frac{1}{2} [(x_2 y_3 - x_3 y_2) + x(y_2 - y_3) + y(x_3 - x_2)]
 \end{aligned} \tag{3.3}$$

Similarly, the volume defined by the point Q and nodes 2, 3, and 4 is

$$V_1 = \frac{1}{3!} \begin{vmatrix} 1 & x & y & z \\ 1 & x_2 & y_2 & z_2 \\ 1 & x_3 & y_3 & z_3 \\ 1 & x_4 & y_4 & z_4 \end{vmatrix} \tag{3.4}$$

Re-utilizing those constant coefficients (a_i^e , b_i^e , c_i^e) the L_i^e functions for all the three nodes of a triangular element can be defined as

$$\begin{bmatrix} L_1^e \\ L_2^e \\ L_3^e \end{bmatrix} = \frac{1}{A^e} \begin{bmatrix} A_1 \\ A_2 \\ A_3 \end{bmatrix} = \frac{1}{2A^e} \begin{bmatrix} a_1^e & b_1^e & c_1^e \\ a_2^e & b_2^e & c_2^e \\ a_3^e & b_3^e & c_3^e \end{bmatrix} \begin{bmatrix} 1 \\ x \\ y \end{bmatrix} \tag{3.5}$$

Here A_1 , A_2 , and A_3 represent the area formed by the point Q and two opposite nodes.

$$\begin{cases} A_1 = \text{area}(Q, \text{node 2, node 3}) \\ A_2 = \text{area}(Q, \text{node 1, node 3}) \\ A_3 = \text{area}(Q, \text{node 1, node 2}) \end{cases} \tag{3.6}$$

The Lagrange functions depend on the choice of point Q in the element. Similarly, for a 3D tetrahedral element the Lagrange functions can be defined in a compact matrix form as

$$\begin{bmatrix} L_1^e \\ L_2^e \\ L_3^e \\ L_4^e \end{bmatrix} = \frac{1}{V^e} \begin{bmatrix} V_1 \\ V_2 \\ V_3 \\ V_4 \end{bmatrix} = \frac{1}{6V^e} \begin{bmatrix} a_1^e & b_1^e & c_1^e & d_1^e \\ a_2^e & b_2^e & c_2^e & d_2^e \\ a_3^e & b_3^e & c_3^e & d_3^e \\ a_4^e & b_4^e & c_4^e & d_4^e \end{bmatrix} \begin{bmatrix} 1 \\ x \\ y \\ z \end{bmatrix} \tag{3.7}$$

Here V_1 , V_2 , V_3 , and V_4 represent the volume section formed by the point Q and three opposite nodes such as

$$\begin{cases} V_1 = \text{volume}(Q, \text{node } 2, \text{node } 3, \text{node } 4) \\ V_2 = \text{volume}(Q, \text{node } 1, \text{node } 3, \text{node } 4) \\ V_3 = \text{volume}(Q, \text{node } 1, \text{node } 2, \text{node } 4) \\ V_4 = \text{volume}(Q, \text{node } 1, \text{node } 2, \text{node } 3) \end{cases} \quad (3.8)$$

For 2D and 3D elements, the Lagrange function depends on the elemental area and volume, respectively. Thus, these functions are also called as area and volume coordinates for 2D and 3D problems.

To formulate the shape function, first each node of the element (linear and quadratic triangular and tetrahedral) are numbered, shown in the Fig. 3.3. For a 2D element, the node numbers consist of three digits whereas, a 3D element has four digits. The number of digit depends on the number of area or volume coordinates (or Lagrange functions) required to define an element. For example, three area and four volume coordinates need to define a 2D triangular and 3D tetrahedral element. The nodes 1, 2, and 3 of a linear triangular element are numbered as (100), (010) and (001), respectively. Thus, the shape function (N_i^e) correlated with node i , can be expressed as [Silvester and Ferrari, 1996]

$$N_i^e = Q_p^{(1)} L_1^e \cdot Q_q^{(1)} L_2^e \cdot Q_r^{(1)} L_3^e \quad \text{here } (p+q+r) = n \quad (3.9)$$

where p , q , r denote the individual digits of a node number and n denote corresponding element order. For example, p , q , and r of node 1 in Fig. 3.3(a) have the values of 1, 0, and 0, respectively. Here the product of the sequence in Eq. 3.9 can be written in a generalised form as

$$Q_{x=p,q,r}^{(1)} L_1^e = \frac{1}{x!} \prod_{m=1}^{x-1} (L_1^e - m) \quad \text{when } p > 0 \quad (3.10)$$

here $Q_0^{(1)}$ is taken as 1. Thus, the relations between the shape functions and corresponding Lagrange polynomials for a linear triangular element shown in Fig. 3.3(a) can be formed with the help of the equations Eqs. 3.9 and 3.10 as

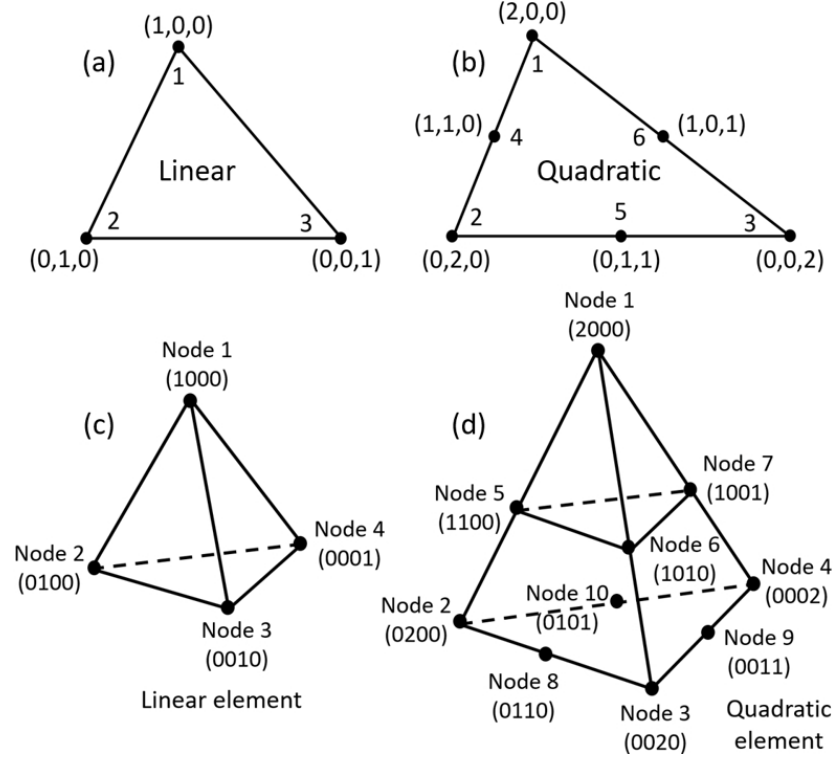


Figure 3.3: Linear and quadratic elements with its node numbering scheme depending on the element order. (a) and (b) depict the 2D triangular elements with linear and quadratic configuration. (c) and (d) are the first and second order tetrahedral elements.

$$\begin{cases} N_1^e = Q_{p=1}^{(1)} L_1^e \cdot Q_{q=0}^{(1)} L_2^e \cdot Q_{r=0}^{(1)} L_3^e = L_1^e \\ N_2^e = Q_{p=0}^{(1)} L_1^e \cdot Q_{q=1}^{(1)} L_2^e \cdot Q_{r=0}^{(1)} L_3^e = L_2^e \\ N_3^e = Q_{p=0}^{(1)} L_1^e \cdot Q_{q=0}^{(1)} L_2^e \cdot Q_{r=1}^{(1)} L_3^e = L_3^e \end{cases} \quad (3.11)$$

Similarly, for a 2D quadratic element shown in Fig. 3.3(b), the element order is $n = 2$ and we can evaluate the shape functions as

$$\begin{cases} N_1^e = Q_{p=2}^{(2)} L_1^e \cdot Q_{q=0}^{(2)} L_2^e \cdot Q_{r=0}^{(2)} L_3^e = L_1^e (2L_1^e - 1) \\ N_2^e = Q_{p=0}^{(2)} L_1^e \cdot Q_{q=2}^{(2)} L_2^e \cdot Q_{r=0}^{(2)} L_3^e = L_2^e (2L_2^e - 1) \\ N_3^e = Q_{p=0}^{(2)} L_1^e \cdot Q_{q=0}^{(2)} L_2^e \cdot Q_{r=2}^{(2)} L_3^e = L_3^e (2L_3^e - 1) \\ N_4^e = Q_{p=1}^{(2)} L_1^e \cdot Q_{q=1}^{(2)} L_2^e \cdot Q_{r=0}^{(2)} L_3^e = 4L_1^e L_2^e \\ N_5^e = Q_{p=0}^{(2)} L_1^e \cdot Q_{q=1}^{(2)} L_2^e \cdot Q_{r=1}^{(2)} L_3^e = 4L_2^e L_3^e \\ N_6^e = Q_{p=1}^{(2)} L_1^e \cdot Q_{q=0}^{(2)} L_2^e \cdot Q_{r=1}^{(2)} L_3^e = 4L_3^e L_1^e \end{cases} \quad (3.12)$$

In a similar fashion, a three-dimensional domain can be discretised with first and second order tetrahedral elements. The numbering scheme of those elements have shown in the Figs. 3.3(c) and (d). The shape functions for those elements can also be written with the help of Eqs. 3.9 and 3.10 as

$$\begin{cases} N_1^e = Q_{p=1}^{(1)} L_1^e \cdot Q_{q=0}^{(1)} L_2^e \cdot Q_{r=0}^{(1)} L_3^e \cdot Q_{s=0}^{(1)} L_4^e = L_1^e \\ N_2^e = Q_{p=0}^{(1)} L_1^e \cdot Q_{q=1}^{(1)} L_2^e \cdot Q_{r=0}^{(1)} L_3^e \cdot Q_{s=0}^{(1)} L_4^e = L_2^e \\ N_3^e = Q_{p=0}^{(1)} L_1^e \cdot Q_{q=0}^{(1)} L_2^e \cdot Q_{r=1}^{(1)} L_3^e \cdot Q_{s=0}^{(1)} L_4^e = L_3^e \\ N_4^e = Q_{p=0}^{(1)} L_1^e \cdot Q_{q=0}^{(1)} L_2^e \cdot Q_{r=0}^{(1)} L_3^e \cdot Q_{s=1}^{(1)} L_4^e = L_4^e \end{cases} \quad (3.13)$$

In case of second order tetrahedral element, the shape function could be listed as

$$\begin{cases} N_1^e = Q_{p=2}^{(1)} L_1^e \cdot Q_{q=0}^{(1)} L_2^e \cdot Q_{r=0}^{(1)} L_3^e \cdot Q_{s=0}^{(1)} L_4^e = L_1^e (2L_1^e - 1) \\ N_2^e = Q_{p=0}^{(1)} L_1^e \cdot Q_{q=2}^{(1)} L_2^e \cdot Q_{r=0}^{(1)} L_3^e \cdot Q_{s=0}^{(1)} L_4^e = L_2^e (2L_2^e - 1) \\ N_3^e = Q_{p=0}^{(1)} L_1^e \cdot Q_{q=0}^{(1)} L_2^e \cdot Q_{r=2}^{(1)} L_3^e \cdot Q_{s=0}^{(1)} L_4^e = L_3^e (2L_3^e - 1) \\ N_4^e = Q_{p=0}^{(1)} L_1^e \cdot Q_{q=0}^{(1)} L_2^e \cdot Q_{r=0}^{(1)} L_3^e \cdot Q_{s=2}^{(1)} L_4^e = L_4^e (2L_4^e - 1) \\ N_5^e = Q_{p=1}^{(1)} L_1^e \cdot Q_{q=1}^{(1)} L_2^e \cdot Q_{r=0}^{(1)} L_3^e \cdot Q_{s=2}^{(1)} L_4^e = 4L_1^e L_2^e \\ N_6^e = Q_{p=1}^{(1)} L_1^e \cdot Q_{q=0}^{(1)} L_2^e \cdot Q_{r=1}^{(1)} L_3^e \cdot Q_{s=0}^{(1)} L_4^e = 4L_1^e L_3^e \\ N_7^e = Q_{p=1}^{(1)} L_1^e \cdot Q_{q=0}^{(1)} L_2^e \cdot Q_{r=0}^{(1)} L_3^e \cdot Q_{s=1}^{(1)} L_4^e = 4L_1^e L_4^e \\ N_8^e = Q_{p=0}^{(1)} L_1^e \cdot Q_{q=1}^{(1)} L_2^e \cdot Q_{r=1}^{(1)} L_3^e \cdot Q_{s=0}^{(1)} L_4^e = 4L_2^e L_3^e \\ N_9^e = Q_{p=0}^{(1)} L_1^e \cdot Q_{q=0}^{(1)} L_2^e \cdot Q_{r=1}^{(1)} L_3^e \cdot Q_{s=1}^{(1)} L_4^e = 4L_3^e L_4^e \\ N_{10}^e = Q_{p=0}^{(1)} L_1^e \cdot Q_{q=1}^{(1)} L_2^e \cdot Q_{r=0}^{(1)} L_3^e \cdot Q_{s=1}^{(1)} L_4^e = 4L_2^e L_4^e \end{cases} \quad (3.14)$$

Once the domains are discretised with sufficient number of elements of one's choice, any unknown function ζ could be approximated at each node in terms of the node coordinates and constant coefficients.

$$\text{For 2D:} \quad \zeta_i^e(x, y) = a_i^e + b_i^e x_i + c_i^e y_i \quad \text{where } i = 1, 2, \text{ and } 3 \quad (3.15)$$

and

$$\text{For 3D:} \quad \zeta_i^e(x, y, z) = a_i^e + b_i^e x_i + c_i^e y_i + d_i^e z_i \quad \text{where } i = 1, 2, 3, \text{ and } 4 \quad (3.16)$$

Next, by solving the constant coefficients (a_i^e , b_i^e , c_i^e , and d_i^e) and the shape functions (N_i^e) for the specific element, the unknown function (ζ^e) could be interpolated for an element as

$$\zeta^e = \sum_i^n N_i^e \zeta_i^e \quad (3.17)$$

3.2.3 Vectorial Variational Formulation for Electromagnetism

The scalar formulation was first used with the finite element method (FEM) in 1960s for electromagnetic waveguide problems. Although, it is adequate to solve quasi-TE, quasi-TM or any waveguide problem downgraded to one dimensional problem, however, it is inadequate for solving hybrid dielectric and plasmonic modes of anisotropic or inhomogeneous or metal assisted two dimensional optical waveguides. In 1956, A. D. Berk suggested several vectorial approaches to formulate the variational formulation based on different electromagnetic field components and its combinations [Berk, 1956]. Generally, four different formulations can be considered, such as, E_z+H_z , \vec{E} -field, \vec{H} -field and $\vec{E}+\vec{H}$ -field based formulations. Both the E_z and H_z fields are continuous at the material interfaces. However, the E_z+H_z formulation ends with a non-standard eigenvalue problem. Extra computational effort needs to convert it into conventional standard form. As the \vec{E} -field does not follow the continuity at the boundaries, the boundary conditions need to implement externally in the \vec{E} -field formulation. Among them, the \vec{H} -field formulation is the most favourable one because the \vec{H} -field components are naturally continuous at the material interfaces. Thus, no extra boundary conditions need to be imposed for this formulation. On the other hand, the $\vec{E}+\vec{H}$ based formulation results in six unknown field components compared to \vec{E} and \vec{H} -field formulations without any extra benefits. With all benefits and numerical advantages, a full-vectorial \vec{H} -field formulation has been considered and modified for our studies. Vector formulation is suitable for both isotropic and anisotropic materials as well as vectorial solutions for electromagnetic wave propagation and determination of resonating modes of a three dimensional resonator. Following [Berk, 1956], the vectorial variational formulation for 2D and 3D electromagnetic problems can be written as

$$\omega^2 = \frac{\int_A \left(\int_v \right) \left(\vec{\nabla} \times \vec{H} \right)^* \cdot \hat{\epsilon}^{-1} \cdot \left(\vec{\nabla} \times \vec{H} \right) dA (dV)}{\int_A \left(\int_v \right) \vec{H}^* \cdot \hat{\mu} \cdot \vec{H} dA (dV)} \quad (3.18)$$

where ϵ and μ define the permittivity and permeability of the medium. Modifying the formulation (Eq. 3.18) by using $\epsilon = \epsilon_0 \epsilon_r$, $\mu = \mu_0 \mu_r$, $\epsilon_0 \mu_0 = 1/c^2$, and $k_0 = \omega/c$ gives

$$k_0^2 = \frac{\int_A \left(\int_v \right) \left(\vec{\nabla} \times \vec{H} \right)^* \cdot \epsilon_r^{-1} \cdot \left(\vec{\nabla} \times \vec{H} \right) dA (dV)}{\int_A \left(\int_v \right) \vec{H}^* \cdot \mu_r \cdot \vec{H} dA (dV)} \quad (3.19)$$

here ϵ_r and μ_r represent the relative permittivity and permeability of the medium, respectively. c and k_0 define the free-space light velocity and wavenumber of the propagating wave, respectively. Eqs. 3.18 and 3.19 show the variational formulations suitable for 2D and 3D waveguides and resonator problems, respectively. The area ($dA = dx dy$) and volume ($dV = dx dy dz$) integrations have been considered for 2D and 3D cases, respectively.

As the \vec{H} field based full-vectorial approach is considered for variational formulation thus, all three field components such as H_x , H_y , and H_z have been taken into account. In cases of 2D and 3D formulations, the \vec{H} field has been considered to be a continuous function of x, y and x, y, z , respectively.

$$\text{For 2D:} \quad \vec{H}(x, y) = \begin{bmatrix} H_x(x, y) \\ H_y(x, y) \\ H_z(x, y) \end{bmatrix} \quad (3.20)$$

and

$$\text{For 3D:} \quad \vec{H}(x, y, z) = \begin{bmatrix} H_x(x, y, z) \\ H_y(x, y, z) \\ H_z(x, y, z) \end{bmatrix} \quad (3.21)$$

3.3 Two Dimensional FV-FEM

To determine the unknown \vec{H} field distribution of a two dimensional computational domain, first, one need to set-up an interpolation equation to determine approximate \vec{H} field components in a discretised element. Finite number of linear triangular elements

have been considered for discretisation. Thus, the unknown field components (H_x , H_y , and H_z) associated with the triangular shape functions (N_1 , N_2 , and N_3) can be written as:

$$H_x^e(x, y) = \begin{bmatrix} N_1 & N_2 & N_3 \end{bmatrix} \begin{Bmatrix} H_{x1} \\ H_{x2} \\ H_{x3} \end{Bmatrix}_e \quad (3.22)$$

$$H_y^e(x, y) = \begin{bmatrix} N_1 & N_2 & N_3 \end{bmatrix} \begin{Bmatrix} H_{y1} \\ H_{y2} \\ H_{y3} \end{Bmatrix}_e \quad (3.23)$$

$$H_z^e(x, y) = \begin{bmatrix} N_1 & N_2 & N_3 \end{bmatrix} \begin{Bmatrix} H_{z1} \\ H_{z2} \\ H_{z3} \end{Bmatrix}_e \quad (3.24)$$

here the superscript and subscript e indicate that those field components are related with only one triangular element with three nodes, three shape functions and nine field values. H_{xi} , H_{yi} , and H_{zi} describe the x, y, and z components of the magnetic fields at each element node. Thus, the magnetic field vector $[\vec{H}]_e$ can be obtained as

$$[\vec{H}]_e = \begin{bmatrix} H_x(x, y) \\ H_y(x, y) \\ H_z(x, y) \end{bmatrix} = \begin{bmatrix} N_1 & N_2 & N_3 & 0 & 0 & 0 & 0 & 0 & 0 \\ 0 & 0 & 0 & N_1 & N_2 & N_3 & 0 & 0 & 0 \\ 0 & 0 & 0 & 0 & 0 & 0 & jN_1 & jN_2 & jN_3 \end{bmatrix} \begin{Bmatrix} H_{x1} \\ H_{x2} \\ H_{x3} \\ H_{y1} \\ H_{y2} \\ H_{y3} \\ H_{z1} \\ H_{z2} \\ H_{z3} \end{Bmatrix}_e \quad (3.25)$$

The j term in the shape function matrix is considered for the lossless cases where the H_z field component is 90° out of phase with the transverse components. In a simplified

manner, Eq. 3.25 could be written as

$$\left[\vec{H} \right]_e = [N] \{ \vec{H} \}_e \quad (3.26)$$

here the $[N]$ defines the matrix form of the shape function and $\{H\}_e$ column vector represent the nodal field values of three components in the triangular element.

Substituting Eq. 3.26 into the vector variational formulation in Eq. 3.19, the following formulation occurs.

$$k_0^2 = \frac{\int_A \left(\vec{\nabla} \times [N] \{ \vec{H} \}_e \right)^* \cdot \hat{\epsilon}_r^{-1} \cdot \left(\vec{\nabla} \times [N] \{ \vec{H} \}_e \right) dA}{\int_A \left([N] \{ \vec{H} \}_e \right)^* \cdot \hat{\mu}_r \cdot [N] \{ \vec{H} \}_e dA} \quad (3.27)$$

The cross product $(\vec{\nabla} \times \vec{H})$ factor in Eq. 3.27 could be written in matrix form as

$$\left(\vec{\nabla} \times \vec{H} \right) = \left(\vec{\nabla} \times [N] \{ \vec{H} \}_e \right) = \begin{bmatrix} 0 & -\frac{\partial}{\partial z} & \frac{\partial}{\partial y} \\ \frac{\partial}{\partial z} & 0 & -\frac{\partial}{\partial x} \\ -\frac{\partial}{\partial y} & \frac{\partial}{\partial x} & 0 \end{bmatrix} [N] \{ \vec{H} \}_e = [Q] \{ \vec{H} \}_e \quad (3.28)$$

The $[Q]$ matrix is a product of $[\vec{\nabla} \times]$ and shape function $[N]$. This matrix multiplication has been carried out and its elements are given in Appendix A. Considering $[Q]$, the simplified form of Eq. 3.27 can be written as

$$k_0^2 = \frac{\int_A \left([Q] \{ \vec{H} \}_e \right)^* \cdot \hat{\epsilon}_r^{-1} \cdot \left([Q] \{ \vec{H} \}_e \right) dA}{\int_A \left([N] \{ \vec{H} \}_e \right)^* \cdot \hat{\mu}_r \cdot [N] \{ \vec{H} \}_e dA} \quad (3.29)$$

Now considering the property of conjugate transpose the simplification can be made as

$$\left([Q] \{ \vec{H} \}_e \right)^* = \{ \vec{H} \}_e^* [Q]^* \quad (3.30)$$

and

$$\left([N] \{ \vec{H} \}_e \right)^* = \{ \vec{H} \}_e^* [N]^* \quad (3.31)$$

Substituting Eqs. 3.30 and 3.31 into variational form (Eq. 3.29) results in

$$k_0^2 = \frac{\int_A \{ \vec{H} \}_e^* [Q]^* \cdot \hat{\epsilon}_r^{-1} \cdot [Q] \{ \vec{H} \}_e dA}{\int_A \{ \vec{H} \}_e^* [N]^* \cdot \hat{\mu}_r \cdot [N] \{ \vec{H} \}_e dA} \quad (3.32)$$

Considering the assumption that $\{ \vec{H} \}_e$ and element shape function ($[N]$) is a real matrix, the simplified variation formulation could be written in the form of a functional as

$$F_e(\vec{H}) = \int_A \{ \vec{H} \}_e^T [Q]^* \cdot \hat{\epsilon}_r^{-1} \cdot [Q] \{ \vec{H} \}_e dA - k_0^2 \int_A \{ \vec{H} \}_e^T [N]^T \cdot \hat{\mu}_r \cdot [N] \{ \vec{H} \}_e dA \quad (3.33)$$

Here the functional $F_e(\vec{H})$ describes the numerical errors that occurs due to domain discretisation. T and $*$ denote the transpose and complex conjugate. By minimizing the variational functional by $\frac{\partial}{\partial\{\vec{H}\}_e} F_e(\vec{H}) = 0$, a stationary solution is obtained.

$$\frac{\partial}{\partial\{\vec{H}\}_e} \left[\int_A \{\vec{H}\}_e^T [Q]^* \cdot \hat{\epsilon}_r^{-1} \cdot [Q] \{\vec{H}\}_e dA - k_0^2 \int_A \{\vec{H}\}_e^T [N]^T \cdot \hat{\mu}_r \cdot [N] \{\vec{H}\}_e dA \right] = 0 \quad (3.34)$$

or,

$$\frac{\partial}{\partial\{\vec{H}\}_e} \left[\{\vec{H}\}_e^T \int_A [Q]^* \cdot \hat{\epsilon}_r^{-1} \cdot [Q] dA \{\vec{H}\}_e - k_0^2 \{\vec{H}\}_e^T \int_A [N]^T \cdot \hat{\mu}_r \cdot [N] dA \{\vec{H}\}_e \right] = 0 \quad (3.35)$$

or,

$$\frac{\partial}{\partial\{\vec{H}\}_e} \left[\underbrace{\{\vec{H}\}_e^T \int_A [Q]^* \cdot \hat{\epsilon}_r^{-1} \cdot [Q] dA}_{[A]_e} \{\vec{H}\}_e - k_0^2 \underbrace{\{\vec{H}\}_e^T \int_A [N]^T \cdot \hat{\mu}_r \cdot [N] dA}_{[B]_e} \{\vec{H}\}_e \right] = 0 \quad (3.36)$$

The two integral parts of the equation can be represented by two matrices, $[A]_e$ and $[B]_e$.

Both of these matrices are real symmetric and they can be defined as

$$[A]_e = \hat{\epsilon}_r^{-1} \int_A [Q]^* \cdot [Q] dA \quad (3.37)$$

and

$$[B]_e = \hat{\mu}_r \int_A [N]^T \cdot [N] dA \quad (3.38)$$

Thus, Eq. 3.36 can be simplified as

$$\frac{\partial}{\partial\{\vec{H}\}_e} \left[\{\vec{H}\}_e^T [A]_e \{\vec{H}\}_e - k_0^2 \{\vec{H}\}_e^T [B]_e \{\vec{H}\}_e \right] = 0 \quad (3.39)$$

Two dimensional computational domain is divided into a number of triangular elements. Thus, solving the vectorial variational formulation for a single element and then summing up contributions of all elements, the Eq. 3.39 can be expressed as a compact global eigenvalue equation as

$$[A]\{\vec{H}\} - k_0^2[B]\{\vec{H}\} = 0 \quad (3.40)$$

here k_0^2 defines the eigenvalue and $\{\vec{H}\}$, a column matrix represents an eigenvector of corresponding eigenvalue. Elements of $\{\vec{H}\}$ are the x, y, and z components of the vectorial \vec{H} field. $[A]$ and $[B]$ are the global matrices can be derived by summing up all the $[A]_e$ and $[B]_e$ element matrices as

$$[A] = \sum_e [A]_e = \sum_e \hat{\epsilon}_r^{-1} \int_A [Q]^* \cdot [Q] dA \quad (3.41)$$

and

$$[B] = \sum_e [B]_e = \sum_e \hat{\mu}_r \int_A [N]^T \cdot [N] dA \quad (3.42)$$

Detailed derivation of $[A]_e$ and $[B]_e$ matrix coefficients are shown in Appendix A.

3.3.1 Spurious Solutions: Direct Divergence Modified Approach

Presence of non-physical spurious solution is a disadvantage of the vectorial finite element method. Scalar formulation is free from these spurious solutions as the operator is positive definite. The vector variational formulation has already been shown in Eq. 3.19. It is based on the Maxwell's two curl equations. The Euler form of the above equation satisfies the Helmholtz's equation but that does not obey the Maxwell's two divergence equations automatically. Thus, the solution of this vector variational results in no-physical spurious solution along with the true physical solutions.

Rahman and Davies proposed a successful way to remove the spurious solutions by balancing the curl and divergence part with a penalty function approach [Rahman and Davies, 1984b]. A global weighting factor close to the value of $1/n_{eff}^2$ was considered to incorporate the effect of the divergence equation, $div \cdot \vec{B} = 0$. In the penalty approach, the value of $(\vec{\nabla} \cdot \vec{H})$ for each eigenvector is calculated over the waveguide cross-section and the solution with a low value of $(\vec{\nabla} \cdot \vec{H})$ is considered as the real physical mode. Therefore, the variational formulation has been modified by adding an additional integral part weighted by a dimensionless penalty factor, p . The resulting modified variational expression can be obtained as [Rahman and Davies, 1984b]

$$k_0^2 = \frac{\int_A (\vec{\nabla} \times \vec{H})^* \cdot \hat{\epsilon}_r^{-1} \cdot (\vec{\nabla} \times \vec{H}) dA + p \int_A (\vec{\nabla} \cdot \vec{H})^* (\vec{\nabla} \cdot \vec{H}) dA}{\int_A \vec{H}^* \cdot \hat{\mu}_r \cdot \vec{H} dA} \quad (3.43)$$

This method is highly efficient to determine the accurate solution of a wide range of passive dielectric based waveguides with all positive dielectric constants. However, it is inadequate for plasmonic waveguides modal solutions where the surface plasmons are guided by the lossy metals. A more direct approach has been proposed in this thesis and developed. In this new method, contributions of both positive and negative permittivity of sub-domain based local materials are taken into account into the additional divergence-divergence part. During global matrix formations of curl-curl and divergence-divergence

sections, individual local dielectric constant of each discretised triangular element is considered. Finally, the divergence modified functional can be written as

$$k_0^2 = \frac{\int_A \left(\vec{\nabla} \times \vec{H} \right)^* \cdot \epsilon_r^{-1} \cdot \left(\vec{\nabla} \times \vec{H} \right) dA + \int_A \left(\vec{\nabla} \cdot \vec{H} \right)^* \epsilon_r^{-1} \left(\vec{\nabla} \cdot \vec{H} \right) dA}{\int_A \vec{H}^* \cdot \hat{\mu}_r \cdot \vec{H} dA} \quad (3.44)$$

The solutions of Eq. 3.44 provide the eigenvalues and corresponding eigenvectors. Implementing this equation with 2D FV-FEM, several hybrid plasmonic complex waveguides are designed and optimised accurately. Results and mode field distributions of those waveguides have been shown and also discussed in Chapters 4, 5, and 6.

3.4 Three Dimensional FV-FEM

Full vectorial \vec{H} -field based three dimensional FV-FEM starts from Maxwell's two curl equations based variational formulation same as 2D FV-FEM, as discussed in section 3.3. The 3D solution region or the complete device is discretised into a number of small unstructured volumetric elemental domains. Firstly, the \vec{H} -field within each element is calculated and then interrelation of the field distributions with other elements are followed such that the field becomes continuous across the inter-element boundaries.

$$\vec{H} = \sum_{e=1}^n H_e(x, y, z) \quad (3.45)$$

where, n = number of tetrahedral elements inside the solution region. The \vec{H} -field for a single element can be derived from the total sum of the product of shape function vector and field value at each node of the element.

$$\vec{H}(x, y, z) = \sum_{i=1}^m N_i H_{ei}(x, y, z) \quad (3.46)$$

here m is number of nodes; H_{ei} represents the \vec{H} -field at each node of the element and N_i defines the shape function of a tetrahedral element. As the first order tetrahedral element has been considered for the 3D FV-FEM, four vertices of the tetrahedron need to be taken into account. Let the magnetic field values at the four nodal points ($j=1, 2, 3, 4$) be defined by H_{eij} ($i = x, y, z$). Three components of the magnetic field vary linearly inside the tetrahedral element. Thus, the field components can be presented in terms of shape functions N_j ($j = 1, 2, 3, 4$) and unknown field values (H_{eij}) ($i = x, y, z$) at the respective

nodes. We can formulate the magnetic field components at any arbitrary point inside the tetrahedral element as

$$\begin{aligned} H_{ex} &= N_1 H_{x1} + N_2 H_{x2} + N_3 H_{x3} + N_4 H_{x4} \\ H_{ey} &= N_1 H_{y1} + N_2 H_{y2} + N_3 H_{y3} + N_4 H_{y4} \\ H_{ez} &= N_1 H_{z1} + N_2 H_{z2} + N_3 H_{z3} + N_4 H_{z4} \end{aligned} \quad (3.47)$$

In a simplified manner

$$[\vec{H}]_{ei} = [N]^T \{H_{ij}\}_e \quad (3.48a)$$

$$i = x, y, z \text{ and } j = 1, 2, 3, 4$$

where the shape function is

$$[N] = \begin{bmatrix} N_1 & N_2 & N_3 & N_4 \end{bmatrix}^T \quad (3.48b)$$

and unknown field components in a matrix form as:

$$\{H_{ij}\}_e = \begin{Bmatrix} H_{i1} & H_{i2} & H_{i3} & H_{i4} \end{Bmatrix}_e^T \quad (3.48c)$$

where T denotes the transpose and e signifies an element. N_1, N_2, N_3, N_4 are shape functions or interpolation functions and they are the function of volumetric coordinate L_1, L_2, L_3, L_4 and also Cartesian coordinates (x, y, z) .

$$N_j = f(L_1, L_2, L_3, L_4) = f(x, y, z) \quad (3.49)$$

$$\text{where } j = 1, 2, 3, 4 \dots$$

As the first order polynomial is considered for calculation, it is being assumed that all the three field components vary linearly inside the an element. For the first order element, the relation between shape function and volumetric coordinates as

$$\begin{aligned} N_1 &= L_1 & N_2 &= L_2 \\ N_3 &= L_3 & N_4 &= L_4 \end{aligned} \quad (3.50)$$

We can rewrite the shape functions as

$$N_1 = L_1 = \frac{1}{6V} [a_1 + a_2x + a_3y + a_4z] \quad (3.51a)$$

$$N_2 = L_2 = \frac{1}{6V} [a_5 + a_6x + a_7y + a_8z] \quad (3.51b)$$

$$N_3 = L_3 = \frac{1}{6V} [a_9 + a_{10}x + a_{11}y + a_{12}z] \quad (3.51c)$$

$$N_4 = L_4 = \frac{1}{6V} [a_{13} + a_{14}x + a_{15}y + a_{16}z] \quad (3.51d)$$

Taking $1/6V$ inside the brackets the equation sets (3.51d) can be written in a simplified manner.

$$N_1 = L_1 = [b_1 + b_2x + b_3y + b_4z] \quad (3.52a)$$

$$N_2 = L_2 = [b_5 + b_6x + b_7y + b_8z] \quad (3.52b)$$

$$N_3 = L_3 = [b_9 + b_{10}x + b_{11}y + b_{12}z] \quad (3.52c)$$

$$N_4 = L_4 = [b_{13} + b_{14}x + b_{15}y + b_{16}z] \quad (3.52d)$$

where $b_1, b_2, \dots, b_{15}, b_{16}$ can be evaluated in terms of x, y , and z coordinates of the tetrahedron element. The set of Eq. 3.47 can be written in matrix form as

$$\begin{Bmatrix} H_x \\ H_y \\ H_z \end{Bmatrix}_e = \begin{bmatrix} N_1 & N_2 & N_3 & N_4 & 0 & 0 & 0 & 0 & 0 & 0 & 0 & 0 \\ 0 & 0 & 0 & 0 & N_1 & N_2 & N_3 & N_4 & 0 & 0 & 0 & 0 \\ 0 & 0 & 0 & 0 & 0 & 0 & 0 & 0 & N_1 & N_2 & N_3 & N_4 \end{bmatrix} \begin{Bmatrix} H_{x1} \\ H_{x2} \\ H_{x3} \\ H_{x4} \\ H_{y1} \\ H_{y2} \\ H_{y3} \\ H_{y4} \\ H_{z1} \\ H_{z2} \\ H_{z3} \\ H_{z4} \end{Bmatrix}_e \quad (3.53a)$$

where

$$[N] = \begin{bmatrix} \{N\} & \{0\} & \{0\} \\ \{0\} & \{N\} & \{0\} \\ \{0\} & \{0\} & \{N\} \end{bmatrix} \quad (3.53b)$$

and

$$\{\vec{H}\}_e = \begin{Bmatrix} \{H_x\} \\ \{H_y\} \\ \{H_z\} \end{Bmatrix}_e \quad (3.53c)$$

In a simplified form the above equation can be expressed as

$$[\vec{H}]_e = [N]^T \{H\}_e \quad (3.54)$$

where $[N]$ is the shape function represented by a 3×12 matrix and $\{H\}_e$ is the 12×1 column vector which represents the components of field, as shown above. The expression for $(\vec{\nabla} \times \vec{H}_e)$ can be written as

$$\vec{\nabla} \times \vec{H}_e = \vec{\nabla} \times [N]^T \{H\}_e \quad (3.55)$$

or,

$$\vec{\nabla} \times \vec{H}_e = \begin{bmatrix} 0 & -\frac{\partial}{\partial z} & \frac{\partial}{\partial y} \\ \frac{\partial}{\partial z} & 0 & -\frac{\partial}{\partial x} \\ -\frac{\partial}{\partial y} & \frac{\partial}{\partial x} & 0 \end{bmatrix} [N]^T \{H\}_e \quad (3.56)$$

or,

$$\vec{\nabla} \times \vec{H}_e = [Q]_e^T \{H\}_e \quad (3.57)$$

where

$$[Q]_e^T = \begin{bmatrix} 0 & -\frac{\partial}{\partial z} & \frac{\partial}{\partial y} \\ \frac{\partial}{\partial z} & 0 & -\frac{\partial}{\partial x} \\ -\frac{\partial}{\partial y} & \frac{\partial}{\partial x} & 0 \end{bmatrix}_{3 \times 3} \begin{bmatrix} N_1 & N_2 & N_3 & N_4 & 0 & 0 & 0 & 0 & 0 & 0 & 0 & 0 \\ 0 & 0 & 0 & 0 & N_1 & N_2 & N_3 & N_4 & 0 & 0 & 0 & 0 \\ 0 & 0 & 0 & 0 & 0 & 0 & 0 & 0 & N_1 & N_2 & N_3 & N_4 \end{bmatrix}_{3 \times 12} \quad (3.58)$$

or,

$$[Q]_e^T = \begin{bmatrix} 0 & 0 & 0 & 0 & -\frac{\partial N_1}{\partial z} & -\frac{\partial N_2}{\partial z} & -\frac{\partial N_3}{\partial z} & -\frac{\partial N_4}{\partial z} & \frac{\partial N_1}{\partial y} & \frac{\partial N_2}{\partial y} & \frac{\partial N_3}{\partial y} & \frac{\partial N_4}{\partial y} \\ \frac{\partial N_1}{\partial z} & \frac{\partial N_2}{\partial z} & \frac{\partial N_3}{\partial z} & \frac{\partial N_4}{\partial z} & 0 & 0 & 0 & 0 & -\frac{\partial N_1}{\partial x} & -\frac{\partial N_2}{\partial x} & -\frac{\partial N_3}{\partial x} & -\frac{\partial N_4}{\partial x} \\ -\frac{\partial N_1}{\partial y} & -\frac{\partial N_2}{\partial y} & -\frac{\partial N_3}{\partial y} & -\frac{\partial N_4}{\partial y} & \frac{\partial N_1}{\partial x} & \frac{\partial N_2}{\partial x} & \frac{\partial N_3}{\partial x} & \frac{\partial N_4}{\partial x} & 0 & 0 & 0 & 0 \end{bmatrix}_{3 \times 12} \quad (3.59a)$$

or, in a compact form

$$[Q]_e^T = \begin{bmatrix} \{0\}^T & -\frac{\partial \{N\}^T}{\partial z} & \frac{\partial \{N\}^T}{\partial y} \\ \frac{\partial \{N\}^T}{\partial z} & \{0\}^T & -\frac{\partial \{N\}^T}{\partial x} \\ -\frac{\partial \{N\}^T}{\partial y} & \frac{\partial \{N\}^T}{\partial x} & \{0\}^T \end{bmatrix} \quad (3.59b)$$

and

$$[Q]_e = \begin{bmatrix} \{0\} & \frac{\partial \{N\}}{\partial z} & -\frac{\partial \{N\}}{\partial y} \\ -\frac{\partial \{N\}}{\partial z} & \{0\} & \frac{\partial \{N\}}{\partial x} \\ \frac{\partial \{N\}}{\partial y} & -\frac{\partial \{N\}}{\partial x} & \{0\} \end{bmatrix} \quad (3.59c)$$

where $\{0\}$ denotes the zero or null vector. It is also noticeable that $[Q]_e$ and $[Q]_e^T$ are the real matrices.

Similarly the expression for the $(\vec{\nabla} \cdot \vec{H})$ is,

$$\vec{\nabla} \cdot \vec{H} = \vec{\nabla} \cdot \{N\}^T \{H\}_e \quad (3.60)$$

$$\vec{\nabla} \cdot \vec{H} = [R]_e^T \{H\}_e \quad (3.61)$$

where,

$$[R]_e^T = \vec{\nabla} \cdot \{N\}^T \quad (3.62)$$

$$\begin{aligned} [R]_e^T &= \begin{bmatrix} \frac{\partial}{\partial x} & \frac{\partial}{\partial y} & \frac{\partial}{\partial z} \end{bmatrix} \begin{bmatrix} \{N\}^T & \{0\} & \{0\} \\ \{0\} & \{N\}^T & \{0\} \\ \{0\} & \{0\} & \{N\}^T \end{bmatrix} \\ &= \begin{bmatrix} \frac{\partial}{\partial x} [N_1 \ N_2 \ N_3 \ N_4] & \frac{\partial}{\partial y} [N_1 \ N_2 \ N_3 \ N_4] & \frac{\partial}{\partial z} [N_1 \ N_2 \ N_3 \ N_4] \end{bmatrix} \\ &= \begin{bmatrix} \frac{\partial}{\partial x} [N]^T & \frac{\partial}{\partial y} [N]^T & \frac{\partial}{\partial z} [N]^T \end{bmatrix} \end{aligned} \quad (3.63)$$

and

$$[R]_e = \begin{bmatrix} \frac{\partial}{\partial x} \{N\} \\ \frac{\partial}{\partial y} \{N\} \\ \frac{\partial}{\partial z} \{N\} \end{bmatrix} \quad (3.64)$$

The vector variational functional for three dimensional electromagnetic problem is shown in Eq. 3.19. As the variational formulation consists of Maxwell's two curl equations, hence their Euler equations follow the Helmholtz's equation but do not necessarily satisfy the divergence equation ($div \cdot \vec{B} = 0$). This causes the presence of unwanted spurious solutions spread all over the eigenvalue spectrum along with the real physical modes. Like the 2D FV-FEM, the appearance of spurious modes are also true for a 3D FV-FEM. To avoid the spurious solutions, we followed the similar penalty method as reported in

[Rahman and Davies, 1984b]. Thus, an additional functional has been introduced with a weighting factor p in the full vectorial \vec{H} -field based formulation as

$$k_0^2 = \left(\frac{\omega}{c}\right)^2 = \frac{\int_v (\vec{\nabla} \times \vec{H})^* \cdot \hat{\epsilon}_r^{-1} \cdot (\vec{\nabla} \times \vec{H}) dV + p \int_v (\vec{\nabla} \cdot \vec{H})^* \cdot (\vec{\nabla} \cdot \vec{H}) dV}{\int_v \vec{H}^* \cdot \hat{\mu}_r \cdot \vec{H} dV} \quad (3.65)$$

where $\hat{\epsilon}_r$ and $\hat{\mu}_r$ are the relative permittivity or dielectric constant and permeability of the medium, respectively. ω is the angular frequency, c is the velocity of light in vacuum and p is the penalty term.

$$\epsilon_r = \frac{\epsilon}{\epsilon_0} \quad (3.66a)$$

$$\mu_r = \frac{\mu}{\mu_0} \quad (3.66b)$$

$$c = \frac{1}{\sqrt{\epsilon_0 \mu_0}} \quad (3.66c)$$

The functional becomes,

$$J(\vec{H}) = \int_v (\vec{\nabla} \times \vec{H})^* \hat{\epsilon}_r^{-1} (\vec{\nabla} \times \vec{H}) dV + p \int_v (\vec{\nabla} \cdot \vec{H})^* (\vec{\nabla} \cdot \vec{H}) dV - k_0^2 \int_v \vec{H}^* \hat{\mu}_r \vec{H} dV \quad (3.67)$$

The difference equation or the functional $J(\vec{H})$ can be stationary with help of Euler's equation. Therefore, $\delta J(\vec{H}) = 0$ and it gives,

$$\int_v (\vec{\nabla} \times \vec{H})^* \hat{\epsilon}_r^{-1} (\vec{\nabla} \times \vec{H}) dV + p \int_v (\vec{\nabla} \cdot \vec{H})^* (\vec{\nabla} \cdot \vec{H}) dV - k_0^2 \int_v \vec{H}^* \hat{\mu}_r \vec{H} dV = 0 \quad (3.68)$$

In the 2D finite element numerical scheme, it is assumed that the light is propagating in the z -direction, hence, the operator $\frac{\partial}{\partial z}$ can be replaced by the term $-j\beta$. On the other hand, for the 3D resonating structures, variational expression calculates the resonant frequencies and associated vectorial mode profiles of the cavity. Thus, the 3D finite element numerical scheme do not have the restriction on the z -variation like 2D FV-FEM. As a result, $(\vec{\nabla} \times \vec{H})$ produces the real matrix without having any β dependence. If we simplify first part of the equation (3.68) with the help of one of the properties¹ of matrix

¹ $(AB)^T = B^T A^T$ for any $m \times n$ matrix A and for any $n \times p$ matrix B. It is notable that the order of the factors are reversed.

transpose², we can write,

$$\begin{aligned}
 \int_v \left(\vec{\nabla} \times \vec{H} \right)^T \hat{\epsilon}_r^{-1} \left(\vec{\nabla} \times \vec{H} \right) dV &= \int_v \{H\}_e^T \left([Q]_e^T \right)^T \hat{\epsilon}_r^{-1} [Q]_e^T \{H\}_e dV \\
 &= \hat{\epsilon}_r^{-1} \{H\}_e^T \int_v [Q]_e [Q]_e^T dV \{H\}_e \\
 &= \{H\}_e^T [A]_e \{H\}_e
 \end{aligned} \tag{3.69}$$

where,

$$[A]_e = \hat{\epsilon}_r^{-1} \int_v [Q]_e [Q]_e^T dV \tag{3.70}$$

is the element $[A]_e$ matrix and $\hat{\epsilon}_r$ is the dielectric permittivity which is considered to be constant in each element.

The second part of the equation can be simplified as,

$$\begin{aligned}
 p \int_v \left(\vec{\nabla} \cdot \vec{H} \right)^T \left(\vec{\nabla} \cdot \vec{H} \right) dV &= p \int_v \left([R]_e^T \{H\}_e \right)^T \left([R]_e^T \{H\}_e \right) dV \\
 &= p \{H\}_e^T \int_v [R]_e [R]_e^T dV \{H\}_e \\
 &= p \{H\}_e^T [C]_e \{H\}_e
 \end{aligned} \tag{3.71}$$

where,

$$[C]_e = \int_v [R]_e [R]_e^T dV \tag{3.72}$$

Similarly, the third part (denominator part) of the equation (3.68) can be simplified as,

$$\begin{aligned}
 \int_v \vec{H}^T \mu \vec{H} dV &= \hat{\mu}_r \int_v \{H\}_e^T \left([N]_e^T \right)^T [N]_e^T \{H\}_e dV \\
 &= \hat{\mu}_r \{H\}_e^T \int_v [N]_e [N]_e^T dV \{H\}_e \\
 &= \{H\}_e^T [B]_e \{H\}_e
 \end{aligned} \tag{3.73}$$

where, $\hat{\mu}_r$ is the relative permeability of the medium. For optical mediums it is to be assumed that the medium contains no magnetic source, hence μ_r is always equal to 1.

$$[B]_e = \hat{\mu}_r \int_v [N]_e [N]_e^T dV \tag{3.74}$$

Since the volume domain is divided into a number of tetrahedral elements, hence by summing the contributions of all tetrahedral elements inside the volume, the equation

²conjugate transpose of a real matrix means simply the transpose of that matrix.

(3.68) can be expressed with the help of equations (3.69), (3.71) and (3.73) as an compact eigenvalue equation same as 2D-FV-FEM

$$\{H\}^T [A] \{H\} + p \{H\}^T [C] \{H\} - k_0^2 \{H\}^T [B] \{H\} = \{0\} \quad (3.75)$$

or,

$$([A] + p[C]) \{H\} - k_0^2 [B] \{H\} = \{0\} \quad (3.76)$$

The eigenvalue problem can be solved by using global matrices $[A]$, $[B]$, and $[C]$ which can be found by summing the contributions of all the element matrices $[A]_e$, $[B]_e$ and $[C]_e$. An appropriate eigenvalue solver with subspace iterative scheme is used to solve eigenvalues and eigenvectors of the above equation. The global matrices can be written as,

$$[A] = \sum_e [A]_e = \sum_e \hat{\epsilon}_r^{-1} \iiint [Q]_e [Q]_e^T dx dy dz \quad (3.77)$$

$$[B] = \sum_e [B]_e = \sum_e \hat{\mu}_r \iiint [N] [N]^T dx dy dz \quad (3.78)$$

$$[C] = \sum_e [C]_e = \sum_e \iiint [R]_e [R]_e^T dx dy dz \quad (3.79)$$

The element matrix $[A]_e$, $[B]_e$, and $[C]_e$ have been evaluated. The evaluation steps and the matrix coefficients are given in detail in Appendix B.

3.5 Boundary Conditions

Optical waveguides may have more than one material with multiple boundaries and interfaces between different media. Thus, appropriate boundary conditions need to be imposed in order to maintain the continuity of the electric and magnetic fields across the material interfaces. As the optical waveguides and resonators are made up of dielectric materials, one can assume that the surface charge and current to be zero. Therefore, the electromagnetic boundary conditions can be obtained as

- The tangential component of the electric field must be continuous across the boundary. If \vec{E}_1 and \vec{E}_2 illustrate the electric field vectors at side 1 and side 2, respectively

of the material interface, then

$$\hat{n} \times (\vec{E}_1 - \vec{E}_2) = 0 \quad (3.80)$$

$$\text{therefore,} \quad \vec{E}_{t1} = \vec{E}_{t2}$$

- The tangential magnetic field component must be continuous

$$\hat{n} \times (\vec{H}_1 - \vec{H}_2) = 0 \quad (3.81)$$

$$\text{therefore,} \quad \vec{H}_{t1} = \vec{H}_{t2}$$

- The normal component of electric flux densities must be continuous at the interface

$$\hat{n} \cdot (\vec{D}_1 - \vec{D}_2) = 0 \quad (3.82)$$

$$\text{therefore,} \quad \epsilon_1 \vec{E}_{n1} = \epsilon_2 \vec{E}_{n2}$$

$$\vec{E}_{n1} \neq \vec{E}_{n2}$$

here ϵ_1 and ϵ_2 are the permittivity in medium 1 and 2, respectively and at the material boundary, $\epsilon_1 \neq \epsilon_2$.

- The normal component of the magnetic flux density must be continuous at the interface

$$\hat{n} \cdot (\vec{B}_1 - \vec{B}_2) = 0 \quad (3.83)$$

$$\text{therefore,} \quad \mu_1 \vec{H}_{n1} = \mu_2 \vec{H}_{n2}$$

$$\vec{H}_{n1} = \vec{H}_{n2}$$

here μ_1 and μ_2 are the permeability of the medium 1 and 2, respectively. As most of the optical media are non-magnetic, thus, $\mu_1 = \mu_2 = 1$.

Apart from these electromagnetic boundary conditions two more boundary conditions can be imposed in practical waveguide and resonator problems.

- Perfect Electric Wall (PEW)

$$\hat{n} \times \vec{E} = 0 \quad \text{or,} \quad \hat{n} \cdot \vec{H} = 0 \quad (3.84)$$

PEW boundary condition signifies that the magnetic field vector \vec{H} is forced to be zero, hence disappear. The electric field \vec{E} remains continuous at the boundary.

- Perfect Magnetic Wall (PMW)

$$\hat{n} \times \vec{H} = 0 \quad \text{or,} \quad \hat{n} \cdot \vec{E} = 0 \quad (3.85)$$

This means that the \vec{H} field at the boundary is continuous and the \vec{E} field is forced to be zero. PEW and PMW boundary conditions are useful to take the advantages of one-fold and two-fold symmetry of the waveguide structure.

At the closed boundaries of an optical waveguide, additional boundary conditions are considered. In cases where the field decays at the boundary, the boundary can be left free without imposing any extra condition. This is often called as natural boundary condition. Whereas, in some cases, the boundary conditions are forced in order to exploit the symmetry of the structure to obtain an accurate result with less computational resources. These conditions can be classified as:

$$\text{Homogeneous Dirichlet} \quad \phi = 0 \quad (3.86)$$

$$\text{Inhomogeneous Dirichlet} \quad \phi = k \quad (3.87)$$

$$\text{Homogeneous Neumann} \quad \frac{\partial \phi}{\partial \hat{n}} = 0 \quad (3.88)$$

here ϕ defines the electric and magnetic field component, k is a prescribed constant value, and \hat{n} signifies the unit vector normal to the boundary surface. The Neumann boundary condition represents the rate of change of the field when it is directed outwards to the surface of the boundary.

3.6 Least Squares Boundary Residual (LSBR) Method

Design and optimisation of a complete photonic device demands an accurate way to overcome the discontinuity problems at the waveguide junctions. Discontinuity could occur in many cases such as butt-coupling of two waveguides of different width, height or radius, tapered waveguide to couple with optical fibre for an efficient mode matching, light coupling in bent waveguides and etc. Waveguide discontinuities can be treated in many ways such as combination of FEM with method of lines (MoL) [Kawano *et al.*, 1998], least squares boundary residual method (LSBR) [Davies, 1973], FEM with analytical approaches [Koshiba *et al.*, 1982], and free space radiation method (FSRM) [Reed *et al.*,

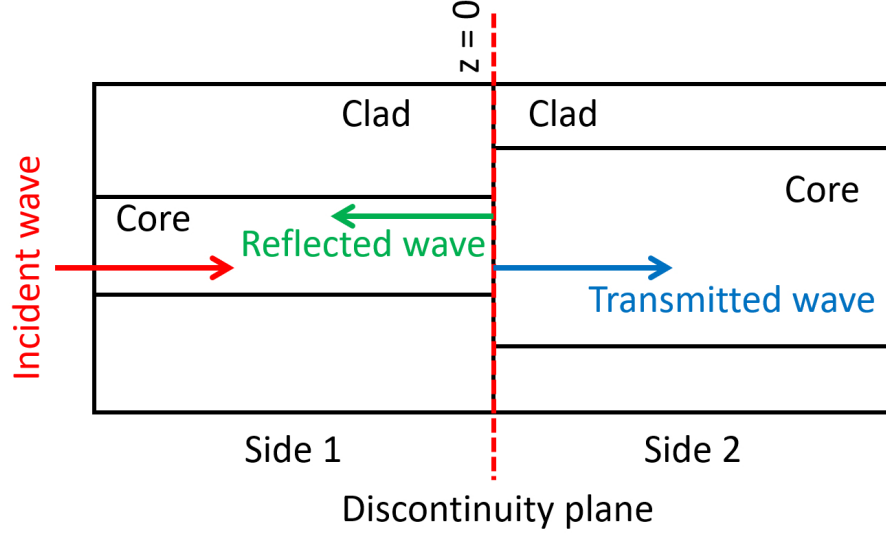


Figure 3.4: Schematic diagram to show waveguide discontinuity at a junction.

1996]. However, in this thesis our study is focused on the LSBR in conjugation with 2D FV-FEM developed by Rahman and Davies [Rahman and Davies, 1988]. It is to be noted that this method satisfies the boundary conditions in a least-squares sense over the discontinuity interface.

Figure 3.4 illustrates a schematic diagram of the waveguide discontinuity due to butt-coupling. It is assumed that the incoming incident wave is propagating through side 1 and it excites one mode of side 1 waveguide. A part of this wave reflects back to side 1 and some part is transmitted through side 2 waveguide. Due to boundary conditions, many modes may occur at the discontinuity plane ($z = 0$). These modes either can be guided or radiated in both sides of the discontinuity. Therefore, the transverse components of the electric and magnetic fields in sides 1 and 2 can be expressed in terms of side 1 and 2 eigenmodes as follows

$$E_t^{s1} = E_t^{in} + \sum_{i=1}^{\infty} a_i E_{ti}^{s1} \quad (3.89)$$

$$H_t^{s1} = H_t^{in} - \sum_{i=1}^{\infty} a_i H_{ti}^{s1} \quad (3.90)$$

$$E_t^{s2} = \sum_{i=1}^{\infty} b_i E_{ti}^{s2} \quad (3.91)$$

$$H_t^{s2} = \sum_{i=1}^{\infty} b_i H_{ti}^{s2} \quad (3.92)$$

here the superscripts $s1$ and $s2$ represent the side 1 and 2 of the junction at $z = 0$. a_i and b_i indicate the amplitudes of the i^{th} order reflected and transmitted mode at side

1 and side 2, respectively. The fields in Eqs. 3.92 can be truncated by considering the finite number of modes as is convenient. In LSBR, a functional K can be formed with the tangential fields. By minimizing that functional in a least squares sense satisfies the the continuity of the tangential field at the discontinuity junction at $z = 0$. The functional is of the form of

$$K = \int_A |E_t^{s1} - E_t^{s2}|^2 + p \cdot Z_0^2 |H_t^{s1} - H_t^{s2}|^2 dA \quad (3.93)$$

here p and Z_0 illustrate a dimensionless weighting factor and free-space wave impedance.

Application of the LSBR method demands that all the reflection, transmission, and radiation fields should be determined in such a way that the functional becomes minimum. This implies

$$\frac{\partial K}{\partial a_i} = 0; \quad \frac{\partial K}{\partial b_i} = 0; \quad \text{where } i = 1 \text{ to } \infty \quad (3.94)$$

This results a simple linear equation as

$$[C]\{x\} = [v] \quad (3.95)$$

A standard matrix solver can be used to solve the Eq. 3.95. The solution gives an array, $\{x\}$ that contains the values of a_i and b_i . $[C]$ defines a square matrix that can be generated from the mode eigenvectors and $[v]$ indicate an array depends on the incident mode. The coefficients of the C and v matrices can be obtained as

$$C_{ij} = \langle E_{ti}, E_{tj} \rangle + p \cdot Z_0^2 \langle H_{ti}, H_{tj} \rangle \quad (3.96)$$

and

$$v_i = \langle E_t^{in}, E_{ti} \rangle + p \cdot Z_0^2 \langle H_t^{in}, H_{ti} \rangle \quad (3.97)$$

here $i, j = 1$ to N and the N defines the total mode numbers in side 1 and side 2. Braces indicate the inner product which can be defined as

$$\langle x, y \rangle = \iint y^* \cdot x \, dx dy \quad (3.98)$$

Employing the FV-FEM program on both sides of the waveguide junction one can obtain the nodal \vec{H} field values for each guided and radiation modes. The \vec{E} field can be obtained from derived \vec{H} fields by applying the Maxwell's equations. Next, all the eigenmodes on both sides of the discontinuity could be used as input of LSBR method.

LSBR forms the functional K as in Eq. 3.93 and minimises that (Eq. 3.94) with respect to a_i and b_i for any given incidence. This results a linear equation as in Eq. 3.95. Solution of that equation provides a column vector x containing unknown reflected and transmitted coefficients of all modes considered for the analysis. In this section, the LSBR method has been described and associating this method with the FV-FEM one can accurately obtain the power transfer between coupled waveguides.

3.7 Perturbation Analysis for Waveguide Modal Loss

Waveguide modal loss is an important parameter that has to be taken into consideration while designing an integrated photonic waveguide and device. Perturbation analysis is a powerful method for modal loss calculation that can be incorporated with the FV-FEM code for 2D and 3D structures with multiple material layers. This method can be applied successfully to the waveguide structure with known analytical or numerical solutions. In case of a lossy waveguide structure, the perturbation scheme can be implemented directly once the unperturbed field distributions and phase constant values are obtained. It can be derived either by approximating the solution using a series expansion or straight from the variational formulation, if exists.

The perturbed phase constant β' and field distributions (\vec{E}' and \vec{H}') due to modal loss could be approximated from the unperturbed phase constant β and field values (\vec{E} and \vec{H}) which are the solutions of similar optical waveguide with loss-free condition. The attenuation constant, α of a waveguide due to material losses can be obtained as

$$\alpha = \frac{P_D}{2P_0} \quad (3.99)$$

where P_D is the dissipated power in the waveguide material and P_0 defines the time-averaged incident power flow. By considering the complex dielectric constant ϵ_e of waveguide material for each discretised sub-domain e , the attenuation constant (α) of the complete waveguide can be expressed in terms of electromagnetic vectorial fields as [Pantic and Mittra, 1986; Mirshekar-Syahkal and Davies, 1982]

$$\alpha = \frac{\omega \sum_e \epsilon_{re} \tan \delta_e \int_A |\vec{E}_0|^2 dA}{2 Re \int_A (\vec{E}_0 \times \vec{H}_0^*) \cdot \hat{z} dA} \quad (3.100)$$

here $\tan \delta_e$ defines the loss tangent of each sub-region defined by e as

$$\tan \delta_e = \frac{\epsilon_{ie}}{\epsilon_{re}} \quad (3.101)$$

where ϵ_{ie} and ϵ_{re} represent the imaginary and real part, respectively of each sub-domain or element. Therefore, the attenuation of the optical waveguide can be modified as

$$\alpha = \frac{\omega \sum_e \epsilon_{ie} \int_A |\vec{E}_0|^2 dA}{2 Re \int_A (\vec{E}_0 \times \vec{H}_0^*) \cdot \hat{z} dA} \quad (3.102)$$

here ω , \hat{z} illustrate the angular frequency and unit vector along z-axis, respectively. The \vec{E}_0 and \vec{H}_0 represent the unperturbed electric and magnetic field vectors, respectively under loss-less condition. The summation is carried over all sub-domains. This perturbation condition follows the assumptions that the unperturbed fields (\vec{E}_0 and \vec{H}_0) under loss-less condition remain unchanged even in presence of loss and the loss tangent has very small value, i.e. $\epsilon_{ie} \simeq \epsilon_{re}$.

3.8 Summary

This chapter elaborates the theoretical overview of the two-dimensional and three-dimensional full-vectorial finite element method in step-wise. A \vec{H} -field based vector variational formulation was considered in association with newly proposed divergence modified approach. Although, earlier penalty approach is efficient to eliminate the spurious modes, however, the newly proposed direct divergence modified approach is highly efficient to eliminate the unwanted non-physical modal solutions especially from the eigenvalue spectrum of plasmonic waveguides. A three-dimensional FV-FEM and its formulation steps also have been presented in detail. It can be used for the evaluation of resonating frequency and resonating modes in a 3D cavity.

MODAL ANALYSES OF INTEGRATED PHOTONIC WAVEGUIDES

4.1 Introduction

Different types of straight and bent waveguides are the basic building blocks of a photonic integrated circuit (PIC). Depending on the applications, one can exploits different design of dielectric, pure metallic, and hybrid waveguides. Before finalizing the waveguide design for expensive fabrications it is necessary to evaluate the light guiding property and guided mode area analyses of the waveguide. Researchers have already designed and optimised different dielectric waveguides. One of the commonly used dielectric waveguide is optical fibre which is widely used in telecommunication [Agrawal, 2012; Kaminow *et al.*, 2010] to critical medical diagnosis [Hocde *et al.*, 2004; Mahadevan-Jansen *et al.*, 1998; Utzinger and Richards-Kortum, 2003] and even in real-time sensing [Chee *et al.*, 2000; Ko and Grant, 2006; Grubsky and Feinberg, 2000; Masson *et al.*, 2004] applications. Single and multi-mode fibres are perturbed with Bragg [Hill and Meltz, 1997] and long period gratings [Bhatia and Vengsarkar, 1996; James and Tatam, 2003] for gas [Gu *et al.*, 2006], strain [Kersey *et al.*, 1993], temperature [Patrick *et al.*, 1996], humidity [Yeo *et al.*, 2008; Kronenberg *et al.*, 2002; Konstantaki *et al.*, 2006], and water [Liang *et al.*, 2005; Cusano *et al.*, 2005] monitoring applications. Besides, low index contrast fibres, silicon-on-insulator (SOI) based waveguides are of significant interest because of its light guidance in a more confined manner. Similarly, plasmonic and

hybrid plasmonic based waveguides have attracted a lot of interest because of its unique light guidance mechanism and applications in nano-dimensioned integrated photonic circuits. Before going into the depth of hybrid plasmonic based waveguide design, it is highly necessary to have a detail knowledge of light guidance by only a metal nano-wire surrounded by different dielectric materials.

In this section, our in-house divergence modified FV-FEM have been applied in modal analyses of metal nano-wire at telecommunication wavelength of 1550 nm. A detail investigation has been carried out for modal evolution of fundamental and higher order surface plasmon modes for identical and non-identical clad metal nano-wire. Mode evolutions depending on metal waveguide dimensions also have been analysed in detail.

A study on recent photonic waveguide related literatures show different definitions of mode effective area are used for different waveguides. Lack of suitable definition of effective area leads to confusions in waveguide design and analyses. In this section, we have conducted a rigorous study to revisit the problem. Several mode effective area formulations have been incorporated with in-house FV-FEM code and a range of different waveguides such as optical fibre, Si ridge, vertical, horizontal slot, and hybrid plasmonic slot have been studied in detail.

4.2 Modal Evolution of Metal Nano-wire by the Divergence Modified FV-FEM Approach

A finite dimensioned silver (Ag) nano-wire embedded in a dielectric media is considered for modal studies. Modal properties of any waveguide also depends on the cladding material refractive indices. Thus, for rigorous studies two different cases have been considered depending on the background materials,

- Ag nano-wire with identical cladding, where semi-infinite lower clad (substrate) and upper clad (superstrate) have the same refractive index ($n_{\text{substrate}} = n_{\text{superstrate}}$)
- Ag nano-wire with non-identical cladding, with the lower and upper clads have different refractive indices ($n_{\text{substrate}} \neq n_{\text{superstrate}}$).

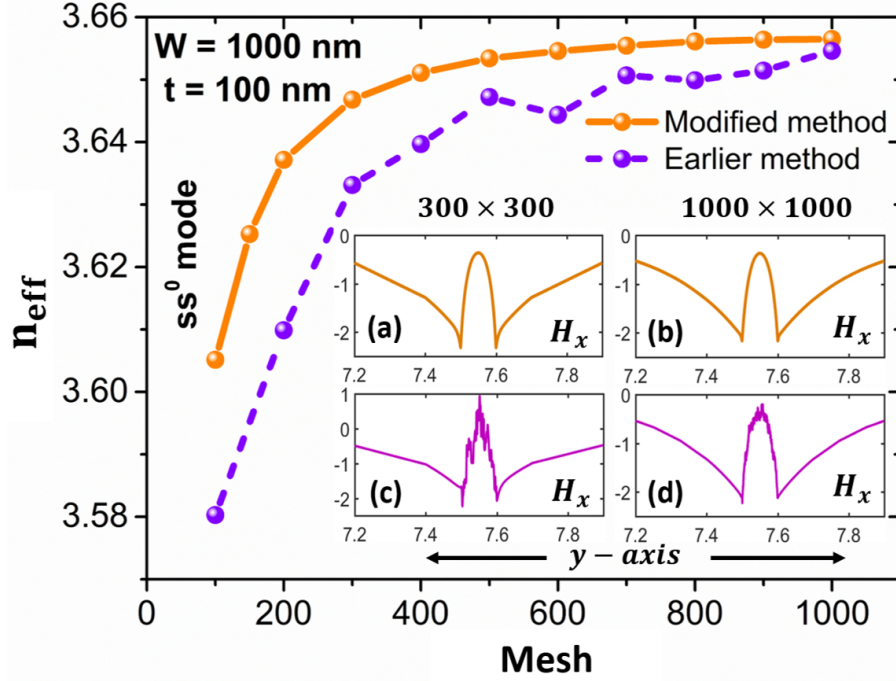


Figure 4.1: Real effective index (n_{eff}) variation of the fundamental plasmonic ss^0 mode in an identical clad metal nano-wire ($W = 1000$ nm, $t = 100$ nm) with the FV-FEM mesh size. The orange solid and purple dashed lines indicate the n_{eff} determined by the new divergence modified FV-FEM and earlier penalty method, respectively. The insets (a), (c) and (b), (d) show the 1D-line plot of the H_x field along y -axis of the ss^0 mode (magnified to the metal-dielectric interfaces) for a lower 300×300 (180,000 elements) and a higher 1000×1000 (2,000,000 elements) FV-FEM meshes, respectively.

Previously, some works on plasmonic bound and leaky modes for 1D planar lossy metal film [Burke *et al.*, 1986] and 2D waveguides have been reported by using semi-analytical and numerical methods, such as reflection pole method [Zia *et al.*, 2004], full-vectorial finite element [Themistos *et al.*, 1995] and finite difference method (FV-FDM) [Zia *et al.*, 2005]. Berini has also reported a modal study of a metallic waveguide using the Method of Lines (MoL) [Berini, 2000, 2001]. In this set of work, a rigorous analysis of the plasmonic modal evolutions and light guidance by a metal nano-wire surrounded by the high index CMOS compatible dielectric material of refractive index around 3.5 has been carried out by using our newly divergence modified dedicated in-house full-vectorial finite element method (FV-FEM) at the widely-used communication wavelength, $\lambda = 1550$ nm. Accurate field profiles of these supermodes have been presented and explained their evolution with the help of mode effective area (MEA), particularly when its width is comparable to its height. Throughout the simulation process the computational domain is discretised with

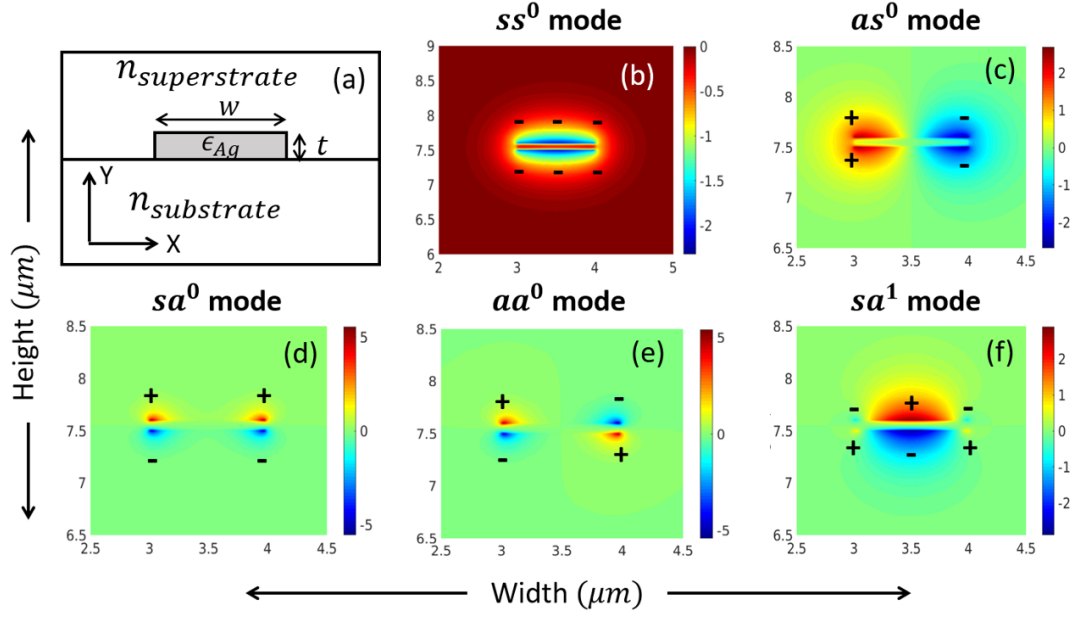


Figure 4.2: Schematic diagram of dielectric clad metal nano-wire and its plasmonic mode field profiles simulated by FV-FEM at 1550 nm. (a) Schematic diagram of a silver (Ag) wire, (b)-(e) are the H_x field distributions of four plasmonic modes, ss^0 , as^0 , sa^0 , and aa^0 , respectively and (f) is a higher order mode (sa^1) guided the metal waveguide. Ag nano-wire of width, $W = 1000$ nm and thickness, $t = 100$ nm are considered.

the 1,280,000 triangular elements (800×800 mesh) and a special care has been taken in mesh distribution, so that the maximum element size was less than 0.2 nm around the metal core to resolve the sub-wavelength light confinement at the metal-dielectric interfaces and corners accurately. The efficiency and stability of the new divergence modified FEM approach is tested for different mesh sizes. Figure 4.1 shows the real effective index (n_{eff}) variation with the mesh sizes. The ss^0 fundamental mode (Fig. 4.2) of the identically clad metal nano-wire of dimension 1000×100 nm² is considered here (discussed in detail in subsection 4.2.1). Results of the new modified approach, shown by the orange solid line, shows a stable and monotonic convergence with the mesh. On the other hand, the n_{eff} obtained by using the earlier penalty method [Rahman and Davies, 1984b] shows a random nature (dashed purple line) with the similar meshes. It can also be noted that the modified method results in higher n_{eff} values and also it converges faster than the earlier method. Thus, the proposed method is more accurate and converges faster. An acceptable result can easily be obtained by a lower 400×400 mesh (320,000 elements) distributions. The insets (a) and (b) of Fig. 4.1 show the ss^0 mode with noise-free dip in the middle (metal), solved by using the modified method. Top left and

right sided insets ((a) and (b)) are the simulated results using a coarser, 300×300 (180,000 elements) and a finer, 1000×1000 (2,000,000 elements) meshes, respectively. Lower left and right sided insets (c) and (d) are the results of the same mesh distributions but with the earlier penalty approach. The mode fields in (c) and (d) show the dip inside the metal region but with considerable noise. However, with a very fine mesh (1000×1000), the field noises reduced by some degrees at expenses of high computational cost and time. Thus, the newly modified FV-FEM has not only successfully eliminated unwanted spurious plasmonic modes with a monotonic and fast converging mode propagation characteristic but also provides a clear and noise-free modal field profiles.

4.2.1 Metal Nano-wire with Identical Cladding

This waveguide structure contains a thin Ag metal strip surrounded by the semi-infinitely extended dielectric material ($n_{\text{substrate}} = n_{\text{superstrate}}$), as shown in Fig. 4.2. When $W \rightarrow \infty$ this structure is equivalent to a plasmonic slab waveguide. In case of $W \gg t$, due to high waveguide aspect ratio (W/t) the plasmonic modes formed at the top and bottom metal-dielectric interfaces, however, when W is comparable to t , modes also form at the vertical sides and also at all four corners. All these modes have dominant magnetic field (H_x). In this section, we only studied the bounded plasmonic modes and followed the same nomenclature as reported in [Berini, 2000, 2001] for SP modes. Symmetric (defined by letter s) and asymmetric (defined by letter a) characteristics of modal profiles show four different combinations for fundamental plasmonic modes and the superscript m denotes the mode order number, such as, ss^0 , as^0 , sa^0 , and aa^0 are four fundamental modes are shown in Fig. 4.2(b) - (e). Here, the first and second letters identify the horizontal and vertical variations, respectively. Higher order modes are defined by the number ($m > 0$) of field lobes at the material interfaces, such as, sa^1 in Fig. 4.2(f) with one Gaussian-like bump on both sides of the metal wire.

4.2.1.1 Modal Dependencies on Wavelength and Surrounding Cladding

Materials

Initially, wavelength (λ) dependencies of four possible fundamental SP modes have been studied, shown in Fig. 4.3. Two different metal widths (W) 1000 and 500 nm for a fixed

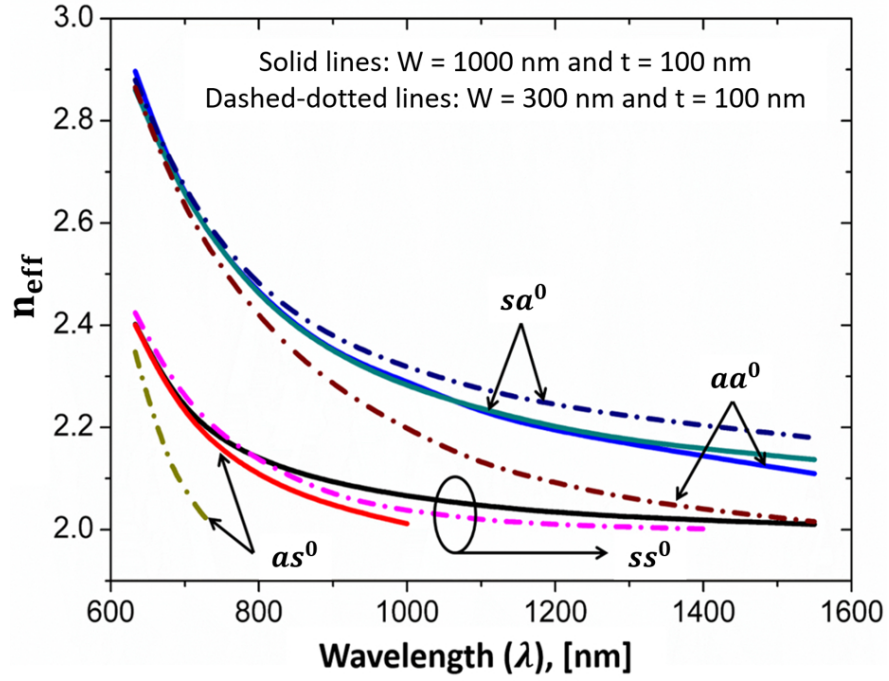


Figure 4.3: Dispersions of different plasmonic modes with the operating wavelength (λ) ranging from 633 nm to 1550 nm.

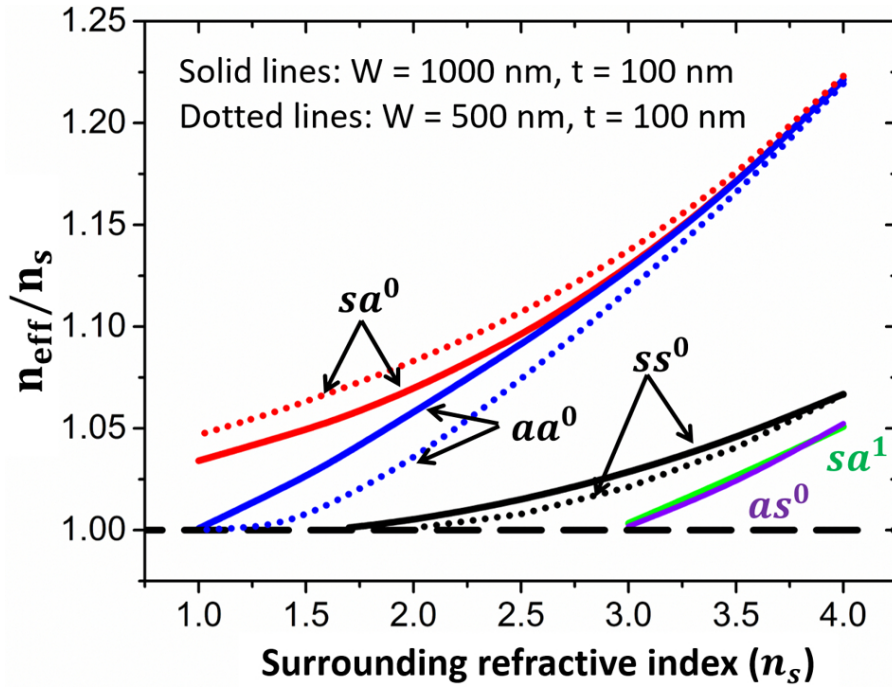


Figure 4.4: Normalised effective indices variations of plasmonic modes with the surrounding identical material. The solid and dotted lines indicate the variations for $W = 1000$ and 500 nm, respectively when t is fixed at 100 nm. The operating wavelength (λ) is fixed at 1550 nm.

thickness, $t = 100$ nm are considered, shown by the solid and dotted lines, respectively. Ag dielectric constant is strongly λ dependent and it can be determined by the Drude model [Bohren and Huffman, 2008].

$$\epsilon_{Ag}(\lambda) = \epsilon_r + j\epsilon_i = \epsilon_\infty - \frac{\omega_p^2}{\omega(\omega + j\omega_c)} \quad (4.1)$$

where ϵ_∞ is related with absorption peaks at very high frequency, $\omega \gg \omega_c$. The value of ϵ_∞ is taken as 3.1. ω_c and ω_p define the collision and plasma frequency. The collision frequency (ω_c) has the value of 0.031×10^{14} rad/s and the plasma frequency can be defined as, $\omega_p = \omega_{p0} \cdot e^{-A_V(T_0)(T-T_0)/2}$. ω_{p0} and A_V define the plasma frequency at the ideal temperature, $T_0 = 25$ °C and thermal volume expansion coefficient of Ag with the value of 5.7×10^{-5} /°C, respectively. However, wavelength dependent dielectric constant of Ag can also be obtained by the Kramers-Kronig relation [Babar and Weaver, 2015] which agrees well with the Drude model (Eq. 4.1). For these studies, we considered recent reported Ag refractive index in [Babar and Weaver, 2015]. Besides, the substrate and superstrate of the waveguide are considered to have same material with its refractive index value of $n_{substrate} = n_{superstrate} = 2$ throughout the wavelength spectrum, ranging from 633 nm to 1550 nm. All the effective indices (n_{eff}) curves for ss^0 , as^0 , sa^0 , and aa^0 modes shown in Fig. 4.3 tend to converge asymptotically to the surrounding refractive index ($n_s = 2$) with the increasing λ . The ss^0 , sa^0 , and aa^0 modes are guided over a broad wavelength spectrum range whereas, the as^0 mode shows a rapid approach to cut-off. The effective indices of sa^0 and aa^0 show almost similar n_{eff} values for $W = 1000$ nm. However, with the decrement of waveguide width (W) these two modes start to separate from each other. For a much lower width this separation becomes more prominent. Here, we considered a waveguide with thickness, $t = 100$ nm but with a much lower width, $W = 300$ nm, the corresponding mode effective indices of sa^0 and aa^0 diverge from each other at higher λ and aa^0 mode shows a much steeper asymptotic convergence to the background index values. This implies that for lower W/t ratio, only the sa^0 mode will exist for further higher wavelengths. The ss^0 mode profile shows a field transition, but not shown here. At lower operating wavelengths, the ss^0 mode supports distinct symmetric field confinement at four nano-wire corners. That modal distribution is comparable with sa^0 mode, shown in Fig. 4.2(d) but with either all + or all - field values at the four corners.

As λ increases, the ss^0 field starts to evolve from four narrow corner spikes to the centre of metal-dielectric interfaces so that the field makes a Gaussian-like distribution along upper and lower interfaces, as shown in Fig. 4.2(b). This shows that at smaller λ , fields are well confined, so weakly coupled and as a result more localised. No such sa^0 and aa^0 mode evolutions were observed over the wavelength range considered here. It can also be noticed in Fig. 4.3 that at the lower operating wavelength region both the sa^0 and aa^0 modes have almost same refractive index thus those two modes are considered to be close to each other. In this condition, the metal waveguide with its single mode operation could be used for sensing applications.

Figure 4.4 depicts how strong all the four fundamental modes approach the background supported TEM modes with the reduction in refractive index value of surrounding material, shown by the normalised effective index (n_{eff}/n_s) variations. In these cases, the wavelength is kept fixed at 1550 nm. Two different metal widths, $W = 1000$ and 500 nm with same thickness, $t = 100$ nm have been considered, shown by the solid and dotted lines, respectively. As the surrounding dielectric material refractive index decreases, for all plasmonic modes not only their effective indices decrease but also normalised effective index reduces and the mode fields spread more into the outer cladding region. At a low index background, the modal effective indices approach the cladding refractive index value and their modal cut-offs. The modes are then less bounded to the metal core and mostly guided by the background dielectric cladding, which also reduce the mode attenuation. Study shows that the fundamental as^0 and a higher order sa^1 mode for $W = 1000$ nm only exist for a high index cladding ($n_s > 3.0$) and approaches to the cut-off faster than the other modes. The ss^0 for both $W = 1000$ and 500 nm, reach to the cut-off earlier than the sa^0 and aa^0 modes. For the background refractive indices lower than 1.7 and 2.0 for $W = 1000$ and 500 nm, respectively only sa^0 and aa^0 exist. With reduction of metal W , the normalised effective indices of all the modes reach to the cut-off line i.e. $n_{eff}/n_s = 1$ faster, except for mode sa^0 which did not converge to the cut-off line for the surrounding material of refractive index even when reached that of the free-space. Other aa^0 mode approaches to cut-off for free-space cladding and there it evolves into background dielectric guided quasi-TEM mode with a very low modal attenuation (α (dB/ μm) = $40\pi Im(n_{eff})/\lambda \ln(10)$) of 1 dB/mm. However, all these behaviours described above are

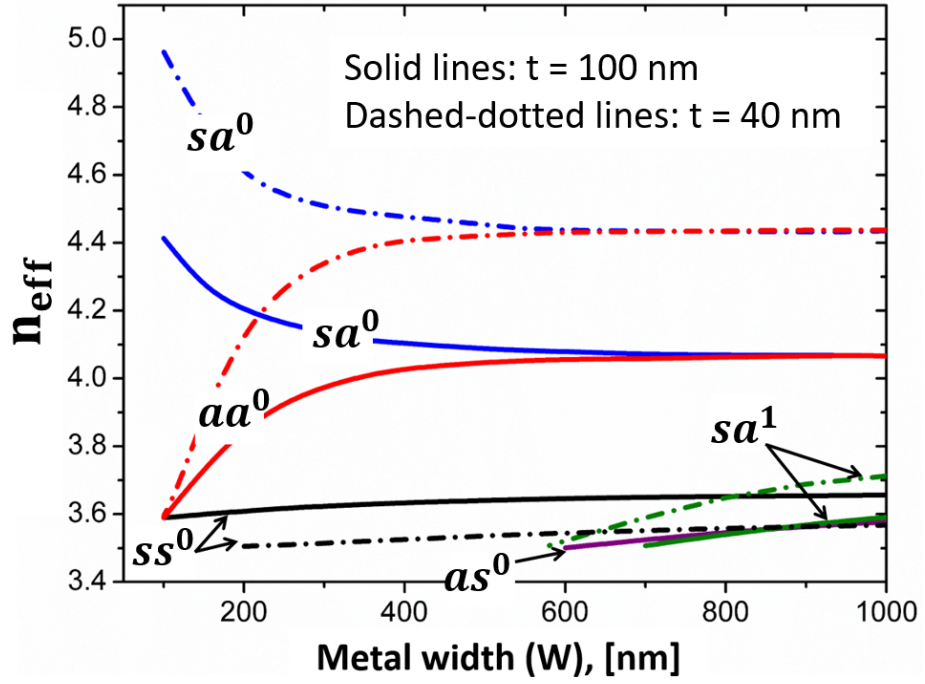


Figure 4.5: n_{eff} variations of plasmonic modes with metal width (W). The solid and dashed lines indicate the variations for two different thickness, $t = 100$ and 40 nm, respectively.

investigated at the operating wavelength of 1550 nm, and their modal evolutions with the wavelength are shown in Fig. 4.3.

4.2.1.2 Modal Dependencies on Waveguide Dimensions

A rigorous study shows a strong SPP modal dependence with the structural parameters (W and t) of the metal film. In both cases, it is being assumed that the finite metal film is bounded by an identical medium, $n_{substrate} = n_{superstrate} = 3.5$. Variations of mode effective index (n_{eff}) with the W for two different t , 100 and 40 nm are shown in Fig. 4.5. The solid and dashed-dotted lines denote the modal n_{eff} variations for $t = 100$ and 40 nm, respectively. The n_{eff} of all modes (aa^0 , ss^0 , as^0 , and sa^1) except sa^0 decrease with the reduction of W . For a large W , modes are well confined at the upper, lower and corners of the metal-dielectric interfaces. Decrease of modal effective indices towards the cladding refractive index indicates that the mode fields are less confined into lossy metal core and mostly spread into background dielectric medium. These also result in lower mode attenuation and consequently long modal propagation length ($L_p = \lambda/4\pi Im(n_{eff})$) which is defined as a waveguide length at which the SPP mode field decays by a factor of

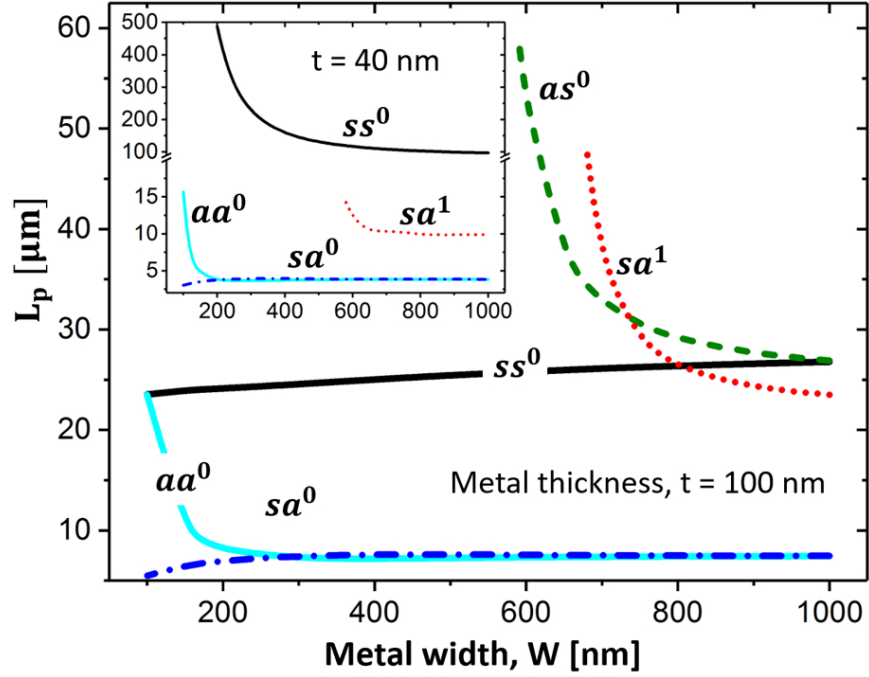


Figure 4.6: The main and inset figures show the mode propagation length (L_p) of different SPP modes with metal width (W) for different thickness, $t = 100$ and 40 nm, respectively.

$1/e$, shown in Fig. 4.6. For a wider W , the symmetrical and asymmetrical fields of sa^0 and aa^0 modes, respectively along x-direction are weakly coupled for a given thickness and both the modes travel with almost same propagation constants. As W reduces, symmetric corner fields of sa^0 mode along x-direction are strongly coupled with each other and the corner fields also spread all along the upper and lower interfaces. Thus, sa^0 mode gets more confined and its n_{eff} increases when W reduces. On the other hand, for the aa^0 mode, due to asymmetrical corner field distributions, fields cannot spread over the metal-dielectric interfaces rather dispersed into cladding medium. Hence its n_{eff} shows a steeper reduction towards background refractive index. These also indicates higher and lower mode attenuations (α) for the sa^0 and aa^0 , respectively (Fig. 4.6). Additionally, with the reduction of t , the upper and lower interfaces come closer and the corner fields show a strong coupling as a result both the sa^0 and aa^0 modes show an increase of n_{eff} , away from the background refractive index, shown in both Figs. 4.5 and 4.7. These also correspond to the higher mode attenuations and lower L_p that can be seen in the Fig. 4.6 and inset of Fig. 4.7. The symmetric mode field distributions along x and y-axes show a comparative low field confinement at the metal core rather mostly guided by the dielectric

cladding. Thus, the n_{eff} of the ss^0 decreases and approaches towards the cut-off with reduction of both W and t (Figs. 4.5 and 4.7). At the cut-off, modes evolve to the cladding supported quasi-TEM mode. Thus, its modal attenuation decreases and L_p increases as it approaches towards cut-off, shown in Fig. 4.6 and inset of 4.7. Another fundamental mode as^0 (Fig. 4.2 (c)) with symmetric field along y -axis only exists for higher W (Fig. 4.5) that approaches to cut-off early. This also results an increasing L_p (Fig. 4.6) with W as it approaches its cut-off. This mode only exists for a limited range of t (do not exist for $t < 50$ nm, Fig. 4.7). This can also be observed in Fig. 4.7 where its n_{eff} and mode attenuation decrease as the metal core thickness decreases. In this study, two fundamental modes ss^0 and as^0 show a much lower modal attenuation (α) of 2.4 dB/mm ($W = 1000$ nm and $t = 15$ nm) and 39.4 dB/mm ($W = 1000$ nm and $t = 50$ nm), respectively. Thus, it is expected that these modes can provide long range stability which could be useful for plasmonic based integrated optical applications. Besides the fundamental modes, we have also studied two higher order modes. Their mode evolutions are more complex. The sa^1 mode (Fig. 4.2(f)) sustains over higher range of W , shown in Fig. 4.6. Due to its asymmetric field distribution along y -axis, the mode field gets more confined as t decreases. Thus, both of its n_{eff} and α increase with the reduction of t (Fig. 4.7). Here aa^2 is another higher order mode with similar modal properties that only appears when metal layer is thinner. Some of their modal properties can be seen in Figs. 4.5, 4.6, and 4.7.

4.2.2 Metal Nano-wire with Non-identical Cladding

Evolution of coupled plasmonic modes with truly 2D confinement, but with identical cladding materials are shown above. However, in most practical cases, upper and lower cladding materials can be totally different ($n_{superstrate} \neq n_{substrate}$), hence not only their plasmonic modal profile will changes but also their phase matching condition. Thus, our next study involves the evolutions of such modes and plasmonic supermode (PSM) for non-identical clad metal nano-wire. Schematic of the structure is shown in Fig. 4.2(a) but here a small index difference is considered with $n_{substrate} = 3.5$ and $n_{superstrate} = 3.3$. The material with refractive index of 3.5 defines Si at the wavelength of 1550 nm. On the other hand, a material having refractive index value of 3.3 is not practically possible at that wavelength. However, for this theoretical study, we considered substrate and

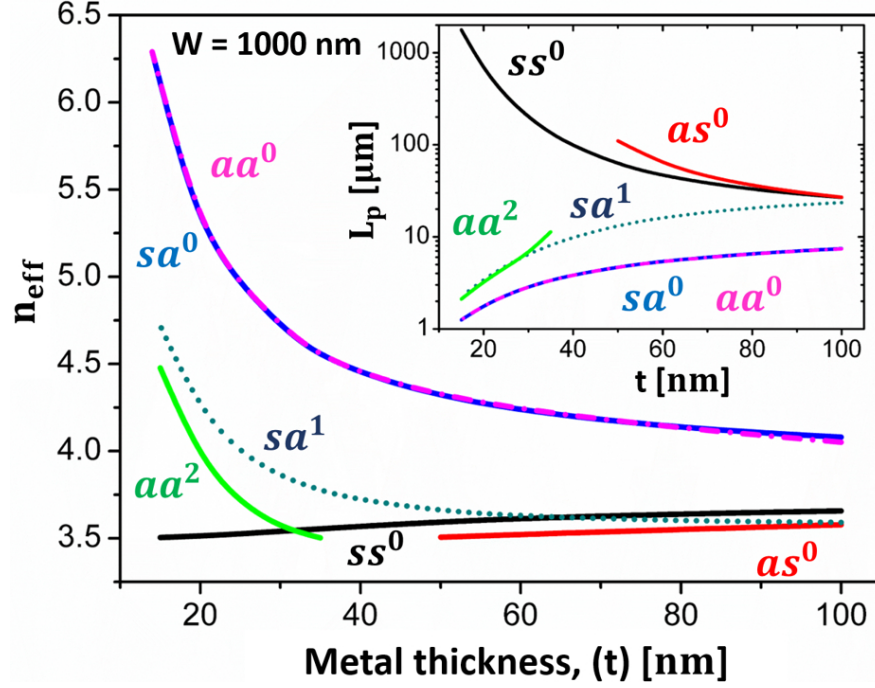


Figure 4.7: Plasmonic modal characteristics with metal nano-wire thickness (t) for a fixed width, $W = 1000$ nm. The main plot shows the n_{eff} variations of all fundamental higher order modes and the inset shows the corresponding modal propagation length (L_p) variations against t .

superstrate materials with refractive indices of 3.5 and 3.3, respectively to emphasise on the plasmonic supermode formation and its evolution due to small index difference in the substrate and superstrate regions. Plasmonic mode evolutions due to a large index difference in top and bottom cladding regions also studied in later section.

4.2.2.1 Asymmetric Modal Evolution with Nano-wire Thickness (t)

In this section, we report the evolution of bound fundamentals and PSMs with metal film thickness (t) for two different widths (W). The modal n_{eff} and L_p variations with the t and W are shown in the main and inset of Fig. 4.8(a). Three different plasmonic modes, such as, a PSM and two fundamental modes (sa^0 and aa^0) were identical during the dimensional changes of metal film. For identical bounding material a given mode at upper and lower interfaces are always phase matched and they couple to form two complete symmetric and antisymmetric SP mode. Similarly, identical modes on the left and right interfaces couple to form SP modes. However, when the superstrate and substrate cladding materials are not the same, identical mode order cannot couple as their phase velocities are different,

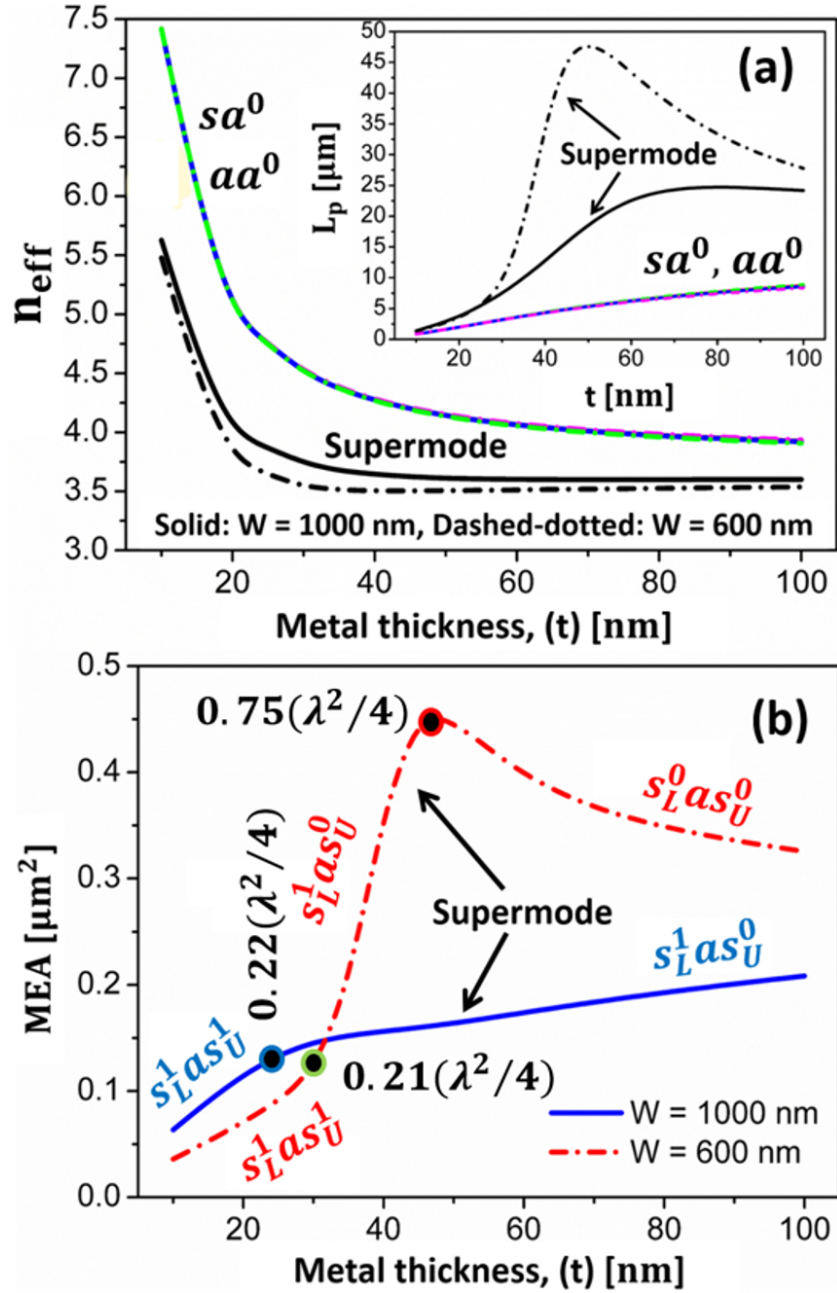


Figure 4.8: SPP modal characteristics its evolutions with metal thickness (t) for a metal nano-wire with a small index-difference ($n_{substrate} = 3.5$ and $n_{superstrate} = 3.3$) in the cladding. The main and inset of (a) show the n_{eff} and L_p variations of long range supermode, sa^0 and aa^0 modes for fixed $W = 1000$ nm and 600 nm shown by the solid and dashed-dotted lines, respectively. The solid blue and dashed-dotted lines in (b) depict the modal effective area (MEA) of supermodes for $W = 1000$ and 600 nm, respectively.

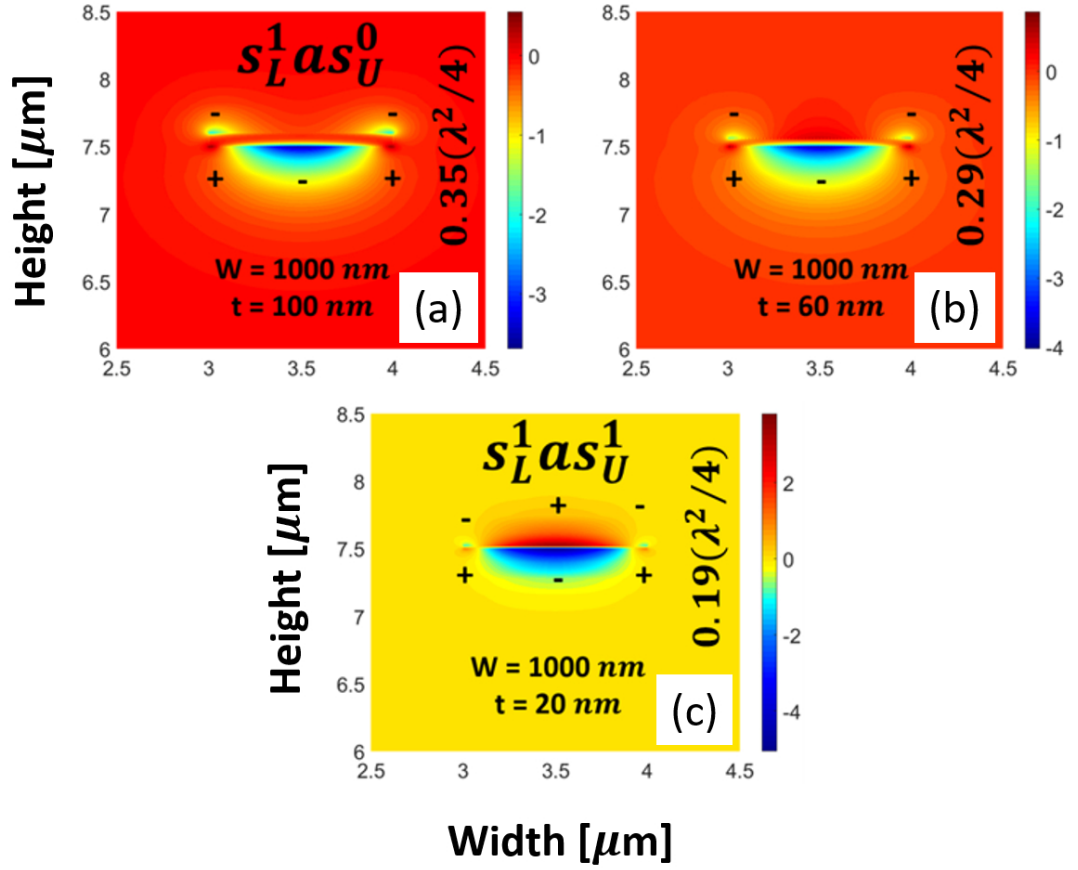


Figure 4.9: (a), (b), and (c) denote the H_x field evolution of the long range plasmonic supermode (PSM) for three different metal thickness, $t = 100, 60$, and 20 nm, respectively. W is fixed at 1000 nm. The operating wavelength is kept fixed at 1550 nm.

but modes of different orders at upper and lower (or left and right) interfaces can couple to form supermode but only when their propagation constants are similar. Here, the PSM forms due to coupling of ss^0 and sa^1 like modes that we had observed for identical clad metal waveguide. With different t , it shows a clear evolution which occurs due to coupling of individual upper and lower interface modes for a particular value of t . This PSM is named in a slightly different manner for better understanding, such as $I_L^m J K_U^m$. The first and third letters i.e. I and K indicate either symmetric (s) or asymmetric (a) horizontal (along x) fields at the lower and upper interfaces with superscript m as the number of intermediate localised field maxima or minima that occurs at these interfaces. The second letter J also indicates either symmetric (s) or asymmetric (a) field distribution but along vertical (along y) direction. A notable field evolution for the long range asymmetrical PSM ($s_L^m a s_U^m$) has been observed and its parameter variations are shown with metal thickness

(t) for a fixed $W = 1000$ nm. Figures 4.9(a), (b), and (c) depict the H_x field profiles of that PSM for $t = 100, 60$, and 20 nm, respectively. In Fig. 4.9(a) the substrate (lower) interface field distribution exhibits two localised maxima at the corners and one minima at the centre (s^1) whereas the superstrate (upper) interface shows only two localised minima at the corners (s^0), which combined to form a $s_L^1 a s_U^0$ PSM. Two different individual modes at upper and lower interfaces have the same propagation constant (β) and together they form the $s_L^1 a s_U^0$ PSM for $t = 100$ nm. As t decreases modes at both the interfaces start to interact as their coupling increases. The centre maxima at the top interface grows gradually (Fig. 4.8(b)) due to a strong influence of the high index guided lower interface's s^1 mode. Finally, at lower $t = 20$ nm, the upper field completely evolved due to strong coupling and the metal waveguide shows a perfect $s a^1$ mode, as shown in Fig. 4.2(f) which could also be named as $s_L^1 a s_U^1$ PSM, shown in Fig. 4.9(e). Its n_{eff} and L_p variations with t for $W = 1000$ nm are shown by the solid black lines in the main and inset of Fig. 4.8(a), respectively.

The light confined by the waveguide and surrounding media is determined by the modal effective area (MEA). As the \vec{E} and \vec{H} fields in a plasmonic mode have significantly different mode field profiles, we have followed the mode effective area calculation that included the z-component of modal Poynting vector

$$S_z = (\vec{E} \times \vec{H}^*) \cdot \hat{z} \quad (4.2)$$

which considers the effect of both \vec{E} and \vec{H} fields as,

$$MEA = \frac{(\iint S_z dx dy)^2}{\iint S_z^2 dx dy} \quad (4.3)$$

The mode effective area (MEA) variations (blue solid line in Fig. 4.8(b)) with t indicates a clear modal evolution. At higher thickness, till $t \simeq 25$ nm, the upper interface s^0 mode evolves slowly whereas the s^1 mode always maintain its form at lower interface. Here, in the substrate with higher refractive index, the mode field localises more strongly than the superstrate with a lower refractive index. The corresponding n_{eff} and MEA curves maintain a continuous variation until t reaches around 25 nm. For the metal thickness, $t = 25$ nm the MEA shows the value of $0.22(\lambda^2/4) \mu\text{m}^2$. At lower t , due to the strong coupling between two interfaces and low index superstrate guiding the upper s^0 mode evolves

faster and when $t < 25$ nm, its n_{eff} shows a steeper increment away from the background dielectric refractive indices. The PSM becomes more localised and well confined into lossy metal core (Fig. 4.9(c)). Thus, its L_p and MEA decreases for a lower t . These PSM characteristics with t for a small non-identical clad waveguide also correlates with the combined behaviours of ss^0 and sa^1 modes for a symmetrical waveguide shown in Fig. 4.7. This proves that this PSM is a blended form of ss^0 and sa^1 modes at two interfaces.

For a lower W (600 nm), the PSM supported by a metal nano-wire evolves with the variation of t , and show three different supermode formations, such as $s_L^1 as_U^1$, $s_L^1 as_U^0$, and $s_L^0 ss_U^0$ at different metal core thicknesses. The black and red dashed-dotted lines in main and inset of Figs. 4.8(a) and (b) show the n_{eff} , L_p , and MEA variations with t for a lower $W = 600$ nm, respectively. It can be observed that as t decreases the n_{eff} decreases and reaches a minimum value (nearly reach the background refractive index). Below $W = 600$ nm the PSM approaches to their cut-off and in that case, fields are mostly guided by the surrounding dielectric media. L_p variations also indicate the modal evolution and a high L_p value is obtained for $W = 600$ nm. The 1D H_x field plot along x-axis of the PSM for $t = 100$, 40, and 20 nm at the superstrate and substrate interfaces are shown in Fig. 4.10(a) and (b) by the green, red, and blue solid lines, respectively. Based on the MEA and L_p variations with t , one can divide those curves into three distinct sections which signify three different forms of the PSM. At lower t (20 nm), the blue field profiles at upper and lower interfaces show the s^1 distributions which couple to form a $s_L^1 as_U^1$ PSM. This mode exists for $t = 10$ to ~ 30 nm. As t increases, its n_{eff} reaches to a minimum value at $t = 48$ nm and then further increases slightly. On the other hand, the L_p and MEA both possess maximum values at that thickness value when n_{eff} shows its minima. This low loss and high mode effective area indicate that the modal confinement was mostly in the surrounding dielectric materials. The field profiles shown by the red lines at both the interfaces indicate that a $s_L^1 as_U^0$ mode exists over a thickness region t from ~ 30 to 50 nm. The MEA at these two metal thicknesses, $t = 30$ and 48 nm are 0.21 and 0.75 times of the diffraction limited mode area ($\lambda^2/4$), respectively. Beyond that, both the L_p and MEA decreases faster with increase of t . At $t = 100$ nm, the field variations shown by the green lines at both interfaces show a completely transformed nature of the PSM. The upper interface shows two symmetrical maxima at both the corners (s^0) whereas

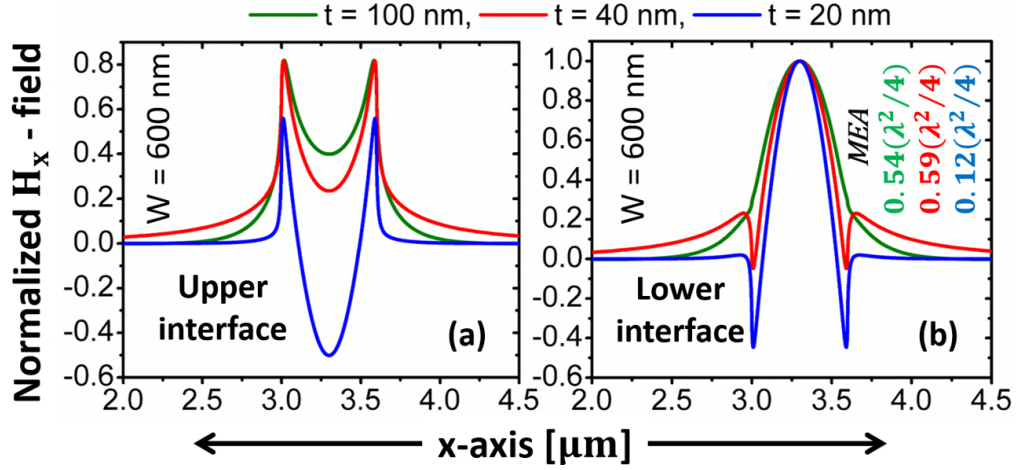


Figure 4.10: Normalised H_x 1D field plot of the long range supermode for three different thickness, $t = 100, 40$, and 20 nm, shown by the solid green, red, and blue lines, respectively. Corresponding mode effective area (MEA) are shown in (b). The metal nano-wire width (W) is fixed at 600 nm. The top ($n_{superstrate} = 3.3$) and bottom ($n_{substrate} = 3.5$) interfaces field distributions are shown in sub-figures (a) and (b), respectively.

the bottom interfaces shows only one Gaussian distribution with field maxima at the middle. These individual distributions at top and bottom interfaces combined to form a $s_L^0 s_U^0$ PSM. In short, with increase of t , the top corner maxima exist throughout but the centre minima vanish gradually, and for the lower interface the centre maxima sustain but corner minima disappear. For lower W (600 nm) the left and right interfaces interact along with the upper and lower interfaces. Thus, the formed PSM shows evolution of field distributions along all the four metal-dielectric interfaces in the both x and y -directions.

For the conditions studied above, the two other fundamental modes sa^0 and aa^0 did not show any modal evolutions. As t increases, its n_{eff} decreases in a rectangular hyperbolic nature. Same n_{eff} and L_p variation indicates that both the modes propagate with almost same propagation constant and have almost similar modal attenuation.

4.2.2.2 Asymmetric Modal Evolution with Nano-wire Width (W)

For a small cladding index difference, the width (W) dependent modal behaviours (n_{eff} and L_p) of long range PSM have also been studied for different $t = 20, 40, 60$, and 80 nm, depicted by the black, blue, red, and green lines, respectively in Figs.4.11(a) and (b). The PSM for $t = 20$ nm shows a distinct trend than other PSMs guided by a higher thickness. These also prove the evolution of PSMs with metal waveguide geometrical dispersion as

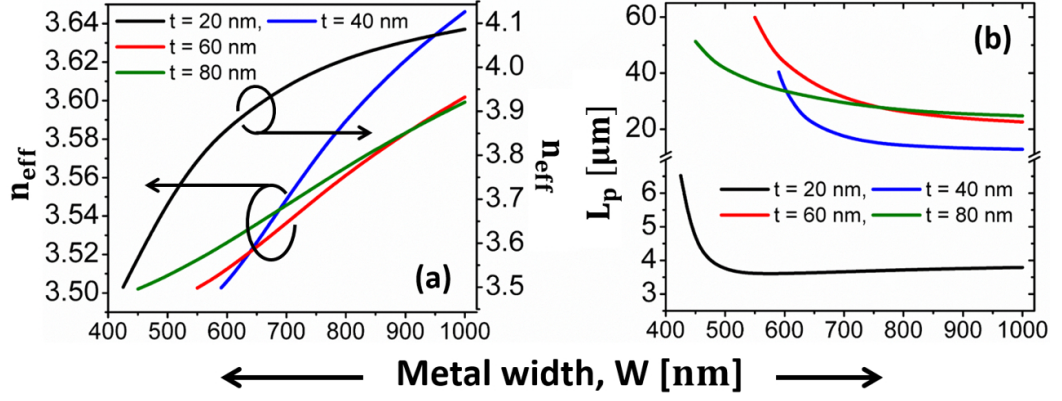


Figure 4.11: Variations of plasmonic supermode (PSM) parameters in non-identical clad metal nano-wire with core metal width (W) for different fixed thickness, $t = 20, 40, 60$, and 80 nm shown by the black, blue, red, and green lines, respectively. Variation of n_{eff} and corresponding L_p variations with W are shown in sub-figures (a) and (b), respectively.

already discussed in the previous section. The n_{eff} of PSM for $t = 20$ nm presented in Fig. 4.11, by a black line, shows a hyperbolic variation whereas other PSMs supported by metal core of $t = 40, 60$, and 80 nm show an almost exponential decay to the surrounding refractive index. For a thin metal core ($t = 20$ nm) both the upper and lower interfaces provide a strong coupling that makes the mode field more localised and confined into metal core. Influencing metal loss makes the modal attenuation high, yielding a smaller L_p (Fig. 4.11(b)) than others. It is also noticeable in Fig. 4.11(a) that the modes with thicknesses $40, 60$, and 80 nm approach faster towards the background quasi-TEM mode i.e. cut-off. However, this is not similar for the PSM supported by $t = 20$ nm as this is appeared to be a completely different mode.

4.2.2.3 Asymmetric Mode Evolution Depending on Cladding Index

Differences

Besides the modal dependencies on the waveguide geometrical dimensions, the modal variations with different non-identical cladding conditions also have been investigated. The main and inset of Fig. 4.12 depicts the n_{eff} and L_p variations of different modes with the variation of superstrate refractive index (S-RI). The substrate material refractive index was fixed at 3.5 for these simulations. The solid and dashed lines indicate different modes for $t = 100$ and 20 nm, respectively. The metal width was kept fixed at $W = 1000$ nm for both the thicknesses. The corresponding H_x field profiles of different guided modes

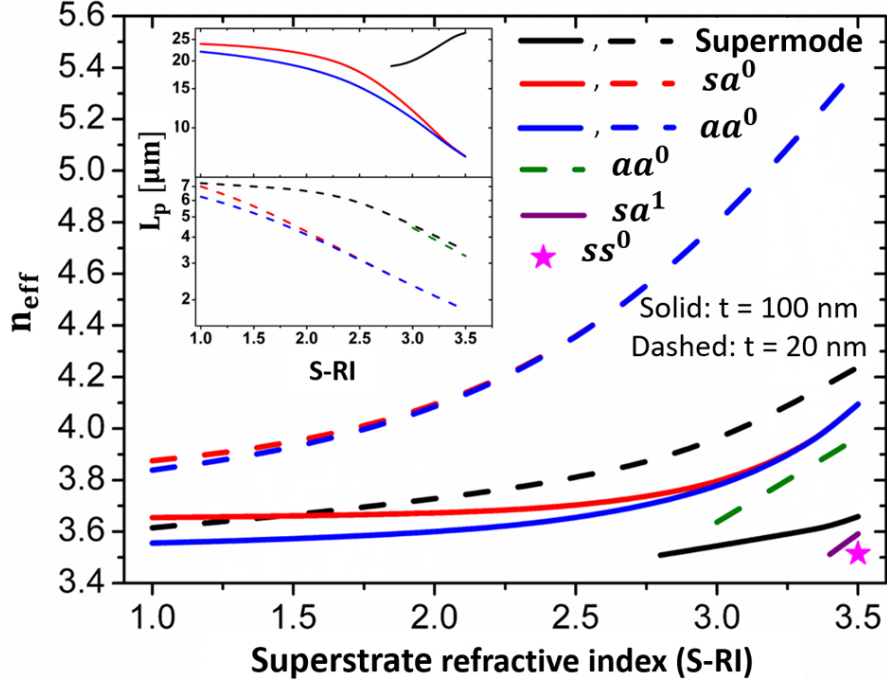


Figure 4.12: n_{eff} and L_p variations of different plasmonic modes with superstrate refractive index (S-RI) shown by the main and the inset plots, respectively. The solid black, red, blue, and purple lines indicate the PSM ($s_L^1 as_U^0$), sa^0 , aa^0 , and sa^1 variations with S-RI, respectively for waveguide dimension, $W = 1000$ nm and $t = 100$ nm. The dashed black, red, blue, and green lines and pink star denote the guided PSM, sa^0 , aa^0 , aa^2 , and ss^0 modal characteristics with S-RI for dimension, $W = 1000$ nm and $t = 20$ nm.

at different conditions are shown in Figs. 4.13(a), (b), (c) and (d). The black, red, blue and green dashed lines indicate the n_{eff} and L_p variations of supported PSM, sa^0 , aa^0 , and aa^2 modes, respectively for $t = 20$ nm, shown in main and inset of Fig. 4.12. The star marker indicates a long range ss^0 mode supported by this structure with attenuation 6.5 dB/mm only when the superstrate and substrate have the same refractive index 3.5. Here mostly the electromagnetic energy was guided by the background dielectric media. The black, red, blue, and purple solid lines depict the n_{eff} and L_p variations for PSM, sa^0 , aa^0 , and sa^1 modes, respectively for $t = 100$ nm, shown in main and top inset of Fig. 4.12. The PSM ($s_L^1 as_U^1$) guided by the waveguide with $t = 20$ nm sustained over the whole S-RI range and evolved into the sa^1 as both the upper and lower cladding have the identical refractive index, shown by the black dashed lines. On the other hand, the PSM ($s_L^1 as_U^0$ in Fig. 4.13(c)) for $t = 100$ nm reached to cut-off much faster at S-RI = 2.8, shown by the solid black lines. Thus, the PSM ($s_L^1 as_U^0$) supported by the $t = 100$ nm exists for small index difference of the background, shows a much lower modal attenuation

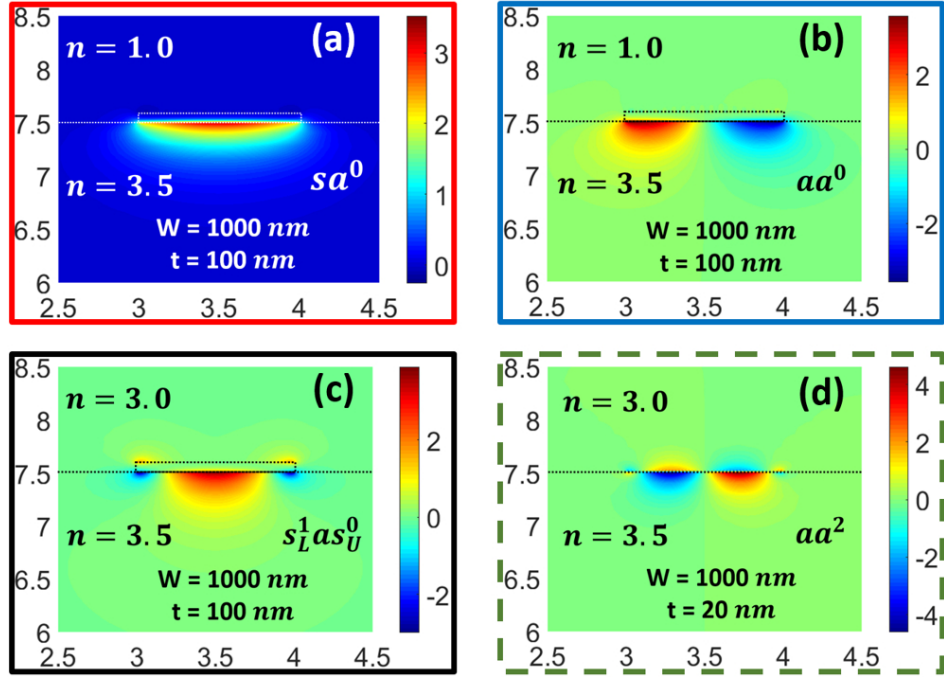


Figure 4.13: The H_x field distribution of different plasmonic modes of non-identical clad plasmonic waveguide simulated by FV-FEM, (a) and (b) depict the sa^0 and aa^0 field distributions for large index difference in the background ($n_{superstrate} = 1.0$ and $n_{substrate} = 3.5$) for metal thickness, $t = 100$ nm, (c) and (d) show the field distributions of $s_L^1 as_U^0$ PSM and aa^2 when $n_{superstrate} = 3.0$ and $n_{substrate} = 3.5$ for metal thickness, $t = 100$ and 20 nm, respectively. Metal width (W) is fixed at 1000 nm.

and longer propagation length compared to the PSM that supported by $t = 20$ nm. With identical background, this mode completely evolves into ss^0 mode. The other two modes sa^0 and aa^0 for $t = 20$ nm propagates with almost the same propagation constant with S-RI variations. Besides, for $t = 100$ nm these two modes have different propagation constants. The dominant H_x field profiles of these two modes (when $n_{superstrate} = 1.0$ and $n_{substrate} = 3.5$) are shown Fig. 4.13(a) and (b), respectively. In case of a large cladding index difference the modes are mostly guided by the substrate with higher refractive index. A higher order mode aa^2 (Fig. 4.13(d)) guided by $t = 20$ nm metal core shows its cut-off at S-RI = 2.8. The sa^1 (Fig. 4.2(f) like) and as^0 (Fig. 4.2(b) like) modes are also guided by $t = 100$ nm metal core for very small cladding index difference.

4.3 Studies of Waveguide Mode Effective Area (A_{eff})

Depending on the material composition, optical waveguide family could be classified into two broad categories, (1) dielectric waveguide and (2) plasmonic waveguide. Low and high index contrasts are two main recipes in designing waveguides depending on suitable photonic applications. Optical fibre has low index contrast whereas nano-wires and slot based waveguides based on silicon-on-insulator (SOI) architecture shows high index contrast. On the other hand, the plasmonic waveguide supports surface plasmons generated due to the excitation of free electrons on the meta surface. Metal is high lossy in light guiding. To overcome this limitation, a hybrid plasmonic waveguide can be designed which consists of a clever design of dielectric materials with metal in a way such that the guided wave is a hybrid combination of excited free electron and dielectric guided electromagnetic wave, called surface plasmon polariton (SPP). Each of these waveguides have an unique light guiding nature through their light-carrying regions. The representation of the light-carrying region in transverse plane of the waveguide is defined as the mode effective area ($MEA = A_{eff}$). It is an important parameter in determining the field distributions in the waveguide. It also provide useful information about mode shape, mode matching at junctions, bending, and bending losses. Besides, any nonlinear phenomenon depends on the intensity (I) of the guided light in the nonlinear medium. The average optical intensity (I) is related to the optical power (P) through the mode effective area (A_{eff}) as

$$I = \frac{P}{A_{eff}} \quad (4.4)$$

Thus, A_{eff} is highly important for waveguide analyses and one should have a clear idea about the specific definition for individual waveguide structure.

4.3.1 Different Definitions of A_{eff}

Mode effective area (A_{eff}) is a frequency domain analysis to determine the transverse mode profile distribution in the context of optical fibre and waveguides. It is very useful for such waveguides where the $1/e^2$ of intensity approach for Gaussian beams is not applicable due to its complex and irregular mode profiles or field distributions.

Numerous numbers of literatures available where different A_{eff} definitions have been used for mode area analyses. In this study, we have accumulated various approaches of A_{eff} and applied each of them on low index contrast optical fibre to high index contrast SOI slot waveguide even on hybrid plasmonic waveguide structure. A comparative study has been organised with the help of our in-house divergence modified full-vectorial 2D finite element method (FV-FEM). This would be helpful to decide the effectiveness of each approach in determining the A_{eff} of different waveguide structure. All the A_{eff} definitions used for the investigations have been short-listed in the following paragraphs.

4.3.1.1 A_{eff} Based on Transverse Field Vectors

For optical fibres where slowly varying refractive index in the transverse plane results in a weak light guidance, a well-known definition [Koshiba and Saitoh, 2003; Agrawal, 2001] of mode effective area is based on the transverse field vectors (\vec{E}_t and \vec{H}_t) as

$$A_{eff}^{H_t} = \frac{\left(\iint_{-\infty}^{\infty} |\vec{H}_t|^2 dx dy \right)^2}{\iint_{-\infty}^{\infty} |\vec{H}_t|^4 dx dy} \quad (4.5)$$

and

$$A_{eff}^{E_t} = \frac{\left(\iint_{-\infty}^{\infty} |\vec{E}_t|^2 dx dy \right)^2}{\iint_{-\infty}^{\infty} |\vec{E}_t|^4 dx dy} \quad (4.6)$$

here $\vec{H}_t = \sqrt{H_x^2 + H_y^2}$ and $\vec{E}_t = \sqrt{E_x^2 + E_y^2}$. The integrations are taken over the whole cross-sectional area of the waveguide.

4.3.1.2 A_{eff} Based on Scalar Field Components

A_{eff} could be formulated depending on the transversely distributed dominant and non-dominant single scalar field components such as $f(x, y) = H_x, H_y$ and E_x, E_y . The generalised equation is of the form like,

$$A_{eff}^{f(x,y)} = \frac{\left(\iint_{-\infty}^{\infty} |f(x, y)|^2 dx dy \right)^2}{\iint_{-\infty}^{\infty} |f(x, y)|^4 dx dy} \quad (4.7)$$

Thus, the definition of A_{eff} depending on the scalar field $f(x, y) = H_x$ is

$$A_{eff}^{H_x} = \frac{\left(\iint_{-\infty}^{\infty} |H_x(x, y)|^2 dx dy \right)^2}{\iint_{-\infty}^{\infty} |H_x(x, y)|^4 dx dy} \quad (4.8)$$

For scalar field $f(x, y) = H_y$,

$$A_{eff}^{H_y} = \frac{\left(\iint_{-\infty}^{\infty} |H_y(x, y)|^2 dx dy \right)^2}{\iint_{-\infty}^{\infty} |H_y(x, y)|^4 dx dy} \quad (4.9)$$

For scalar field $f(x, y) = E_x$,

$$A_{eff}^{E_x} = \frac{\left(\iint_{-\infty}^{\infty} |E_x(x, y)|^2 dx dy \right)^2}{\iint_{-\infty}^{\infty} |E_x(x, y)|^4 dx dy} \quad (4.10)$$

For scalar field $f(x, y) = E_y$,

$$A_{eff}^{E_y} = \frac{\left(\iint_{-\infty}^{\infty} |E_y(x, y)|^2 dx dy \right)^2}{\iint_{-\infty}^{\infty} |E_y(x, y)|^4 dx dy} \quad (4.11)$$

Depending on the dominant and non-dominant fields, the corresponding $A_{eff}^{f(x,y)}$ could be used. These formulations are specially useful for mode effective area evaluations of highly polarisation dependent waveguides.

4.3.1.3 A_{eff} Based on Longitudinal Component of Poynting Vector ($\vec{S}(x, y)$)

In waveguide analysis, propagating and guided beam power is an important parameter to determine the power associated with the guided beam in the z-direction. A guided mode is always comprises of electric $\vec{E}(x, y)$ and magnetic $\vec{H}(x, y)$ fields. Thus, the power confinement by the waveguide can be determined in terms of time-averaged z-component of Poynting vector (S_z). In some waveguide design, the \vec{E} and \vec{H} field profiles may have significantly different mode field distributions, thus, the A_{eff} could be formulated with the contribution of both $\vec{E}(x, y)$ and $\vec{H}(x, y)$ field components as

$$A_{eff}^{S_z} = \frac{\left(\iint_{-\infty}^{\infty} S_z(x, y) dx dy \right)^2}{\iint_{-\infty}^{\infty} S_z^2(x, y) dx dy} \quad (4.12)$$

For a much localised field distribution, the maximum S_z value could be considered in the A_{eff} denominator instead of square of the S_z distribution all over the x-y plane. Thus, the equation could be formulated as

$$A_{eff}^{S_z/max} = \frac{\iint_{-\infty}^{\infty} S_z(x, y) dx dy}{\max[S_z(x, y)]} \quad (4.13)$$

where $\max[S_z(x, y)]$ defines the maximum value of the S_z in the transverse plane.

4.3.1.4 A_{eff} Based on Energy Density ($\vec{U}(x, y)$)

The modal effective area can be defined by the ratio of the total mode energy (U_m) per unit length and the peak energy density in the distribution as

$$A_{eff}^{U_{max}} = \frac{U_m}{\max[U(x, y)]} \quad (4.14)$$

here $U(x, y)$ defines the energy density per unit length in the direction of propagation. It is a sum of electric and magnetic energy. Thus, for a dispersive medium the energy density ($U(x, y)$) can be written as

$$U(x, y) = \frac{1}{2} \left[\frac{d(\omega \epsilon)}{d\omega} \right] |\vec{E}(x, y)|^2 + \frac{1}{2} \mu_0 |\vec{H}(x, y)|^2 \quad (4.15)$$

and total mode energy (U_m) is in the form of

$$U_m = \iint_{-\infty}^{\infty} U(x, y) dx dy \quad (4.16)$$

Substituting Eq. 4.15 and 4.16 into Eq. 4.14 the formulation of the modal effective area is

$$A_{eff}^{U_{max}} = \frac{\iint_{-\infty}^{\infty} U(x, y) dx dy}{\max[U(x, y)]} \quad (4.17)$$

This formulation is mostly used for sub-wavelength plasmonic and hybrid plasmonic waveguide analysis [Oulton *et al.*, 2008].

Also, another form of the mode effective area (A_{eff}^U) based on the waveguide energy density ($U(x, y)$) without considering the localised maximum energy density, can be written as

$$A_{eff}^U = \frac{\left(\iint_{-\infty}^{\infty} U(x, y) dx dy \right)^2}{\iint_{-\infty}^{\infty} U^2(x, y) dx dy} \quad (4.18)$$

4.3.2 Waveguide Modal Effective Area Analyses

In this section, mode effective area (A_{eff}) for different waveguide configurations have been studied in detail. It is to be noted that various alternative definitions could be used to define this single parameter, discussed in section 4.3.1. All these A_{eff} definitions are incorporated with our in-house 2D FV-FEM code to determine the modal effective area (A_{eff}) values. Although, all the A_{eff} definitions are correct but may have different compatibility depending on the waveguide structures and its dominant and non-dominant field distributions. For a rigorous investigation, first a low-index contrast circular-symmetric step-index optical fibre is considered. Later, SOI based vertical and horizontal waveguides are considered as high-index contrast waveguides. Finally, a metal assisted hybrid plasmonic waveguide is considered to investigate the effectiveness of different definitions of A_{eff} . Results has been shown in the following sections.

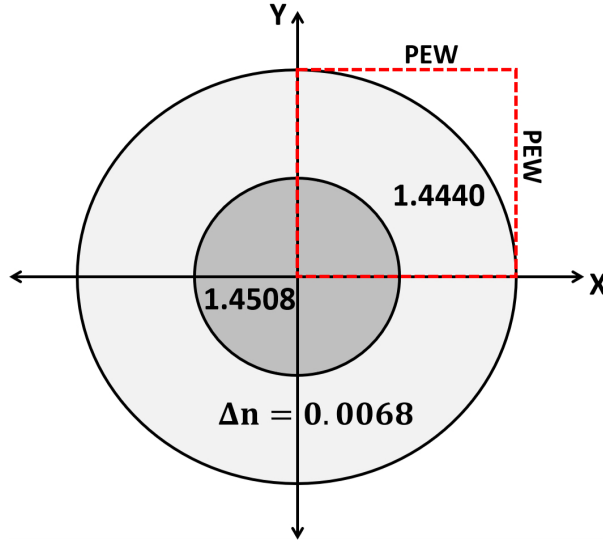


Figure 4.14: Schematic cross-section of the step index circular optical fibre.

4.3.2.1 Optical Fibre

A low index contrast step-index optical fibre with Ge-doped core and silica clad is considered at the operating wavelength, $\lambda = 1550$ nm. The core and clad refractive indices at this wavelength are $n_{core} = 1.4508$ and $n_{clad} = 1.4440$, respectively. The schematic cross-section of the fibre is shown in Fig. 4.14. A two-fold symmetry is exploited during 2D FV-FEM modal solutions which provides better accuracy with less computation resources.

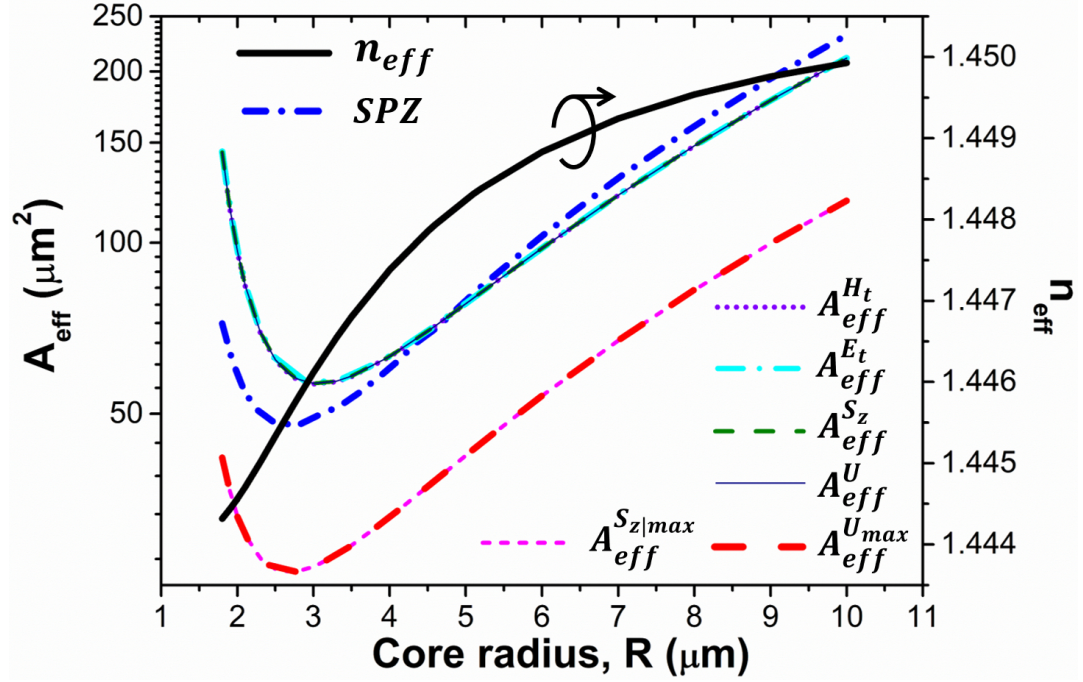


Figure 4.15: Mode effective area (A_{eff}) and effective index (n_{eff}) variations with fibre core radius (R).

Its quasi-TE and TM modes have identical modal profiles, so only the dominant quasi-TE mode is considered here. The effective index (n_{eff}) and mode effective area (A_{eff}) against fibre core radius are shown in Fig. 4.15. Variation of n_{eff} is shown by the black solid line. It represents that the n_{eff} gradually reduces with the reduction of fibre core radius (R). Several A_{eff} definitions have been considered to determine the A_{eff} for different core radii. The spot-size (SPZ) of a fibre mode is defined as the waveguide area where the field intensity falls $1/e$ times to its maximum value. The SPZ variation with core radii has been shown in blue dashed-dotted line. The $A_{eff}^{H_t}$, $A_{eff}^{E_t}$, $A_{eff}^{S_z}$, and A_{eff}^U determined by using Eqs. 4.5, 4.6, 4.12, and 4.18 have been shown by the green dotted, yellow dashed-dotted, green dashed, and blue solid lines, respectively. All these A_{eff} values show a perfect overlap with the variation of core radii because \vec{H}_t , \vec{E}_t , dominant \vec{H} , dominant \vec{E} , and S_z field profiles are identical for low index contrast waveguides. As for low index guides, these profiles are identical. It is to be noted that, A_{eff} s and SPZ decrease monotonically with the reduction of core radius but as the cut-off region approaches, they start to increase again. Although, $A_{eff}^{H_t}$, $A_{eff}^{E_t}$, $A_{eff}^{S_z}$, and A_{eff}^U curves determined by Eqs. 4.5, 4.6, 4.12, and 4.18, respectively and the SPZ curve have slightly different values but they intersect at

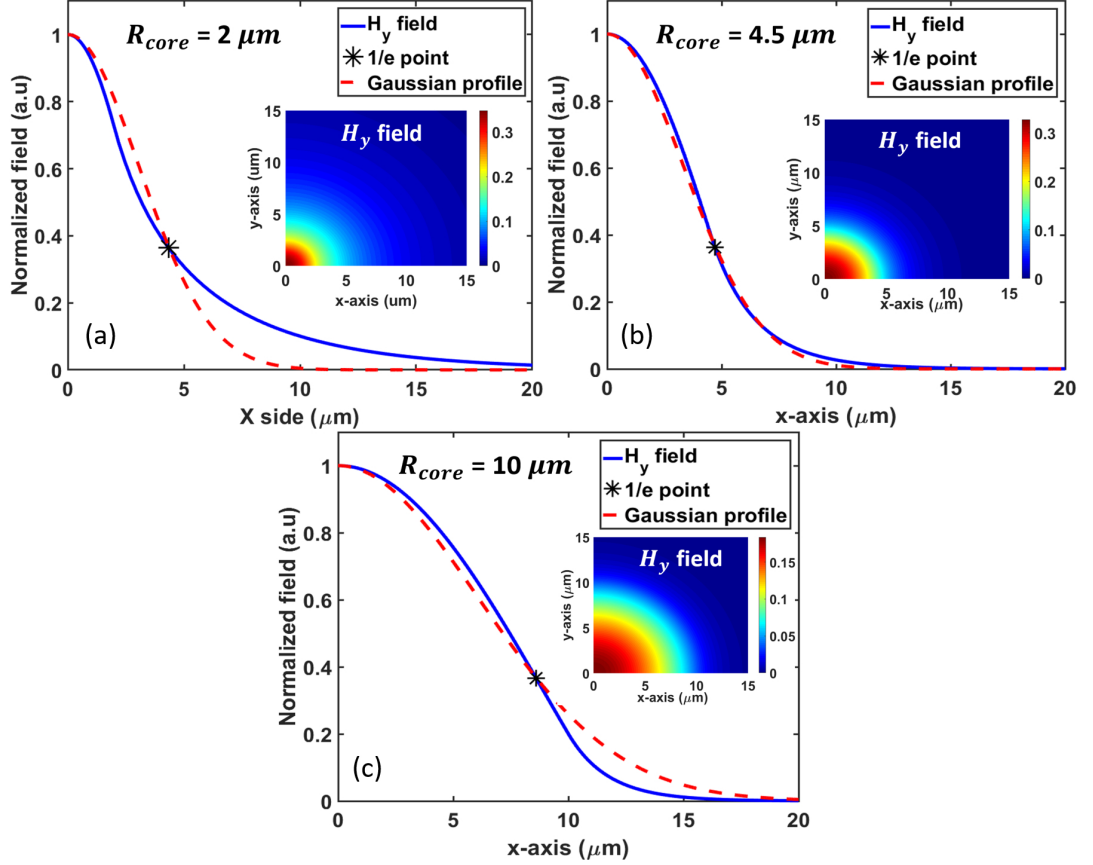


Figure 4.16: (a), (b), and (c) depicts the H_y field profile of the quasi-TE mode and its Gaussian fitting profile shown by solid blue and dashed red lines, respectively. Insets are showing the fundamental 2D mode field distributions.

radius, $R = 4.5 \mu\text{m}$ which is the core radius of a single mode fibre (SMF). This difference is due to different mode field profiles when the core radius is varied. Often, it may be assumed that the mode profile is Gaussian in nature but this is not strictly true. Quasi-TE H_y field profile for three different core radii, $R = 2, 4.5$, and $10 \mu\text{m}$ have been shown in Fig. 4.16(a), (b), and (c), respectively. The actual field profile is shown by blue lines and its equivalent Gaussian profiles are shown by red dashed lines. Insets show the 2D mode field distributions for those three fibre radii. As we already mentioned that the A_{eff} s and SPZ became identical at $R = 4.5 \mu\text{m}$ when the field profile very closely follows a perfect Gaussian profile shown in Fig. 4.16(b). However, for a fibre of radius smaller than $4.5 \mu\text{m}$ (shown here for $R = 2 \mu\text{m}$), the mode field decays slowly in the cladding region than its equivalent fitted Gaussian profile, shown in Fig. 4.16(a). On the other hand, for a core radius greater than $4.5 \mu\text{m}$, the cladding field decays much faster than its fitted Gaussian profile, shown in Fig. 4.16(c). Besides, the A_{eff} s determined by Eqs. 4.13 and 4.17 using

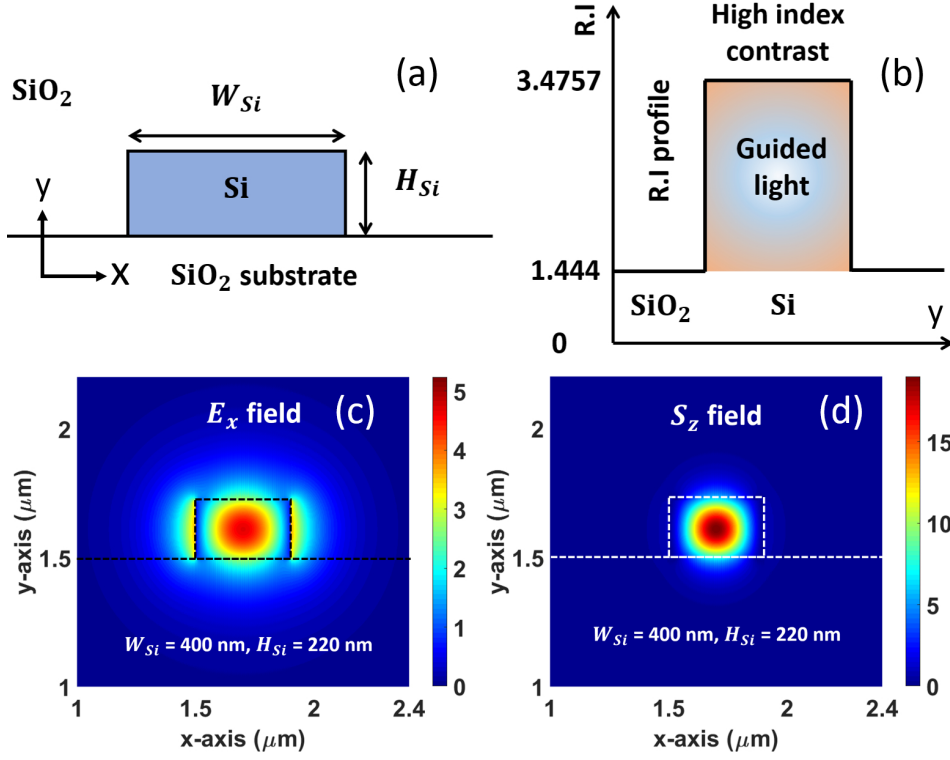


Figure 4.17: (a) and (b) show the schematic cross-section of the rectangular silicon (Si) ridge waveguide and its refractive index profile, respectively. (c) and (d) represent the FV-FEM simulated quasi-TE E_y and S_z field profiles, respectively.

the maximum values again show a perfect overlap are presented by the magenta and red dashed lines, respectively. Thus, mode effective area by different approaches such as $A_{eff}^{H_t}$, $A_{eff}^{E_t}$, $A_{eff}^{S_z}$, and A_{eff}^U are only acceptable for optical fibres where the mode field follows the Gaussian shape. On the other hand, the A_{eff} s determined by Eqs. 4.13 and 4.17 does not intersect with SPZ values and yields a significant smaller value. Therefore, for low index contrast optical fibre mode area analyses these two A_{eff} definitions related to maximum intensities are not acceptable.

4.3.2.2 Silicon Ridge Waveguide

A rectangular silicon (Si) ridge waveguide surrounded by silica (SiO₂) clad is considered as an high index contrast waveguide. Figure 4.17(a) and (b) depict the schematic cross-section and refractive index profile of the waveguide. Si ridge can be fabricated using silicon-on-insulator (SOI) wafer. The ridge can be formed by etching down the Si layer to SiO₂ buffer layer. The Si ridge is buried under SiO₂. The refractive index of the Si (n_{Si}) core and SiO₂ (n_{SiO_2}) clad have been taken as 3.4757 [Li, 1980] and 1.4440 [Malitson,

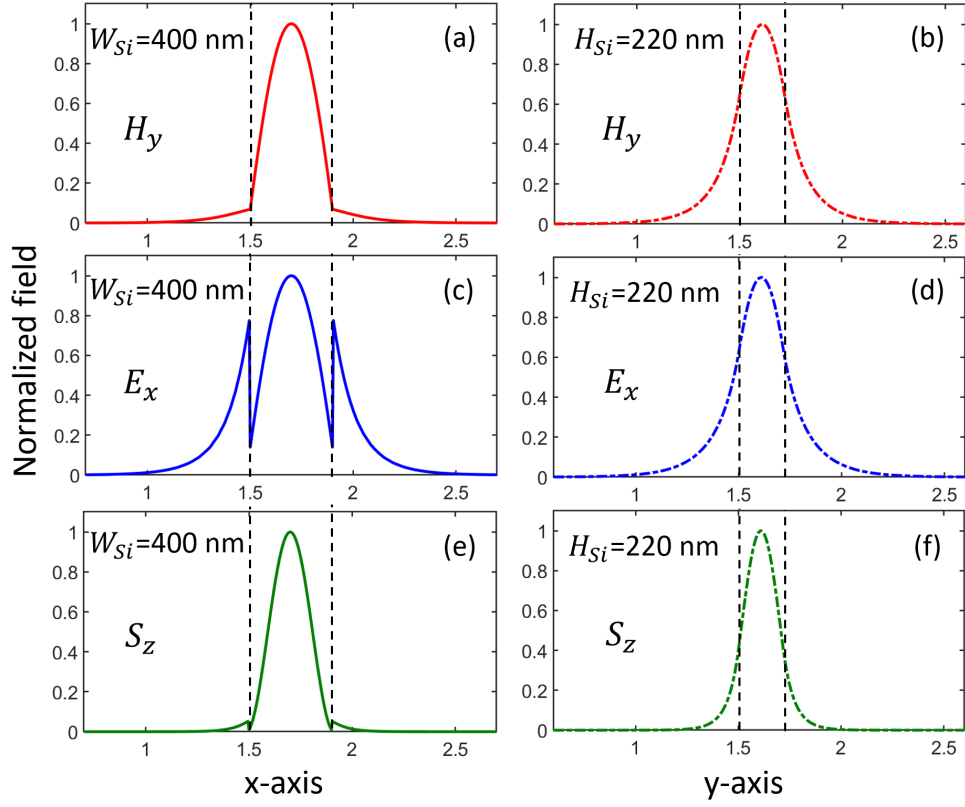


Figure 4.18: Quasi-TE H_y , E_x , and S_z profiles of the Si ridge ($W_{Si} = 400$ nm, $H_{Si} = 220$ nm) waveguide along x and y axes passing through the centre of the waveguide. (a), (c), and (e) present the fields along x-axis; (b), (d), and (f) present the fields along y-axis.

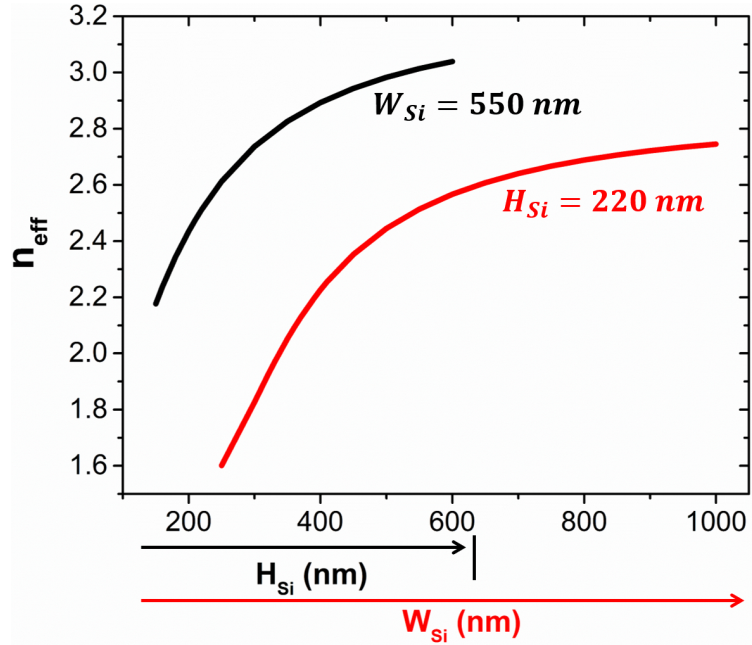


Figure 4.19: Effective index (n_{eff}) variation of the Si ridge waveguide with Si core width (W_{Si}) and height (H_{Si}), shown by the red and black solid lines, respectively. For W_{Si} and H_{Si} variation the H_{Si} and W_{Si} was kept fixed at 220 and 350 nm, respectively.

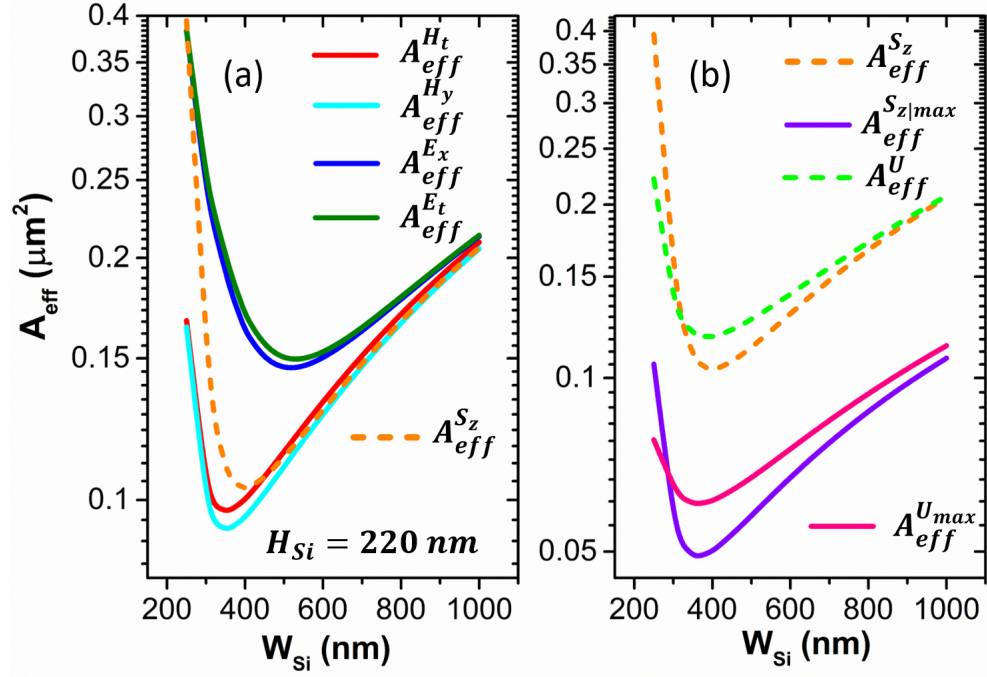


Figure 4.20: (a) and (b) depict the different A_{eff} variations with W_{Si} . Si ridge height (H_{Si}) is kept fixed at 220 nm.

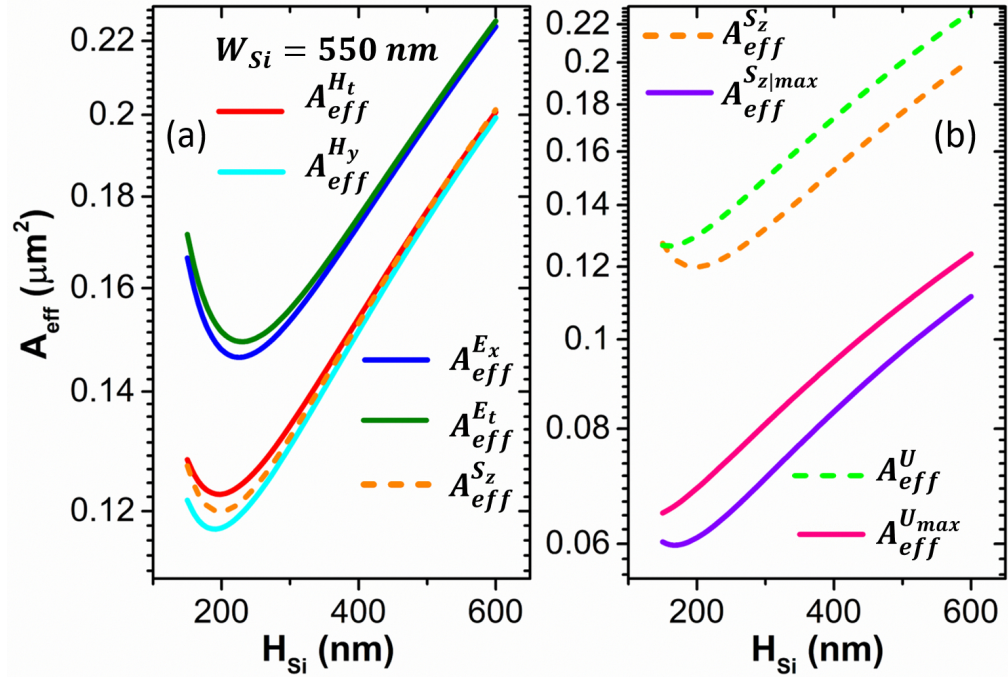


Figure 4.21: (a) and (b) depict the different A_{eff} variations with H_{Si} . Si ridge width (W_{Si}) is kept fixed at 550 nm.

1965], respectively at wavelength, $\lambda = 1550$ nm. Such a large difference in core and clad provides a high index contrast which results in most of the light guidance through high index core (Fig. 4.17(b)). Dominant E_x field and S_z intensity profiles of the fundamental quasi-TE mode of the waveguide are presented in Fig. 4.17(c) and (d), respectively. Figures 4.18(a), (c), and (e) present the normalised H_y , E_x fields, and S_z intensity distributions, respectively along x-axis and (b), (d), and (f) depict the same but along y-axis passing through the centre of the waveguide. As the H_y field is continuous across the material interface, it shows a continuous distribution along x and y axes. The normal component of the \vec{E} field has discontinuity at the material interface. Thus, a part of the E_x field shows a noticeable field enhancement at the left and right side edges of the Si ridge. Besides, the S_z distribution shows a high confinement in the Si core as the H_y is continuous at the material interfaces and also a dominant magnetic field component of the quasi-TE mode. Small discontinuities at the side edges (Fig. 4.18(e)) are due to the influence of the E_x field of the quasi-TE mode.

For a commercially available SOI wafer, generally the thickness of the Si layer is 220 nm. In this investigation, initially the Si ridge height/thickness (H_{Si}) is kept fixed at 220 nm and different mode effective area definitions such as $A_{eff}^{H_t}$, $A_{eff}^{H_y}$, $A_{eff}^{E_t}$, $A_{eff}^{E_x}$, $A_{eff}^{S_z}$, $A_{eff}^{H_z|max}$, A_{eff}^U , and $A_{eff}^{U_{max}}$ have been utilised to calculate the mode effective area (A_{eff}) with the variation of ridge width (W_{Si}). The effective index variation of the waveguide with W_{Si} has been shown in Fig. 4.19 by red solid line. As the W_{Si} is increased, the quasi-TE n_{eff} increases rapidly and get saturated for higher W_{Si} s. As W_{Si} decreases, n_{eff} also decreases and gets closer to the refractive index of SiO_2 where the mode reach to its cut-off. The A_{eff} variations with W_{Si} are shown in Fig. 4.20. Only the fundamental quasi-TE mode is considered here for the analyses. It can be observed that all the A_{eff} values shown in Fig. 4.20(a) and (b) decreases to a minimum value as W_{Si} reduces and with the further reduction, the A_{eff} s show rapid increment as the mode approaches its cut-off. As expected, $A_{eff}^{H_t}$, $A_{eff}^{H_y}$ and $A_{eff}^{E_t}$, $A_{eff}^{E_x}$ show similar variation with very close values. The $A_{eff}^{H_y}$ and $A_{eff}^{E_x}$ have the minimum values of 0.0921 and 0.1455 μm^2 at $W_{Si} = 350$ and 500 nm, respectively whereas the $A_{eff}^{H_t}$ and $A_{eff}^{E_t}$ have the minimum values of 0.0969 and 0.1494 μm^2 which show slightly higher values. Both the $A_{eff}^{H_t}$ and $A_{eff}^{H_y}$ shows very close variation and a minimum effective area at the same $W_{Si} = 350$ nm. The minimum

mode effective area indicates that the mode is more confined at that condition. The $A_{eff}^{H_t}$ and $A_{eff}^{E_t}$ approaches include both the dominant and non-dominant field components. Thus, the slightly higher values of $A_{eff}^{H_t}$ and $A_{eff}^{E_t}$ are due to the influences of the added non-dominant field component. Figure 4.20(a) also includes the $A_{eff}^{S_z}$ variation which shows a minimum effective area of $0.1035 \mu\text{m}^2$ for $W_{Si} = 400 \text{ nm}$. These $A_{eff}^{S_z}$ values are much closer to that of the $A_{eff}^{H_t}$ and $A_{eff}^{H_y}$ formulae. Figure 4.20(b) shows the $A_{eff}^{S_z}$, $A_{eff}^{S_z|max}$, A_{eff}^U , and $A_{eff}^{U_{max}}$ variations against W_{Si} . The minimum values of $A_{eff}^{S_z}$, $A_{eff}^{S_z|max}$, A_{eff}^U , and $A_{eff}^{U_{max}}$ are obtained as 0.1035 , 0.0492 , 0.1179 , and $0.0606 \mu\text{m}^2$ for the W_{Si} values of 400 , 360 , 390 , and 360 nm , respectively. $A_{eff}^{S_z}$ and A_{eff}^U show close variations but the A_{eff}^U presents higher effective area values compared to $A_{eff}^{H_t}$, $A_{eff}^{H_y}$, and $A_{eff}^{S_z}$. Besides, both the $A_{eff}^{S_z|max}$ and $A_{eff}^{U_{max}}$ formulae are based on localised maximum S_z and U values, thus have the lowest and close value of the mode effective areas (0.0492 and $0.0606 \mu\text{m}^2$, respectively) at the same $W_{Si} = 360 \text{ nm}$. $A_{eff}^{H_t}$, $A_{eff}^{H_y}$, and $A_{eff}^{S_z}$ exhibit close variations and lower effective area than the $A_{eff}^{E_t}$ and $A_{eff}^{E_x}$ definitions. Therefore, $A_{eff}^{H_t}$, $A_{eff}^{H_y}$, and $A_{eff}^{S_z}$ provides satisfactory mode effective area.

Next, the Si ridge height (H_{Si}) is varied keeping the ridge width (W_{Si}) fixed at 550 nm . The H_{Si} is varied from 150 nm to 600 nm such that the waveguide structure only confine the dominant quasi-TE mode. The n_{eff} variation with H_{Si} is shown in Fig. 4.19 by black line. As the H_{Si} decreases, the n_{eff} reduces towards its substrate refractive index i.e. the fundamental quasi-TE mode approaches to its cut-off. Figure 4.21(a) and (b) show the mode effective area variations against H_{Si} . Results of $A_{eff}^{H_t}$, $A_{eff}^{H_y}$, $A_{eff}^{E_t}$, and $A_{eff}^{E_x}$ have been shown in Fig. 4.21(a) and Fig. 4.21(b) contains the results of $A_{eff}^{S_z}$, $A_{eff}^{S_z|max}$, A_{eff}^U , and $A_{eff}^{U_{max}}$. All effective area definitions except $A_{eff}^{U_{max}}$ reduces with the decrement of H_{Si} to a minimum value and then increases with further reduction of H_{Si} as the mode approaches towards cut-off. $A_{eff}^{U_{max}}$ do not follow the previous trend. It shows a continuous A_{eff} decrement with H_{Si} . The minimum values obtained for $A_{eff}^{H_t}$, $A_{eff}^{H_y}$, $A_{eff}^{E_t}$, $A_{eff}^{E_x}$, $A_{eff}^{S_z}$, $A_{eff}^{S_z|max}$ and A_{eff}^U are of 0.1226 , 0.1174 , 0.1494 , 0.1463 , 0.1199 , 0.0598 , and $0.1264 \mu\text{m}^2$ at $H_{Si} = 200$, 200 , 220 , 220 , 200 , 160 , and 160 nm , respectively. $A_{eff}^{H_t}$, $A_{eff}^{H_y}$, and $A_{eff}^{S_z}$ closely follow the same trend and have their minimum value at a same $H_{Si} = 200 \text{ nm}$.

In Si ridge waveguide, the guided mode spreads beyond the high index core region

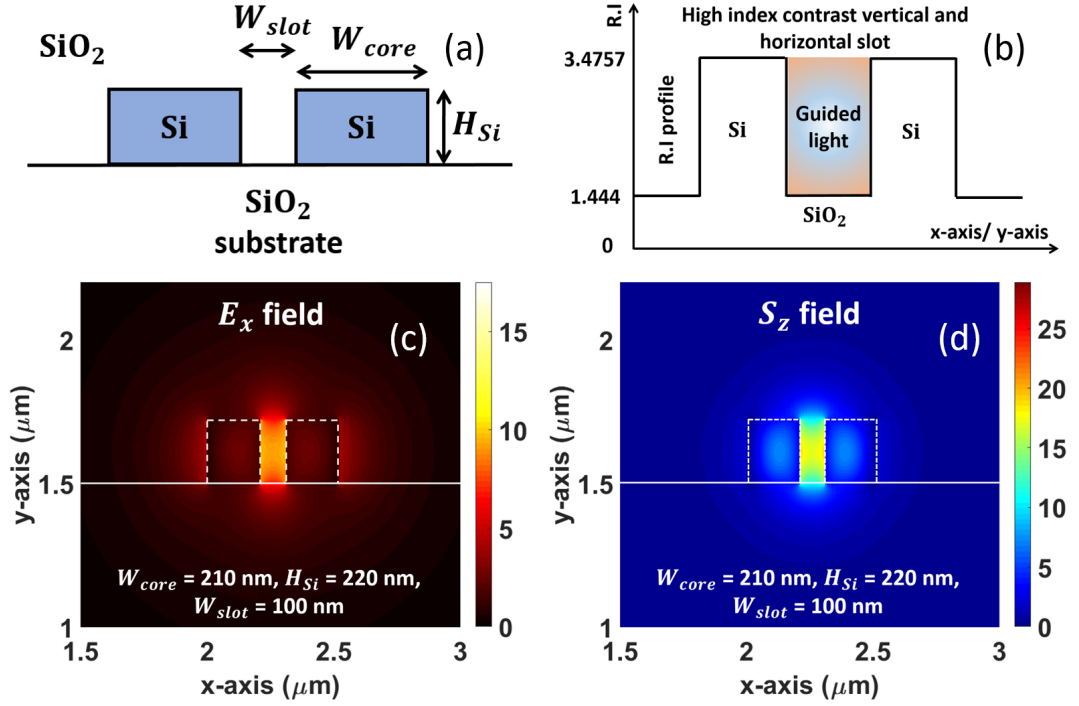


Figure 4.22: (a) and (b) show the schematic cross-section of a SOI based vertical slot waveguide and its refractive index profile, respectively. (c) and (d) represent the FV-FEM simulated quasi-TE E_x and S_z field profiles, respectively.

and its mode shape also depends on the waveguide dimensions. Here the guided mode field is not localised rather distributed over a certain region. In this investigation, $A_{eff}^{H_x}$, $A_{eff}^{H_y}$, and $A_{eff}^{S_z}$ results correlate with each other in both W_{Si} and H_{Si} variations of the ridge. Although, $A_{eff}^{S_z|_{max}}$ and $A_{eff}^{U_{max}}$ have shown the lowest A_{eff} values but these formulae could be more effective in cases of localised light confinement but may not be suitable for Si nano ridge waveguide. Thus, the mode effective area determined by Eqs. 4.5, 4.9, and 4.12 are more appropriate and useful for high index contrast nano-ridge waveguide mode analyses.

4.3.2.3 Vertical Slot Waveguide

Figure 4.22(a) shows the usual configuration of a vertical slot waveguide. In this case, the slot section is formed by two adjacent high index contrast Si slab waveguides of refractive index, $n_{Si} = 3.4757$. The slot can be filled with low index air, SiO_2 , nonlinear organic materials, polymers depending on the applications. In this study, the slot is filled with SiO_2 and also the complete waveguide structure is covered by SiO_2 clad of refractive

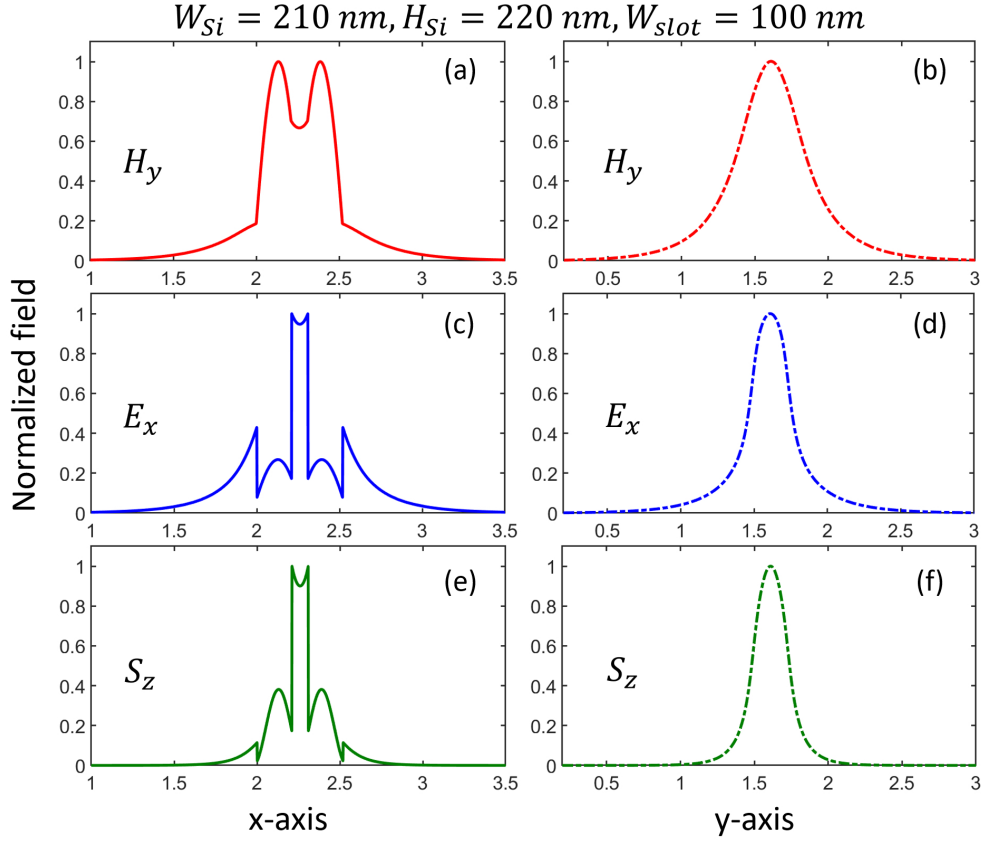


Figure 4.23: Quasi-TE H_y , E_x fields and S_z intensity distribution of a SOI based vertical slot waveguide ($W_{Si} = 210$ nm, $H_{Si} = 220$ nm, and $W_{slot} = 100$ nm) along x and y axes passing through the centre of the waveguide. (a), (c), and (e) show the distributions along x-axis; (b), (d), and (f) show the distributions along y-axis.

index, $n_{SiO_2} = 1.4440$. The refractive index profile of the waveguide along x is shown Fig. 4.22(b). It can be fabricated with commercially available SOI wafer where a resist mask with a slot configuration can be used on top of Si light guiding layer and the unwanted Si layer may be etched down to the SiO_2 buffer layer to form two adjacent Si slabs and the slot region simultaneously. According to the electromagnetic boundary conditions, the tangential electric (\vec{E}) and magnetic fields (\vec{H}) to be continuous across the interface. It also demands normal component of \vec{H} to be continuous. As it is considered that the permeability of dielectric materials is 1 (constant), this component also becomes continuous. However, as permittivity is different across the dielectric interface, the continuity of the electric flux density (\vec{D}) would results in discontinuity of the normal component of the electric-field (\vec{E}) at the material interface. This gives rise to an enhancement of the normal component of \vec{E} in the low index slot than the high index Si cores. This high

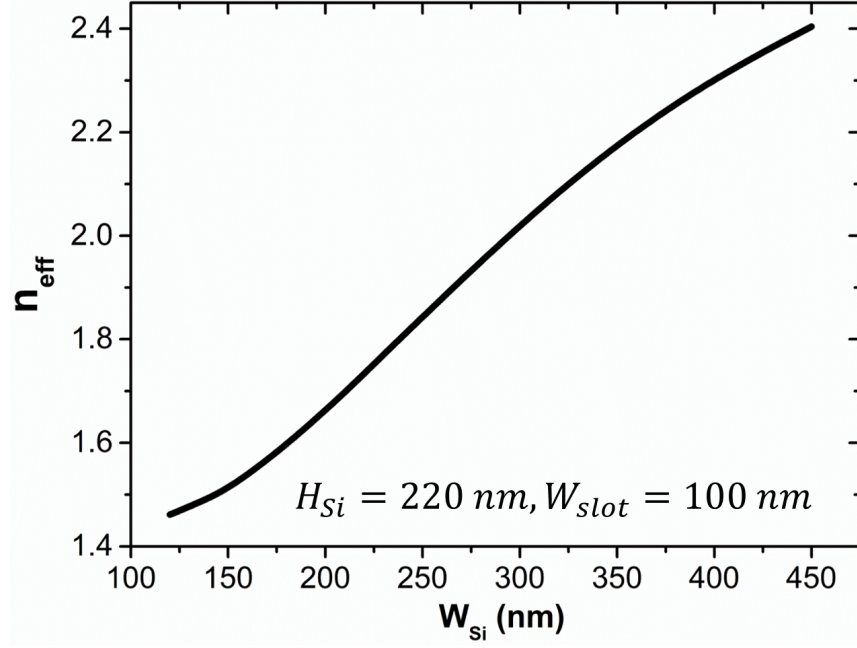


Figure 4.24: SOI based vertical slot effective index (n_{eff}) variation with Si slab width (W_{Si}) for a fixed Si slab height (H_{Si}) and slot width (W_{slot}) of 220 and 100 nm, respectively.

power confinement could be exploited for designing various sensing and nonlinear devices. In this section, the slot is considered to be placed vertically, thus E_x field would have discontinuity across the interface and being the dominant component of quasi-TE mode, this polarisation state would guide higher power in the slot region. This makes this waveguide highly polarisation dependent. In-house 2D FV-FEM is used for modal analyses and the Figs. 4.22(c) and (d) depict the E_x field and S_z intensity component of the quasi-TE mode which concentrates mostly in the low index slot region rather than high index Si cores. Figure 4.23(a) - (f) depict the normalised H_y , E_x fields, and S_z intensity variations along x and y axes passing through the centre of the waveguide. H_y field mostly confines in the Si cores also with a less confinement in the slot (Fig. 4.23(a)). On the other hand, E_x shows an enhanced field confinement in the slot due to its discontinuous nature (Fig. 4.23(c)). S_z intensity distribution (Fig. 4.23(e)) follows a similar trend that of the E_x as this component is the product of E_x and H_y profiles. All these fields and intensity have a quasi-Gaussian type distribution along y-axis (Fig. 4.23(b), (d), and (f)).

Figure 4.24 presents the effective index (n_{eff}) variation of the SOI based vertical slot waveguide with the Si slab width (W_{Si}) keeping Si height (H_{Si}) and slot width (W_{slot}) fixed at 220 and 100 nm, respectively. It can be seen that for higher W_{Si} the slot n_{eff}

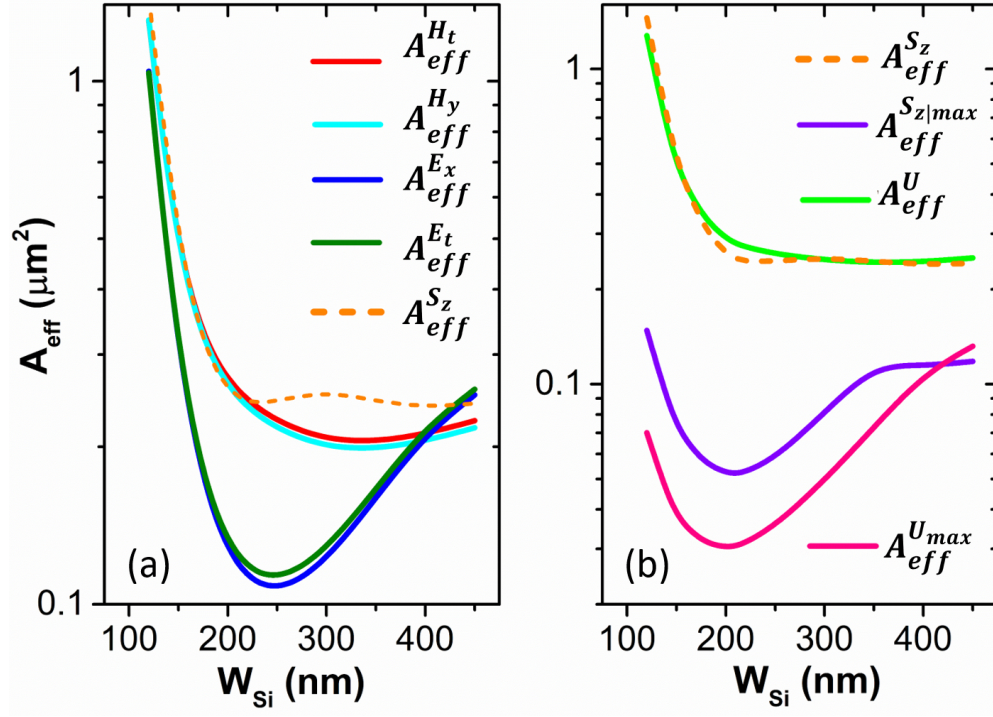


Figure 4.25: (a) and (b) depict the mode effective area variations by different approaches such as $A_{eff}^{H_t}$, $A_{eff}^{H_y}$, $A_{eff}^{E_t}$, $A_{eff}^{E_x}$, $A_{eff}^{S_z}$, $A_{eff}^{S_z|max}$, A_{eff}^U , and $A_{eff}^{U|max}$ against W_{Si} . The H_{Si} and W_{slot} are kept fixed at 220 and 100 nm, respectively.

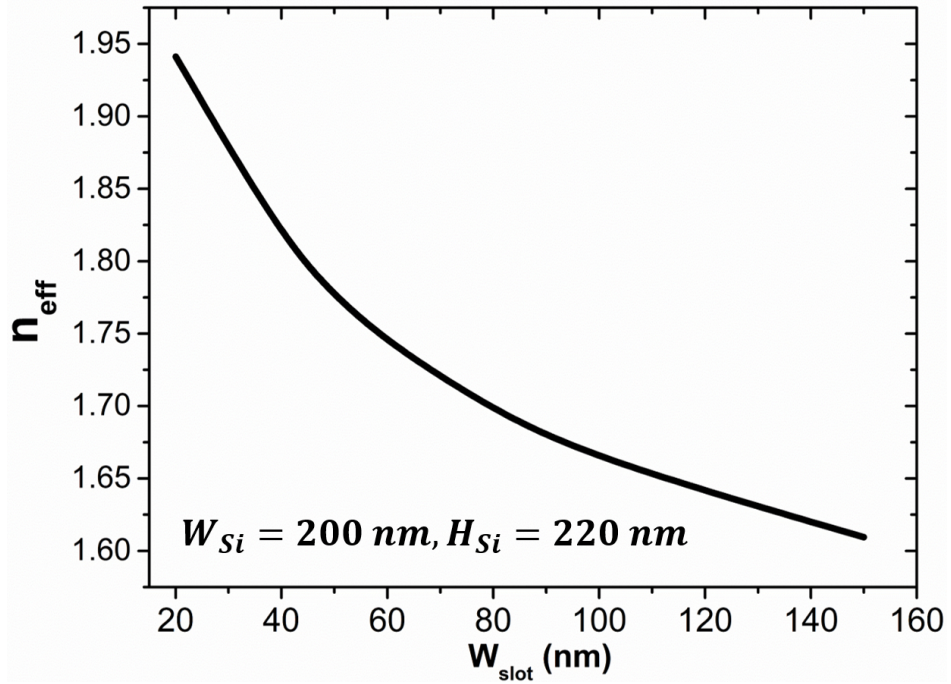


Figure 4.26: SOI based vertical slot effective index (n_{eff}) variation with slot width (W_{slot}) for a fixed Si slab height (H_{Si}) and width (W_{Si}) of 220 and 200 nm, respectively.

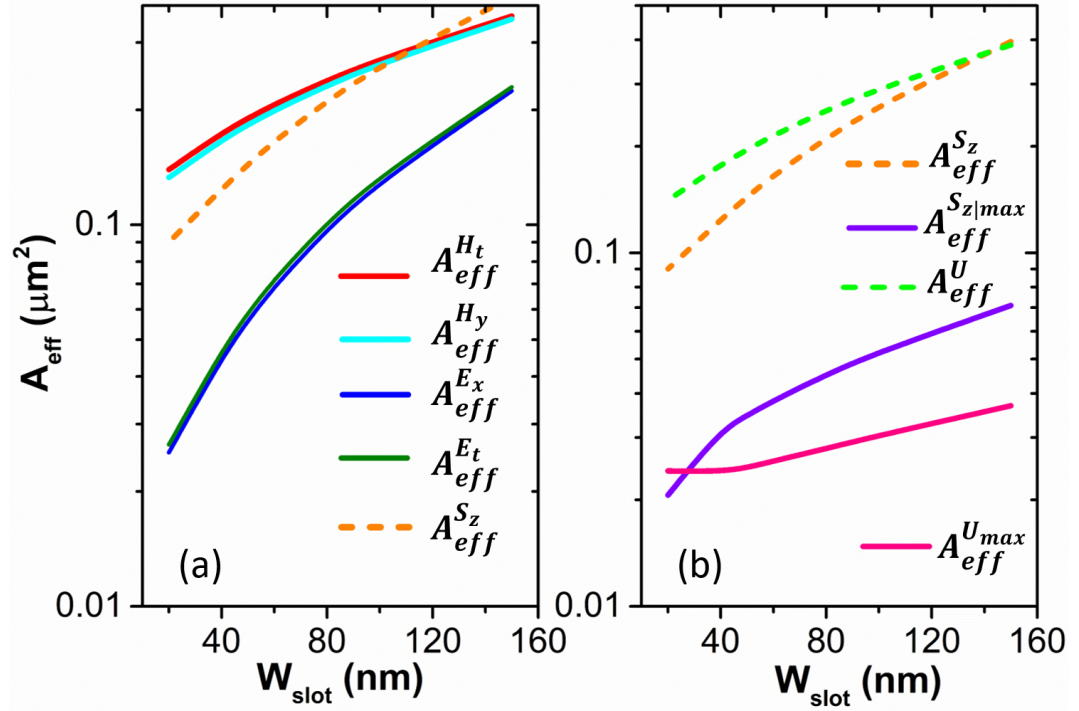


Figure 4.27: (a) and (b) depict the mode effective area variations by different approaches such as $A_{eff}^{H_t}$, $A_{eff}^{H_y}$, $A_{eff}^{E_t}$, $A_{eff}^{E_x}$, $A_{eff}^{S_z}$, $A_{eff}^{S_z|max}$, A_{eff}^U , and $A_{eff}^{U_{max}}$ against W_{slot} . The H_{Si} and W_{Si} are kept fixed at 220 and 200 nm, respectively.

shows higher values indicates that the light is mostly guided by the high index Si slabs. On the other hand, lower W_{Si} results in light guidance by slot and also corresponding n_{eff} is much closer to the surrounding refractive index i.e. cut-off. Figure 4.25(a) and (b) depicts the mode effective area variations by different definitions such as $A_{eff}^{H_t}$, $A_{eff}^{H_y}$, $A_{eff}^{E_t}$, $A_{eff}^{E_x}$, $A_{eff}^{S_z}$, $A_{eff}^{S_z|max}$, A_{eff}^U , and $A_{eff}^{U_{max}}$ as a function of W_{Si} for a fixed $H_{Si} = 220$ nm and $W_{slot} = 100$ nm. All the definitions show parabolic variation with W_{Si} . It can be seen that different definitions show different A_{eff} minima but for slightly different values of W_{Si} . The E_x field is a dominant component of the fundamental quasi-TE mode, it only carries high power through the slot region. Thus, the $A_{eff}^{E_t}$ and $A_{eff}^{E_x}$ definitions show minimum mode effective area of 0.1138 and 0.1085 μm^2 , respectively for a same value of $W_{Si} = 250$ nm. Besides, $A_{eff}^{H_t}$ and $A_{eff}^{H_y}$ provide higher values of A_{eff} minima as 0.2059 and 0.1994 μm^2 , respectively for $W_{Si} = 350$ nm, as the H_y and H_x carries less power for a vertical slot waveguide. A close look on the figures (Fig. 4.25(a) and (b)) also indicate that the $A_{eff}^{H_t}$, $A_{eff}^{H_y}$, $A_{eff}^{S_z}$, and A_{eff}^U have very close variation. However, the $A_{eff}^{S_z|max}$ and $A_{eff}^{U_{max}}$ show a much lower effective area values of 0.0524 and 0.0304 μm^2 , respectively at $W_{Si} =$

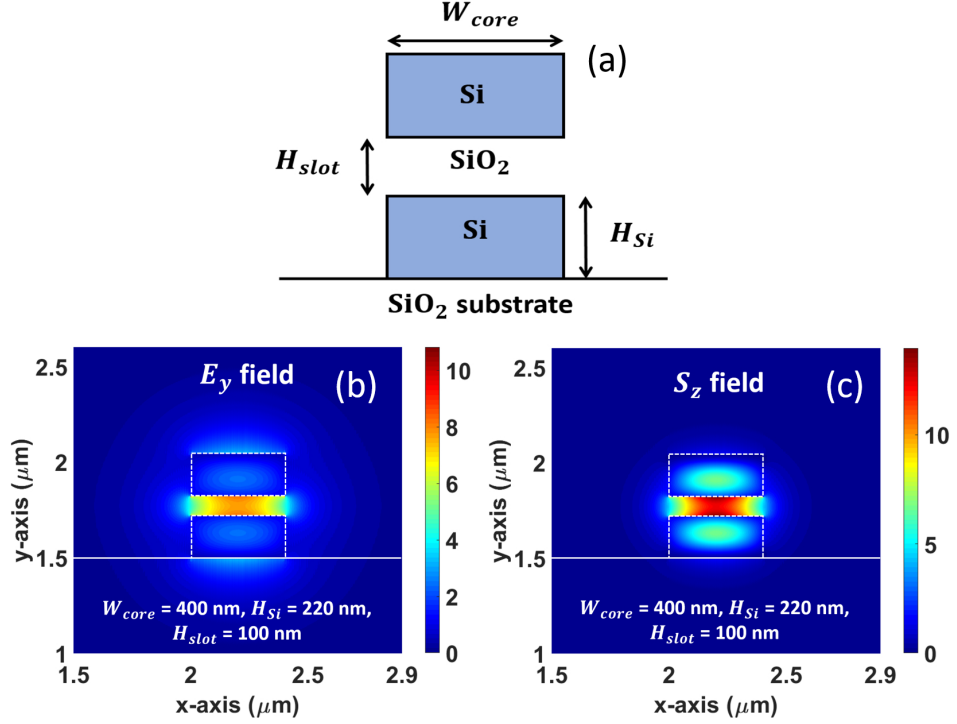


Figure 4.28: (a) shows the schematic cross-sectional diagram of a SOI based horizontal slot waveguide. (b) and (c) depict the FV-FEM simulated E_y and S_z field distributions of the fundamental quasi-TM mode.

200 nm.

Next, the Si slab height (H_{Si}) and width (W_{Si}) are fixed at 220 and 200 nm, respectively and slot width (W_{slot}) is varied. Waveguide n_{eff} variation is shown in Fig. 4.26 which indicates that as the W_{slot} is narrower, the n_{eff} increases whereas the effective areas determined by different definitions (Eqs. 4.5, 4.6, 4.9, 4.10, 4.12, 4.13, 4.17, and 4.18) decrease, shown in Fig. 4.27(a) and (b). As expected, the $A_{eff}^{E_t}$ and $A_{eff}^{E_x}$ approaches towards lower A_{eff} values compared to $A_{eff}^{H_t}$, $A_{eff}^{H_y}$, $A_{eff}^{S_z}$, and A_{eff}^U . Besides, $A_{eff}^{S_{z|max}}$ and $A_{eff}^{U_{max}}$ give much lower A_{eff} values with narrower W_{slot} as the slot confined field becomes more localised. It is interesting to notice that for a very low value of $W_{slot} = 20$ nm, the $A_{eff}^{E_t}$, $A_{eff}^{E_x}$, and $A_{eff}^{U_{max}}$ provide almost same effective area ($\sim 0.024 \mu\text{m}^2$) for a SOI based vertical slot. Thus, for a high index contrast vertical slot waveguide, $A_{eff}^{E_t}$, $A_{eff}^{E_x}$ are more effective to determine the effective area and for a very low slot width, $A_{eff}^{U_{max}}$ could also be considered for an accurate mode effective area analysis.

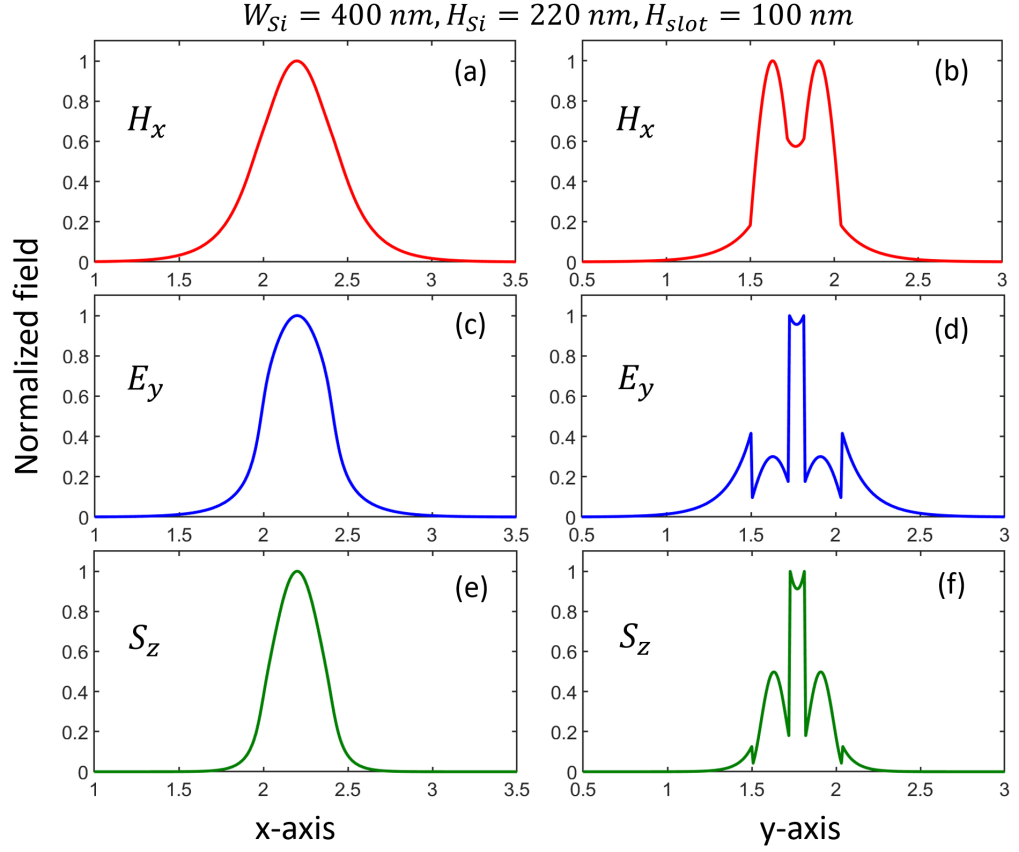


Figure 4.29: Quasi-TM H_x , E_y fields, and S_z intensity distributions of the SOI based horizontal slot waveguide along x and y axes passing through the centre of the waveguide. (a), (c), and (e) present the distributions along x-axis and (b), (d), and (f) present the same but along y-axis.

4.3.2.4 Horizontal Slot Waveguide

A SOI based horizontal slot waveguide mode effective area also has been analysed with different approaches. Figure 4.28 shows the schematic cross-section of the horizontal slot waveguide where a single low index SiO_2 layer is considered to be sandwiched between two symmetric high index Si slabs. The complete waveguide structure is considered to be surrounded by the SiO_2 . It can be fabricated with SOI wafer by layer deposition [Almeida *et al.*, 2004; Sun *et al.*, 2007]. Its refractive index profile variation along y-axis has been shown in Fig. 4.22(b). In this case, the low index slot is formed in horizontal direction. Thus, the normal component of \vec{E} field (here E_y) undergoes discontinuity at the interfaces therefore results in an enhanced power confinement in the slot region. Figure 4.28(b) and (c) show the FV-FEM simulated E_y field and S_z intensity distributions of the fundamental quasi-TM mode. The dominant H_x , E_y field components and S_z intensity

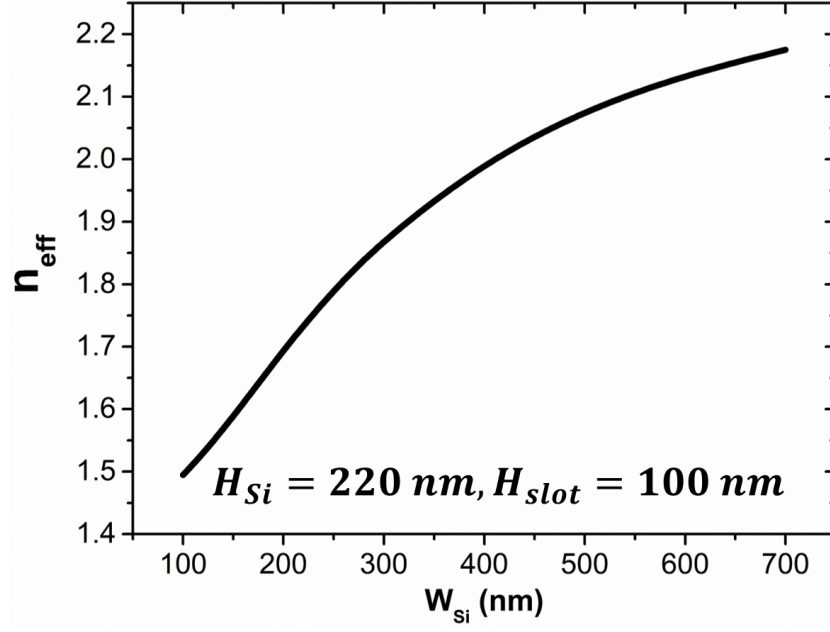


Figure 4.30: Fundamental quasi-TM mode effective index (n_{eff}) variation with Si slab width (W_{Si}) for a fixed Si slab height (H_{Si}) and slot height (H_{slot}) of 220 and 100 nm, respectively.

distributions along x and y axes are shown in Fig. 4.29(a) - (f). Field variations along x-axis show a Gaussian type distributions (Fig. 4.29(a), (c), and (e)). Fig. 4.29(b) shows H_x field distribution along y-axis where field is mostly confined in the Si cores and a small confinement is observed into slot. E_y and S_z in Fig. 4.29(d) and (f), respectively show their maximum confinement in the low index horizontal slot region.

Figure 4.30 shows the horizontal slot effective index (n_{eff}) variation with the waveguide width (W_{Si}) for a fixed Si slab height (H_{Si}) and slot height (H_{slot}) of 220 and 100 nm, respectively. It can be seen that the n_{eff} increases as the waveguide is wider. The higher n_{eff} value indicates that as the Si slab becomes wider the mode field is more guided by the top and bottom high index Si slabs. Figure 4.31 (a) and (b) show the mode effective area variations by different definitions such as $A_{eff}^{H_t}$, $A_{eff}^{H_x}$, $A_{eff}^{E_t}$, $A_{eff}^{E_y}$, $A_{eff}^{S_z}$, $A_{eff}^{S_z|max}$, A_{eff}^U , and $A_{eff}^{U_{max}}$ as a function of W_{Si} while the H_{Si} and H_{slot} are kept fixed at 220 and 100 nm, respectively. The parabolic trend of A_{eff} indicate that with the reduction of W_{Si} , mode effective area reduces, reaches a minimum and then increase rapidly with further W_{Si} as the guided mode moves toward its cut-off. The $A_{eff}^{E_t}$ and $A_{eff}^{E_y}$ present a much lower A_{eff} value of $\sim 0.10 \mu m^2$ at $W_{Si} = 300$ nm compared to the $A_{eff}^{H_t}$, $A_{eff}^{H_x}$, and $A_{eff}^{S_z}$ based effective area ($\sim 0.22 \mu m^2$) approaches. As the E_y field component carries a large

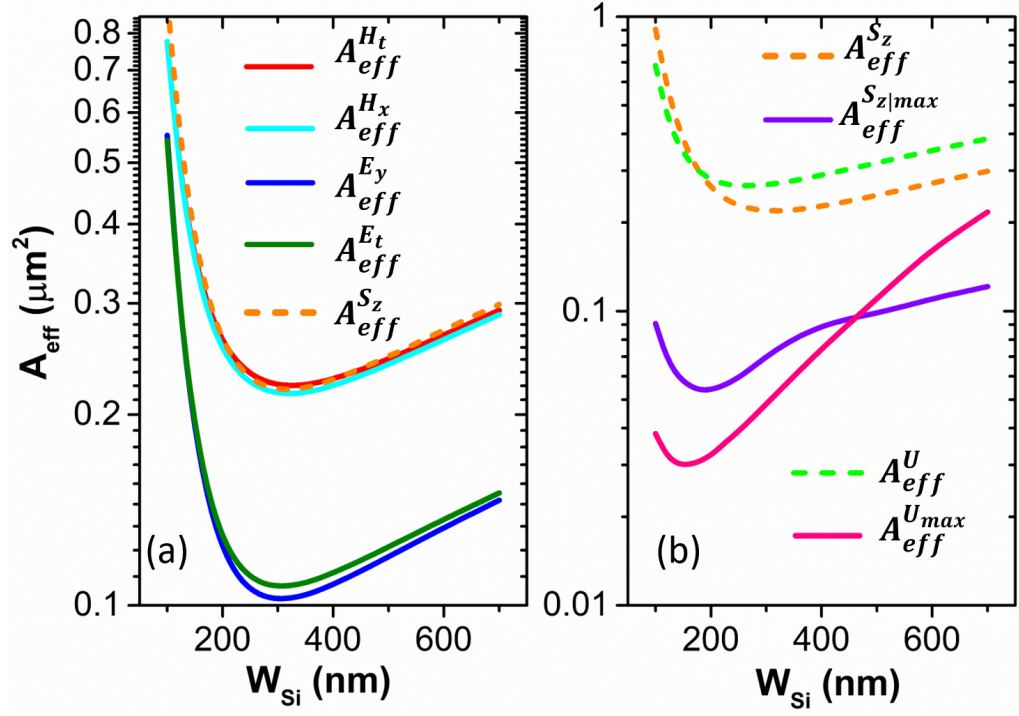


Figure 4.31: (a) and (b) show the mode effective area variations by different approaches such as $A_{eff}^{H_t}$, $A_{eff}^{H_x}$, $A_{eff}^{E_t}$, $A_{eff}^{E_y}$, $A_{eff}^{S_z}$, $A_{eff}^{S_z|max}$, A_{eff}^U , and $A_{eff}^{U|max}$ against Si slab width W_{Si} . The H_{Si} and H_{slot} are kept fixed at 220 and 100 nm, respectively.

portion of energy of the fundamental quasi-TM mode, the \vec{E}_t and E_y based approaches are more effective than the \vec{H} field and S_z based approaches. A close look on Fig. 4.31(b) indicates that the A_{eff}^U values are slightly higher than the $A_{eff}^{H_t}$, $A_{eff}^{H_x}$, and $A_{eff}^{S_z}$, thus may not be acceptable. For $W_{Si} > 400$ nm, light starts to be guided by the high index core regions thus $A_{eff}^{S_z|max}$ shows a shallow variation in this region. However, its parabolic profile indicates a much lower A_{eff} value of $0.0542 \mu m^2$ at $W_{Si} = 180$ nm. Similarly, $A_{eff}^{U|max}$ shows a lowest effective area of $0.0302 \mu m^2$ for $W_{Si} = 150$ nm. Interestingly, both the $A_{eff}^{S_z|max}$ and $A_{eff}^{U|max}$ have shown their minimum A_{eff} s when more than 50% light is being confined and guided by the surrounding clad region.

Figure 4.32 shows the quasi-TM mode effective index (n_{eff}) variation against Si slab height (H_{Si}) for a fixed W_{Si} and H_{slot} of 300 and 50 nm, respectively. It can be seen that the n_{eff} increases gradually with the increment of the height of Si slab. As the high index si slab height increases, the light starts to be guided more by the Si slab than the low index slot. For $H_{Si} = 400$ nm, 78% power confines in the Si slab and only 7.5% power confines into slot. Figure 4.33(a) and (b) show the results of mode effective area solved

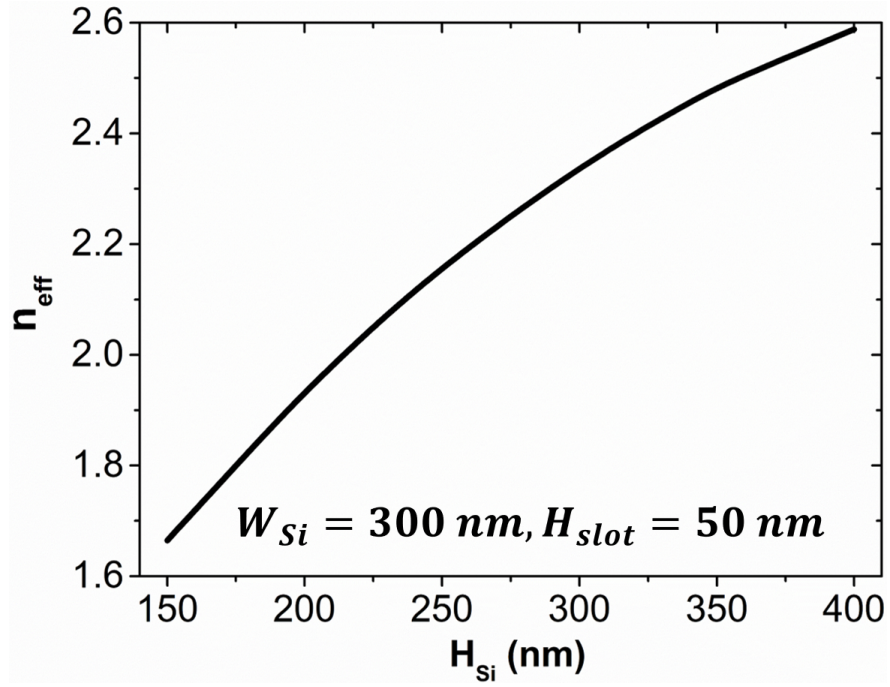


Figure 4.32: Fundamental quasi-TM mode effective index (n_{eff}) variation with Si slab height (H_{Si}) for a fixed Si slab width (W_{Si}) and slot height (H_{slot}) of 300 and 50 nm, respectively.

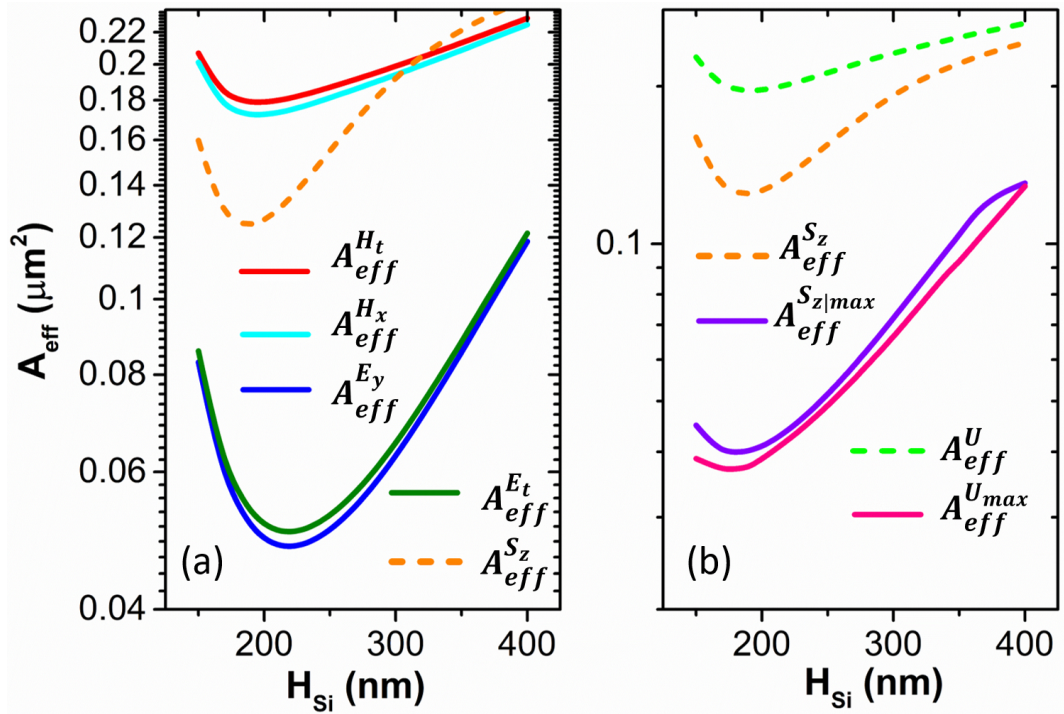


Figure 4.33: (a) and (b) show the mode effective area variations by different approaches such as $A_{eff}^{H_t}$, $A_{eff}^{H_x}$, $A_{eff}^{E_t}$, $A_{eff}^{E_y}$, $A_{eff}^{S_z}$, $A_{eff}^{S_z|max}$, A_{eff}^U , and $A_{eff}^{U|max}$ against Si slab height H_{Si} . The W_{Si} and H_{slot} are kept fixed at 300 and 50 nm, respectively.

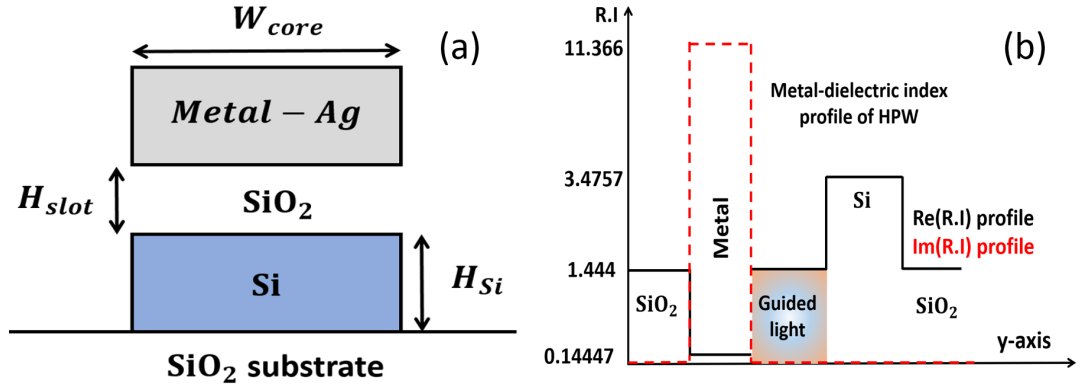


Figure 4.34: (a) and (b) depict a schematic cross-section of horizontal slot hybrid plasmonic waveguide and its refractive index profile along y-axis, respectively.

by different approaches against H_{Si} for a fixed W_{Si} and H_{slot} values of 300 and 50 nm, respectively. All the approaches show a parabolic nature of A_{eff} variation. When the Si waveguide thickness increases, more field confines in upper and lower Si slabs, thus the mode effective area increases. As E_y is a dominant quasi-TM field component, the $A_{eff}^{E_t}$ and $A_{eff}^{E_y}$ show the minimum effective area of 0.0503 and 0.0482 μm^2 at $H_{Si} = 220$ nm compared to other \vec{H} , S_z , and U based approaches. The minimum effective area indicates that the mode field is more confined at that condition. Other two definitions such as $A_{eff}^{S_z|_{max}}$ and $A_{eff}^{U_{max}}$ although have similar variation of $A_{eff}^{E_y}$ but they show their minimum A_{eff} values of 0.040 and 0.037 μm^2 , respectively at different H_{Si} values of 180 and 170 nm, respectively when the quasi-TM mode moves towards its cut-off. Thus, in assessment of SOI based horizontal slot waveguide, $A_{eff}^{E_y}$ and $A_{eff}^{E_t}$ provide more acceptable results compared to other effective area definitions.

4.3.2.5 Horizontal Slot Hybrid Plasmonic Waveguide (HPW)

In previous sections, low index contrast optical fibre and high index contrast ridge and slot waveguides have been studied. In this section, a horizontal slot hybrid plasmonic waveguide have been considered where the light guiding mechanism is not straightforward as dielectric waveguides discussed above. This waveguide is considered to be formed by placing a low index slot section horizontally in between a silver (Ag) and high index Si layers. Figure 4.34(a) shows the schematic cross-section of the hybrid plasmonic waveguide. Its refractive index profile has been shown in Fig. 4.34(b) with Si, SiO_2 , and Ag refractive

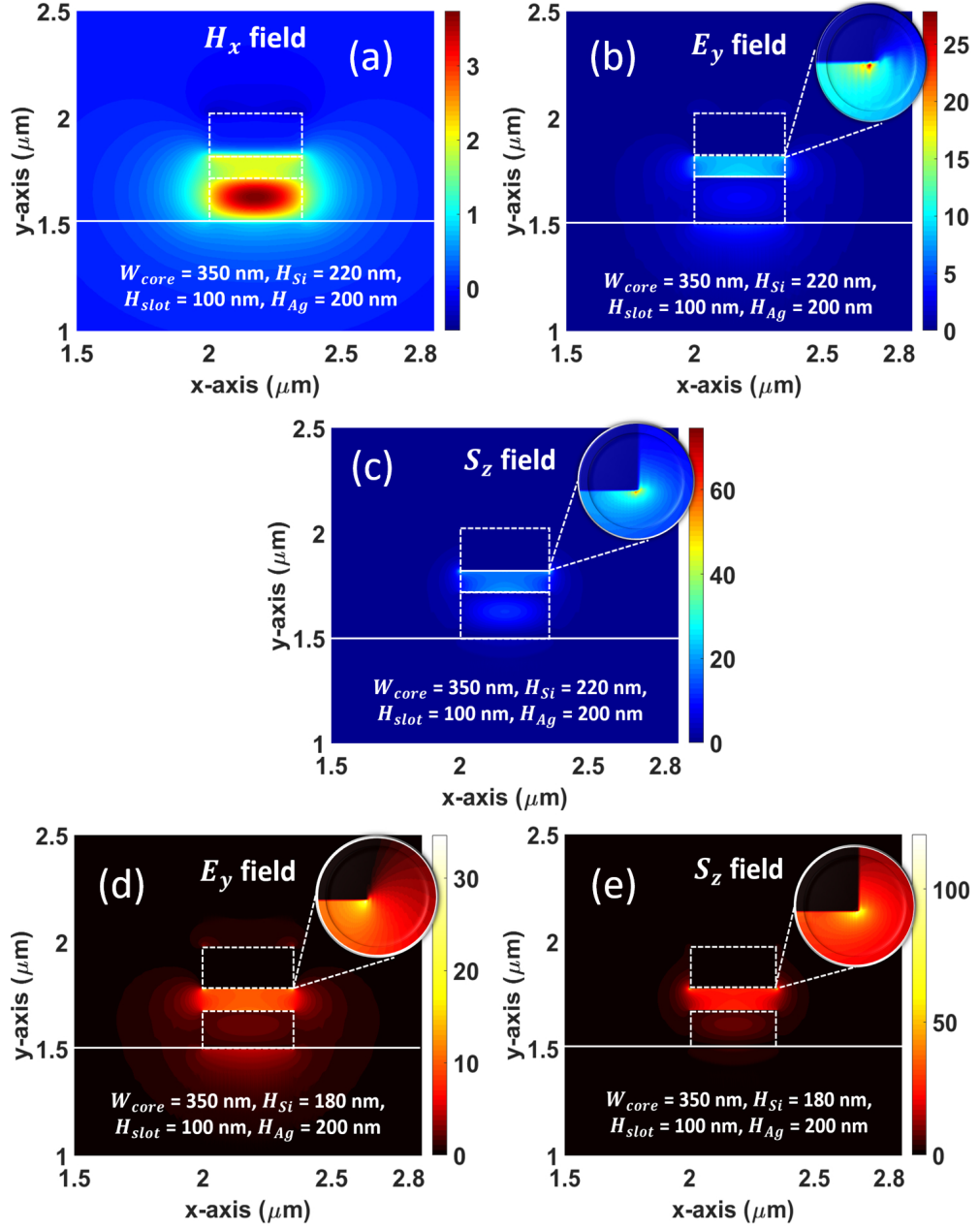


Figure 4.35: In-house 2D FV-FEM simulated field distribution of horizontal slot hybrid plasmonic waveguide. (a), (b), and (c) represent the quasi-TM H_x , E_y fields, and S_z intensity distributions, respectively when Si slab height (H_{Si}) is considered as 220 nm. (d) and (e) depict the quasi-TM E_y and S_z profiles for 180 nm Si slab height (H_{Si}). The circular highlighted sections present the sub-wavelength field confinement at the corners of the metal layer. Other parameters are considered as $W_{core} = 350$ nm, $H_{slot} = 100$ nm, and $H_{Ag} = 200$ nm.

indices of 3.4757, 1.4440, and $0.13880 + j11.310$ [Babar and Weaver, 2015], respectively at the wavelength of 1550 nm. The black line represents the real refractive index profile along y-axis of the HPW. Whereas, red dashed line shows the imaginary refractive index profile that indicates waveguide loss only exists due to the Ag layer. The structure is compatible with SOI fabrication technology and it can be fabricated by layer deposition process on top of commercially available SOI wafer having Si thickness of 220 nm. If necessary, the Si layer thickness could be altered by dry etching [Solehmainen *et al.*, 2005; Sun *et al.*, 2007]. The complete waveguide is considered to be buried under SiO_2 clad. The Ag layer's free surface electrons get excited by the operating electromagnetic light and the generated surface plasmon (SP) mode is guided by the Ag- SiO_2 interface. Besides, the dielectric mode is guided by the high index Si layer. However, the dominant hybrid supermode also known as surface plasmon polariton (SPP) which is a combination of both SP and dielectric mode is always guided by the low index slot region. The fundamental quasi-TM mode of the HPW situated in close locality of the metal thus it gets influenced by the SP which results in a high mode attenuation. Whereas, the quasi-TE mode is more localised in the high index dielectric region thus uninfluenced by the surface plasmon (SP). The HPW is modelled with in-house divergence modified 2D FV-FEM code and the simulated field profiles are shown in Fig. 4.35. Figures 4.35(a), (b), and (c) show the quasi-TM H_x , E_y fields, and S_z intensity profiles for $H_{Si} = 220$ nm. In the H_x distribution, maximum field is concentrated in the Si layer, whereas dominant E_y and S_z are mostly confined into horizontal slot. Figure 4.35(d) and (e) shows the E_y and S_z components of the quasi-TM mode for $H_{Si} = 180$ nm. Other parameters are kept fixed as 350 nm core width (W_{core}), 100 nm slot height (H_{slot}), and 200 nm Ag layer thickness (H_{Ag}). It can be seen from the colour bars of Fig. 4.35(b), (c), (d), and (e) that a smaller thickness of Si slab introduces larger field to be confined into low index slot region. It is also noticeable that the slot confined hybrid supermode is highly localised at the corners of the Ag layer, zoomed in the circular insets.

Figure 4.36 shows the real part of effective index ($Re(n_{eff})$) and mode propagation length (L_p) of the hybrid quasi-TM supermode with Si slab height (H_{Si}) shown by the red and blue solid lines, respectively. Both the $Re(n_{eff})$ and L_p increase with the increment of H_{Si} as the mode is more confined in the dielectric Si slab. This results in lower mode

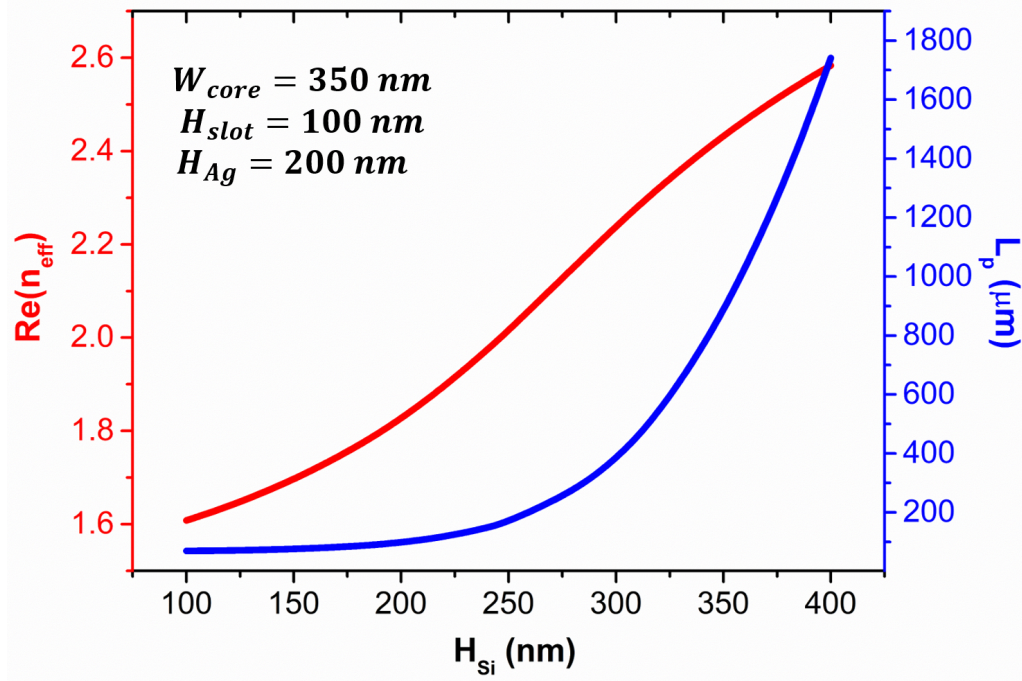


Figure 4.36: Effective index ($Re(n_{eff})$) and mode propagation length (L_p) variation of the HPW as a function of Si slab height (H_{Si}). Waveguide core (W_{core}), slot height (H_{slot}), and Ag height (H_{Ag}) are considered to be fixed as 350, 100, and 200 nm, respectively.

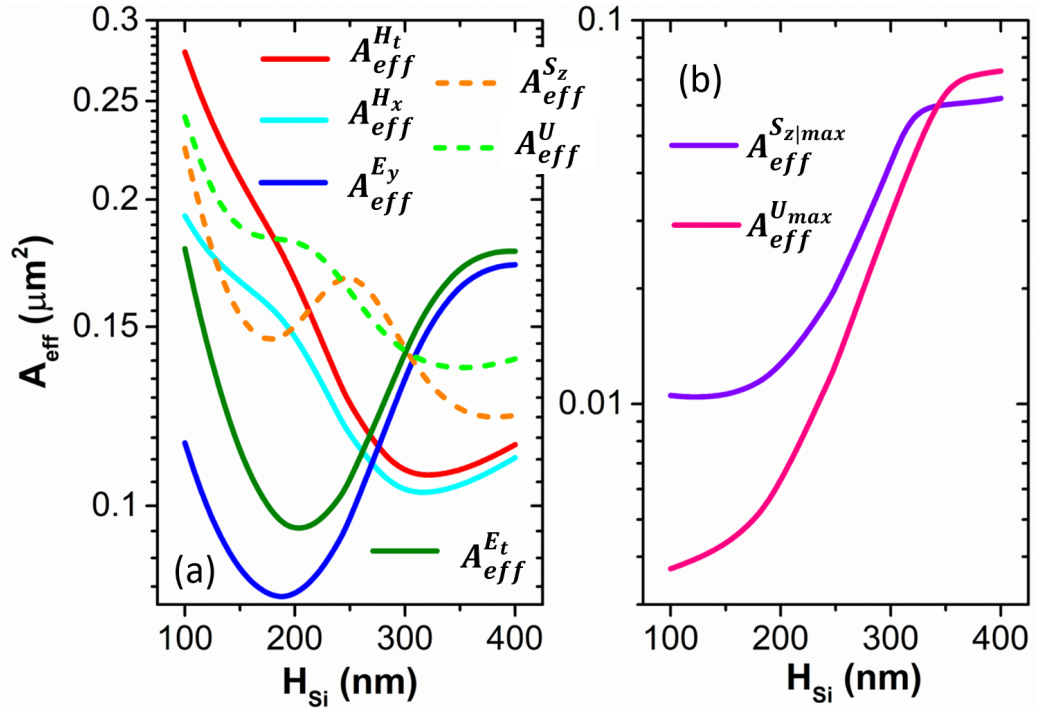


Figure 4.37: (a) and (b) show the evaluation of mode effective area A_{eff} of the HPW by different definitions as a function of H_{Si} . Other design parameters are considered as $W_{core} = 350$ nm, $H_{slot} = 100$ nm, and $H_{Ag} = 200$ nm.

attenuation for higher H_{Si} . Figure 4.37(a) and (b) depict the modal effective area of the HPW by different approaches such as $A_{eff}^{H_t}$, $A_{eff}^{H_x}$, $A_{eff}^{E_t}$, $A_{eff}^{E_y}$, $A_{eff}^{S_z}$, $A_{eff}^{S_z|max}$, A_{eff}^U , and $A_{eff}^{U_{max}}$ against H_{Si} while other design parameters are considered to be fixed. $A_{eff}^{E_t}$ and $A_{eff}^{E_y}$ have shown a parabolic trend which decrease, reach a minimum value and then further increase with the increment of H_{Si} . It is noticeable that $A_{eff}^{E_t}$ and $A_{eff}^{E_y}$ have shown comparative minimum effective areas of 0.0945 and $0.0810 \mu\text{m}^2$, respectively than other definitions plotted in Fig. 4.37(a). For lower H_{Si} values, the quasi-TM supermode into slot is mostly influenced by the SP thus in this region \vec{E} field based approaches show minimum mode area. On the other hand, as H_{Si} increases, the supermode mostly confined into Si region thus the \vec{E} field based results increase and \vec{H} field based results decrease. The $A_{eff}^{S_z}$ and A_{eff}^U (orange and green dashed lines, respectively) represent resultant A_{eff} variations which show lower values of effective area for lower and higher H_{Si} values and they also show a higher effective area in between during to modal transition from low index slot region to high index Si slab due to increment of H_{Si} . Other two definitions, such as $A_{eff}^{S_z|max}$ and $A_{eff}^{U_{max}}$ indicate much lower effective areas for lower H_{Si} s but effective area increase and almost get saturate with the H_{Si} increment. Instead of using the field distribution as a whole, these two approaches considered the $S_z|_{max}$ and U_{max} which are only localised at the corners of metal layer that results in a different effective area trend than others.

Next, the waveguide mode effective area has been studied as a function of slot height (H_{slot}) by considering other parameters to be fixed as 350 nm core width (W_{core}), 220 nm Si slab height and 200 nm thicken Ag layer. The red and blue lines in Fig. 4.38 indicate the real effective index ($Re(n_{eff})$) and mode propagation length (L_p) of the dominant quasi-TM mode. As the H_{slot} increases, the hybrid supermode (quasi-TM) confines more into low index slot in close vicinity of Ag layer which results in simultaneous decrement and increment of $Re(n_{eff})$ and L_p . Figure 4.39 depict the evaluation results of the HPW mode effective area as a function of H_{slot} with different effective area approaches such as $A_{eff}^{H_t}$, $A_{eff}^{H_x}$, $A_{eff}^{E_t}$, $A_{eff}^{E_y}$, $A_{eff}^{S_z}$, $A_{eff}^{S_z|max}$, A_{eff}^U , and $A_{eff}^{U_{max}}$. As the H_{slot} increases, all the A_{eff} s increase gradually. For a lower H_{slot} , the mode field especially quasi-TM E_y filed is more confined into slot thus results in a lower effective area. The $A_{eff}^{E_t}$ and $A_{eff}^{E_y}$ show much lower effective area values of 0.0057 and $0.0053 \mu\text{m}^2$, respectively compared

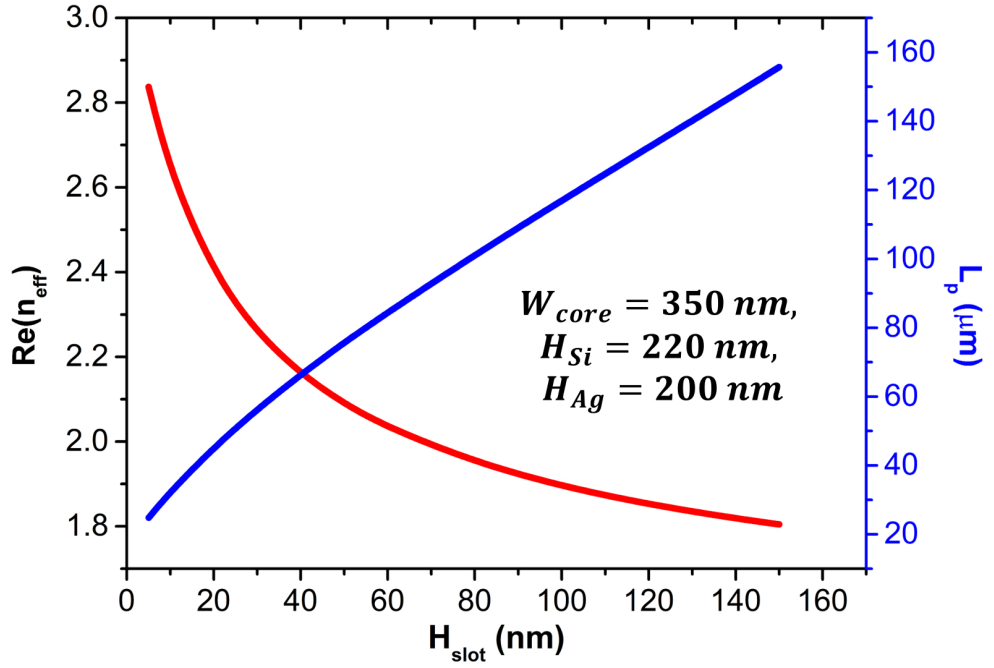


Figure 4.38: Effective index ($Re(n_{eff})$) and mode propagation length (L_p) variation of the HPW as a function of slot height (H_{slot}). Waveguide core (W_{core}), Si slab height (H_{Si}), and Ag height (H_{Ag}) are considered to be fixed as 350, 220, and 200 nm, respectively.

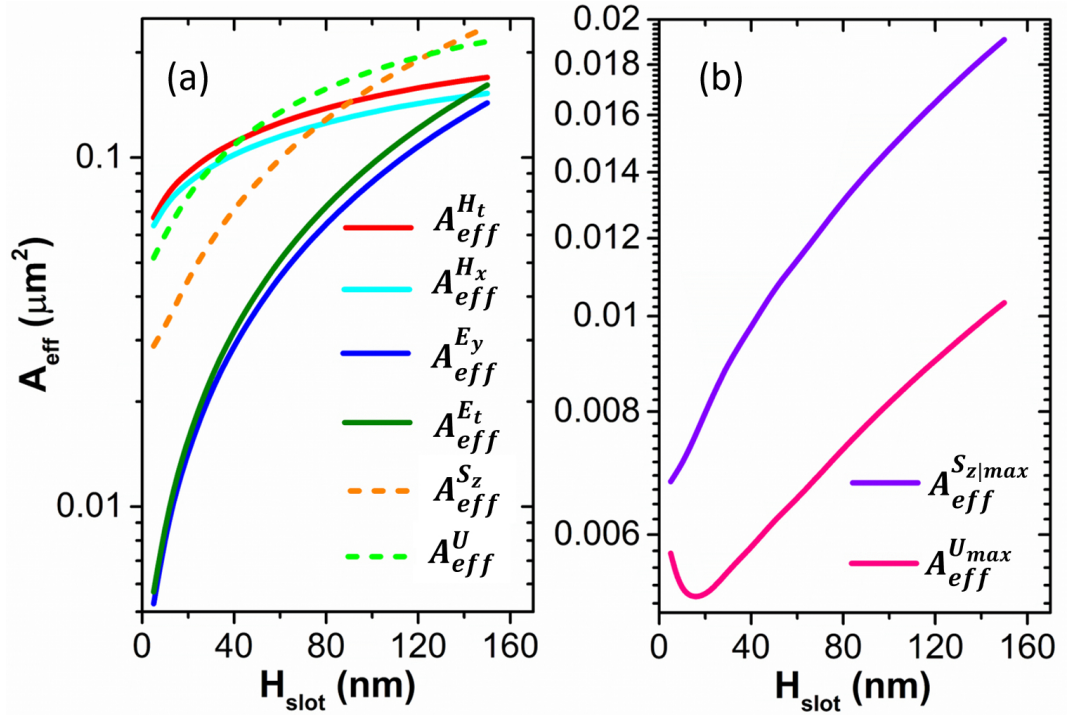


Figure 4.39: (a) and (b) show the evaluation of mode effective area A_{eff} of the HPW by different definitions as a function of H_{slot} . Other design parameters are considered as $W_{core} = 350$ nm, $H_{Si} = 220$ nm, and $H_{Ag} = 200$ nm.

to other approaches shown in Fig. 4.39(a). On the other hand, the $A_{eff}^{S_{z|max}}$ and $A_{eff}^{U_{max}}$ show almost similar variation with H_{slot} . Its behaviour mostly depend on the localised field concentration at the metal corners. Thus, it can be clearly observed that for sub-wavelength localised plasmonic field confinement the $A_{eff}^{S_{z|max}}$ and $A_{eff}^{U_{max}}$ based formulae are more useful. Whereas, for a field distribution over waveguide region the effective area definitions based on dominant fields are more effective and appropriate. Also a combine effect of dominant and non-dominant field components on mode effective area could be evaluated by $A_{eff}^{S_z}$ and A_{eff}^U based approaches.

4.4 Summary

A detail modal investigation has been carried out to study nano-plasmonic modal behaviour of guided modes supported by a simple metal (Ag) film embedded into dielectric background materials. Plasmonic modes have higher effective indices than the surrounding cladding refractive index. As they approach to cut-off, the mode fields spread into cladding region and plasmonic modes evolve into background quasi-TEM mode which leads to a reduction in mode propagation loss. Depending on different light guiding conditions long and short range plasmonic fundamental and higher order modes have been studied. The ss^0 and as^0 are the long-range modes for metal core bounded by identical cladding. At different cut-off conditions ($W = 200$ nm, $t = 40$ nm and $W = 1000$ nm, $t = 15$ nm), the ss^0 shows a much lower attenuation of 8.9 dB/mm and 2.4 dB/mm compared to other guided modes. As the cladding becomes non-identical, a long range plasmonic supermode (PSM) appears due to coupling of different individual modes of all four metal-dielectric interfaces when they travel with similar propagation constant. An interesting notable modal evolution of this PSM was observed with its dimensions. A small thickness of metal film causes a strong upper and lower interface modal coupling which results a prominent modal evolution from $s_L^1 as_U^0$ to $s_L^1 as_U^1$ for $W = 1000$ nm. On the other hand, for a smaller and near cut-off metal width ($W = 600$ nm) three different types of PSMs appeared due to modal coupling from all the four interfaces which makes the evolution process more complex. In that case, a comparative low modal attenuation with a large L_p was observed at a particular metal thickness, $t = 48$ nm. Additionally, surrounding

dielectric cladding materials also influence the modal evolutions. Optically dense media confine and localise more light to the metal-dielectric interfaces than the optically lighter media. This also results in increase of mode effective area with the reduction of cladding index.

Later, the FV-FEM has been used as a numerical tool to investigate on the ambiguities of the mode effective area formulations. Different effective area definitions such as $A_{eff}^{H_t}$, $A_{eff}^{H_x}$, $A_{eff}^{E_t}$, $A_{eff}^{E_y}$, $A_{eff}^{S_z}$, $A_{eff}^{S_z|max}$, A_{eff}^U , and $A_{eff}^{U_{max}}$ are mentioned in many published literatures have been incorporated to judge the mode effective area of different types of waveguides. Determination of appropriateness demands a through analysis. In this study, those mentioned approaches have been applied on low index, high index, and hybrid plasmonic waveguides and the results have been compared for final judgement. For a low index contrast optical fibre, $A_{eff}^{H_t}$, $A_{eff}^{E_t}$, $A_{eff}^{E_y}$, $A_{eff}^{S_z}$, and A_{eff}^U based approaches intersect with spot-size (SPZ) curve when its field profile follows its fitted Gaussian distribution. Thus, these formulae could be considered to be suitable for low index contrast fibres and waveguides. But in cases of high index contrast polarisation dependent waveguides, the A_{eff} definitions based on dominant and its transverse field components of the respective mode are more suitable compared to others. It is also noted that, \vec{H} and S_z based effective area definitions have closer values, and \vec{E} -field based definition gives slightly lower values, this could be due to larger field profile deviation for this profile. On the other hand, mode field distribution of a hybrid plasmonic waveguide (HPW) could be either highly localised or distributed type depending on the waveguide configuration. $A_{eff}^{S_z|max}$ and $A_{eff}^{U_{max}}$ based definitions could be useful for sub-wavelength confined mode area assessments as they consider the localised maximum field. But for the distributed type mode fields, polarisation dependent field based effective area formulations have shown their effectiveness.

Thus, the numerically investigated bounded SPP modal analyses of a simple Ag nano-wire successfully demonstrate the usefulness of our proposed divergence modified 2D FV-FEM. Additionally, rigorous analyses of mode effective area of different types of waveguides under different light guiding conditions provide intuitive ideas in design and optimisation of complex dielectric and hybrid plasmonic integrated photonic waveguides such as logic gates, switch, BUS router, modulator, polarisation controller, mode converter, nonlinear and sensing devices.

HORIZONTAL SLOT COMPOSITE PLASMONIC WAVEGUIDE (HSCPW) FOR DETECTION OF ETHANOL VAPOUR AND DNA HYBRIDISATION

5.1 Introduction

Integration of photonic devices and nano-electronics now became a challenge due to ingrained diffraction limit of electromagnetic energy supported by dielectric media. The surface plasmon polaritons (SPPs) can be one of the solutions to overcome this difficulty. Comparing other nano-scale waveguides, such as, high-index contrast silicon-on-insulator (SOI) nano-wires and photonic crystals (PCs), surface plasmon (SP) shows a nano-scale light guiding [Maier, 2007; Oulton *et al.*, 2008] in true sense. The light guiding characteristics of conventional dielectric waveguides and pure plasmonic waveguides show opposite characteristics. A high-index contrast SOI nano-wire confines light in the high index region. A very low propagation loss and hundred nano-meter scaled mode area are also key properties of these structures [Kejalakshmy *et al.*, 2010]. However, a pure metal plasmonic waveguide provides a sub-wavelength enhanced scale light confinement but with very high propagation loss [Veronis and Fan, 2005; Krasavin and Zayats, 2010; Berini, 2000, 2001]. This in turn requires an accurate evaluation and engineering to design the plasmonic based waveguides to channelise the unique features

of SPPs in the field of linear, nonlinear photonic devices [Alam *et al.*, 2011; Lu *et al.*, 2011] and sensing applications [Alam *et al.*, 2014; Homola *et al.*, 1999; Homola, 2003].

Surface Plasmon Polaritons (SPPs) are the surface waves tightly confined at the interface between metal and dielectric media. The SPP surface wave is a combination of free charge motion in the metal i.e. *surface plasmon* and electromagnetic waves in the dielectric media i.e. *polariton*. At optical and near infra-red (IR) region, metal has negative dielectric constant whereas dielectrics show a positive value. This complimentary nature at the interface excites electromagnetic surface wave that propagates until the field dies by material absorptions and scattering into surrounding media. The electromagnetic surface wave is a unique light-matter interaction that contains a coupled state of the electromagnetic wave to conductor's free electrons plasma oscillations. The SPPs are transverse magnetic (TM)-polarised in nature and evanescently confined in the direction of propagation. The SPPs can be excited either by electrons or photons with same frequency and momentum. In this work the photons having telecommunication wavelength of $\lambda = 1550$ nm is used for SPP excitations. Analytical solution to characterise the modal properties of electromagnetic field generated on both side of the metal and its integration with dielectric waveguide mode for a complex structure is not easy. Numerical modelling of complex plasmonic structure offers possible solution for sub-wavelength plasmonic device design and its performance analysis. A full-vectorial \vec{H} -field based 2D FV-FEM is used as a simulation tool for the device designs.

5.2 Ethanol Vapour Sensing by HSCPW

In modern industries, ethanol (CH_3CH_2OH) is considered as one of the most important constituent for productions of various goods. It has very high impact on daily life, from chemical and pharmaceutical products to heavy auto-mobile and fuel engineering but it is also a highly flammable substance. When ethanol vapour mixes with air, explosive fire can result if accidentally ignited. Only 3.5% ethanol vapour in air can causes explosion, this often termed as lower explosion limit. Besides, the upper explosion limit is 19% by volume of air [Gas, 2013]. Mishandling, leaking, spilling contamination failures can release the liquid ethanol which causes flammable vapour. This results environmental pollution

and also severe health risks. Human body initially breaks ethanol into acetaldehyde which increases the risk factor of liver cirrhosis and cancer. Therefore, accurate and high sensitive sensing of ethanol vapour in industrial environment is crucial. Several gas sensing mechanisms, such as spectrometric sensing [Kuze *et al.*, 2009], electrochemical [Chen *et al.*, 2005; Zhang *et al.*, 2006], solid state semiconductor [Gibson and MacGregor, 2013], and micro-controller based devices [Abraham and Li, 2014], have been reported and demonstrated in recent years. Besides, dielectric waveguide based interferometric and resonating structure, for breathing [Favero *et al.*, 2012], H_2 [Yebo *et al.*, 2009] and CH_3CH_2OH [Yebo *et al.*, 2010] sensing is more convenient for its high sensitivity and compact lab-on-a-chip design. In this chapter, we proposed a novel, compact ethanol vapour sensor based on hybrid plasmonic based horizontal slotted waveguide which offers a high sensitivity along with nano-meter scale footprint.

5.2.1 Porous ZnO (P-ZnO) Capillary Condensation

The proposed design of ethanol vapour sensor contains a horizontal layer of porous ZnO (P-ZnO) as a low index medium to absorb the ethanol vapour into its pores. P-ZnO has lower refractive index than a bulk ZnO, as the material pores are filled with air ($n = 1$). The equivalent refractive index (n_e) has an inverse relation with the number of pores in unit volume, called porosity (P). Pores in the material increase curved empty space which results in absorption and condensation of vapour or gaseous substances. Pore sizes ranging from 2 to 50 nm (mesoporous) of a P-ZnO layer possess the surface area around $1000 \text{ m}^2/\text{g}$ [Yebo *et al.*, 2010]. When the porous layer is kept in contact with the measuring analyte the air ($n = 1$) filled voids are replaced by condensed analyte ($n > 1$). Depending on the different volume fraction of absorbed and condensed analyte, the effective refractive index as well as dielectric constant of P-ZnO changes.

For making our waveguide design more efficient, different types of P-ZnO layer templates could be used, such as, porous flakes composed ZnO spheres [Wang, Tian, Wang, He, Xu, He and Li, 2013], P-ZnO nano-sheets [Zhang, Zhao, Lu, Li, Zheng, Li and Zhu, 2012], and nano-plates [Jing and Zhan, 2008]. All these types of P-ZnO layers composites of nano-meter scaled pores exploit ultra-high pore density with great enhancement of surface-to-volume ratio. P-ZnO spheres, nano-sheets and nano-plates are mesoporous

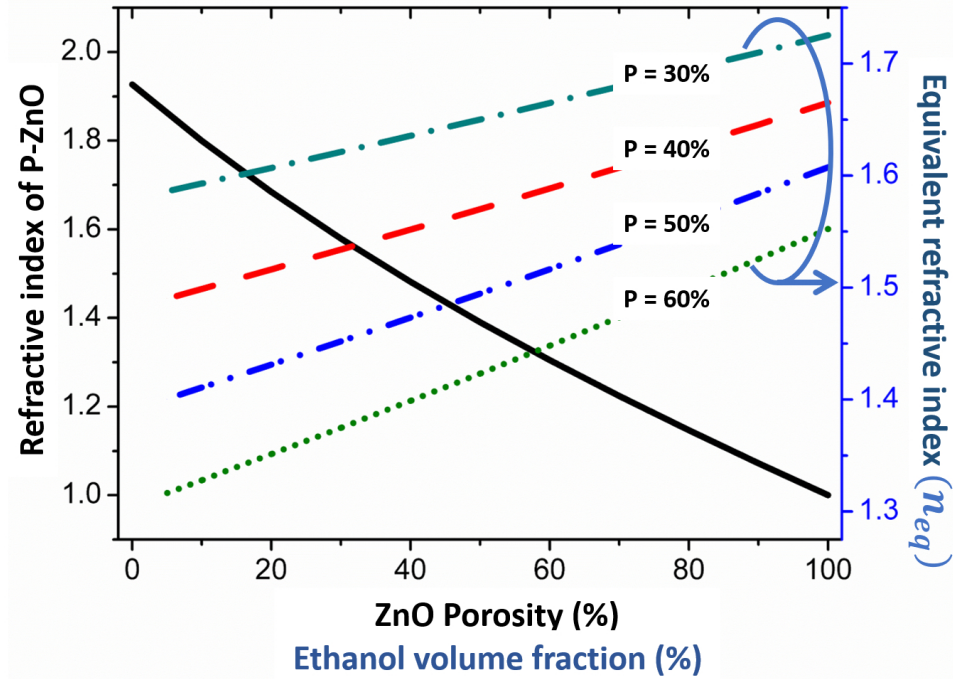


Figure 5.1: Refractive index variation with porosity (P) and change of equivalent refractive index of P-ZnO with volume fraction (V) of capillary condensed ethanol.

with pore diameters ranging from 2 to 50 nm. The nano-sheet contains average pore size of 39 nm [Zhang, Zhao, Lu, Li, Zheng, Li and Zhu, 2012]. Operating temperature is an important parameter for metal-oxide semiconductor based sensors. The P-ZnO sphere layer shows an enhanced selective response to 100 ppm ethanol at 280°C. Similarly, a strong response in ethanol sensing can be observed around 400°C to 450°C for nano-sheets and nano-plates [Zhang, Zhao, Lu, Li, Zheng, Li and Zhu, 2012; Jing and Zhan, 2008]. In terms of selectivity and response-recovery time, all three P-ZnO configurations show excellent selectivity and much shorter response and recovery time (10 and 15 s, 7 and 19 s, 32 and 17 s) to ethanol vapour compared to methanol, acetone, chlorobenzene, and methane at 280°C [Wang, Tian, Wang, He, Xu, He and Li, 2013], 400°C [Zhang, Zhao, Lu, Li, Zheng, Li and Zhu, 2012], and ~ 450°C [Jing and Zhan, 2008] for 2, 200 and 100 ppm of ethanol, respectively. Use of these P-ZnO templates in the horizontal slot section make the HSCPW more stable and efficient for ethanol vapour sensing. The size of an ethanol vapour molecule is 4.53 Å or 0.453 nm [Zhou *et al.*, 2018]. Therefore, sufficient numbers of ethanol gaseous and vapour molecules can easily accommodate themselves into the mesoporous P-ZnO layer. Various effective quantitative models such as Maxwell-Garnet

theory, Bruggeman model and Lorentz-Lorenz model have been proposed to determine the equivalent permittivity of heterogeneous media [Garahan *et al.*, 2007]. In this work, we used the Lorentz-Lorenz model to determine the refractive index of ZnO layer depending on its porosity (P) as:

$$\frac{n_{P-ZnO}^2 - 1}{n_{P-ZnO}^2 + 2} = (1 - P) \left(\frac{n_c^2 - 1}{n_c^2 + 2} \right) + P \left(\frac{n_a^2 - 1}{n_a^2 + 2} \right) \quad (5.1)$$

and equivalent refractive index (n_{eq}) variation of the P-ZnO due to absorption of ethanol vapour.

$$\frac{n_{eq}^2 - 1}{n_{eq}^2 + 2} = (1 - P) \left(\frac{n_c^2 - 1}{n_c^2 + 2} \right) + (P - V) \left(\frac{n_a^2 - 1}{n_a^2 + 2} \right) + V \left(\frac{n_d^2 - 1}{n_d^2 + 2} \right) \quad (5.2)$$

Here P is the ZnO layer porosity, V is the volume fraction of liquid after capillary condensation. n_a , n_c , and n_d are the index of refraction of air ($n_a = 1$), homogeneous (bulk ZnO) and dispersed medium (condensed vapour), respectively. We have considered the P-ZnO layer of porosity $P = 30\%$, 40% , 50% , and 60% . Corresponding refractive index (n_{P-ZnO}) variations and equivalent refractive index of P-ZnO due to different volume fraction of ethanol are presented in Fig. 5.1. As expected, n_{P-ZnO} decreases with the porosity increment, shown by a solid black line. On the other hand, while these air pores are partially replaced by the condensed ethanol the equivalent index of refraction (n_{eq}) increases. At room temperature (20°C), the bulk ZnO refractive index is taken as 1.9267 at the wavelength of 1550 nm, derived from the dispersion formula in [Bond, 1965]. The ethanol refractive index is derived at the same wavelength of 1550 nm by using the Sellmeier equation given in [Kedenburg *et al.*, 2012]

$$n^2(\lambda) = 1 + \frac{A_1 \lambda^2}{\lambda^2 - B_1} + \frac{A_2 \lambda^2}{\lambda^2 - B_2} \quad (5.3)$$

Here $A_{1,2}$ and $B_{1,2}$ denotes the material property parameters and absorption wavelengths. The constant values used for mathematical analysis are, $A_1 = 0.83189$, $A_2 = -0.15582$, $B_1 = 0.00930 \mu\text{m}^{-2}$ and $B_2 = -49.45200 \mu\text{m}^{-2}$.

5.2.2 Horizontal Slotted Composite Plasmonic Waveguide (HSCPW)

Plasmonic waveguides are very useful for nano-dimensioned photonic sensing devices. In pure and hybrid plasmonic waveguides, enhanced sub-diffraction limited light confinement on the metal-dielectric interface make this structure very attractive for local

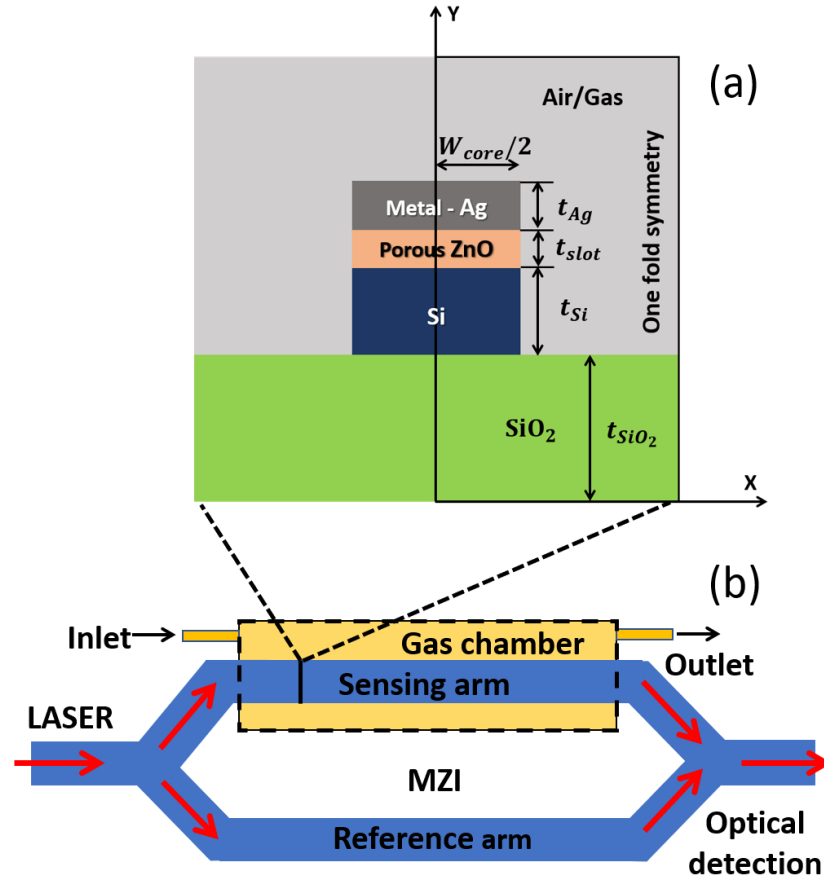


Figure 5.2: Schematic diagram of a horizontal slotted composite plasmonic waveguide (HSCPW). (a) shows the geometrical cross-section of the proposed HSCPW where P-ZnO is used as low index medium sandwiched between high index silicon (Si) and lossy metal (Ag). The black bordered region depicts the one folded computational domain. (b) depicts the symmetrical arm Mach-Zehnder interferometer (MZI) where the HSCPW is used.

surface and bulk bio-chemical and gas sensing. The schematic diagram of our proposed horizontal slotted HSCPW and the composite plasmonic waveguide incorporated symmetric Mach-Zehnder interferometer (MZI) is shown in Fig 5.2. The waveguide consists of composite materials, such as lossy metal (Ag), porous ZnO (P-ZnO), silicon (Si) and silica (SiO_2). A horizontal slot waveguide can be formed by depositing a nano-scaled thick (t_{Ag}) silver layer on top of a P-ZnO, which is used as a low index slot region in between the metal and high index Si. Due to the presence of lossy metal, the bounded SPP modes can only be guided over a small distance. To utilise the benefits of localised plasmonic fields along with short mode propagation length (L_p) the metal layer is integrated with other loss-less dielectric materials. The refractive indices considered for the simulations are, $n_{Ag} = 0.13880 + j11.310$ [Babar and Weaver, 2015], $n_{Si} = 3.4757$

[Li, 1980], and $n_{SiO_2} = 1.4440$ at the operating wavelength of 1550 nm. The necessary boundary condition of electromagnetic field demands a continuity of normal component of electric flux density (\vec{D}) at the interface boundaries that results a high E_y field discontinuity ($E_{y,Si} \neq E_{y,P-ZnO} \neq E_{y,Ag}$) at those interfaces. These field characteristics make this waveguide very attractive for integrated sensing device due to strong light-matter interaction in the slot region. Here ethanol vapour is used as a sensing medium. Due to capillary condensation ethanol vapour molecules are absorbed by the ZnO pores and condensed as liquid ethanol. Thus, depending on percentage of absorbed ethanol vapour the refractive index of P-ZnO layer changes. The relation between equivalent refractive index of P-ZnO and volume fraction of ethanol already has been discussed in Section 5.2.1. These refractometric change can easily be detectable by an accurate measurement of real part of effective index change, $\Delta Re(n_{eff})$ of the quasi-TE and TM modes. The propagation length (L_p) of the guided modes by the designed waveguide can be calculated as

$$L_p = \frac{1}{2\alpha} = \frac{\lambda}{4\pi \cdot Im(n_{eff})} \quad (5.4)$$

where α denotes the attenuation constant and $Im(n_{eff})$ denotes the imaginary part of the effective index. This metal dielectric composite structure helps the plasmonic modes to propagate over a comparative longer distance. Thus, with proper engineering a composite plasmonic waveguide can be designed, which can be useful for local bio-chemical and gas sensing.

To simulate the HSCPW our in-house \vec{H} -field based full-vectorial 2D FV-FEM code is used. In order to get accurate simulations, only the right hand side section bordered by black line in Fig. 5.2(a) have been considered exploiting the available symmetry of the structure. To obtain an accurate field distribution of the dominant and non-dominant modes, the necessary boundary conditions are applied along the symmetry line. In this structure, a perfect magnetic wall (PMW), $\hat{n} \times \vec{H} = 0$ is applied along the symmetry line (along y-axis) as the H_x and E_y fields of fundamental mode have even symmetry along the y-axis. Other three boundaries are considered as the perfect electric wall (PEW). Mesh distribution is an important step for a plasmonic waveguide simulation. As the metal surface possess a sub-wavelength field confinement into nano-scaled region, a

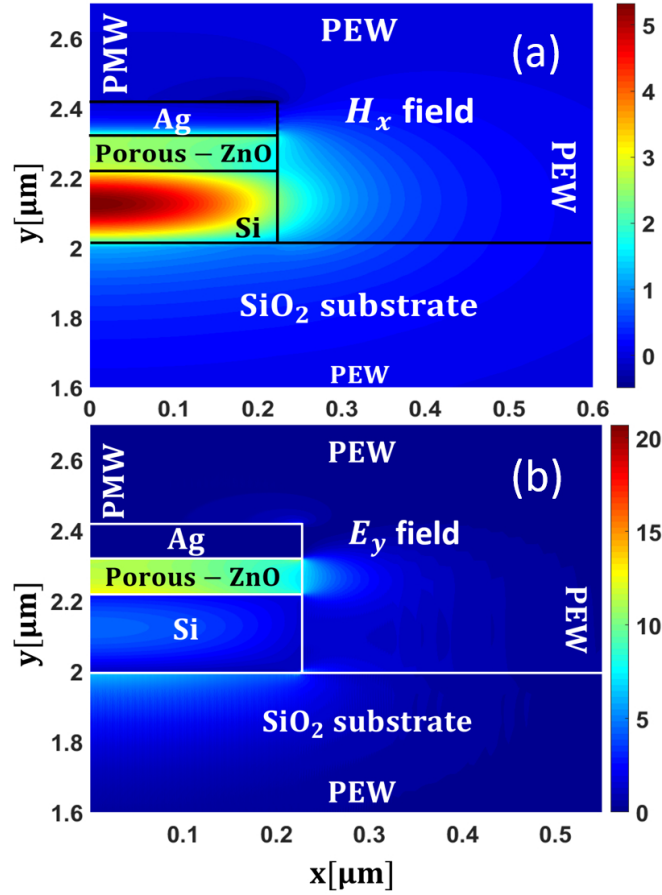


Figure 5.3: Simulated field profile of the dominated quasi-TM mode of the HSCPW. (a) and (b) illustrate the H_x and E_y field distributions, respectively.

sufficient dense mesh is required in the thin metal area for accurate solutions. The maximum element size used around the metallic area was 0.2 nm. Throughout the simulation process, half of the waveguide structure is discretised with 1,280,000 first order triangular mesh elements. For the plasmonic waveguides, fundamental quasi-TM is the dominant than the quasi-TE mode. Figures 5.3(a) and (b) depict the H_x and E_y field contours of fundamental quasi-TM (H_x^{11} and E_y^{11}) mode. The H_x field shows maximum distribution in the high index Si. However, the E_y field confines in the P-ZnO slot region. Thus, the maximum power is confined and guided by the low index slot region. The 1D-line plot of the E_y and H_x fields of fundamental H_x^{11} mode are shown in Fig. 5.4. The E_y field shown by a red solid line indicates a sharp field enhancement into low index horizontal slot region. The H_x field is denoted by blue-dashed dotted line which shows a greater light confinement in the high index Si-core. Figures 5.5 (a), (b) and (c) shows the H_y field distribution of the non-dominant quasi-TE mode. The H_y field plot shows a high

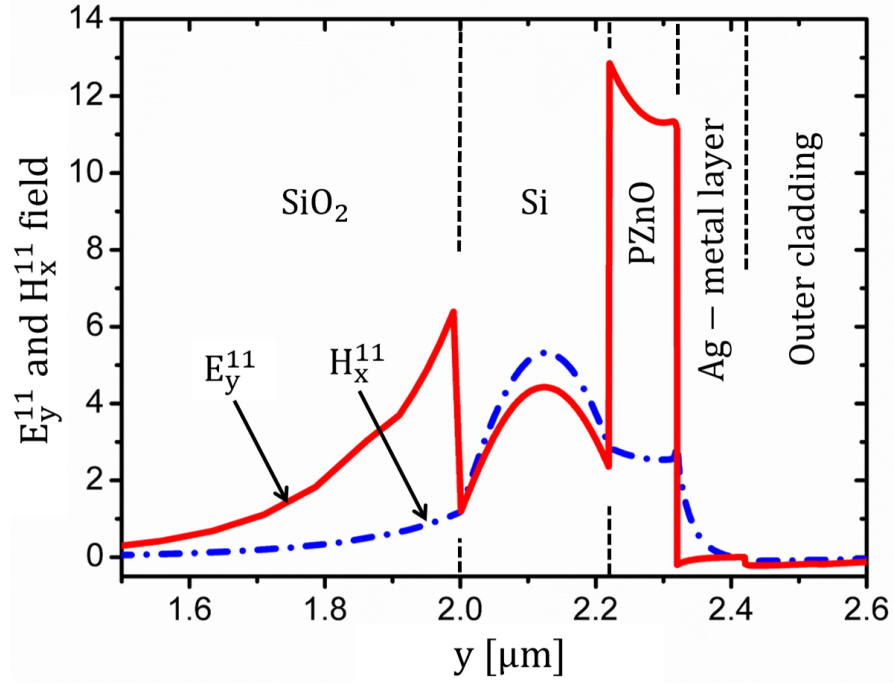


Figure 5.4: 1D line plot of fundamental mode E_y and H_x field along the symmetry line (y-axis). The red solid curve shows E_y field enhancement in the low index horizontal slot region, effective for sensing applications. The blue dashed-dotted line shows light guidance by the dielectric Si core.

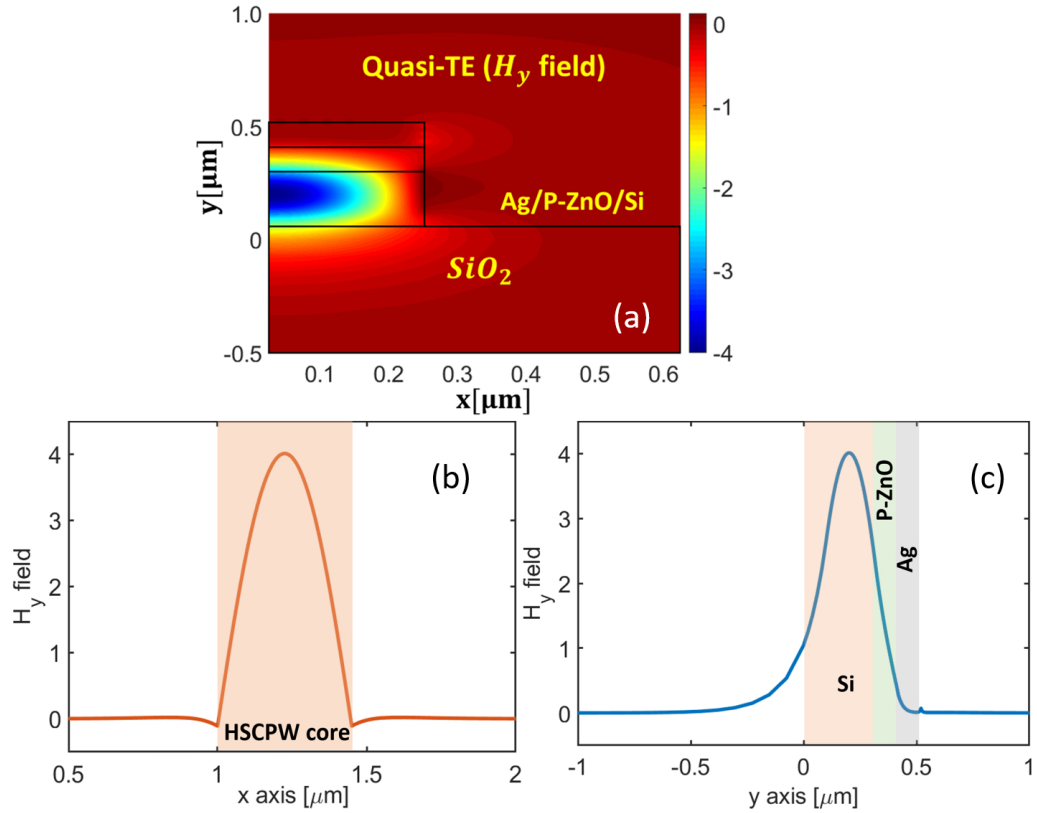


Figure 5.5: Simulated H_y field profile of quasi-TE mode; (a) and (b) illustrate the H_y field distributions along x and y axes, respectively.

light guidance by the high index Si and P-ZnO layer and field shows continuity at the material interfaces. The Ag layer has less influence on the mode distribution thus it have a comparative high mode propagation length (L_p) and less modal loss than dominant quasi-TM mode (discussed later). The 1D line plot of the H_y field distribution along x and y axes have been shown in Figs. 5.5(b) and (c), respectively.

The Si nano-wire could be realised by modern CMOS fabrication technologies. Lithography masking and then controlled dry-etching of a commercially available silicon-on-insulator (SOI) wafer can be used to fabricate a finite width (W_{core}) fixed height ($t_{Si} = 220$ nm) Si nano-wire. Although different chemical strategies are available to grow P-ZnO, such as, sol-gel, thermal decomposition, laser ablation that uses a high temperature, a low temperature synthesis mechanism using precipitation method [Yebo *et al.*, 2010; Lommens *et al.*, 2008] could be useful to grow a controlled thickness (t_{slot}) P-ZnO nano layer on Si. A ZnO nano-crystal layer can be formed by using additive materials with the pure Zn based solution and then deposit it onto Si nano-wire by the process of uniform precipitation method. To achieved mesoporous crystallised ZnO, the additive materials residue need to be evaporate by heat treatment. The pore dimensions and quality could be controlled by the additive material concentration, molecular size and operating temperature. Here we considered a mesoporous ZnO layer with pore sizes between 2 to 50 nm.

To obtain an explicit sensor design a rigorous investigation is needed to estimate the optimised waveguide parameters, dominant, non-dominant field distributions and power confinement into different waveguide regions due to refractometric changes into slot area. Most easily available thickness of the Si layer of a SOI wafer is 220 nm. Thus, simply etching the unwanted Si layers could form the nano-wire like structure without manual Si growth. For simplicity, we fixed the Si nano-wire and Ag metal thickness as 220 nm and 100 nm, respectively. The rest of device geometries, such as, waveguide core width (W_{core}) and slot thickness are (t_{slot}) are optimised for the best performance.

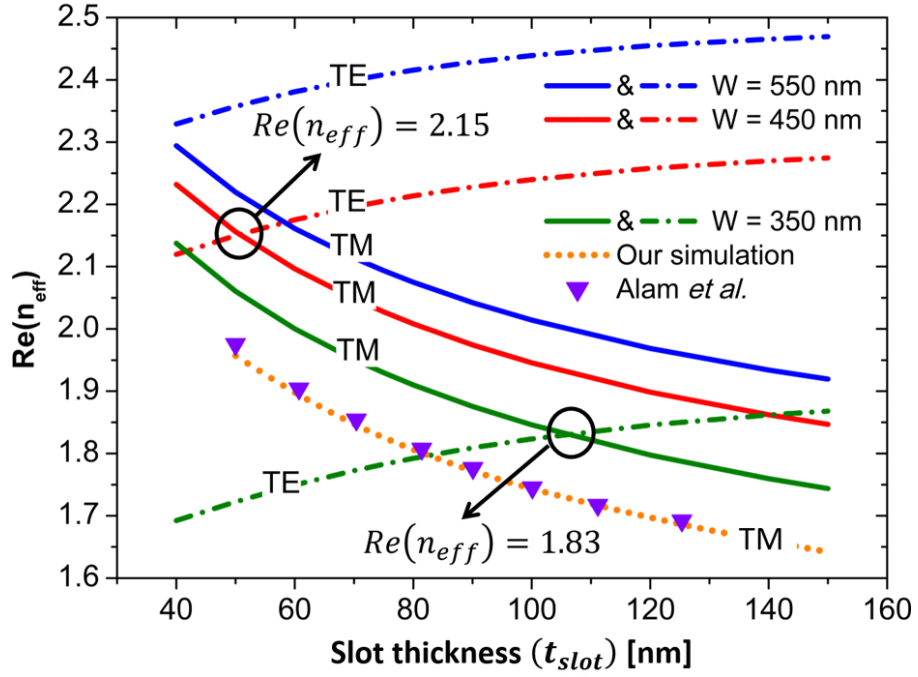


Figure 5.6: Real effective index ($Re(n_{eff})$) variation with the slot thickness (t_{slot}). Fundamental quasi-TE (H_y^{11}) and TM (H_x^{11}) modal real effective indices with t_{slot} variations are shown by green, red and blue dashed-dotted and solid lines for three different core widths (W_{core}) 350, 450, and 550 nm, respectively. The orange dotted line denotes the $Re(n_{eff})$ of the quasi-TM mode simulated by our code for benchmarking with [Alam *et al.*, 2011] shown by purple triangular markers.

5.2.3 Optimisation of Design Parameters and Waveguide Performance as a Sensor

Figures 5.6 and 5.7 show variation of the real part of the effective index, $Re(n_{eff})$ and modal propagation length L_p against the horizontal slot thickness t_{slot} , respectively. To benchmark our newly modified in-house code, we have simulated a SOI based horizontal slotted hybrid plasmonic waveguide proposed by [Alam *et al.*, 2011]. We have considered the same waveguide dimensions ($W_{core} = 350$ nm, $t_{Ag} = 200$ nm, $t_{Si} = 200$ nm, and $t_{substrate} = 2.0$ μ m) and same material refractive indices and simulate that with our in-house FV-FM code. Our simulated $Re(n_{eff})$ data are shown by the orange dotted lines in Fig. 5.6. Our results matches excellently with the published results (purple triangles) reported in [Alam *et al.*, 2011] where they have used a commercial software COMSOL for their simulations.

In this study, we have considered a HSCPW with three different widths 350 nm, 450 nm and 550 nm. Corresponding $Re(n_{eff})$ variations of the fundamental quasi-TE

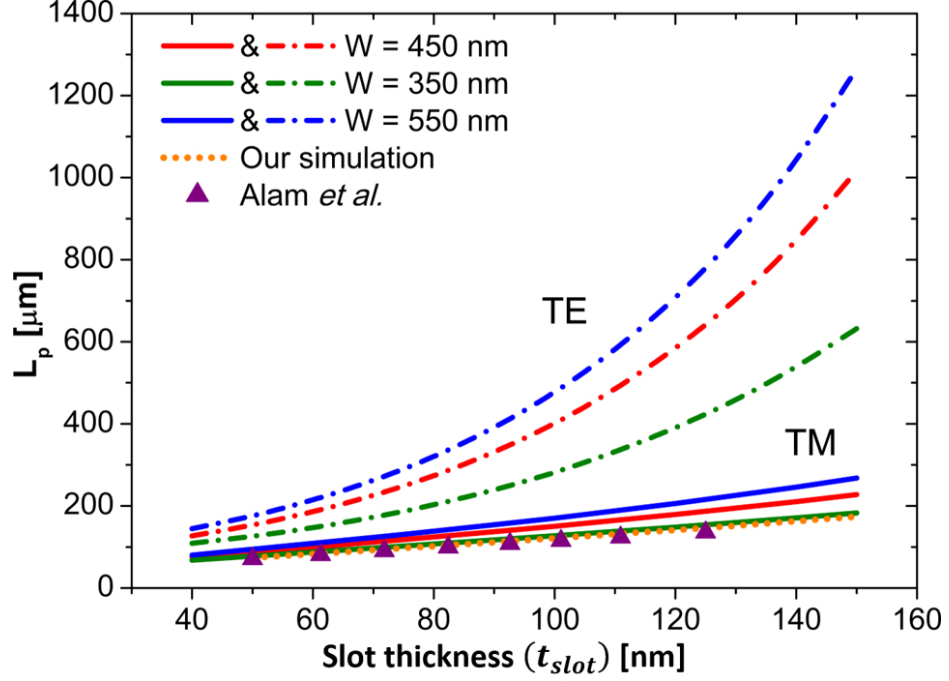


Figure 5.7: Variation of the mode propagation length (L_p) with the t_{slot} . Quasi-TE modes (dashed-dotted lines) show higher L_p than quasi-TM mode (solid lines), shown by dashed-dotted and solid lines, respectively. 350, 450 and 550 nm W_{core} are represented by green, red and blue lines, respectively. The orange dotted line denotes the L_p of the quasi-TM mode simulated by our code for benchmarking with [Alam *et al.*, 2011] shown by purple triangular markers.

and TM mode are shown by the green, red, and blues coloured dashed-dotted and solid lines, respectively. As t_{slot} increases the $Re(n_{eff})$ decreases gradually for fundamental quasi-TM mode but increases for fundamental quasi-TE mode, respectively. It can be observed that for $W_{core} = 350$ and 450 nm modal degeneracy occurs at $t_{slot} = 108$ nm and 48 nm, respectively when effective indices of the quasi-TE and quasi-TM modes became equal. Modal degeneracy points are encircled by black line and corresponding $Re(n_{eff})$ values are also given in Fig. 5.6. Here for the HSCPW, effective dominant mode for sensing is the quasi-TM supermode where a surface plasmonic mode is coupled with dielectric mode into low index slot region. It can also be noted from Fig. 5.6 that for a fixed t_{slot} the $Re(n_{eff})$ also decreases with W_{core} . Variations of mode propagation length (L_p) against t_{slot} has been shown in Fig. 5.7 for the quasi-TE and TM modes for $W_{core} = 350$, 450 , and 550 nm. The L_p variations with t_{slot} show a rapid increment for quasi-TE as here the field is mostly confined and also guided by the low-loss dielectric regions but the quasi-TM mode shows a comparative slow increment with thickness of P-ZnO dielectric

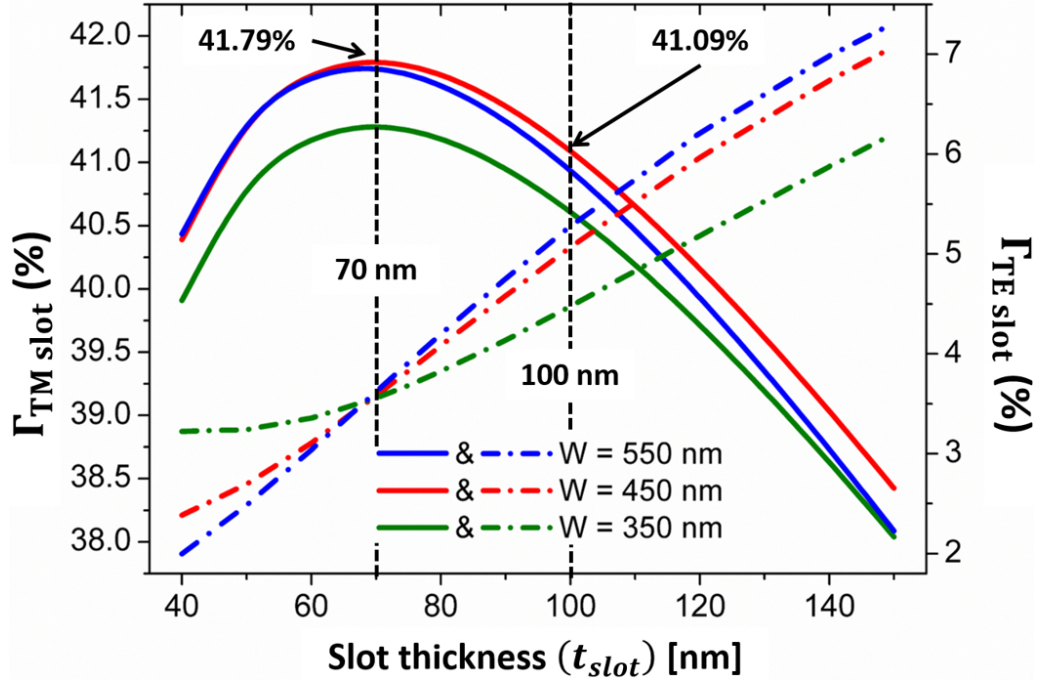


Figure 5.8: Quasi-TM and TE slot confinement variations with t_{slot} . The TM slot confinement ($\Gamma_{TM\ slot}$) and TE slot confinement ($\Gamma_{TE\ slot}$) variations for three different $W_{core} = 350, 450$, and 550 nm are indicated by solid and dashed-dotted green, red and blue lines, respectively. $W_{core} = 450$ nm shows maximum $\Gamma_{TM\ slot}$ at $t_{slot} = 70$ nm.

material into slot as here the field profile is influenced by the SPPs generated by the lossy metal-dielectric interface. The orange dotted line in Fig. 5.7 shows our simulated results of the hybrid plasmonic waveguide proposed by Alam *et al.*, which is matching well with the published result (purple triangles) reported in [Alam *et al.*, 2011].

Figure 5.8 shows variation of mode confinement of the quasi-TE and TM modes with t_{slot} . The TE and TM slot confinements ($\Gamma_{TM\ slot}$ and $\Gamma_{TE\ slot}$) with t_{slot} show an interesting feature. For three fixed core widths, W_{core} , the $\Gamma_{TM\ slot}$ increases with t_{slot} , reaches maximum and then decreases gradually with further increment. It can also be noticed that the HSCPW with $W_{core} = 450$ nm, shown by the red solid line, confines a higher 41.79% electromagnetic energy at $t_{slot} = 70$ nm than other two core widths (550 and 350 nm), shown by blue and green solid lines, respectively. The $\Gamma_{TE\ slot}$ for all three W_{core} s increase with increase of slot thickness shown by the dashed-dotted lines. But these values are much lower than the TM mode confinement. These curves intersect each other at $t_{slot} = 68$ nm and exhibits only around 3.56% power confinement. As we are designing a plasmonic sensor, the slot confinement due to SPP and dielectric supermode

is our most concern. As a result, we focused only on $\Gamma_{TM\ slot}$ variation and the maximum confinement is obtained for optimised slot thickness, $t_{slot} = 70$ nm. The 1D-line plot of the quasi-TM E_y and H_x field for different slot heights, $t_{slot} = 70, 100$, and 150 nm have been shown in Figs. 5.9 (a) and (b), respectively. The field distributions for $70, 100$, and 150 nm slot height are illustrated by the blue, black, and red solid lines, respectively. W_{core} , t_{Ag} , and t_{Si} is kept fixed at $450, 100$, and 220 nm, respectively. At $t_{slot} = 70$ nm, the E_y shows maximum slot confinement and less confinement in Si core. With the increment of t_{slot} , the slot confinement ($\Gamma_{TM\ slot}$) decreases gradually which in turn give rise to a gradual increase of light confinement in the Si core and SiO_2 buffer layer (Fig. 5.9).

Further optimisation of W_{core} has been carried out for a fixed 70 and 100 nm slot height and the corresponding results are presented in Fig. 5.10. Here, the red and green solid lines represent the $\Gamma_{TM\ slot}$ variations with W_{core} for two fixed $t_{slot} = 70$ and 100 nm, respectively. As W_{core} increases the $\Gamma_{TM\ slot}$ grows and confines maximum 41.80% and 41.09% TM field into 70 and 100 nm slot, respectively at $W_{core} = 450$ nm. Thus, the optimised HSCPW core width can be taken as 450 nm. From the plots in Figs. 5.8 and 5.10 it can be seen that a 100 nm slot confines 41.09% TM field. As there was not much difference in $\Gamma_{TM\ slot}$ for $t_{slot} = 70$ and 100 nm and a few nm extra thickness may be convenient to accommodate more number of pores in mesoporous ZnO layer, we have finally considered slot thickness as 100 nm. The effective indices ($Re(n_{eff})$) variations of quasi-TE and TM modes with W_{core} have shown in Fig. 5.11. The solid and dashed-dotted lines represent the $Re(n_{eff})$ of the quasi-TM and TE modes, respectively for two optimised t_{slot} values, such as 70 and 100 nm. It can be noticed that with the variation of t_{slot} from 70 to 100 nm the quasi-TE $Re(n_{eff})$ curves stay close which signifies that the variation of t_{slot} has less effect on the TE mode. Whereas, t_{slot} variation from 70 to 100 nm has a noticeable influence on quasi-TM mode which is clearly seen from effective index difference of the HSCPW for $t_{slot} = 70$ and 100 nm shown by the blue and black solid curves, respectively. Throughout the optimisation process, the Si nano-wire and Ag thickness are kept fixed at $t_{Si} = 220$ nm and $t_{Ag} = 100$ nm, respectively but if desired these can also be optimised. Hence all the optimised HSCPW parameters can be listed as, $W_{core} = 450$ nm, $t_{slot} = 100$ nm, $t_{Si} = 220$ nm and $t_{Ag} = 100$ nm for 40% ZnO

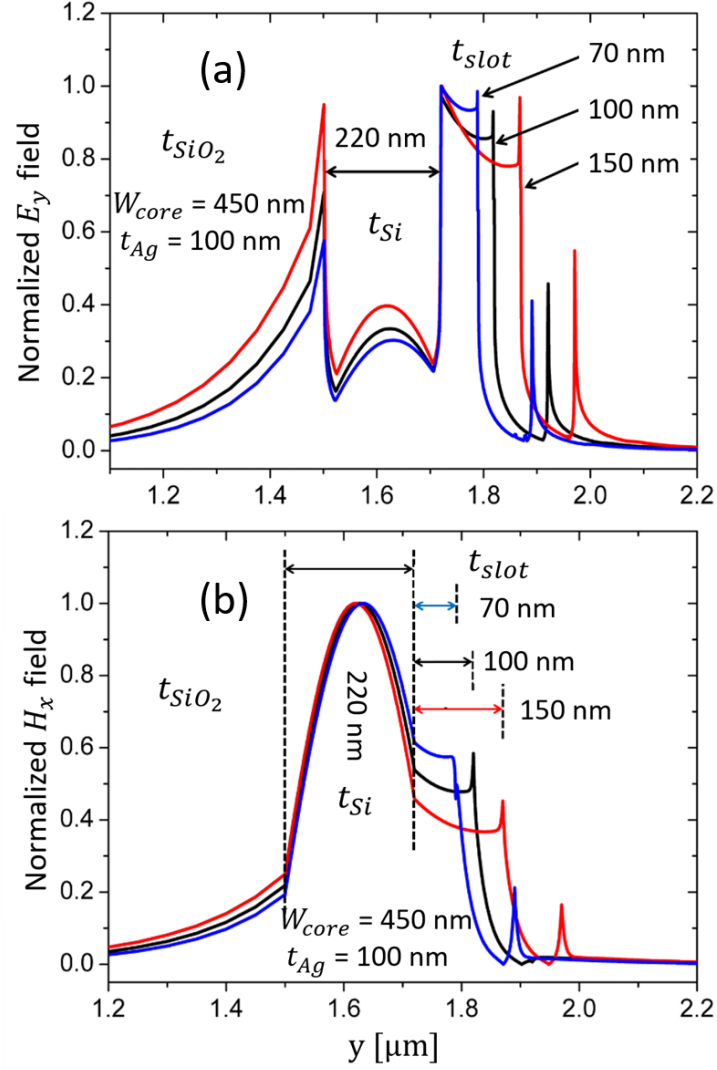


Figure 5.9: (a) and (b) illustrates the normalised 1D-line plot of the dominant fundamental quasi-TM (E_y and H_x) field variations along y-axis for three different slot heights, $t_{slot} = 70, 100$, and 150 nm . The field distribution along y-axis is taken at the left or right side of the HSCPW. Other parameters are kept fixed as, $W_{core} = 450 \text{ nm}$, $t_{Ag} = 100 \text{ nm}$, and $t_{Si} = 220 \text{ nm}$.

porosity.

5.2.4 Waveguide Sensitivity

Next, we analysed the HSCPW performance with the presence of ethanol vapour. Absorption of different percent ethanol vapour changes the equivalent refractive index of P-ZnO with the help of capillary condensation. The equivalent refractive index depending on the volume fraction of ethanol was calculated by using Lorentz-Lorenz formulation (Eqs. 5.1 and 5.2) and results are shown in Fig. 5.1. The quasi-TM and TE real effective

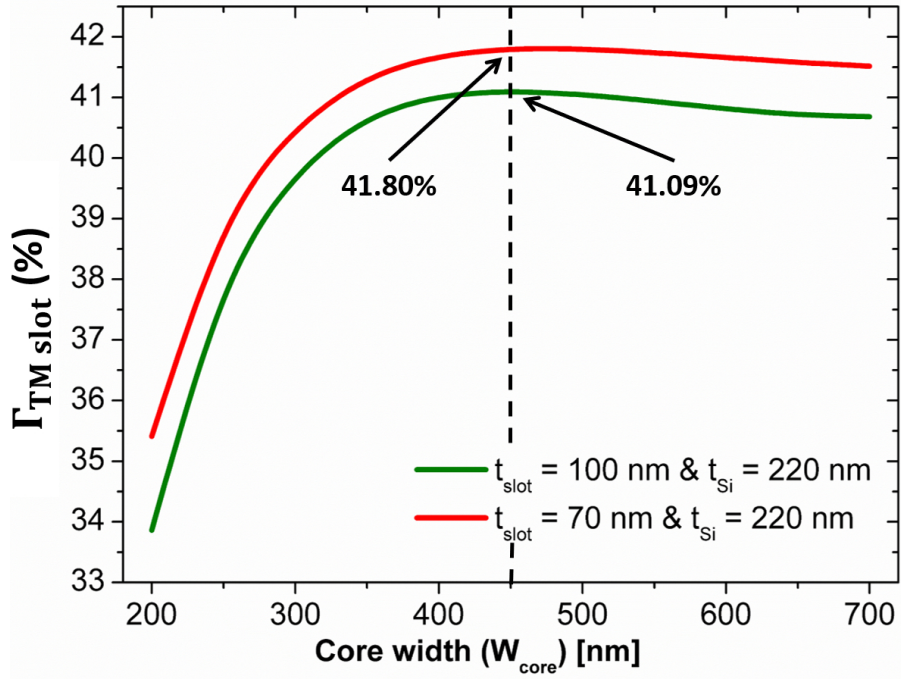


Figure 5.10: The $\Gamma_{TM\ slot}$ variations with HSCPW core width (W_{core}) for two different t_{slot} s. The red and green solid lines depict the same variations for $t_{slot} = 70$ and 100 nm, respectively. An over 41% power confinement is observed for $W_{core} = 450$ nm at $t_{slot} = 70$ and 100 nm.

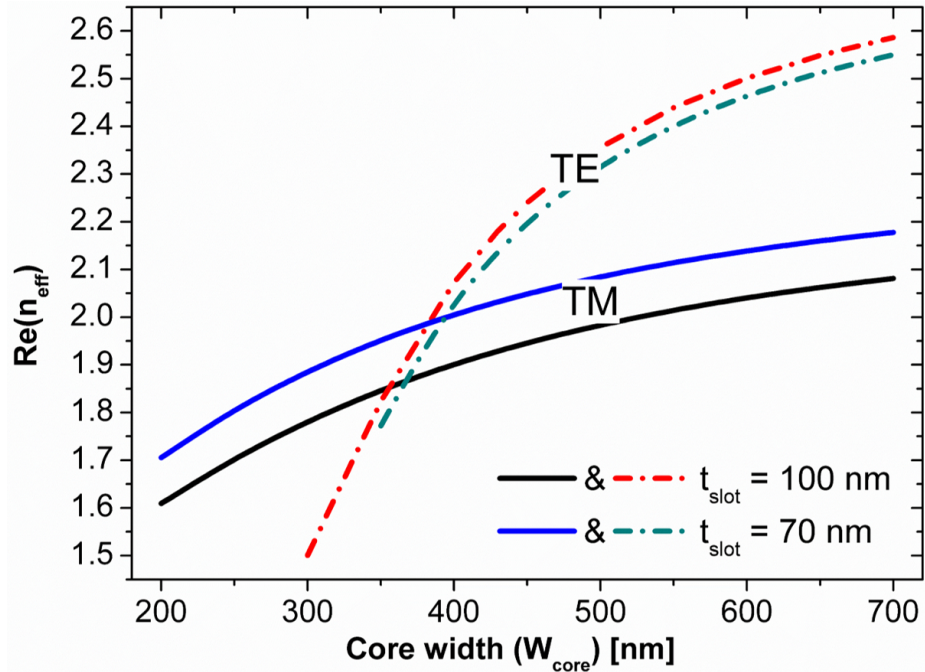


Figure 5.11: Real part of the effective index ($Re(n_{eff})$) variations of the quasi-TE and TM modes against W_{core} for fixed values of $t_{slot} = 70$ and 100 nm. The solid and dashed-dotted lines depict the TM and TE modes, respectively. Other parameters, such as t_{Si} , t_{Ag} were kept fixed at 220 and 100 nm, respectively.

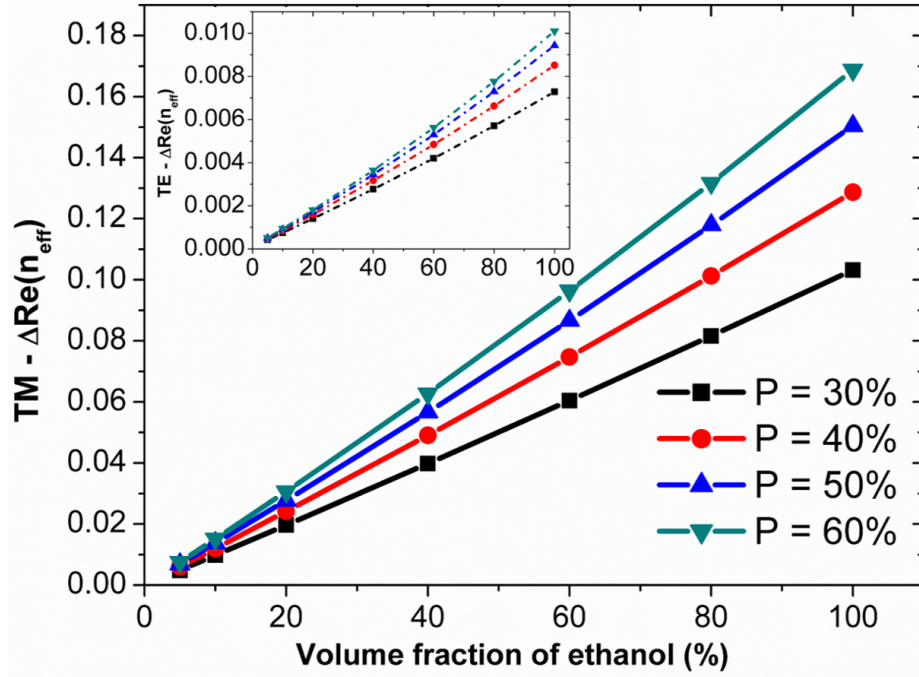


Figure 5.12: Variation of effective index change ($\Delta Re(n_{eff})$) of quasi-TM mode against volume fraction of ethanol into P-ZnO layer. Quasi-TE changes are shown as inset. The black, red, blue and cyan solid and dashed lines in main and inset plot depict the TM and TE modal $\Delta Re(n_{eff})$ changes due to different volume fraction of ethanol into 30%, 40%, 50%, and 60% porous ZnO layers, respectively.

index difference ($\Delta Re(n_{eff})$) of the HSCPW with volume fraction of ethanol for different P-ZnO are depicted in Fig. 5.12. The black, red, blue, and green solid lines indicate the TM- $\Delta Re(n_{eff})$ variation whereas the dashed lines show the same for TE- $\Delta Re(n_{eff})$, respectively. Although, our structure is optimised for $P = 40\%$, but for a comparative study we also considered three other different ZnO porosity, $P = 30\%$, 50% , and 60% . As the volume fraction of ethanol into P-ZnO layer increases both the TM- $\Delta Re(n_{eff})$ and TE- $\Delta Re(n_{eff})$ increase. 5% to 100% absorbance of ethanol vapour makes a 0.31% to 6.62% TM- $\Delta Re(n_{eff})$ change for $P = 40\%$ whereas a much lower value only 0.02% to 0.38% TE- $\Delta Re(n_{eff})$ change is observed for same porosity, shown by red solid and dashed lines in Fig. 5.12 main and inset, respectively. For other ZnO porosity, such as $P = 30\%$, the TM- $\Delta Re(n_{eff})$ shows a change from 0.24% to 5.13% for 5% to 100% ethanol vapour absorption. On the other hand, P-ZnO with porosity $P = 60\%$, a higher TM- $\Delta Re(n_{eff})$ change from 0.41% to 9.24% can be observed for the same volume fraction of ethanol. Thus, higher porosity shows better quasi-TM effective index change. The quasi-TM modal sensitivity of HSCPW with the volume fraction of absorbed ethanol also has been studied.

The black star, red ball, blue triangle, and cyan diamond markers in Figs. 5.13(a) and (b) show the real effective index refractometric sensitivity as

$$S_{Re(TM)} = \frac{\Delta Re(n_{eff})}{\Delta n_{slot}} \quad (5.5)$$

and normalised waveguide attenuation sensitivity as

$$S_{Im(TM)} = \frac{\Delta Im(n_{eff})}{\Delta n_{slot}} \quad (5.6)$$

of the fundamental quasi-TM mode for P-ZnO layer having porosity, $P = 30\%$, 40% , 50% , and 60% , respectively. For each P-ZnO layer, the $S_{Re(TM)}$ and $S_{Im(TM)}$ initially decrease up to $\sim 15\%$ ethanol absorption and then increases as the volume fraction of ethanol increase. Figure 5.13(a) and (b) also indicate that a P-ZnO layer with lower porosity ($P = 30\%$) shows higher $S_{Re(TM)}$ and $S_{Im(TM)}$ (black stars) than a P-ZnO layer with double porosity ($P = 60\%$), shown by cyan diamonds. In the case of waveguide based sensor design, the $S_{Re(TM)}$ is more important than $S_{Im(TM)}$. The result in Fig. 5.13(a) shows a much higher $S_{Re(TM)}$ (≈ 0.71 per RIU) can be achieved with our proposed HSCPW structure. Besides, Fig. 5.13(b) depicts that the normalised attenuation of the HSCPW is less sensitive to slot refractometric changes. This indicates a very small loss change due to different volume fraction of ethanol into P-ZnO. Figure 5.12 demonstrates that a P-ZnO layer with high porosity is good for detection of refractometric changes due to ethanol absorption whereas, in terms of waveguide sensitivity (Figs. 5.13(a) and (b)), a P-ZnO layer with lower porosity shows higher effectiveness. This contradictory result can be explained with the help of Fig. 5.1. Equivalent refractive index variation of 60% P-ZnO layer with volume fraction of ethanol is much steeper than 30% P-ZnO layer. This makes the HSCPW $S_{Re(TM)}$ and $S_{Im(TM)}$ higher for a P-ZnO layer having lower porosity.

5.2.5 Mach-Zehnder Interferometer (MZI) using HSCPW

To determine the effective index change during ethanol vapour sensing process, a Mach-Zehnder interferometer (MZI) could be used as a transducer device. The MZI schematic is shown in Fig. 5.2 where two parallel arms are connected with one input and one output by using well designed 3 dB optical splitters. Our proposed HSCPW is incorporated in MZI arms. One arm is called sensing arm where the integrated HSCPW is passed through

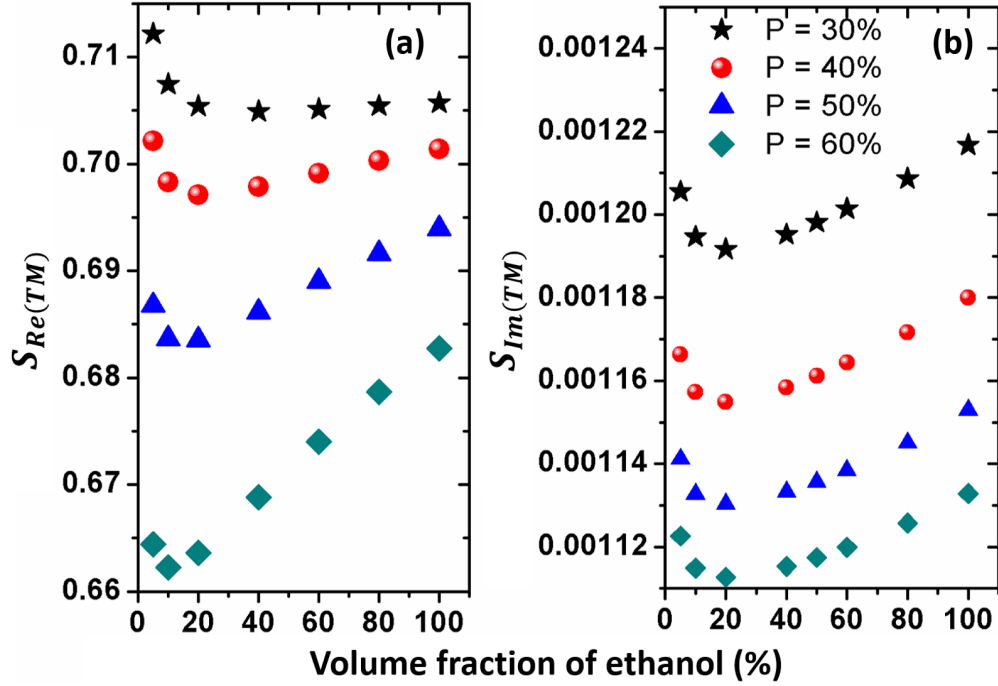


Figure 5.13: (a) and (b) represent the HSCPW quasi-TM real effective index sensitivity ($S_{Re(TM)}$) and normalised attenuation sensitivity ($S_{Im(TM)}$) variations with volume fraction of ethanol into horizontal slotted P-ZnO layer, respectively. The black star, red ball, blue triangle, and cyan diamond markers on both figures illustrate the sensitivity variation with absorbed ethanol vapour into P-ZnO slot having porosity, $P = 30\%$, 40% , 50% , and 60% , respectively.

ethanol vapour filled gas chamber to measure the volume fraction of ethanol and while another CPWG is used in reference arm. The insertion phase difference ($\Delta\phi$) between sensing and reference arm could be measured from the effective index change $\Delta Re(n_{eff})$ due to different volume fraction of ethanol, as

$$\Delta\phi = \frac{2\pi}{\lambda} \cdot \Delta Re(n_{eff}) \cdot L \quad (5.7)$$

Here, L denotes the HSCPW incorporated MZI arm length. A π phase difference between sensing and reference arm makes a destructive interference that results a zero MZI output. The HSCPW incorporated MZI arm lengths are calculated as 7.51, 6.02, 5.15, and 4.59 μm for each type of P-ZnO layer having porosity, $P = 30\%$, 40% , 50% , and 60% , respectively. Thus, higher porosity gives higher Δn_{eff} which results shorter L . Same optimised design parameters ($W_{core} = 450$ nm, $t_{slot} = 100$ nm, $t_{Si} = 220$ nm, and $t_{Ag} = 100$ nm) are used for HSCPW structure. We have also studied the corresponding propagation loss arises due to different HSCPW length and a much low loss value around

0.2 dB has been calculated for each of the HSCPW with their aforementioned lengths. More precisely, with and without ethanol vapour the waveguide loss change in HSCPW incorporated MZI arms are 0.045 dB for $P = 30\%$, 40%, and 50% and 0.047 dB for $P = 60\%$, respectively. Although, HSCPW has high loss compared to conventional dielectric waveguide however, the small footprint of HSCPW provides a much lower propagation loss.

The normalised output power (P_{norm}) of HSCPW incorporated MZI carries the $\Delta Re(n_{eff})$ information in terms of $\Delta\phi$, is given by

$$P_{norm} = \frac{P_{out}}{P_{in}} = \frac{1}{2}e^{-2\alpha L}(1 + \cos\Delta\phi) \quad (5.8)$$

Here α is the attenuation constant of the waveguide. All the MZI powers are normalised with respect to the input power (P_{in}). The normalised output power (P_{norm}) have a cosine variation with phase difference. Often it is assumed that the attenuation (α) is same for both MZI arms with identical waveguides. However, for sensing purpose, the reference and the sensing arm waveguides may have different attenuations, $\alpha_{ref} = \alpha$ and $\alpha_{sen} = \alpha \pm \Delta\alpha_{sen}$, respectively. The sensing waveguide attenuation is modified by a small change $\Delta\alpha_{sen}$ due to different absorption levels of ethanol vapour. It can be shown that, this modifies the normalised MZI output power as [Berini, 2008]

$$P_{norm} = \frac{1}{2}e^{-2\alpha L}e^{-\Delta\alpha_{sen}L}\cosh(\Delta\alpha_{sen}L)(1 + V\cos\Delta\phi) \quad (5.9)$$

Here, the V is identified as interferometric fringe contrast or visibility parameter, which depends on $\Delta\alpha_{sen}$ as,

$$V = \frac{1}{\cosh(\Delta\alpha_{sen}L)} \quad (5.10)$$

Additionally, a section of the Eq. 5.9 could be termed as power fraction

$$PF = e^{-\Delta\alpha_{sen}L}\cosh(\Delta\alpha_{sen}L) \quad (5.11)$$

which indicates the increase or decrease in power compared to the reference arm waveguide. P_{norm} is only measurable parameter that changes with the phase difference in

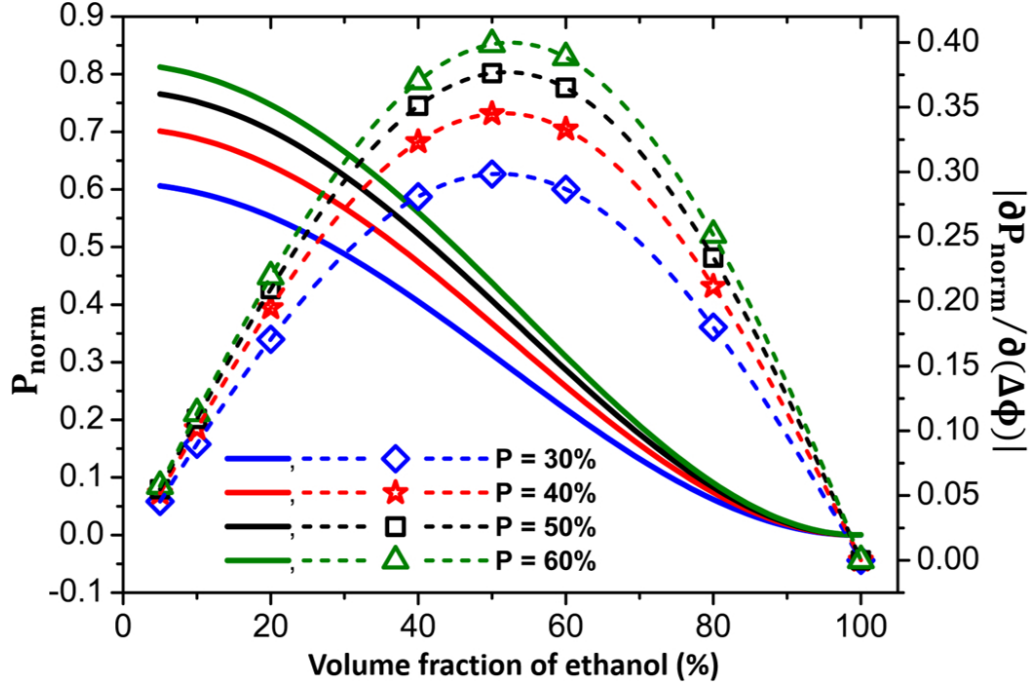


Figure 5.14: Normalised output power (P_{norm}) and phase sensitivity $|(\partial P_{norm})/(\partial(\Delta\phi))|$ variations against volume fraction of ethanol into P-ZnO. Blue diamond, red star, black square, and green triangle markers with dashed lines denote sinusoidal $|(\partial P_{norm})/(\partial(\Delta\phi))|$ variations for different porosity, $P = 30\%$, 40% , 50% , and 60% , respectively. The solid blue, red, black, and green lines indicate cosine natured P_{norm} variations for all four P-ZnO layers.

between sensing and reference arms. Thus, a phase sensitivity of the device is an important parameter which can be defined by

$$\frac{\partial P_{norm}}{\partial(\Delta\phi)} = -\frac{1}{2} \cdot e^{-(2\alpha + \Delta\alpha_{sen})L} \cdot \cosh(\Delta\alpha_{sen}L) \cdot V \cdot \sin(\Delta\phi) \quad (5.12)$$

The equation shows that the maximum phase sensitivity occurs for $\Delta\phi = \pi/2$. Figure 5.14 shows the normalised power (P_{norm}) and absolute value of phase sensitivity $|(\partial P_{norm})/(\partial(\Delta\phi))|$ variations of proposed HSCPW incorporated MZI against ethanol volume fraction for different P-ZnO. Different markers with dashed and solid lines are used to indicate the $|(\partial P_{norm})/(\partial(\Delta\phi))|$ and P_{norm} variations. Blue, red, black, and green solid lines indicate cosine variations of P_{norm} with volume fraction of ethanol into P-ZnO of porosity, $P = 30\%$, 40% , 50% , and 60% , respectively. This figure depicts that 100% ethanol vapour absorption in sensing arm makes a π phase difference with zero MZI output and a 5% (considered as minimum) volume fraction of ethanol imposes a minimum phase difference with maximum 60%, 70%, 76%, and 81% light output for 30%, 40%,

50%, and 60% P-ZnO, respectively. Higher porosity provides better light output. The $\Delta\phi$ shows an almost linear relationship with ethanol volume fraction. Blue diamond, red star, black square, and green triangles with dashed lines depicts a sinusoidal variation of $|(\partial P_{norm})/(\partial(\Delta\phi))|$ for four different porosity of the P-ZnO layers. Lower porosity ($P = 30\%$) shows lower phase sensitivity, shown by the blue dashed line with diamond marker, whereas, the green dashed line with triangular marker shows a much better phase sensitivity for porosity, $P = 60\%$. Considering device sensitivity, all ZnO layers with different porosity, $P = 30\%$, 40% , 50% , and 60% exhibit maximum phase sensitivities of 0.30, 0.34, 0.38, and 0.40 when 51.57%, 52.05%, 52.59%, and 53.16% of the ZnO pores are filled by the condensed ethanol, respectively when an exact $\pi/2$ phase difference is obtained in between sensing and reference arms. The output power intensity of the symmetric MZI design varies depending on the waveguide effective index change occurring due to ethanol vapour absorption. In this work, instead of direct concentration measurement (in terms of ppm) of ethanol vapour we emphasised on the detection of refractive index change due to absorption of and condensation of ethanol vapour into P-ZnO. Therefore, the presence and the quantity of ethanol vapour is determined in terms of volume fraction of absorbed ethanol into P-ZnO layer in the HSCPW slot section. A MZI with lossless identical waveguide exhibits almost same phase sensitivities for all P-ZnO layers. In this HSCPW incorporated MZI, the balance between both arms break down due to different attenuations ($\alpha_{ref} \neq \alpha_{sen}$). To make an error-free MZI design, the device attenuation should be controlled in a way such that it does not reduce the interferometer balance. In our study, for all volume fractions of ethanol into 30%, 40%, 50%, and 60% P-ZnO the fringe contrast (F) was ~ 0.99 and the power fraction (PF) was ~ 0.96 . This ($V \simeq PF \simeq 1$) indicates that in this case the extra attenuation change in the sensing waveguide is very small to cause any noticeable effect in the HSCPW incorporated MZI performance.

5.2.6 Fabrication Tolerance

Study on fabrication tolerance is important to obtain a robust sensor design. The horizontal slot hybrid plasmonic waveguide (HSHPW) is optimised for maximum slot confinement of the fundamental quasi-TM mode. The slot power confinement ($\Gamma_{TM\ slot}$) has a strong correlation with the waveguide and complete device sensitivity. The maximum $\Gamma_{TM\ slot}$

is obtained as 41.79% for $t_{slot} = 70$ nm and $W_{core} = 450$ nm. But for an easy fabrication and to accommodate a large number of ZnO pores into slot section, the t_{slot} is considered as 100 nm which results in a 41.09% slot confinement. Therefore, a 100 nm slot thickness compromises only 1.68% power decrement from the maximum optimised value. Even >40% slot confinement can be obtained for $t_{slot} = 110$ nm. During etching of the waveguide it is not always possible to maintain the the exact optimised value of $W_{core} = 450$ nm. It can be observed in Fig. 5.10 that a $\pm 5\%$ change in W_{core} still maintain the $\Gamma_{TM\ slot} > 40.5\%$. The quasi-TM waveguide refractometric sensitivity defines as the ratio of real effective index change of the waveguide to slot refractive index change due to ethanol vapour absorption. During fabrication processes, the waveguide design parameters such as W_{core} and t_{slot} may show a maximum $\pm 5\%$ deviation from the optimised values. Figures 5.6 and 5.11 show much slower quasi-TM mode effective index variation with those design parameters. Therefore, $\pm 5\%$ fabrication imperfection could results in a very small $\sim 1.2\%$ change in waveguide mode effective index. As a result, the waveguide refractometric sensitivity and MZI phase sensitivity also show very small, negligible deviations as they strongly depends on the waveguide quasi-TM mode effective index.

5.3 Detection of DNA Hybridisation by SOI Based HSCPW

Besides the matured optical fibre based sensors, recent advanced CMOS technology opens up the possibilities of nano-scaled waveguide based bio-sensors [Kress-Rogers, 1996] suitable for environmental monitoring, harmful heavy metal ions and micro-organisms sensing in drinking water [Haron and Ray, 2006], quality control of food [Mello and Kubota, 2002] and medical diagnoses [Heinemann and Schmelzeisen-Redeker, 1998]. Commonly, bio-sensors could be classified into two categories depending on their detection approaches, such as labelled and label-free bio-sensors. Fluorescence based sensors are highly versatile and sensitive even for detection of single molecule where labelling of target analyte by fluorescence-tag requires covalent bonding between bio-molecules and fluorophore or simply fluors. The excited photon is absorbed by an electron of fluorescent particle that raises the energy level of the electron to an excited state. During excitation, a short amount of energy may transferred to the nearest molecules and some may be

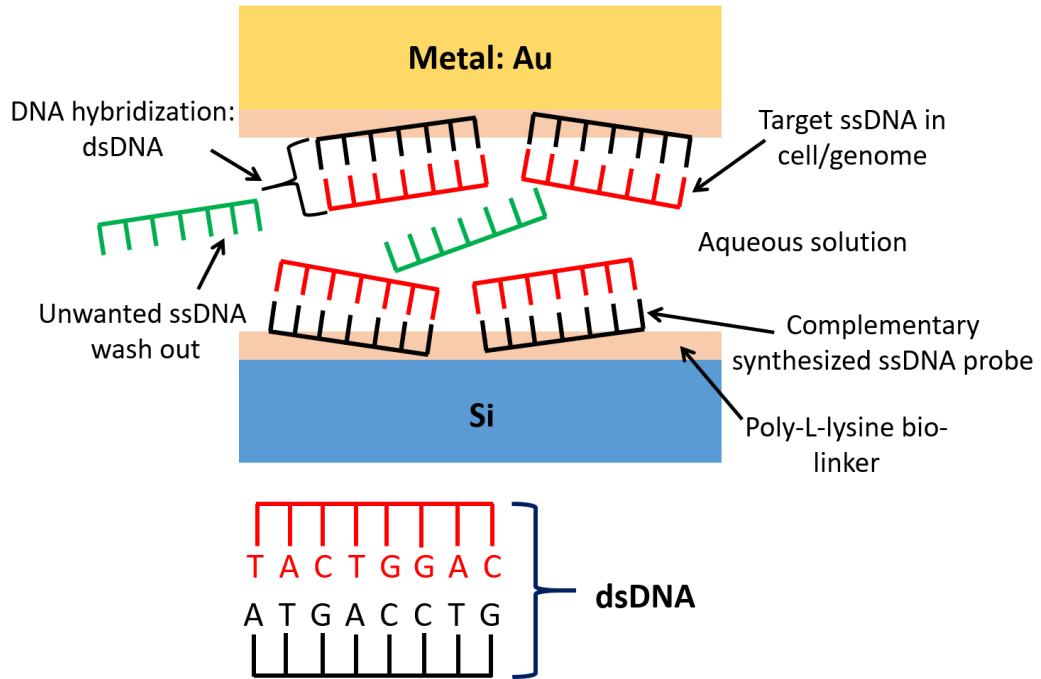


Figure 5.15: DNA hybridisation process in the horizontal slot region. A poly-L-lysine bio-linker layer is used to attach the target ssDNA.

dissipated by the molecular collisions. The remaining energy emits as a photon to bring the electron back to the ground state. The excited electron carries lower energy compared to the excitation photon thus the emitted fluorescence has a longer wavelength i.e. different light colour. Although it is a cyclic process, but in case of bio-sensors the ability of fluors to fluoresce may irreversibly damage due to accumulation of chemical conversion from the excited electrons, is known as photo-bleaching [Cox and Singer, 2004]. Besides, the label-free bio-sensors does not require to tag the target analyte for detection. Utilizing a cleverly design integrated optical waveguides one can easily detect the change in optical properties of the natural bio-molecules without any external chemical labelling.

5.3.1 DNA Hybridisation

It is a process where a single stranded DNA (ssDNA) is subsequently combined with another complementary natured ssDNA and reform a double stranded DNA (dsDNA). A small example of the DNA hybridisation process is shown in Fig. 5.15 where a single stranded DNA (ssDNA) is subsequently combined with another complementary ssDNA and reform a double stranded DNA (dsDNA). The DNA hybridisation is one of the

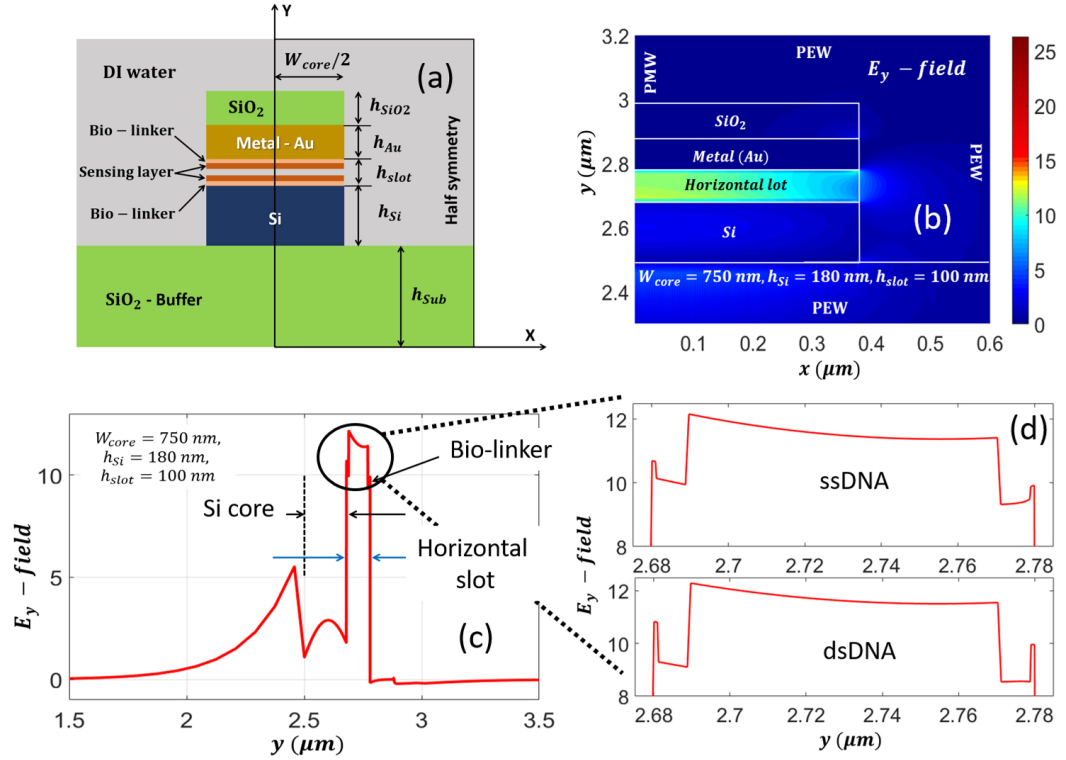


Figure 5.16: (a) Schematic cross-section of the SOI based HSCPW to detect DNA hybridisation. (b) Quasi-TM E_y field profile of half symmetric HSCPW, (c) depicts the variation of the E_y field along the y-axis symmetry line and (d) denotes the light confinement variations due to presence of ssDNA and dsDNA.

important method to determine the genetic similarity or dissimilarity between two organisms, which has a great application in the field of microbiology, zoology, medicine and medical diagnoses. To immobilise the selective DNA on lower Si and top metal (Au) surfaces a 1 nm bio-linker layer, such as a poly-L-lysine layer of refractive index 1.42 is used to increase the selectivity. In formation of dsDNA, the base-pairing takes place in between complimentary natured adenine (A) and thymine (T), and guanine (G) and cytosine (C). Adenine and thymine are paired by two hydrogen bonds, and guanine and cytosine are connected with three hydrogen bonds. The refractive of the ssDNA is 1.456 [Elhadj *et al.*, 2004; Dar *et al.*, 2012; Viphavakit *et al.*, 2015] and when it forms the double helix dsDNA the refractive index becomes 1.530 [Elhadj *et al.*, 2004; Dar *et al.*, 2012; Viphavakit *et al.*, 2015].

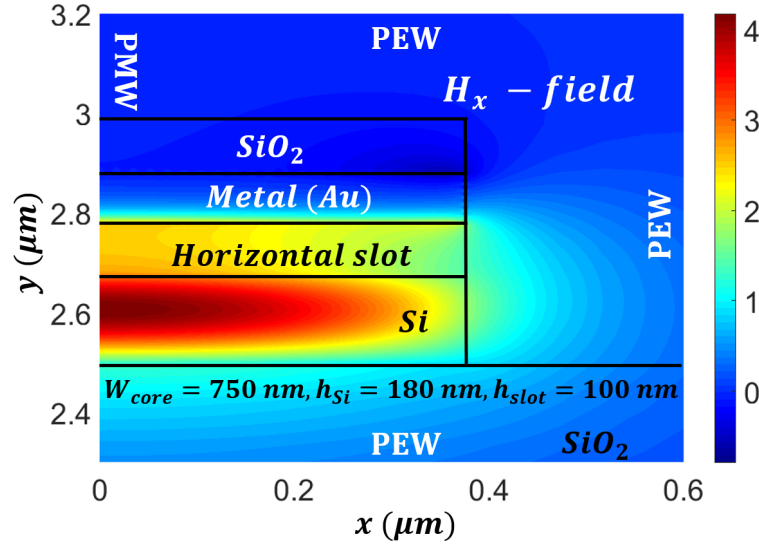


Figure 5.17: shows the H_x field of the quasi-TM mode. One-fold waveguide symmetry is used for FV-FEM simulation.

5.3.2 Horizontal Slot Composite Plasmonic Waveguide (HSCPW) and its Mode Analyses

A silicon-on-insulator (SOI) based horizontal slot composite plasmonic waveguide (HSCPW) structure, shown in Fig. 5.16(a), is modelled and comprehensively studied to detect the DNA hybridisation process. In this HSCPW, a low index horizontal slot is formed in between metal (Au) and high index dielectric Si medium. The thin gold layer is deposited on the lower surface of the hanging SiO_2 slab. This SiO_2 slab has no significant effect in the light guidance by the low-index horizontal slot waveguide section. The thin metallic layer generates a hybrid surface mode, called surface plasmon (SP), which is a combination of free electrons in the metallic surface and the exciting electromagnetic waves. The advantage of this waveguide is a true nano-scale light confinement into the slot. The effectiveness of a HSCPW has been investigated as a bio-sensor mainly for the detection of DNA hybridisation.

An in-house divergence modified full-vectorial finite element code (Section 3.3) is used for design and performance analysis of the proposed HSCPW. The \vec{H} -field within each element is calculated and then interrelation of the field distributions in other elements have been followed to make the field continuous across the inter-element boundaries. The available half symmetry of the structure is exploited to achieve higher accuracy. All the

boundaries in computational domain are perfect electric walls (PEW) except the symmetry boundary line, where a perfect magnetic wall (PMW) is imposed. Total 720,000 triangular elements are used for accurate simulations. This waveguide supports both quasi-TE and TM modes and both the modes are guided but in different waveguiding layers. The dominant quasi-TM mode E_y field profile and its variation along the symmetry line (y-axis) are shown in Figs. 5.16(b) and (c), respectively. The E_y field profile shows a maximum confinement in the slot which is used as the sensing region. The sharp changes at the peak of the slot confinement shown in Fig. 5.16(d) illustrates the difference in optical field confinement during DNA hybridisation. While the ssDNA converts into dsDNA the corresponding refractive index changes from 1.456 to 1.530. The line plot in Fig. 5.16(d) shows a comparative lesser light confinement in the nano-dimensioned high index dsDNA compared to the low index ssDNA. This change in light guiding property is detectable by the effective index difference of the HSCPW during DNA hybridisation. Figure 5.17 shows the H_x field distribution of the dominant quasi-TM mode of the waveguide. Although, a large portion of the light is guided by the high index Si core however, a sufficient fraction of light is distributed in the slot which is also helpful for the detection process.

5.3.3 Optimisation and Performance Analysis of HSCPW Bio-sensor

Schematic cross-sectional waveguide structure is shown in Fig. 5.16(a), where a nano-fluidic slot is formed in between fixed 100 nm gold (Au) layer and Si strip ($n = 3.4757$). A 100 nm top SiO_2 ($n = 1.444$) layer is used to deposit Au metal layer. During hybridisation process the thickness of the DNA layer is considered as 8 nm. Cladding and rest of the slot region is filled with DI water based stock solution ($n = 1.3154$) at the operating wavelength of 1550 nm. Au refractive indices have been taken from [Johnson and Christy, 1972]. For sensing mechanism, quasi-TM is more effective as this is guided by the low index slot region. Figure 5.18 shows the variation of power confinement ($\Gamma_{Bio-layer}$) in the nanometre thick DNA layer with Si core height (h_{Si}) for three different waveguide core widths such as, $W_{core} = 350, 550$, and 750 nm. Other waveguide parameters such as thickness of top SiO_2 layer (h_{SiO_2}), Au layer (h_{Au}), and slot height (h_{slot}) are kept fixed at 100 nm. The $\Gamma_{Bio-layer}$ variations with ssDNA and dsDNA are shown by the dashed-dotted lines and solid lines, respectively. It can be seen in Fig. 5.18 that the

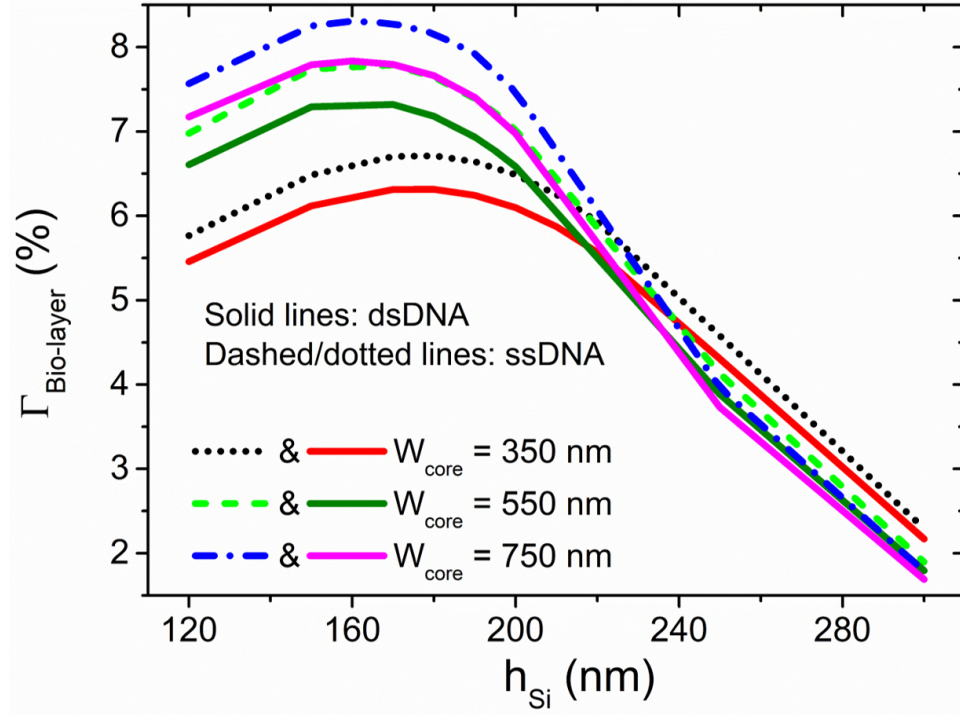


Figure 5.18: Variation of the power confinement in the DNA bio-layer ($\Gamma_{Bio-layer}$) with Si core height (h_{Si}) for three different waveguide core widths, $W_{core} = 350, 550,$ and 750 nm. Other parameters such as thickness of top SiO_2 layer h_{SiO_2} , Au layer (h_{Au}), and slot height (h_{slot}) are kept fixed at 100 nm. The variation $\Gamma_{Bio-layer}$ for ssDNA and dsDNA are shown by the dashed-dotted and solid lines, respectively.

$\Gamma_{Bio-layer}$ increases, reaches its maximum value and then decreases with an incremental variation of h_{Si} . A considerably high 8.31% and 7.83% light can be confined in the ssDNA and dsDNA layer, respectively for the HSCPW parameters of $h_{Si} = 160$ nm and $W_{core} = 750$ nm. For other two W_{core} s (350 and 550 nm), the corresponding optimised h_{Si} that shows maximum $\Gamma_{Bio-layer}$ are 210 and 190 nm.

Figure 5.19 shows the variation of $\Gamma_{Bio-layer}$ against slot height h_{slot} for previously optimised W_{core} and h_{Si} values. As the h_{slot} increases from 40 nm to 120 nm, the $\Gamma_{Bio-layer}$ decreases gradually. For lower h_{slot} , slot confinement may reduce. But power density in slot increases as slot area reduces. So for surface sensing power density is more important than just total slot power. As a result, $\Gamma_{Bio-layer}$ increases. Thus, a high light confinement in the sensing layer is obtained for lower values of h_{slot} . For an effective sensor design, high slot confinement is always desirable. Although, a smaller h_{slot} shows greater confinement in the bio-layer but it is difficult to fabricate a very small h_{slot} channel. Thus, $h_{slot} = 80$ to 100 nm could be a trade-off.

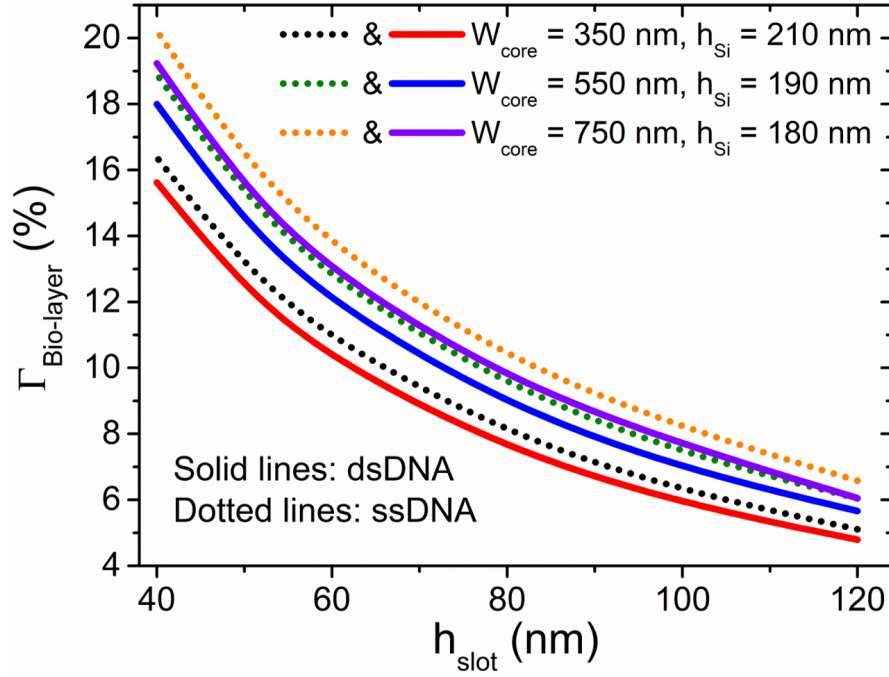


Figure 5.19: Variation of the power confinement in the DNA bio-layer ($\Gamma_{Bio-layer}$) with slot height (h_{slot}) for three different waveguide core width and height combinations, such as $W_{core} = 350$ and $h_{Si} = 210$ nm, $W_{core} = 550$ and $h_{Si} = 190$ nm, and $W_{core} = 750$ nm and $h_{Si} = 180$ nm. Other parameters such as h_{SiO_2} and h_{Au} are kept fixed at 100 nm. The variation $\Gamma_{Bio-layer}$ for ssDNA and dsDNA are shown by the dashed-dotted and solid lines, respectively.

The real effective index ($Re(n_{eff})$) and effective index difference (Δn_{eff}) variation of the quasi-TM mode due to DNA hybridisation with silicon core height (h_{Si}) are shown in Fig. 5.20. A correlation also has been noticed in Δn_{eff} variation and power confinement in the bio-layers. It can be observed that Δn_{eff} increases first, then reaches at its maximum and finally decreases with increment of h_{Si} for a fixed W_{core} value. The red, green, and blue lines depict the Δn_{eff} variation against h_{Si} for $W_{core} = 350, 550$, and 750 nm, respectively. The maximum values of Δn_{eff} have been obtained for different combinations of W_{core} and h_{Si} . For $W_{core} = 350, 550$, and 750 nm the maximum Δn_{eff} have the values of 0.00612, 0.00679, and 0.00712 for $h_{Si} = 210, 190$, and 180 nm, respectively. Thus, $W_{core} = 750$ nm and $h_{Si} = 180$ nm show a higher Δn_{eff} value. Figure 5.21 shows the propagation distance variation with h_{Si} . Lower W_{core} shows higher modal loss. With the increment of h_{Si} , light is mostly guided by the high index Si core thus have lower modal loss and higher propagation length (L_p). The variations of ssDNA are shown in dashed or dotted lines whereas for dsDNA, the solid lines are used. Both the graphs are showing the

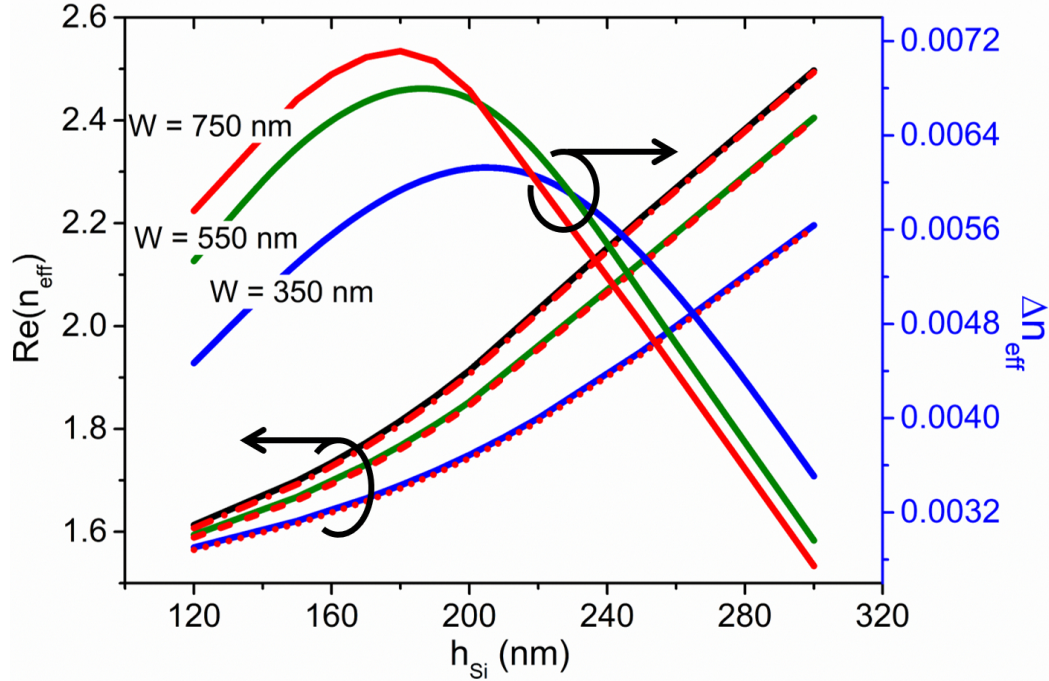


Figure 5.20: Variation of real part of the effective index ($Re(n_{eff})$) of the sensitive quasi-TM mode and effective index change (Δn_{eff}) of the same mode due to DNA hybridisation against Si core height (h_{Si}) for three fixed core widths, $W_{core} = 350, 550,$ and 750 nm. A 100 nm h_{slot} is considered. The variation of $Re(n_{eff})$ for ssDNA and dsDNA are shown by dashed-dotted and solid lines, respectively.

importance of h_{Si} , as it has a significant impact on the formation of the hybrid supermode (Fig. 5.16(b) and 5.17) that occurs due to combination of a surface plasmon mode from Au-dielectric interface and a dielectric waveguide mode.

Figure 5.22 depicts variation of waveguide effective index change ($\Delta Re(n_{eff})$) with the slot height (h_{slot}) for three optimised combinations of W_{core} and h_{Si} . The $\Delta Re(n_{eff})$ increases with the reduction of h_{slot} . Power confinement into bio-layer (Fig. 5.19) also follows the same trend as $\Delta Re(n_{eff})$. Recent state-of-the-art fabrication technology allows one to fabricate a few tens of nanometer dimension nano-fluidic channel [Liang *et al.*, 2007] which gives us a freedom to go below 100 nm h_{slot} to increase the device sensitivity. However, in practical it may be difficult to accommodate the bio-layers in a very small slot height (h_{slot}). Therefore, further waveguide sensitivity has been investigated for $h_{slot} = 80$ and 100 nm. Naturally, the bio-layer grows on top of poly-L-lysine linker and they stick together with the help of covalent bond. It is also very hard to maintain the bio-layer thickness. Therefore, a rigorous study is needed on waveguide surface sensitivity for device characterisations. HSCPW surface sensitivity has been investigated

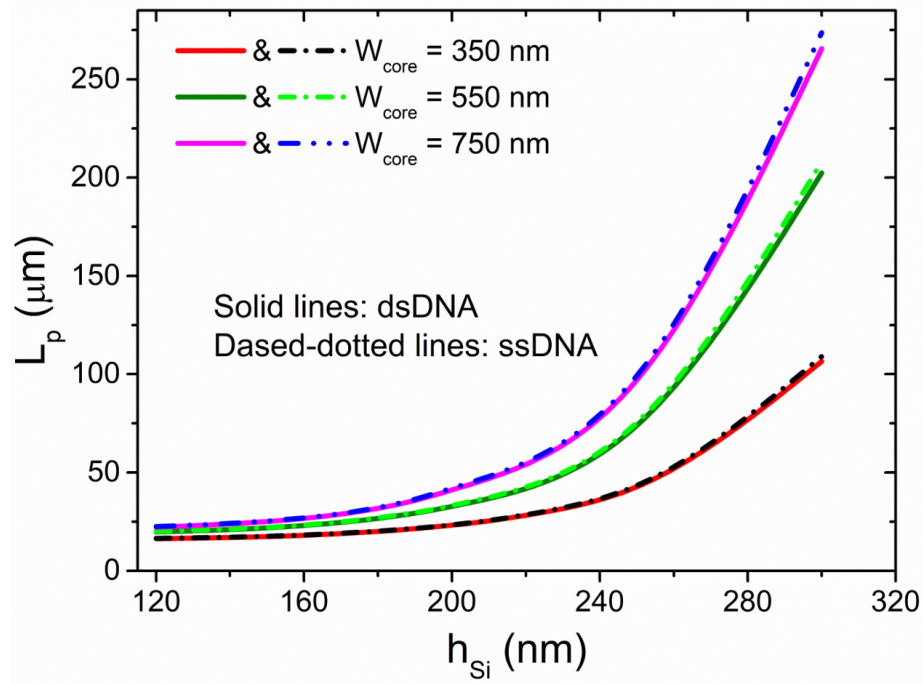


Figure 5.21: Variation of real part of the effective index ($Re(n_{eff})$) of the sensitive quasi-TM mode and effective index change (Δn_{eff}) of the same mode due to DNA hybridisation against Si core height (h_{Si}) for three fixed core widths, $W_{core} = 350, 550$, and 750 nm. A 100 nm h_{slot} is considered. The variation of $Re(n_{eff})$ for ssDNA and dsDNA are shown by dashed-dotted and solid lines, respectively.

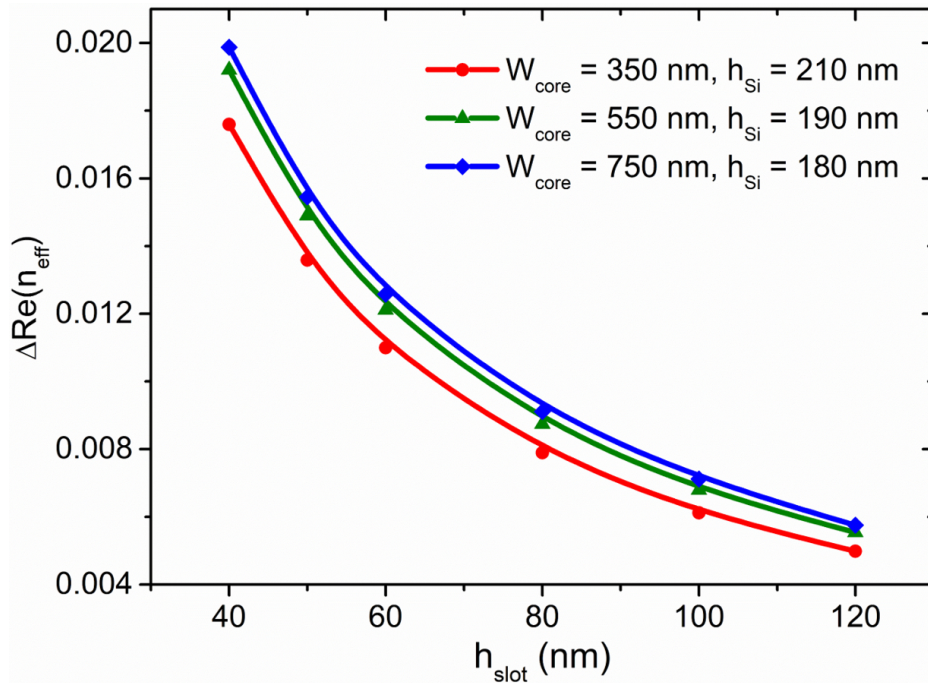


Figure 5.22: Variation of quasi-TM effective index change ($\Delta Re(n_{eff})$) against horizontal slot height (h_{slot}) for optimised W_{core} and h_{Si} combinations. The red, green, and blue solid lines indicate the $\Delta Re(n_{eff})$ variation for $W_{core} = 350, 550$, and 750 , and $h_{Si} = 210, 190$, and 180 nm, respectively.

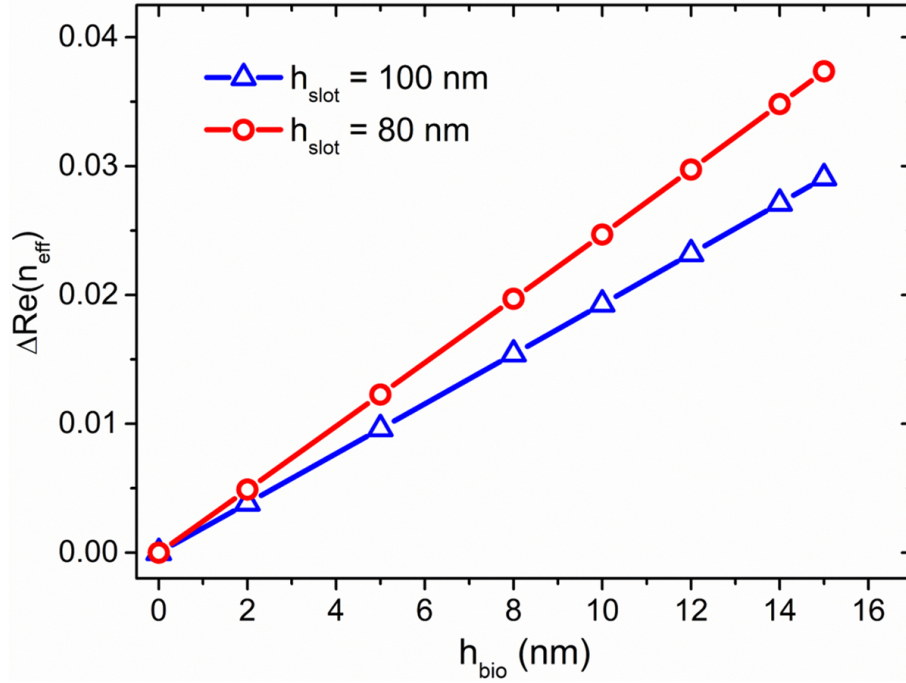


Figure 5.23: Variation of quasi-TM effective index change ($\Delta Re(n_{eff})$) with bio-layer thickness (h_{bio}).

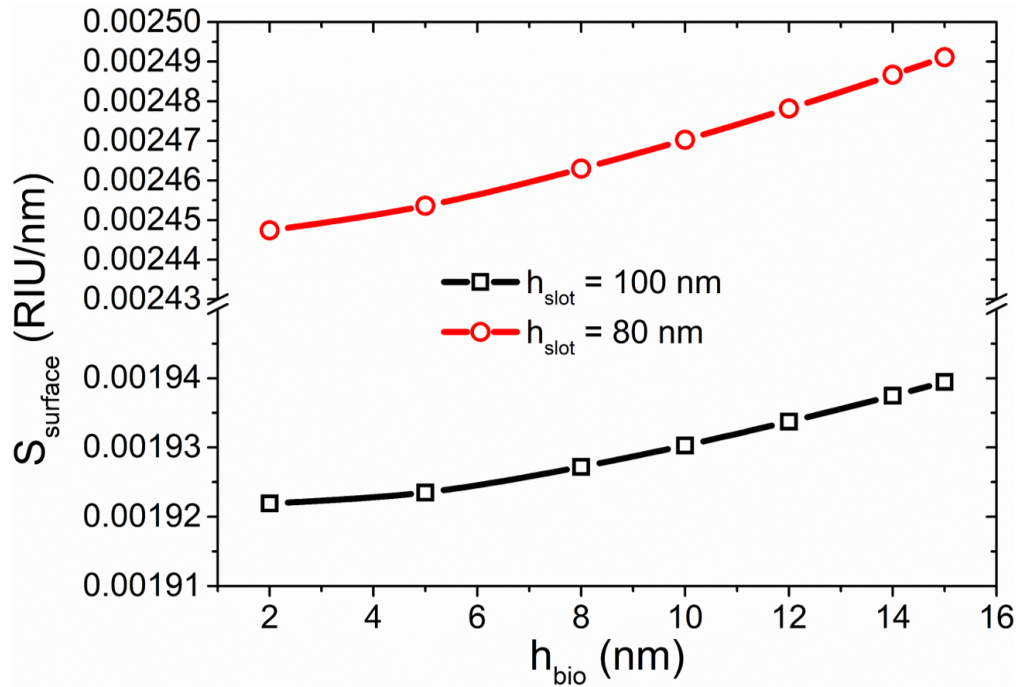


Figure 5.24: Variation of waveguide surface sensitivity ($S_{surface}$) with bio-layer thickness (h_{bio}) for 80 and 100 nm slot heights (h_{slot}).

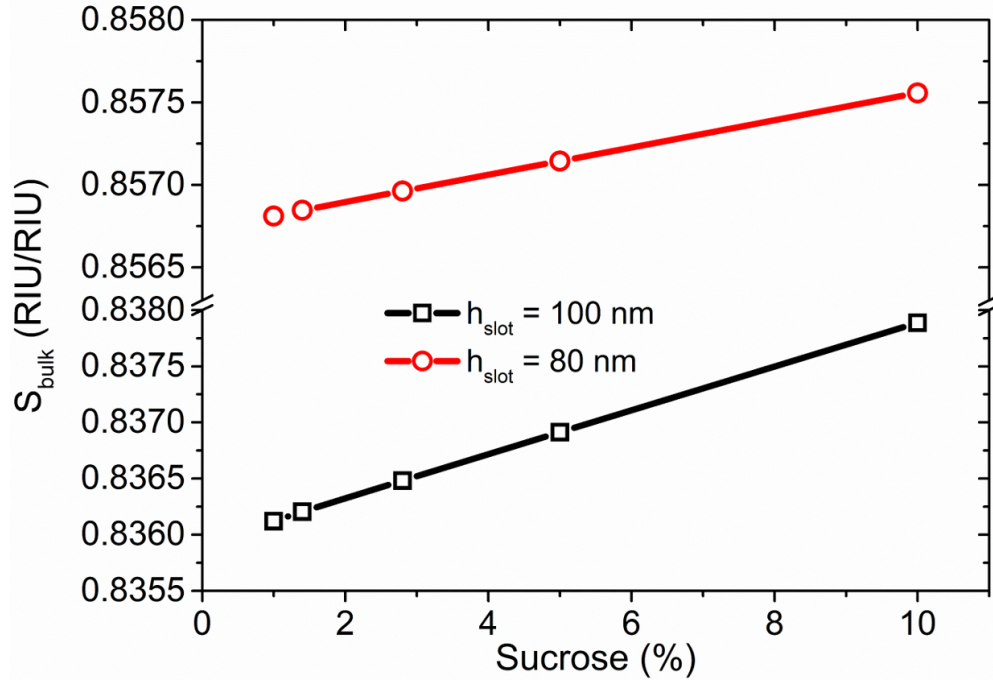


Figure 5.25: Variation of waveguide bulk sensitivity (S_{bulk}) against sucrose solution concentrations for two different slot heights, $h_{slot} = 80$ and 100 nm.

with the variation of h_{bio} for optimised waveguide design ($W_{core} = 750$ nm, $h_{Si} = 180$ nm, $h_{Au} = h_{SiO_2} = 100$ nm). Two different slot heights ($h_{slot} = 80$ and 100 nm) have been considered. An 80 nm slot confines more light than a 100 nm slot thus expects to show high effective index change. Figure 5.23 shows the $\Delta Re(n_{eff})$ variation with h_{bio} for $h_{slot} = 80$ and 100 nm, shown by the red and blue solid lines, respectively. HSCPW surface sensitivity ($S_{surface} = \Delta Re(n_{eff})/h_{bio}$) has been investigated and plotted in Fig. 5.24. The waveguide sensitivity increases with the bio-layer thickness (h_{bio}) as the more light interacts with the bio-molecules attached to the slot regions. The $S_{surface}$ shows higher values for $h_{slot} = 80$ nm compared to the $h_{slot} = 100$ nm, shown by the red and black solid lines, respectively. The $S_{surface}$ values for $h_{slot} = 80$ and 100 nm are around 0.0025 and 0.0019 RIU/nm, respectively. Besides, the effectiveness of HSCPW for bulk sensing also have been studied and the obtained results are shown in Fig. 5.25. Here, different percentages of sucrose solution are considered to cover the top clad and the nano-dimensioned slot region. HSCPW with two different slot heights, $h_{slot} = 80$ and 100 nm have been used and the corresponding responses have been indicated by red and black solid lines, respectively. The S_{bulk} increases linearly with the concentration of sucrose

solution. Similar to surface sensing, the HSCPW with $h_{slot} = 80$ nm shows greater bulk sensitivity (S_{bulk}) than that with $h_{slot} = 100$ nm. The S_{bulk} values for $h_{slot} = 80$ and 100 nm are around 0.83 and 0.85 RIU/RIU, respectively.

5.4 Summary

In summary, a composite plasmonic waveguide (HSCPW) is investigated where a porous ZnO layer is used as a horizontal slot for ethanol vapour sensing. A \vec{H} -field based FV-FEM is used for analyses. These simulations reveal that the HSCPW can guide a hybrid plasmonic supermode, comprises of SPPs and dielectric mode, over a sufficiently long distance. A nano-scale ($450 \text{ nm} \times 100 \text{ nm}$) field confinement is obtained and then exploited to detect the refractometric changes due to ethanol vapour absorption and condensation. All the design parameters are optimised for the best possible result. The proposed HSCPW shows a high waveguide sensitivity 0.7 per RIU for 40% porous ZnO layer as horizontal slot. This HSCPW is used in both arms of a compact Mach-Zehnder interferometer (MZI) to measure the refractive index change. The MZI output power with different volume fraction of absorbed ethanol into P-ZnO for various porosity also have been analysed and reported. Different phase sensitivities (0.30, 0.34, 0.38, and 0.40) for the proposed sensors are observed for 51.57%, 52.05%, 52.59%, and 53.16% ethanol condensation into horizontally slotted ZnO layer with porosity, $P = 30\%$, 40% , 50% , and 60% , respectively. Thus, numerically simulated investigation successfully serves a demonstration of label free ethanol vapour sensor using a coupled SPP and dielectric field confined in a low index nano-scale horizontal slot. In practice, due to simplicity this compact HSCPW can be easily achieved with modern fabrication technologies and advanced surface chemistry. Based on the reported results, the present work shows a potential application of this composite plasmonic waveguide in environmental gas and vapour sensing mechanism.

Through a rigorous numerical study, a novel design of horizontal slotted composite plasmonic waveguide (HSCPW) is proposed and optimised to perform as a bio-sensing device. When a ssDNA attaches with the poly-L-lysine linker layer and a complementary ssDNA combines with another probe ssDNA to reform a dsDNA, a noticeable change in effective index and power confinement into bio-layer have been observed. Each step of

DNA hybridisation was successfully detected with the help of hybrid surface plasmonic supermode confined into nanometer wide horizontal slot region. Our proposed HSCPW performs better compared to pure dielectric based vertical and horizontal slot waveguide. The reported results in this work are useful for the design of on-chip integrated MZI and coupler based bio-sensors. An optimisation of waveguide design parameters has been reported for the operating wavelength of 1550 nm. The FEM modelling of a bio-sensor HSCPW design also provides a valuable intuition which may be useful for other waveguide based sensing applications.

METAL STRIP LOADED HYBRID PLASMONIC WAVEGUIDE AS A TEMPERATURE AND LIQUID CONCENTRATION SENSOR

6.1 Introduction

On-chip integrated photonic and plasmonic sensors have great potential in applications for biochemical industries, real-time rapid medical diagnosis, early-stage detection of critical diseases, DNA characterisations, environmental monitoring, food and water quality screening, pharmaceutical industries, particle tracing and tweezing etc. [Passaro, La Notte, Troia, Passaquindici, De Leonardis and Giannoccaro, 2012; Passaro, Tullio, Troia, Notte, Giannoccaro and Leonardis, 2012; Homola *et al.*, 1999; Homola, 2003]. Several electronic and mechanical sensors have already been commercialised to achieve these functionalities but with a lower detection accuracy, bulky design, and high-power consumption. In recent years, integrated optical technology based sensors are gaining interests as attractive alternative approaches to the electronic technology due to its immunity from electromagnetic interference (EMI), compact portable lab-on-a-chip scale design for low-cost mass production, suitable for real-time monitoring, low power requirements, remote operation, fast response and above all, a much higher sensitivity for accurate detection of targets even at the atomic level. Monitoring and control of most fundamental parameters of organic, inorganic, and hazardous chemical

solution such as temperature and concentration of analyte represent a major concern to the biochemical industries and health organisations for improvement of their manufacturing process and protection of public health from hazardous accidents. Instead of the commonly used thermocouple and resistance thermometer, optical temperature sensors are attracting substantial interests. Refractometric based photonic sensors inscribed with guiding materials of large thermo-optic coefficients (TOC) are promising in many biochemical applications, such as DNA, RNA, and protein precipitation from aqueous solution [Tan and Yiap, 2009; Chen *et al.*, 2010] and temperature sensitive biochemical characterisations where distinct chemical behaviours depend on a small fractional change in temperature [Chen *et al.*, 1994].

In recent years, various optical fibre based device configurations, e.g. fibres with Bragg gratings [Hirayama and Sano, 2000; Rao *et al.*, 1997], in-line interferometer [Sun *et al.*, 2012; Qiu *et al.*, 2012], graphene assisted microfibre interferometer [Sun *et al.*, 2016], surface plasmon resonance (SPR) supported fibre sensors [Zhu *et al.*, 2017; Weng *et al.*, 2017], modal interferometers in microstructured optical fibres (MOFs) [Qiu *et al.*, 2012; Deng *et al.*, 2017] have been developed and investigated for temperature monitoring. However, on-chip integrated optical temperature sensors based on ring resonators [Kim *et al.*, 2010; Klimov, Berger and Ahmed, 2015], Fabry-Perrot cavities [Klimov, Purdy and Ahmed, 2015], Bragg reflectors [Chang and Solgaard, 2013; Klimov, Mittal, Berger and Ahmed, 2015], and interferometers [Irace and Breglio, 2003; Tao *et al.*, 2015] have also been demonstrated and are envisaged to be favourable candidates for integration with electronic circuits for lab-on-a-chip information processing and calibration compared with their fibre-optic siblings. All these sensing mechanisms are restricted to a much lower temperature sensitivity of around 70 - 80 pm/°C. Recently published reports by Guan *et al.* [Guan *et al.*, 2016] and Zhang *et al.* [Zhang *et al.*, 2016] have demonstrated an improved sensitivity of 172 pm/°C and 162.9 pm/°C for Si/SU-8 hybrid waveguide assisted MZI sensor and Si/SU-8 based photonic crystal nanobeam cavities, respectively. Besides temperature sensing, an accurate detection of chemical concentration is of considerable interest in biomedical research and chemical industries [Tan and Yiap, 2009; Chen *et al.*, 1994; Liu *et al.*, 2013b; Nam *et al.*, 1999]. Different exotic waveguide schemes such as disk [Wang, Guan, Huang, Zheng, Shi and Dai, 2013], ring [Claes *et al.*, 2009; Chandran

et al., 2017] and straight resonators [Ghosh and Rahman, 2017b; Hameed *et al.*, 2017], sub-wavelength gratings [Flueckiger *et al.*, 2016], and interferometers [Sun *et al.*, 2015a] are proposed and evaluated as biochemical sensors depending on the changes of mode effective index (n_{eff}) by homogeneous or bulk sensing and localised or surface sensing. A recent report shows a maximum isopropanol refractometric sensitivity of 160 nm/RIU for a hollow hybrid plasmonic MZI liquid sensor [Sun *et al.*, 2017].

In this chapter, we introduce a novel metal strip loaded horizontal slot hybrid plasmonic waveguide (MSLHSPW) assisted asymmetric unbalanced Mach-Zehnder interferometer (MZI) with dynamic sensing ability. In MSLHSPW, a nano-scale low index plasmonic slot region is formed by suspending a high index silicon (Si) slab on top of a thin silver (Ag) layer deposited on silica (SiO_2) buffer layer. The key objective of the sensing mechanism would be to enhance light-matter interactions in the low index slot region to obtain a high waveguide sensitivity to a small refractive index change of the sensing material. Dominant quasi-TE mode of a vertical slot waveguide is highly sensitive to the side-wall roughness resulting from dry-etching. It causes high scattering loss. Due to the advantageous structural geometry the dominant quasi-TM mode is less sensitive to the uneven side-walls. Thus, the horizontal slot provides lower scattering loss [Sun *et al.*, 2007] compared to vertical one and higher sensitivity in biochemical and gas sensing applications [Ghosh and Rahman, 2016, 2017a; Kumari *et al.*, 2016, 2018]. The waveguide design parameters optimisations for the maximum sensitivity have been investigated by using our in-house accurate two-dimensional full-vectorial finite element method (FV-FEM). The least squares boundary residual (LSBR) method along with the FV-FEM has also been used to obtain scattering matrices at waveguide discontinuity junctions. The MZI consist of non-identical waveguides in sensing and reference arms. The MSLHSPW incorporated sensing arm with isopropanol in cover and the slot region provides a negative temperature dependent phase change whereas, the reference arm with SiO_2 clad Si/ SiO_2 /Si dielectric horizontal slot (DHS) waveguide guides the mode with positive temperature dependent phase change. Thus, the opposite phase changes in both arms offer a much higher phase difference for a small temperature variation. The same MZI configuration is also capable to detect a small fractional change of isopropanol concentration in a water/isopropanol binary solution for a fixed temperature. Thus, our

proposed MZI sensor not only have a high response to refractive index based temperature sensing but also have an excellent ability to detect liquid concentration which is promising for a lab-on-chip sensor arrays. To the best of our knowledge, no such on-chip integrated photonic device has been reported which shows a single optimised device design that is highly sensitive to temperature and refractometric changes of volume concentration of liquids.

6.2 Optical Properties of the Waveguide Materials

6.2.1 Silicon (Si), Silica (SiO_2), and Isopropanol(C_3H_8O) Solution

The tetravalent metalloid, Silicon (Si) has a great importance in CMOS friendly photonics devices. It is a member of Group 14 in the periodic table. Si is opaque and transparent under visible and infra-red (IR) region of the spectrum, respectively. It is mostly found in nature in the form of silica (SiO_2). For waveguide modelling, bulk material refractive indices variations with temperature and wavelength are of high interest. The Si refractive indices dependence on wavelength and temperature are obtained from the Sellmeier equation [Li, 1980], valid for the near to mid-IR wavelength and temperature range of 1.2 to 14 μm and -173 to 476 $^{\circ}C$ (100 to 750 K), respectively.

$$n_{Si}^2(\lambda, T) = n_0^2(T) + (A_0 + A_1T + A_2T^2) \cdot \frac{F(T)}{\lambda^2} \quad (6.1)$$

where,

$$n_0^2(T) = 11.4445 + 2.7739 \times 10^{-4}T + 1.7050 \times 10^{-6}T^2 - 8.1347 \times 10^{-10}T^3 \quad (6.2)$$

$$F(T) = e^{-3 \frac{d(\delta F(T)/F_{293})}{dT}} \quad (6.3)$$

here, for $20K < T < 293K$,

$$\frac{d(\delta F(T)/F_{293})}{dT} = -4.149 \times 10^{-7} - 9.24 \times 10^{-10}T + 4.446 \times 10^{-11}T^2 \quad (6.4)$$

and for $293 K < T < 1600 K$,

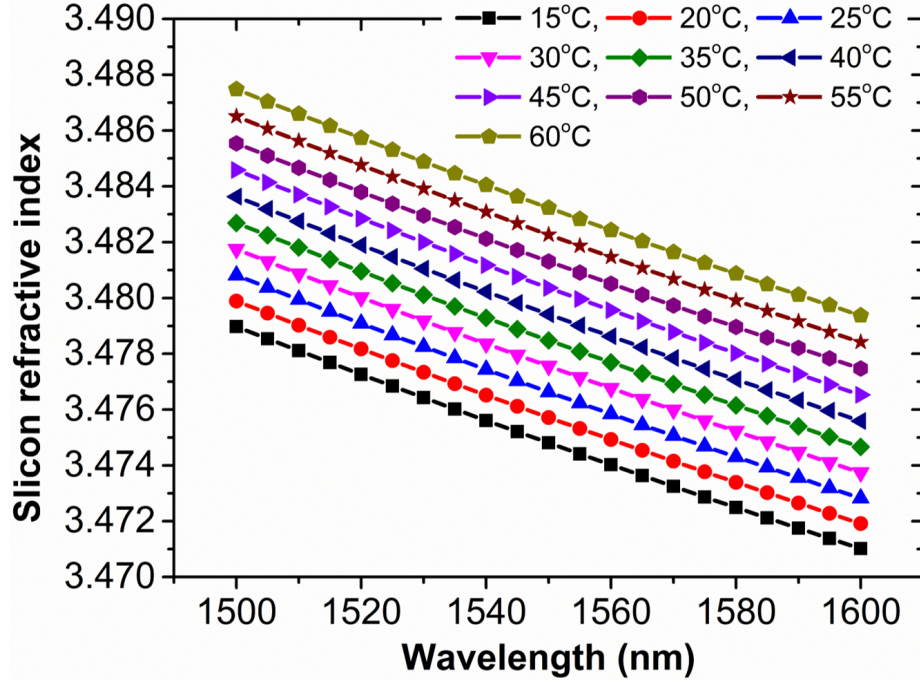


Figure 6.1: *Si* refractive index variations with wavelength (λ) and temperature (T).

$$\frac{d(\delta F(T)/F_{293})}{dT} = -1.887 \times 10^{-6} - 3.868 \times 10^{-9}T + 13.632 \times 10^{-13}T^2 \quad (6.5)$$

and $A_0 = 0.8948$, $A_1 = 4.3977 \times 10^{-4}$, $A_2 = 7.3835 \times 10^{-3}$. The Eq. 6.2 gives the refractive index of *Si* at the room temperature. Figure 6.1 shows the wavelength and temperature dependent refractive indices of *Si*, obtained from Eq. 6.1 with TOC (dn/dT) of $1.83 \times 10^{-4}/^\circ\text{C}$.

SiO₂ has positive TOC (dn/dT) of $+1.1 \times 10^{-5}/^\circ\text{C}$ and its refractive indices have been calculated by the three term Sellmeier equation in [Malitson, 1965].

$$n_{SiO_2}^2 = 1 + \frac{B_0\lambda^2}{\lambda^2 - C_0^2} + \frac{B_1\lambda^2}{\lambda^2 - C_1^2} + \frac{B_2\lambda^2}{\lambda^2 - C_2^2} \quad (6.6)$$

here $B_{0,1,2}$ and $C_{0,1,2}$ denote the material property parameters and absorption coefficients and they are, $B_0 = 0.6961663$, $B_1 = 0.4079426$, $B_3 = 0.8974794$, $C_1 = 0.0684043$, $C_2 = 0.1162414$, and $C_2 = 9.896161$. The temperature dependence of the material refractive index is obtained by,

$$n_T = n_{T_0} + (T - T_0) \cdot \frac{dn}{dT} \quad (6.7)$$

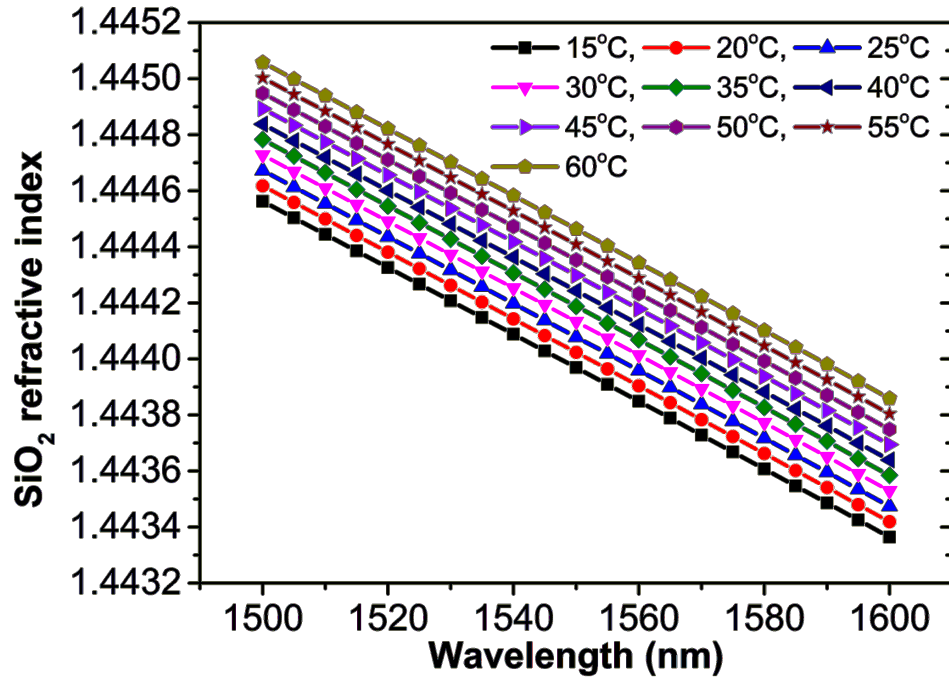


Figure 6.2: SiO_2 refractive index variations with wavelength (λ) and temperature (T).

where n_{T_0} and n_T are the refractive indices of the material at a known and desired temperature T_0 and T , respectively. Using Eqs. 6.6 and 6.7, SiO_2 refractive indices depending on both wavelength and temperature have been calculated and shown in Fig. 6.2.

Liquid isopropanol is used as an temperature sensitive material because of its high negative TOC of $-4.5 \times 10^{-4}/^\circ C$. Isopropanol refractive index dispersion is obtained from a least-squares approximation based Sellmeier equation [Sani and Dell'Oro, 2016] acceptable for the wavelength range of 0.185 to 2.8 μm .

$$n_{isopropanol}^2 = 1 + \frac{D_1 \lambda^2}{\lambda^2 - D_2} + \frac{D_3 \lambda^2}{\lambda^2 - D_4} \quad (6.8)$$

where the material and absorption coefficients are, $D_1 = 0.0107 \pm 0.0003$, $D_2 = 8.88 \pm 0.03$, $D_3 = 0.8702 \pm 0.0002$, and $D_4 = 0.01036 \pm 0.00002$. Refractive index variation with temperature for each wavelength also have been studied by Eq. 6.7 and the corresponding refractive index data have been shown in Fig. 6.3.

It can be seen from the Figs. 6.1 and 6.2 that with the temperature increases, Si and SiO_2 refractive indices increase linearly but compared to Si , SiO_2 refractive index increases slowly because of its lower TOC value. Besides, isopropanol refractive index

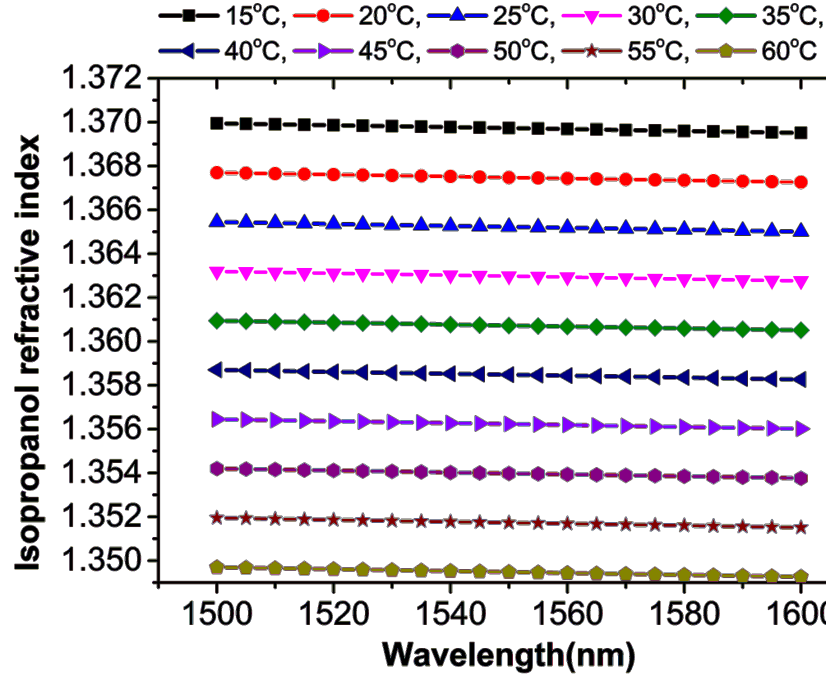


Figure 6.3: Isopropanol (C_3H_8O) refractive index variations with wavelength (λ) and temperature (T).

in Fig. 6.3 decreases with temperature and also its decrement or variation rate is much higher than the Si and SiO_2 thus isopropanol is more temperature sensitive than other two dielectric materials.

In our design, aqueous solution of isopropanol has been considered as a target liquid for the analysis of chemical concentration detection. Thus, it is mandatory to calculate the refractive indices of isopropanol-water solution for different concentrations of isopropanol and water. Instead of using arithmetic weighting equation, we have used more efficient the Lorentz-Lorenz [Garahan *et al.*, 2007] method in determining the equivalent refractive index (n_{eq}) of the binary mixtures and is given by,

$$\frac{n_{eq}^2 - 1}{n_{eq}^2 + 2} = (1 - V) \left(\frac{n_{isopropanol}^2 - 1}{n_{isopropanol}^2 + 2} \right) + V \left(\frac{n_{water}^2 - 1}{n_{water}^2 + 2} \right) \quad (6.9)$$

here V defines the volume fraction of the water in the -isopropanol-water solution. The n_{eq} of the mixture solution for different volume fraction of isopropanol and water has been evaluated from Eq. 6.9 and illustrated in the Fig. 6.4.

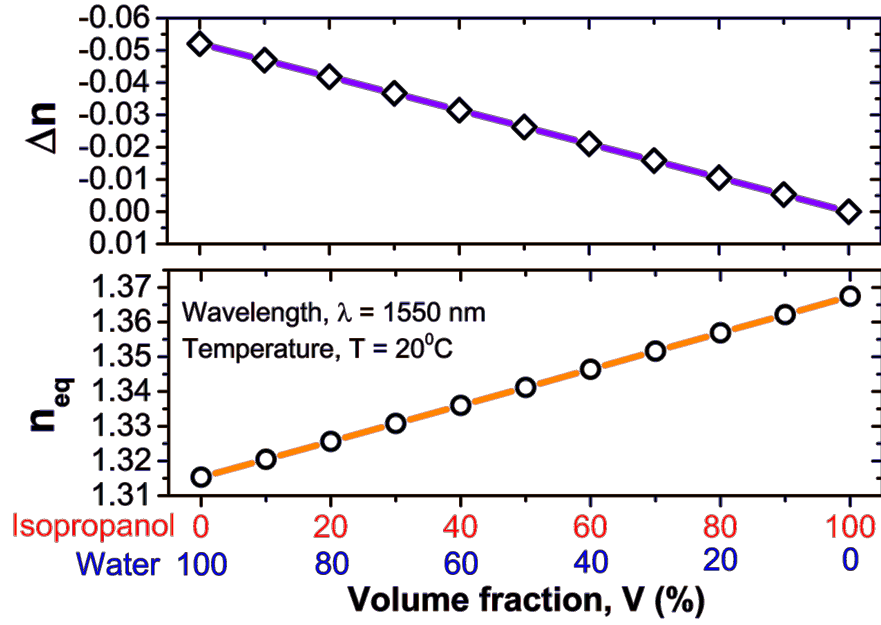


Figure 6.4: Equivalent refractive index (n_{eq}) and index difference (Δn) of the isopropanol-water solution depending on the volume fraction (V%) of isopropanol (C_3H_8O) and water (H_2O) at the temperature, $T = 20^\circ\text{C}$. Isopropanol and water concentrations are highlighted in red and blue, respectively along the x-axis.

6.2.2 Metal - Silver (Ag)

The noble metal, silver (Ag) is used for the design of the HSHPW. The wavelength dependent dielectric permittivity (ϵ_{Ag}) can be obtained appropriately from the Drude model [Bohren and Huffman, 2008].

$$\epsilon_{Ag}(\lambda) = \epsilon_r + j\epsilon_i = \epsilon_\infty - \frac{\omega_p^2}{\omega(\omega + j\omega_c)} \quad (6.10)$$

here ϵ_∞ is associated with absorption peaks in the spectrum at very high frequency, $\omega \gg \omega_c$. ω_c and ω_p are defined as the collision and plasma frequency. The values of ϵ_∞ and ω_c are taken as 3.1 and 0.031×10^{14} rad/s, respectively. The plasma frequency (ω_p) has a strong temperature dependency and is given by,

$$\omega_p = \omega_{p0} \cdot e^{-A_V(T_0)(T-T_0)/2} \quad (6.11)$$

where ω_{p0} and A_V are the plasma frequency at the ideal or room temperature, $T_0 = 25^\circ\text{C}$ and thermal volume expansion coefficient ($A_V = 3 \times (A_L = 18.96 \times 10^{-6}/^\circ\text{C}) = 5.7 \times 10^{-5}/^\circ\text{C}$) of Ag, respectively. In determining the thermal expansion of metal layer in the normal

direction, the modified form of the linear expansion coefficient (A'_L) is used and it is given by,

$$A'_L = A_L \frac{1+\mu}{1-\mu} \quad (6.12)$$

where μ is the Poisson number of Ag, $\mu = 0.37$. The dispersion of real and imaginary part of the silver (Ag) dielectric constant using above mentioned formulae for the room temperature ($T = 25^\circ\text{C}$) is shown in Fig. 6.5. Dielectric constants of Ag for any desirable temperature can easily be determined by the Eqs. 6.10 - 6.12.

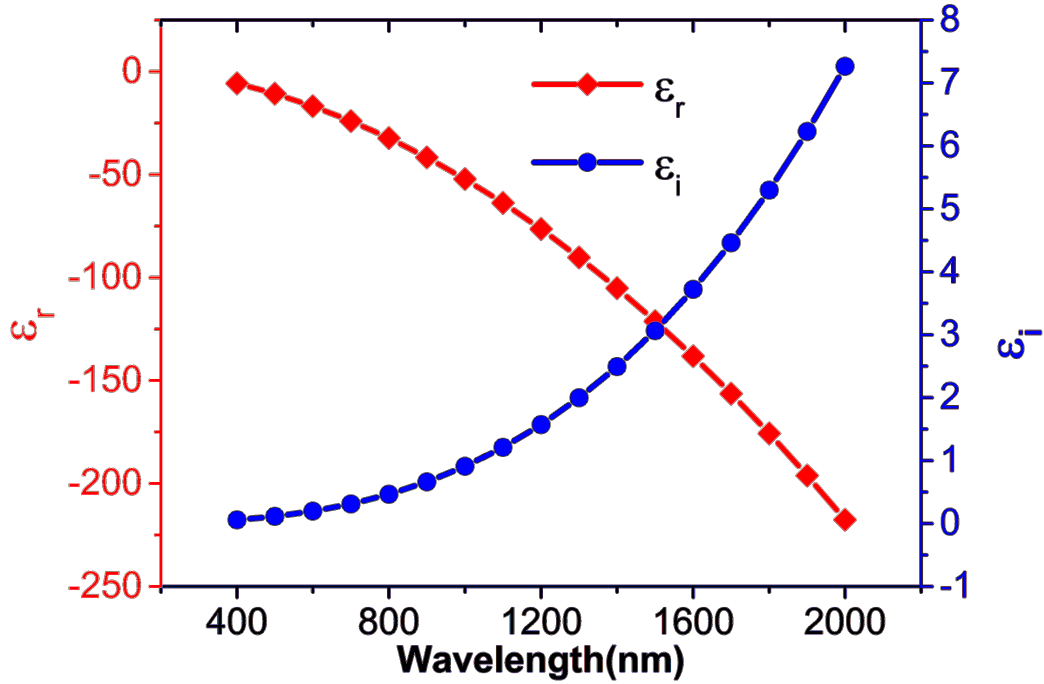


Figure 6.5: Dispersion of real and imaginary dielectric constants (ϵ_r and ϵ_i , respectively) of silver (Ag) at the room temperature ($T = 25^\circ\text{C}$).

6.3 Hybrid Plasmonic Waveguide Incorporated

Mach-Zehnder Interferometer

A single output, unbalanced, asymmetric arm and unequal power split/combine MZI is used as a transducer device in the detection of a small refractive index change of isopropanol depending on either temperature and volume concentration of isopropanol solution. The complete optical characterisation set-up and a schematic diagram of MSLHSPW (in sensing arm) and DHS (in reference arm) incorporated MZI are shown

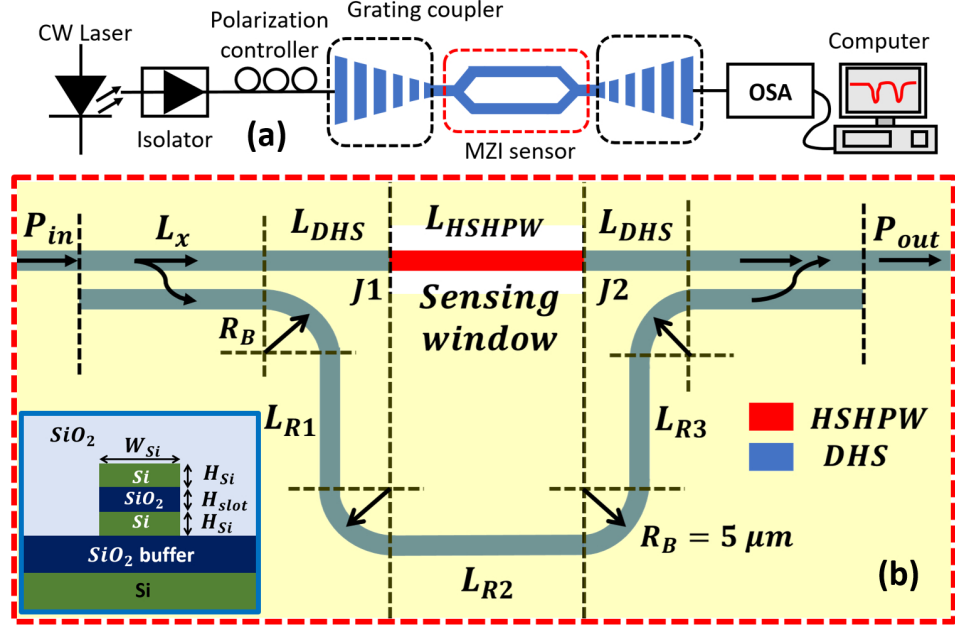


Figure 6.6: Optical characterisation set-up (a) and schematic top view (b) of the metal strip loaded hybrid plasmonic waveguide (MSLHSPW) incorporated MZI. The MSLHSPW is butt-coupled with SiO_2 clad dielectric horizontal slot (DHS) waveguide at both ends in the sensing arm of length, $L_{Ref} = 2L_{DHS} + L_{MSLHSPW}$. Only DHS is employed in the reference arm having four bending sections of radius, $R_B = 5 \mu m$ and three straight sections, L_{R1} , L_{R2} , and L_{R3} . Thus, total length of the reference arm is $L_{Ref} = 2\pi R_B + L_{R1} + L_{R2} + L_{R3}$.

in Figs. 6.6(a) and (b), respectively. The light from a tunable CW laser can be launched into MZI with the help of a grating coupler. The isolator can be used to prevent unwanted feedback to the CW laser cavity. The polarisation controller is set-up at the input for allowing only TM mode. At the device end, an optical fibre is used to carry the characterisation response to a high precision optical spectrum analyser (OSA) for further analyses.

The MSLHSPW, shown in Fig. 6.7, is inserted in between fixed length SiO_2 clad DHS waveguides ($L_{DHS} = 10 \mu m$) on both sides, together they form the sensing arm of length, $L_{Sen} = 2 \cdot L_{DHS} + L_{MSLHSPW}$. On the other hand, the reference arm of length L_{Ref} consists of only SiO_2 clad DHS with four 90° bends of radius $R_B = 5 \mu m$ (very low bending loss, thus, neglected in further calculations) and straight sections (L_{R1} , L_{R2} , and L_{R3}) to make the device feasible to change the arm length for calibration of frequency spectral range (FSR) and sensitivity (S_D). Thus, the L_{Ref} can be expressed as, $L_{Ref} = (2\pi R_B) + L_{R1} + L_{R2} + L_{R3}$. The DHS straight section, L_{R2} is considered to have same length as $L_{MSLHSPW}$ in sensing arm. Therefore, only L_{R1} and L_{R3} ($L_{R1} = L_{R3}$)

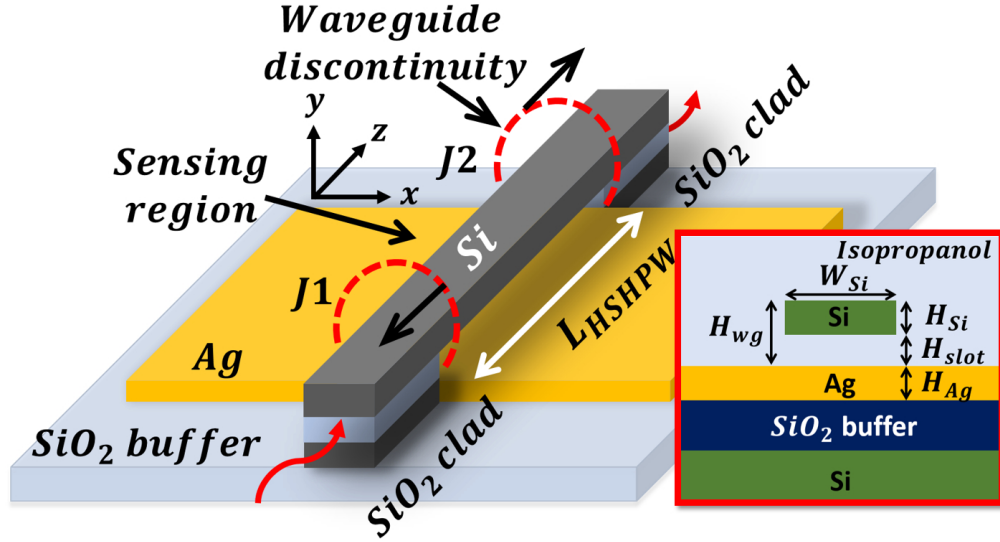


Figure 6.7: 3D schematic diagram of the hybrid plasmonic waveguide assisted sensing arm section. The metal strip loaded horizontal slot hybrid plasmonic waveguide (MSLHSPW) acts as an active sensing region. The MSLHSPW is butt-coupled with the SiO_2 clad dielectric horizontal slot (DHS) waveguide at both ends. The inset figure shows a cross-section of the MSLHSPW.

are left free of length calibration. The MZI has SiO_2 cladding as cover medium except for MSLHSPW that creates a sensing window, by which the liquid isopropanol is infiltrated in the sensing region (slot + cover medium).

6.3.1 Metal Strip Loaded Horizontal Slot Hybrid Plasmonic

Waveguide (MSLHSPW)

The metal suspended horizontal slot hybrid plasmonic waveguide (MSLHSPW) supports a low index guided slot mode which is a combination of photonics and plasmonic modes arise from dielectric-dielectric (Si/isopropanol) and dielectric-metal (isopropanol/Ag) interfaces, respectively. The 3D schematic of MSLHSPW structure is shown in Fig. 6.7 which contains a nano-dimension slot in between suspended Si slab and Ag layer deposited on top of SiO_2 substrate. The MSLHSPW is butt coupled to SiO_2 clad Si/ SiO_2 /Si dielectric horizontal slot (DHS) waveguides at both ends (J1 and J2). Thus, the Si slab forms a bridge over the metal layer and offers a plasmonic slot that is exploited as a sensing region in our proposed design. Inset of Fig. 6.7 shows the cross-section view of the MSLHSPW. The plasmonic waveguide design, optimisations and performance analyses demand a powerful mode solver to solve the partial differential equations (PDEs). In most cases,

the PDEs for plasmonic problems are much complex to be solved by using conventional analytical and semi-analytical approaches. An in-house \vec{H} -field based full-vectorial finite element method (FV-FEM) has been developed [Rahman and Davies, 1984a] and refined [Rahman and Davies, 1984b; Ghosh and Rahman, 2017a,b] over thirty years, discussed in previous chapters, is used for the modal solutions. The variational formulation used for 2D FV-FEM (Section 3.3) is modified by considering local dielectric constant of each discretised element for the elimination of spurious modes, particularly for plasmonic waveguides so that their Euler equations not only follow the Helmholtz equation but also satisfy the Maxwell's two divergence equations (Section 3.3.1).

The modal phase constant (β) and effective index ($N_{eff} = n_{eff} - jk_{eff} = \beta/k_0 - j\alpha/k_0$) can be evaluated from the eigenvalues. Here α is the mode attenuation constant in Np/m and $k_0 = 2\pi/\lambda_0$ is the plane wave phase constant in free-space and λ_0 is free-space wavelength of light. An accurate solution of a plasmonic waveguide requires a sufficient dense mesh distribution around the metal film to resolve the sub-wavelength field confinement. Our flexible meshing technique associated with FV-FEM helps in this regard. The mode propagation length ($L_p = \lambda/4\pi k_{eff}$, the waveguide length where the guided mode power is $1/e$ times of its initial value) and mode power attenuation ($\alpha' = 4.343/L_p$ in dB/ μm) are also important in evaluation of plasmonic waveguides. Optimisation to maximum waveguide sensitivity requires a rigorous assessment of power confinement factor (Γ) in the specific regions (slot and sensing regions) which can be defined as

$$\Gamma_{\Delta} = \frac{\iint_{\Delta} \text{Re}(\vec{E} \times \vec{H}^*) dx dy}{\iint_{\infty} \text{Re}(\vec{E} \times \vec{H}^*) dx dy} \quad (6.13)$$

here Δ represents the horizontal slot and/or cover medium, together forms the sensing region. The vectorial \vec{E} and complex conjugate of \vec{H} (\vec{H}^*) fields are used to formulate the modal Poynting vector. Two butt-coupling junctions ($J1$ and $J2$) of the MSLHSPW and DHS waveguide in the MZI sensing arm create waveguide discontinuities. The least squares boundary residual (LSBR) method (Section 3.6) is used in conjugation with FV-FEM for rigorous investigations of power transfer and transmission loss of these two butt-coupled waveguides.

6.3.2 Design and Optimisation of Waveguides

The sensing slot in MSLHSHPW is sandwiched between a thin metal (Ag) layer and another suspended high index Si slab bridged between two DHS waveguides at both the ends (Fig. 6.7, inset). The thin Ag layer on SiO_2 buffer not only provides the sub-wavelength confinement but also restricts penetration of evanescent field into the buffer region. This restricted field that otherwise would have expanded into the dielectric substrate for the all-dielectric slot waveguide is now guided through the low index slot above the metal. This in turn increases the power confinement in the slot and sensing region (slot + cover medium) compared to a conventional dielectric horizontal slot waveguide. The MSLHSHPW dimensions, such as waveguide width (W_{Si}), metal thickness (H_{Ag}), Si slab height (H_{Si}) and slot height (H_{slot}) are optimised to confine the maximum power inside the low index slot region at the operating wavelength of 1550 nm. In this case, the slot and cover medium are considered to be filled with 100% isopropanol. Throughout FV-FEM simulations, the existing one-fold symmetry is exploited and only half of the waveguide is discretised with 1,280,000 non-uniform triangular elements with minimum element size of 0.2 nm close to the metal surface to resolve the sub-wavelength field confinement accurately.

Figures 6.8(a) and (b) depict the H_x and E_y field distributions of the quasi-TM fundamental mode of the MSLHSHPW simulated by FV-FEM. The H_x field of the MSLHSHPW shows maximum distributions in the top Si and moderate in low index isopropanol slot region (Fig. 6.8(a)) whereas, its dominant E_y field shows its maximum field confinement in the low index horizontal slot region containing isopropanol, as preferred (Fig. 6.8(b)).

Figure 6.9 shows the simulated E_y field profile of the quasi-TM mode of the DHS waveguide. As expected, most of the light confined and guided by the low index slot region. Figure 6.10 depicts the E_y and H_x field line plot along y-axis of the dominant quasi-TM mode of both waveguides. Figure 6.10(a) shows the 1D-line plot of the dominant E_y field and the lower part Fig. 6.10(b) shows the dominant H_x field. The red dashed and solid blue lines depict the 1D field plot of the DHS and MSLHSHPW, respectively. The quasi-TM H_x field of the DHS (red dashed line) is continuous and shows its two peaks in the top and bottom Si layers and a lower value in the low index SiO_2 slot. The

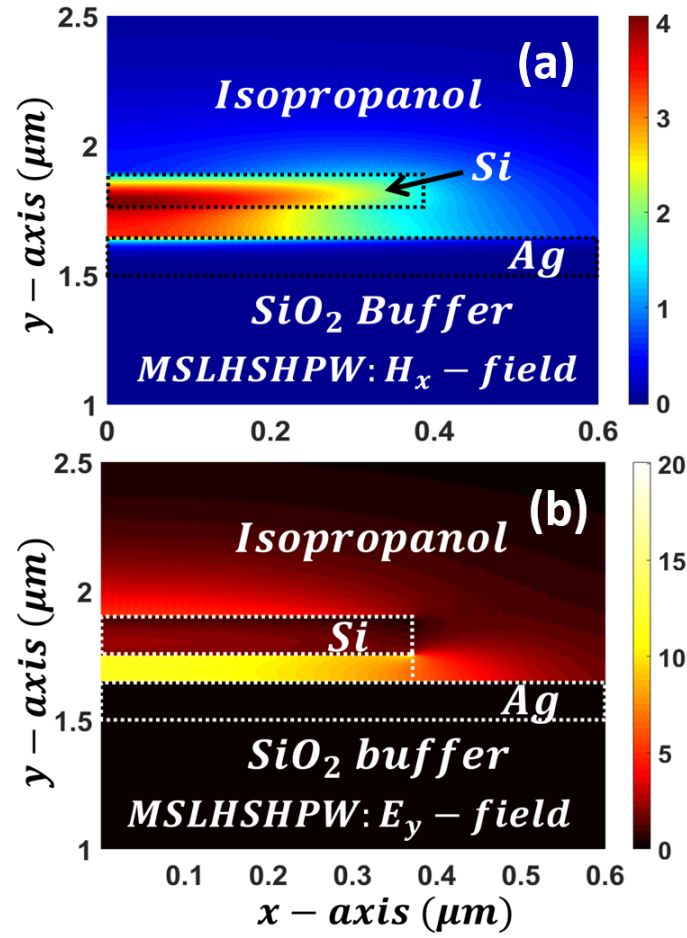


Figure 6.8: (a) and (b) show the FV-FEM simulated quasi-TM H_x and E_y -field distributions of MSLHSHPW, respectively.

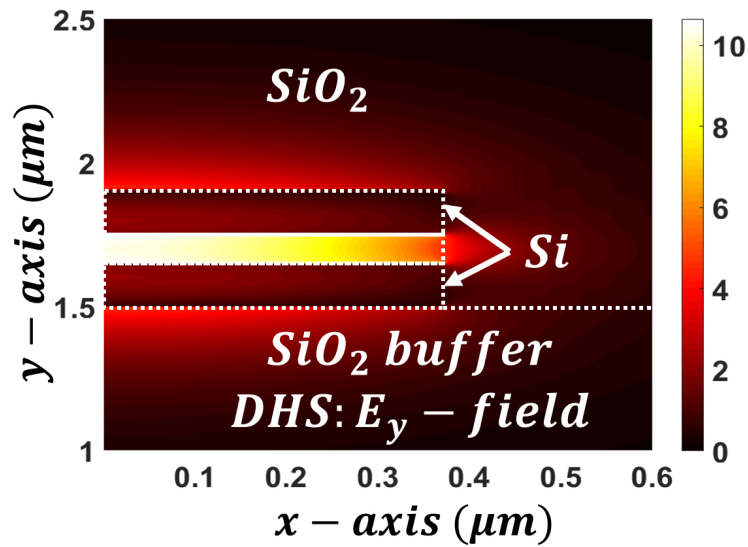


Figure 6.9: shows the FV-FEM simulated quasi-TM E_y field distributions of the $\text{Si}/\text{SiO}_2/\text{Si}$ dielectric horizontal slot (DHS) waveguide.

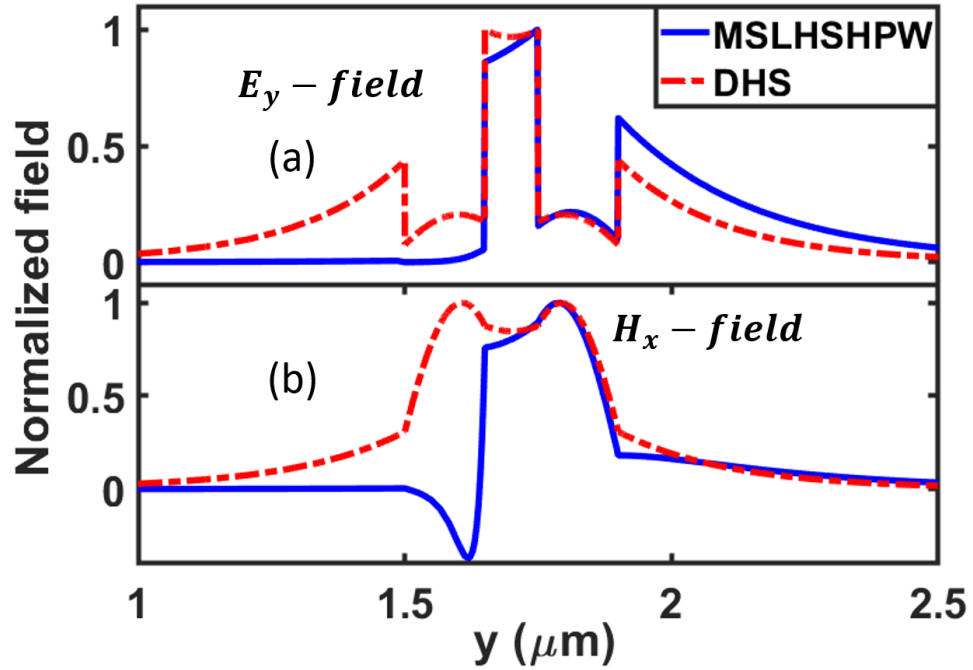


Figure 6.10: The blue solid and red dashed lines represent the (a) E_y and (b) H_x field line plots along y-axis of the MSLHSPW and DHS, respectively. Maximum quasi-TM E_y field confines in the slot which is highly sensitive to a small refractive index change in that region.

dominant E_y field of the similar waveguide shows a symmetric distribution along y-axis with maximum confinement in the slot. The quasi-TM H_x field of the MSLHSPW shows a positive peak in the Si layer and a small negative peak can also be observed in the thin Ag layer. On the other hand, the dominant E_y confines maximum in the low index isopropanol contained slot and moderate in the top clad region (blue solid line). Moreover, in the MSLHSPW, a very low $\sim 0.1\%$ light confines in the Ag+SiO₂ buffer layer which in turn enhance the light confinement in the slot.

Variations of n_{eff} , α' (dB/ μ m) and slot confinement (Γ_{slot}) of MSLHSPW with H_{Ag} are shown in Fig. 6.11. The inset figure shows the confinement in the Ag layer (Γ_{Ag}) against H_{Ag} . Other parameters, W_{Si} , H_{Si} and H_{slot} are kept fixed at 700, 150 and 100 nm, respectively. It can be observed that for the fixed values of W_{Si} , H_{Si} and H_{slot} , the H_{Ag} variations within the range of 80 to 1000 nm have no effect on n_{eff} , α' , and Γ_{slot} . But for H_{Ag} value lower than 80 nm, all four parameters increase rapidly. Γ_{slot} increases from its base value of 58.59% to 59%. But, the confinement in the lossy Ag layer (Γ_{Ag}) jumps from its base value of 0.101% to a high 4.044%, which results in a larger change of α'

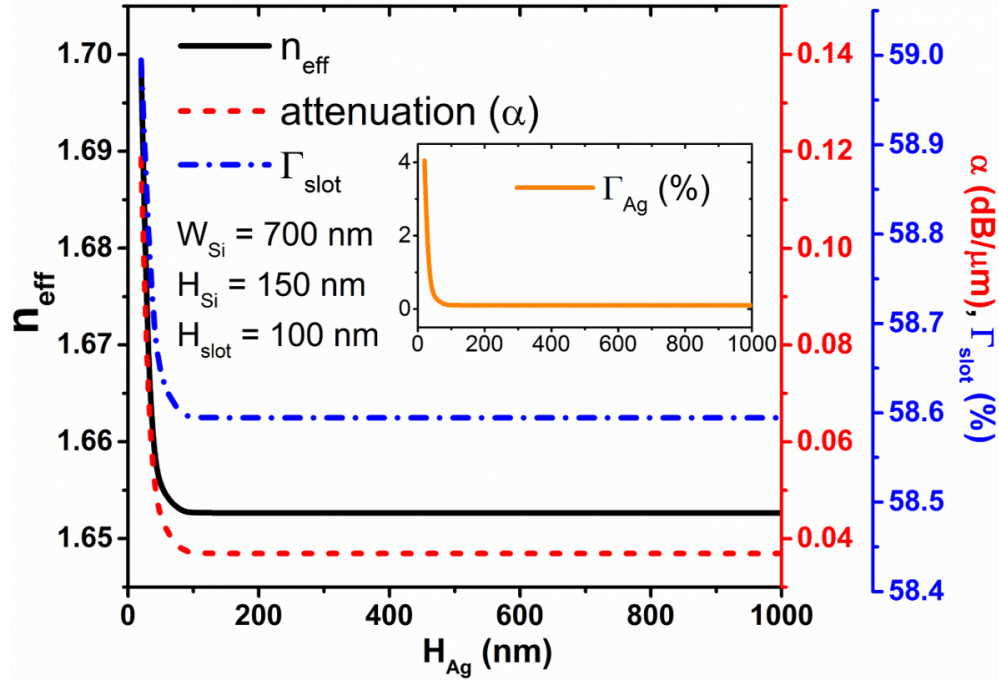


Figure 6.11: Effective index (n_{eff}), mode power attenuation (α') and slot confinement (Γ_{slot}) variations with the thickness (H_{Ag}) of silver metal film deposited on the SiO_2 buffer layer. The inset figure shows the confinement (Γ_{Ag}) variation of the Ag layer against H_{Ag} . Other parameters such as, Si slab width (W_{Si}), height (H_{Si}) and slot height (H_{slot}) are kept fixed at 700, 150 and 100 nm, respectively.

form 0.037 dB/ μ m to 0.12 dB/ μ m which is unacceptable for this design. With the variation of the temperature, Ag metal thickness may be expanded in the normal direction. Thus, over the complete range of temperature variation (20°C – 60°C), using the augmented thermal expansion coefficient expression Eq. 6.12, shows only a 0.16% H_{Ag} increment in its thickness, where $\mu = 0.37$ is the Poisson number of Ag. Such a small thickness variation of the Ag metal film with temperature would have negligible effect on n_{eff} , α' (dB/ μ m) and Γ_{slot} .

The contour plots in Figs. 6.12(a) and (b) show a combined effect of W_{Si} and H_{Si} on the n_{eff} and Γ_{slot} , respectively. Here, H_{Ag} and H_{slot} are fixed at 150 and 100 nm, respectively. In this case, n_{eff} increases faster with the H_{Si} for a fixed W_{Si} than that of the W_{Si} increase for a fixed H_{Si} . The Γ_{slot} contour distribution shows an enhanced slot confinement of over 50% for the W_{Si} and H_{Si} range of 700 to 800 nm and 100 to 180 nm, respectively. An abrupt Γ_{slot} variation is observed when $W_{Si} > 800$ nm and H_{Si} is in the range of ~ 150 to 300 nm. This local change has been identified due to the influence of 2nd order quasi-TE mode (more light confines in the Si slab) within a

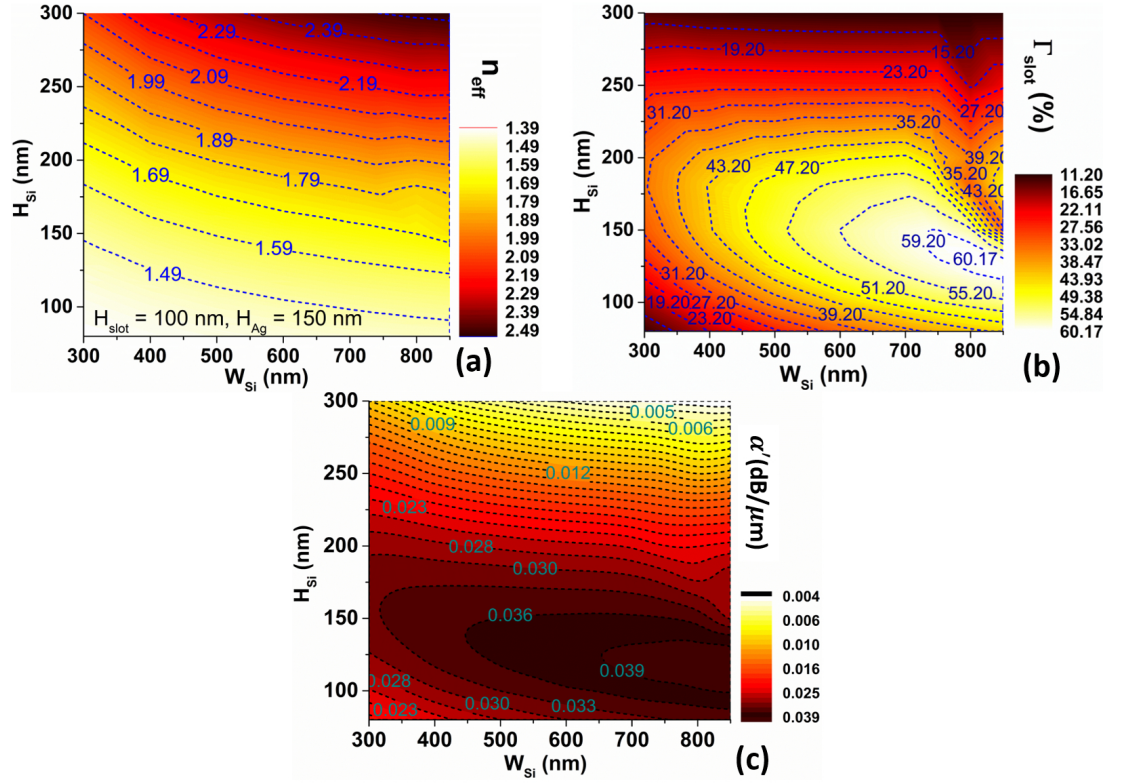


Figure 6.12: The contour plots in (a), (b), and (c) show the variations of n_{eff} , α' (dB/ μ m), and Γ_{slot} as a function of W_{Si} and H_{slot} . The H_{slot} and H_{Ag} are kept fixed at 100 and 150 nm, respectively. An abrupt variation of Γ_{slot} is observed due to the other higher order quasi-TE mode in a close proximity of the quasi-TM fundamental mode.

close proximity of the quasi-TM fundamental mode. Figure 6.12(c) shows the quasi-TM modal loss (α') depending on both W_{Si} and H_{Si} . The contour plots depict that the H_{Si} has a greater influence on α' , compared to W_{Si} . With the increase of H_{Si} , the light is more guided by the high index Si that corresponds a small modal loss. However, as the W_{Si} increases, the α' does not show significant change for a high value of H_{Si} . But, for a range of H_{Si} , from 50 nm to 200 nm, the α' changes significantly with W_{Si} . In this range, further investigations were carried out to identify the optimum values of these design parameters. Figure 6.13 shows the Γ_{slot} , Γ_{clad} , and $\Gamma_{slot} + \Gamma_{clad}$ variations against W_{Si} when the H_{slot} and $H_{Si} = H_{Ag}$ are fixed at 100 and 150 nm, respectively. The Γ_{slot} increases with W_{Si} , reaches a maximum value of 59.24% for $W_{Si} = 740$ nm and then decreases. On the other hand, Γ_{clad} shows a linear reduction with the increase of W_{Si} . As a result, the resultant $\Gamma_{slot} + \Gamma_{clad}$ also decreases with the increase of W_{Si} . The optimum value of W_{Si} is considered to be 740 nm which gives maximum slot confinement, $\Gamma_{slot} =$

59.24% and corresponding $\Gamma_{slot+clad} = 82.04\%$. Similarly, these confinement variations with H_{Si} have been shown in Fig. 6.14. In this case, the Γ_{slot} increases with H_{Si} shows a maximum confinement of 59.60% at $H_{Si} = 140$ nm and then decreases. However, $H_{Si} = 140$ nm has slightly higher loss ($\alpha' = 0.038$ dB/ μ m) compared to the 150 nm ($\alpha' = 0.036$ dB/ μ m). The Γ_{clad} decreases in a hyperbolic nature and shows $\Gamma_{clad} = 22.80\%$ when $H_{Si} = 150$ nm. Therefore, with the $\Gamma_{slot+clad} = 82.04\%$, the optimum value of H_{Si} is considered to be 150 nm.

Figures 6.15(a) and (b) show the quasi-TM and TE power confinements (Γ_{slot} , Γ_{clad} , and $\Gamma_{slot+clad}$) with H_{slot} when W_{Si} , H_{Si} and H_{slot} are kept fixed at 740, 150 and 150 nm, respectively. Figure 6.15(a) shows that with the increment of H_{slot} , the Γ_{slot} of quasi-TM mode, shown by a black solid line, increases and reaches its maximum value of 59.38% at $H_{slot} = 90$ nm and then decreases gradually with further increase. The Γ_{clad} increases with the H_{slot} shown by a red dashed line and shows a 22.80% power confinement for $H_{slot} = 100$ nm. The resultant $\Gamma_{slot+clad}$, shown by a blue dashed-dotted line, shows a bell-shaped variation with its peak value of $\Gamma_{slot+clad} = 82.04\%$ for 100 nm slot height (shown by the right-hand side scale). On the other hand, the MSLHSPW with $H_{slot} = 90$ nm has a comparatively higher loss (0.040 dB/ μ m) than that of the 100 nm (0.036 dB/ μ m).

Likely, Fig. 6.15(b) shows a similar variation with the H_{slot} for the fundamental quasi-TE mode. Within the complete range (40 to 150 nm) of H_{slot} , the slot and clad regions confine much lower power (Γ_{slot} and Γ_{clad}) than that of the quasi-TM mode. As a result, the sensing region shows only ~30 to 34% power confinement ($\Gamma_{slot+clad}$) within the range of H_{slot} . The lower power confinement in the low index slot makes the quasi-TE mode less sensitive to the small refractometric changes of liquid isopropanol.

Summarizing the above studies, it can be concluded that the fundamental quasi-TM mode of MSLHSPW is highly sensitive to slot refractometric changes. With the optimising design parameters, the metal strip loaded MSLHSPW has shown an enhanced performance in terms of the slot, sensing region power confinement ($\Gamma_{slot} = 59.24\%$, $\Gamma_{slot+clad} = 82.04\%$) and the mode power attenuation, $\alpha'_{MSLHSPW} = 0.036$ dB/ μ m. Finally, all the optimised MSLHSPW dimensions with 100% isopropanol can be summarised as, Si slab/waveguide width (W_{Si}) = 740 nm, height (H_{Si}) = 150 nm, slot

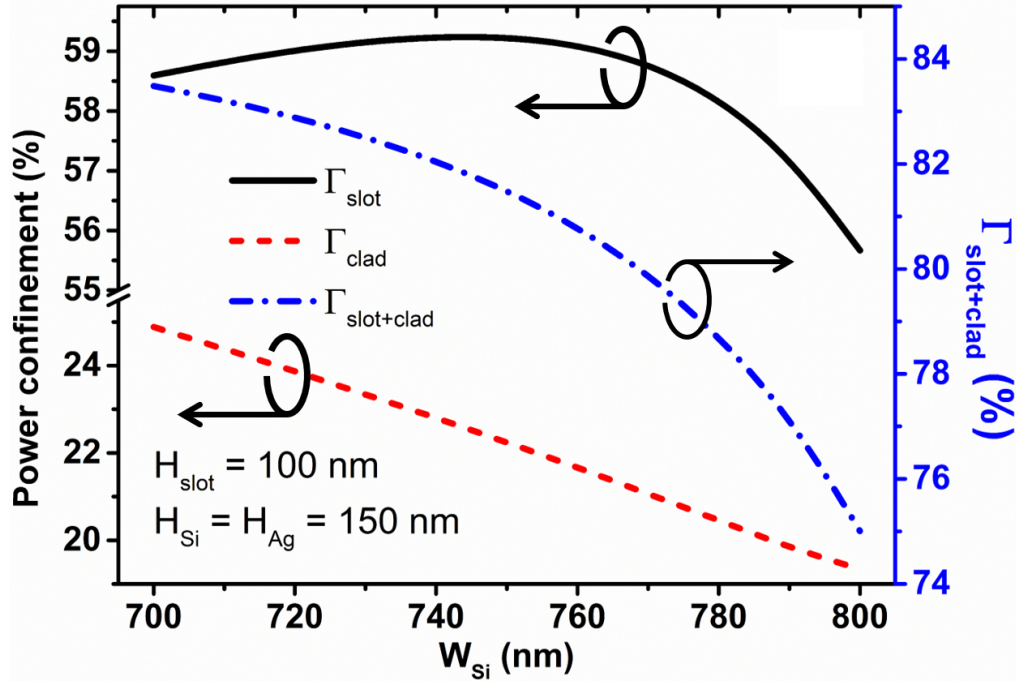


Figure 6.13: Variations of power confinement in slot (Γ_{slot}), clad (Γ_{clad}) and sensing region ($\Gamma_{slot+clad}$) with W_{Si} are shown in the figure. The solid black, red dashed and blue dashed-dotted curves represent the Γ_{slot} , Γ_{clad} , and $\Gamma_{slot+clad}$ variations, respectively. H_{slot} and $H_{Si} = H_{Ag}$ are kept fixed at 100 and 150 nm, respectively.

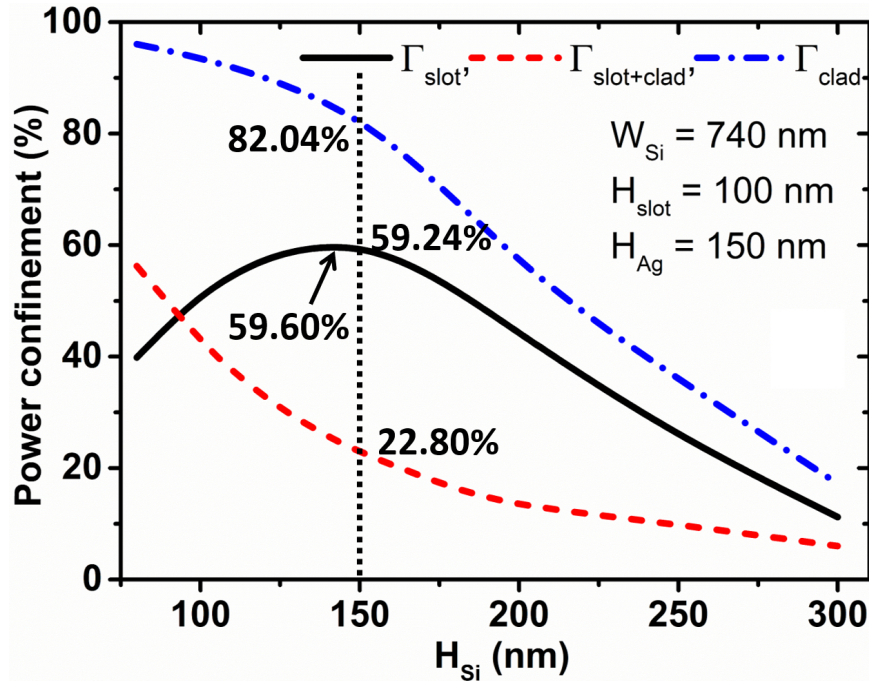


Figure 6.14: Variations of power confinement in slot (Γ_{slot}), clad (Γ_{clad}) and sensing region ($\Gamma_{slot+clad}$) with H_{Si} are shown in the figure. The solid black, red dashed, and blue dashed-dotted curves represent the Γ_{slot} , Γ_{clad} , and $\Gamma_{slot+clad}$ variations, respectively. W_{Si} , H_{slot} , and H_{Ag} are kept fixed at 740, 100, and 150 nm, respectively.

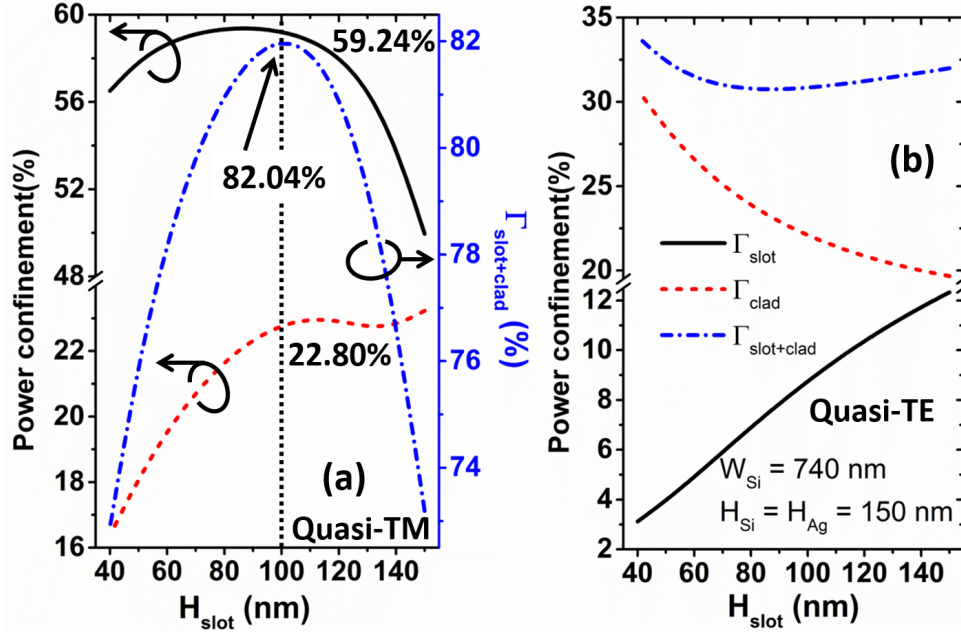


Figure 6.15: (a) and (b) show the power confinement (Γ) variations in the horizontal slot, clad and sensing region (slot + clad) of the quasi-TM and TE modes against slot height (H_{slot}). W_{Si} and $H_{Si} = H_{Ag}$ are kept fixed at 740 and 150 nm, respectively.

height (H_{slot}) = 100 nm and the thickness of Ag strip (H_{Ag}) = 150 nm for the operating wavelength of $\lambda = 1550$ nm.

6.3.3 MZI design with MSLHSPW and DHS waveguides

During sensing process, the differential phase change ($\Delta\phi$) between sensing and reference arms of the MZI depends on the optical path difference (OPD) arises due to refractive index change of sensing analyte as

$$\Delta\phi = \frac{2\pi}{\lambda} [(n_{eff,DHS} \cdot 2L_{DHS} + n_{eff,MSLHSPW} \cdot L_{MSLHSPW}) - (n_{eff,DHS} \cdot L_{Ref})] \quad (6.14)$$

where n_{eff} with additional subscripts DHS and MSLHSPW denote the real part of the effective indices of the corresponding waveguide. Thus, for a plasmonic waveguide assisted MZI, operating at a wavelength (λ) the output power (P_{out}) depends on the OPD value through $\Delta\phi$ and that can be expressed as [Berini, 2008]

$$P_{out} = \frac{1}{4} P_{in} (e^{-2\alpha_{Ref} L_{Ref}} + e^{-2\alpha_{Sen} L_{Sen}}) \cdot (1 + V \cos \Delta\phi) \quad (6.15)$$

Here α_{Ref} and α_{Sen} represent the attenuation constants in Np/ μ m associated with the reference and sensing arm waveguides, respectively and V represents the fringe visibility

of the MZI output given as:

$$V = \frac{2e^{-\alpha_{Ref}L_{Ref}}e^{\alpha_{Sen}L_{Sen}}}{e^{-2\alpha_{Ref}L_{Ref}} + e^{-2\alpha_{Sen}L_{Sen}}} \quad (6.16)$$

It is being assumed that the input power is distributed equally (P_{in}) in both the arms. The MSLHSHPW in the sensing arm has a significant amount of quasi-TM modal loss compared to the DHS which can be assumed to be loss-less (quasi-TM) [Sun *et al.*, 2007] i.e. $\alpha_R = 0$ and the transmittance, $e^{-2\alpha_R L_{Ref}} = 1$ for a short length waveguide. Small scattering loss in both the branches can be included separately if necessary. The mode propagation loss in MSLHSHPW and butt-coupling losses at the junction 1 and 2 ($J1$ and $J2$) in sensing arm (Fig. 6.6(b)) affect the overall device output power and its fringe visibility (V). However, it can be compensated by tuning the coupling section (L_x) of the input directional coupler so that, the sensing arm receives more power to balance the device insertion loss and thus, also improve the interference fringe visibility (V). Furthermore, the only unaccounted loss comes from the small attenuation perturbation ($\Delta\alpha_S$) in the sensing MSLHSHPW during homogeneous refractometric changes of isopropanol solution. Therefore, the formulation of the MZI output power (P_{out}) can be shown to be as:

$$P_{out} = \frac{1}{2} \left[P_{inR} + \left(P_{inS} \cdot \tau_{J1} \cdot \tau_{J2} \cdot e^{-2(\alpha_{MSLHSHPW} \pm \Delta\alpha_S)L_{MSLHSHPW}} \right) \right] (1 + V' \cdot \cos\Delta\phi) \quad (6.17)$$

where the modified form of the fringe visibility (V') is given by

$$V' = \frac{2\sqrt{P_{inR} \cdot P_{inS} \cdot \tau_{J1} \cdot \tau_{J2}} \cdot e^{-(\alpha_{MSLHSHPW} \pm \Delta\alpha_S)L_{MSLHSHPW}}}{P_{inR} + P_{inS} \cdot \tau_{J1} \cdot \tau_{J2} \cdot e^{-(\alpha_{MSLHSHPW} \pm \Delta\alpha_S)L_{MSLHSHPW}}} \quad (6.18)$$

The P_{inR} and P_{inS} represent the unequally distributed input power at the reference and sensing arms, respectively. The τ_{J1} and τ_{J2} denote the transmittance at the waveguide discontinuities $J1$ and $J2$, respectively and $\alpha_{MSLHSHPW}$ is the quasi-TM mode attenuation constant of the MSLHSHPW. The frequency spectral range (FSR) of the plasmonic waveguide assisted MZI is calculated as

$$FSR = \frac{\lambda^2}{[(n_{g,DHS}L_{DHS} + n_{g,MSLHSHPW}L_{MSLHSHPW}) - n_{g,DHS}L_{Ref}]} \quad (6.19)$$

where λ , $n_{g,DHS}$, and $n_{g,MSLHSHPW}$ are the operating wavelength and group index of DHS and MSLHSHPW, respectively. In our design, the key point is to achieve a highly sensitive temperature sensor design to increase the differential phase change between

the two arms. This is achieved by light guiding through materials with negative and positive TOCs in sensing and reference arms, respectively. The temperature sensitivity (S_T) of the MZI device i.e. the wavelength shift ($\Delta\lambda$) of destructive fringes with respect to temperature (T) is defined as [Dwivedi *et al.*, 2013]

$$S_T = \frac{FSR \cdot \left[\left\{ \left(\frac{dn_{eff,DHS}}{dT} \right) \cdot L_{DHS} + \left(\frac{dn_{eff,MSLHSHPW}}{dT} \right) \cdot L_{MSLHSHPW} \right\} - \left(\frac{dn_{eff,DHS}}{dT} \right) \cdot L_{Ref} \right]}{\lambda} \quad (6.20)$$

The sensing arm of the MZI consists of active and optimised isopropanol filled MSLHSHPW butt-coupled with DHS waveguides at both the ends. The waveguide discontinuities at the MSLHSHPW-DHS junctions ($J1$ and $J2$) incur additional coupling losses along with the inherent plasmonic mode propagation loss of the MSLHSHPW. These waveguide discontinuities have been analysed by using the LSBR (Section 3.6) method and the result shows the transmission coefficient at the MSLHSHPW-DHS junction is $\rho_{J1} = \rho_{J2} = 0.85339$. Thus, the junction transmittance has the value of $\tau_{J1} = \tau_{J2} = |\rho|^2 = 0.73$ which yields the insertion loss at each junction of 1.377 dB. For the MZI design purpose, we have considered three different MSLHSHPW lengths ($L_{MSLHSHPW}$) such as 20, 30, and 40 μm . These three waveguide lengths provide the transmittance ($\tau_{MSLHSHPW} = e^{-2\alpha_{MSLHSHPW}L_{MSLHSHPW}}$) values of 0.84, 0.78, and 0.71, respectively. Thus, the total transmittance values ($\tau_{Sen} = \tau_{J1} \cdot \tau_{J2} \cdot \tau_{MSLHSHPW}$) of the MSLHSHPW incorporated sensing arm for $L_{MSLHSHPW} = 20, 30, \text{ and } 40 \mu\text{m}$ are 0.45, 0.41, and 0.38, respectively. An equal power division (50:50) at the reference and sensing arms of this type of plasmonic waveguide assisted MZI will result in an imbalance of light intensity at both the arms which in turn provides a poor interference fringe visibility (V) at the output (P_{out}). Figure 6.16 shows how the coupling length (L_c) varies with the gap between SiO_2 clad two DHS waveguides. Optimised design parameters ($W_{Si} = 740 \text{ nm}$, $H_{Si} = 150 \text{ nm}$, and $H_{slot} = 100 \text{ nm}$) have been used for simulations. Figure 6.16 shows that the coupling length (L_c) gradually increases with the increase of gap or separation between the waveguides. Thus, to design a compact device the L_c need to be chosen carefully.

The shortcoming arises due to equal power distribution of the conventional 50:50

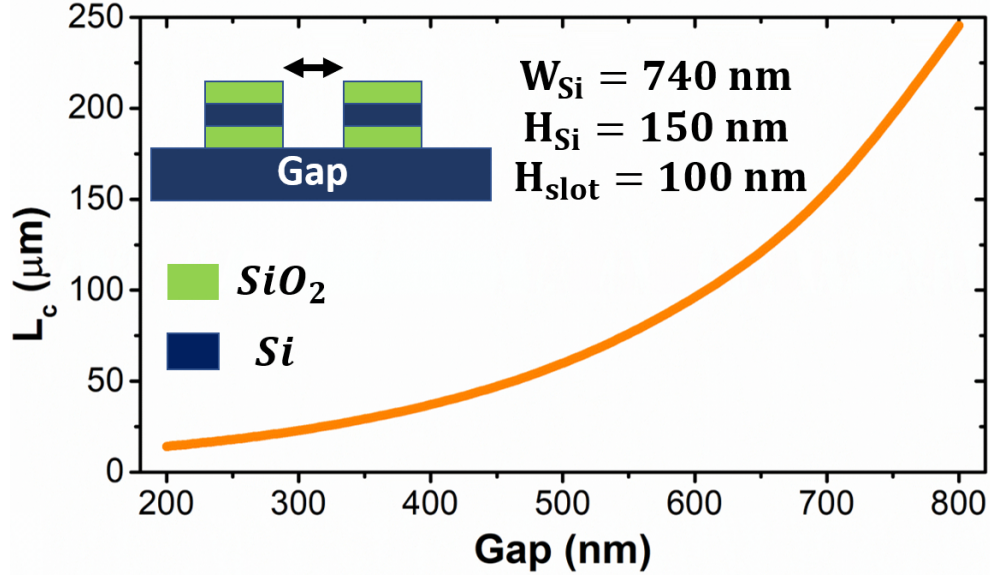


Figure 6.16: Variation of the coupling length (L_c) with gap or separation of the dielectric horizontal slot (DHS) based coupler. Inset shows the cross-section of the $Si/SiO_2/Si$ DHS waveguide coupler whose dimensions are taken as, $W_{Si} = 740$ nm, $H_{Si} = 150$ nm, and $H_{slot} = 100$ nm.

directional coupler in the hybrid plasmonic waveguide incorporated MZI can be mitigated by using asymmetric power splitting in the sensing and reference arms. To obtain unequal power splitting, the coupling section (L_x) of the input directional coupler can be adjusted depending on the power requirements in the sensing and reference arms. The required power in the sensing arm can be calculated by

$$P_{in-Sen} = \frac{1}{(1 + \tau_{Sen})} \quad (6.21)$$

and reference arm by

$$P_{in-Ref} = (1 - P_{in-Sen}) \quad (6.22)$$

Figure 6.17(a) shows a graphical representation of the P_{in-Sen} and P_{in-Ref} requirement depending on the length of MSLHSPW ($L_{MSLHSPW}$) used for sensing. As the junction ($J1$ and $J2$) losses due to waveguide discontinuities are constant, so the only variable loss is considered for power fraction calculation is the modal loss due to different $L_{MSLHSPW}$. With the increment of $L_{MSLHSPW}$ from 10 to 50 μm , the mode propagation loss increases from 0.36 to 1.84 dB. To counter that, the input power distribution ratio (P_{in-Sen}/P_{in-Ref}) needs to be changed from 67% / 33% to 74% / 26%. The required P_{in-sen} and P_{in-Ref} for $L_{MSLHSPW} = 20, 30$ and 40 μm are 0.69, 0.71, 0.72 and 0.31, 0.29 and

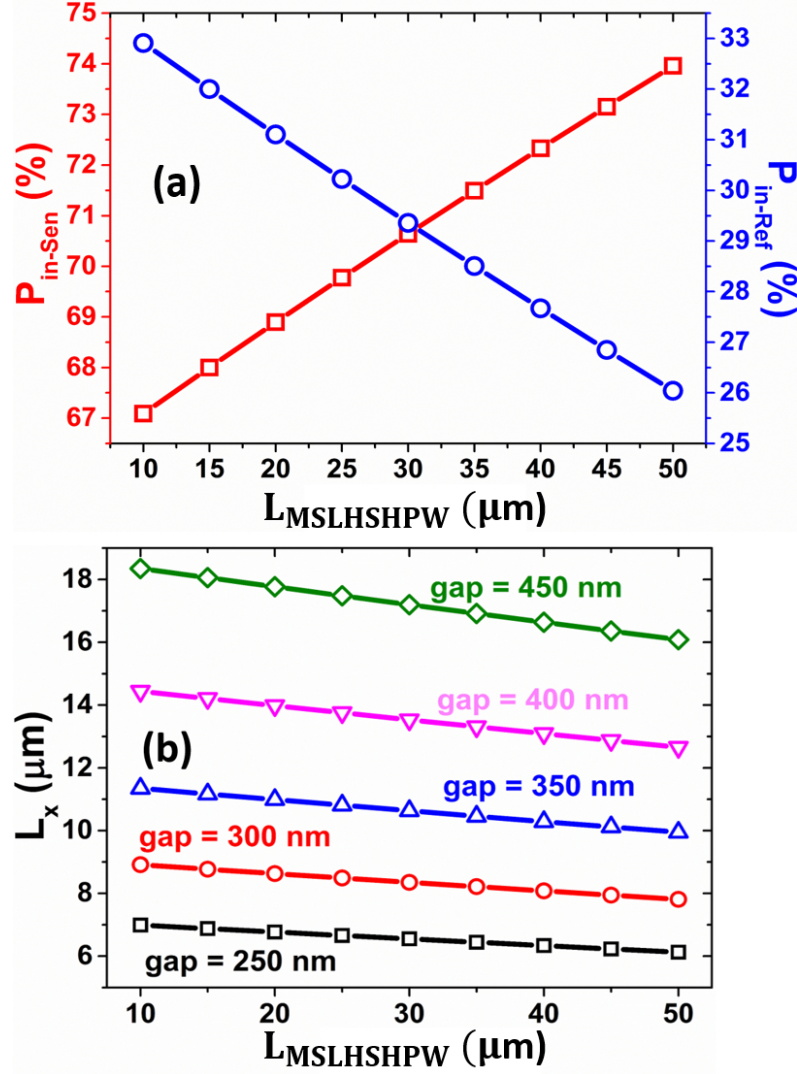


Figure 6.17: (a) depicts the input power requirements in the sensing (P_{in-Sen}) and the reference arms (P_{in-Ref}) depending on the MSLHSPW length ($L_{MSLHSPW}$) in the MZI sensing arm. (b) shows the desired coupling section (L_x) variations of the input directional coupler as a function of MSLHSPW length ($L_{MSLHSPW}$) and gap.

0.28, respectively, shown by the red and blue lines. These unequal power distributions not only compensate the losses in sensing arm but also improve the P_{out} with a very high interference fringe visibility ($V \sim 1$), which is highly required for an accurate output measurement. The asymmetric power distribution demands an appropriate tuning of coupling section at the input directional coupler. Figure 6.17(b) represents the desired coupling section (L_x) variations of SiO_2 clad DHS waveguide based directional coupler (inset of Fig. 6.16) as a function of gap (separation) between two DHS waveguides and the $L_{MSLHSPW}$. The desired length of the coupling section (L_x) can be calculated from the

original coupling length (L_c) and the P_{in-Sen} as,

$$L_x = \frac{2L_c}{\pi} \cdot \cos^{-1} \sqrt{P_{in-Sen}} \quad (6.23)$$

The L_x value increases as the gap increases from 250 nm to 450 nm. Moreover, with the increase of $L_{MSLHSPW}$ the L_x linearly decreases for a constant gap. For a smaller gap, the L_x has a smaller value than that of a higher gap. Hence, depending on user's preferences, one can easily select a suitable gap and the corresponding L_x values for different hybrid plasmonic waveguide length ($L_{MSLHSPW}$). As an example, for the gaps of 350 and 400 nm, the L_x values for $L_{MSLHSPW} = 20, 30$, and $40 \mu\text{m}$ are 10.99, 10.64, 10.29 μm and 13.98, 13.53, and 13.09 μm , respectively, to achieve the required asymmetric power distributions.

6.4 MZI Transducer: Performance Evaluation

A well designed MZI sensor needs a significant attention on the calibration of free spectral range (FSR) and interference fringe visibility (V') of the output power, P_{out} . After setting up the optimised waveguide design parameters for the MZI arms, $L_{MSLHSPW}$ and L_x for the input directional coupler, the FSR and V' parameters are investigated and evaluated as a function of L_{Ref} and $L_{MSLHSPW}$, respectively. The fringe visibility will have the maximum value ($V = V' = 1$) when the two MZI light beams have equal intensity. Inherent modal and junctional losses drop the sensing arm light output thus degrade the interference fringe visibility. With the unequal power distributions, more power is launched at the sensing arm input which not only balance the losses but also provides equal output at both MZI arms.

Figure 6.18 depicts the advantages of using an unequal power distribution over the more traditional 50:50 power splitting. The black line indicates a significant reduction of the V parameter with the increase of $L_{MSLHSPW}$. However, the unequal power splitting shows a significant improvement with almost ideal value of $V' \simeq 1$. Under this condition the V' parameters are calculated with the augmented visibility equation (Eq. 7) and the results show a very high fringe visibility ($V' \simeq 1$) for all $L_{MSLHSPW}$ s in expenses with increasing insertion loss. For these three $L_{MSLHSPW}$ s (20, 30, and 40 μm) incorporating unequal power splitting the device insertion losses are 2.06, 2.32, and

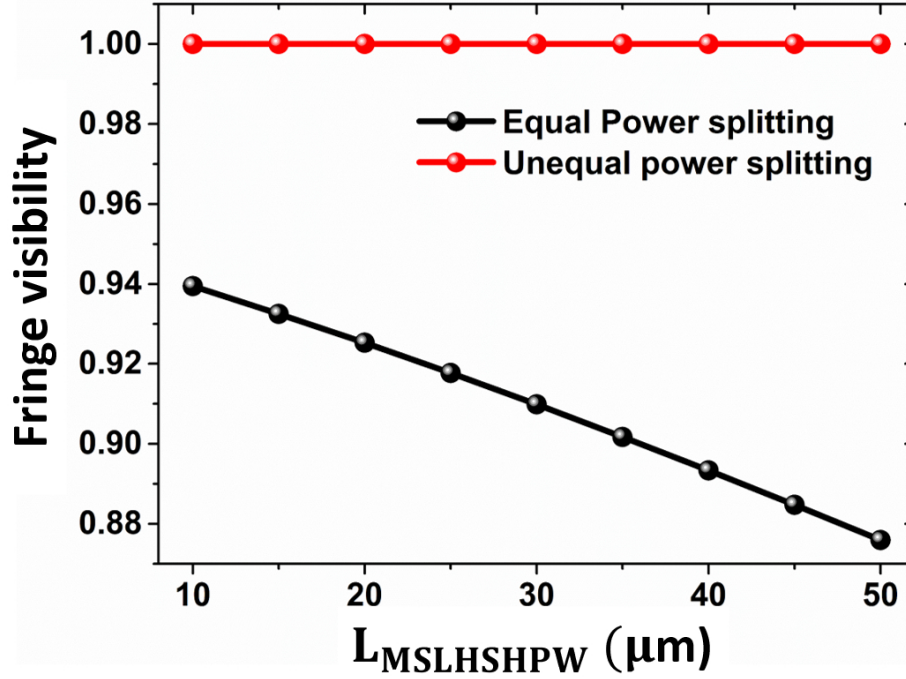


Figure 6.18: shows the fringe visibility (V , V') of the MZI interference output with equal and unequal power splitting. For the 50:50 equal and unequal power splitting, the V -parameters are calculated using Eq. 6.16 and 6.18, respectively.

2.56 dB, respectively when 100% isopropanol is used at temperature $T = 20^\circ\text{C}$. Beside the visibility, the FSR is another important parameter which indicates the frequency spacing of the MZI transmission peaks. A unit wavelength changes with very small power change results in a large FSR which may be unacceptable due to added difficulties in detection of the interference wavelength by optical spectrum analyser (OSA). Thus, as a compromise, a relatively small FSR values of 10 and 15 nm have been considered and the arm lengths are calibrated accordingly. The FSR is calculated as a function of L_{Ref} and L_{Sen} (Eq. 6.19) and the results are shown in Fig. 6.19. The variations indicate that the lower FSR requires higher L_{Ref} for a fixed $L_{MSLHSPW}$. The horizontal black dashed lines indicate the 10 and 15 nm FSR and its corresponding L_{Ref} values for a fixed $L_{MSLHSPW}$. In our design, the L_{Ref} calibration only demands the change in the straight waveguide sections (L_{R1} , L_{R2} , and L_{R3}) as the bending sections of radius $5\ \mu m$ cover a fixed length of $L_B = 31.42\ \mu m$. For the three fixed $L_{MSLHSPW}$ values (20, 30, and $40\ \mu m$) the reference arm length ($L_{Ref} = 2\pi R_B + L_{R1} + L_{R2} + L_{R3}$) with different sections to obtain $FSR = 10$ and 15 nm are tabulated in Table 6.1.

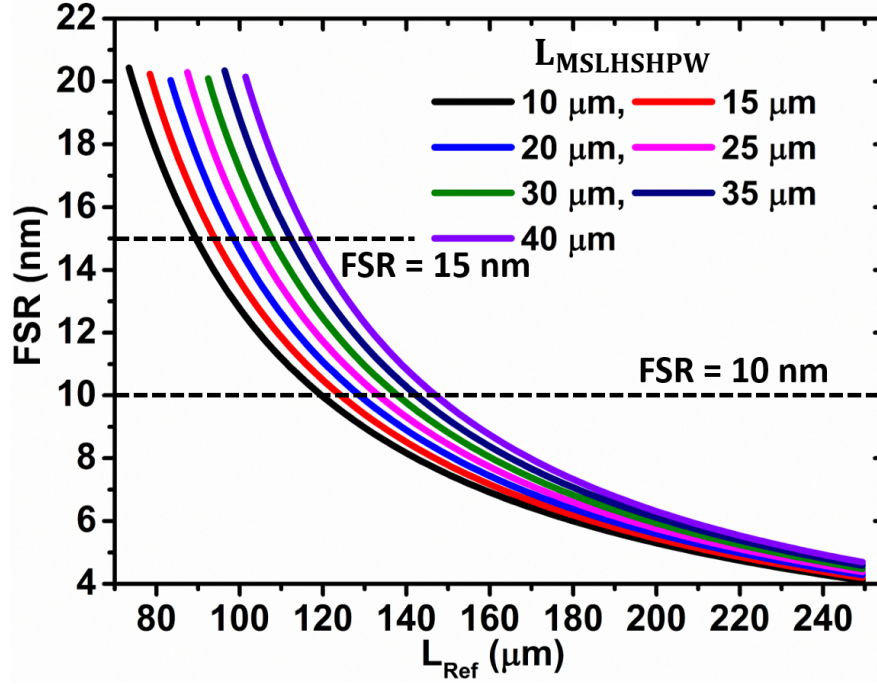


Figure 6.19: illustrates the variation of the MZI FSR as a function of L_{Ref} for fixed length of MSLHSPW.

Table 6.1: Different sections of the MZI arms for calibrations of FSR .

FSR (nm)	$L_{MSLHSPW}$ (μm)	Reference arm sections			L_{Ref} (μm)
		L_B (μm)	$L_{R1} = L_{R3}$ (μm)	L_{R2} (μm)	
10	20	31.42	28.5	20	108.42
	30		38.0	30	137.42
	40		37.5	40	146.42
15	20	31.42	23.5	20	98.42
	30		23.0	30	107.42
	40		22.5	40	116.42

Our aim is to design the MZI for temperature and volume concentration sensing of any liquid. In this study, we have considered liquid isopropanol for our investigations. The quasi-TM effective index difference ($\text{TM}-\Delta n_{eff}$) of the optimised MSLHSPW and the DHS waveguide with the temperature for 100% isopropanol are shown in Fig. 6.20(a). The red line shows a positive and linear Δn_{eff} variation of SiO_2 clad DHS waveguide, whereas, the blue dashed line shows the same Δn_{eff} variation of the MSLHSPW but in the negative direction. The positive and negative $\text{TM}-\Delta n_{eff}$ variations of the MSLHSPW and DHS provide a temperature dependent opposite phase change in both arms which enhance the temperature sensitivity of the complete MZI device. The quasi-TM effective

index variation with temperature (dn_{eff}/dT) of both the MSLHSHPW and DHS are $-4.61 \times 10^{-4}/^\circ\text{C}$ and $+6.62 \times 10^{-5}/^\circ\text{C}$, respectively. The black line in Fig. 6.20(b) represents a negative quasi-TM Δn_{eff} variation of the optimised MSLHSHPW with the volume fraction of isopropanol in the isopropanol/water solution at a fixed temperature, $T = 20^\circ\text{C}$. During volume concentration sensing, the temperature is kept fixed so that the only refractive index change occurs at the MSLHSHPW due to the different concentration of isopropanol in the solution. The refractometric sensitivity of the MSLHSHPW can be evaluated as, $S_{MSLHSHPW} = \Delta n_{eff}/\Delta n = 1.13$. The MSLHSHPW shows a higher refractive index sensitivity compared to a recently published complex hollow hybrid plasmonic design scheme [Sun *et al.*, 2017].

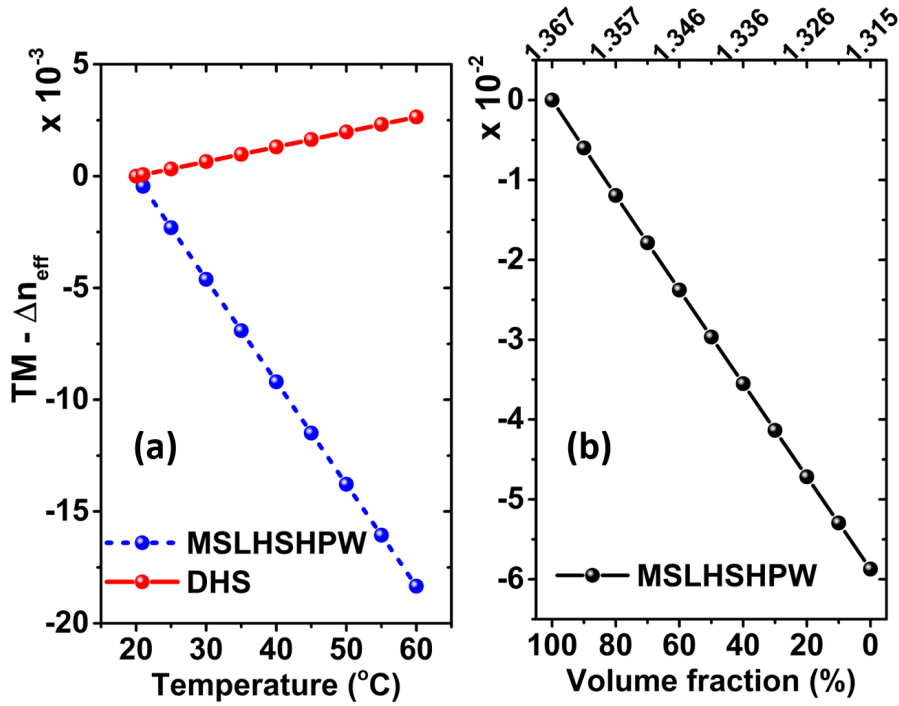


Figure 6.20: illustrates the variation of the MZI FSR as a function of L_{Ref} for fixed length of MSLHSHPW.

6.4.1 Temperature Sensing

Figures 6.21(a), (b), and (c) on left show the transmitted P_{out} spectra for the proposed MZI temperature sensor with $L_{MSLHSHPW} = 20, 30$, and $40 \mu\text{m}$, respectively for $10 \text{ nm } FSR$. Whereas, the figures in the right columns (6.21(d), (e), and (f)) depict the MZI responses for the same three $L_{MSLHSHPW}$ values, but for $15 \text{ nm } FSR$. Different colour

curves signify different temperatures (varied from 20°C to 60°C) of 100% isopropanol infiltrated in the sensing MSLHSPW region. It can be clearly observed that with the temperature increment the MZI transmission spectra show the red shift (towards right) because of a larger TOC of isopropanol compared to other materials such as Si, Ag and SiO_2 . It should be noted that the wavelength shifts ($\Delta\lambda_T$) increase with the increment of $L_{MSLHSPW}$ and FSR . A temperature variation from 20°C to 60°C for the MZI design with $L_{MSLHSPW} = 20, 30$, and 40 μm shows the $\Delta\lambda_T$ of 4.25, 5.66, and 6.87 nm red shift, respectively, for $FSR = 10$ nm. Similarly, for the same temperature variations with aforementioned $L_{MSLHSPW}$ lengths the output transmission spectra are red shifted more by 5.48, 7.43, and 9.76 nm for $FSR = 15$ nm. Device insertion losses for 20, 30, and 40 μm long MSLHSPW have the values around 2.06, 2.32, and 2.58 dB, respectively and the corresponding extinction ratios are larger than 25 dB.

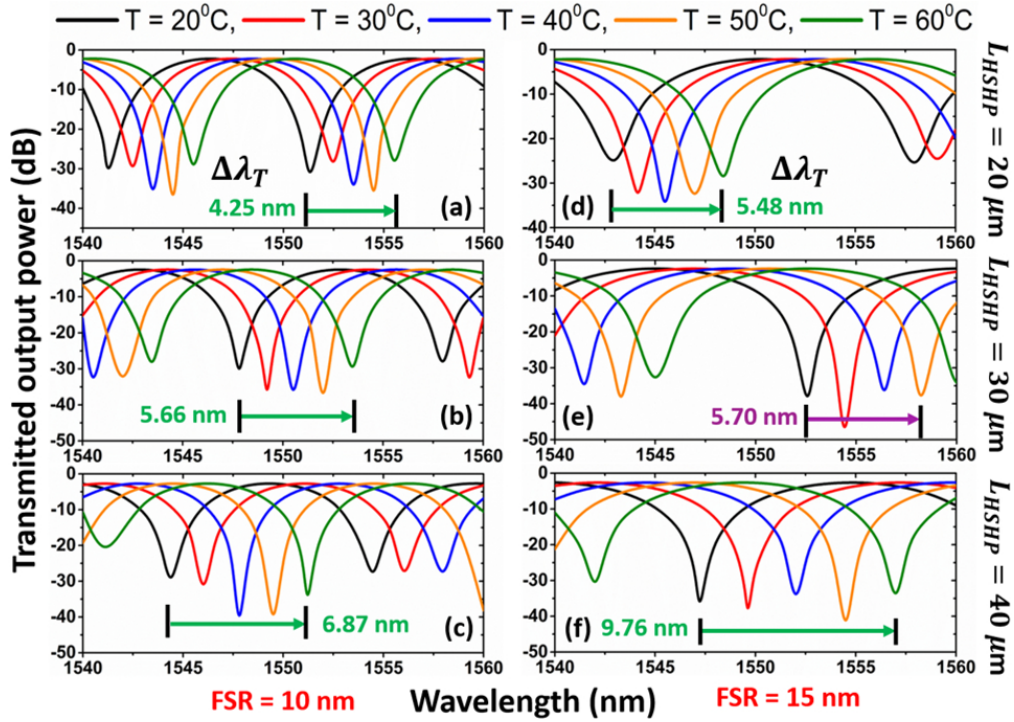


Figure 6.21: (a) - (f) MZI transmitted output power for the temperature sensing of 100% isopropanol liquid. The figures (a), (b), and (c) on the left column indicate the transmission spectra with the FSR value of 10 nm. The right-sided figures (d), (e), and (f) indicate the same with the $FSR = 15$ nm. Figures in each row (a, d), (b, e) and (c, f) depict the output responses of the MZI with 20, 30, and 40 μm long $L_{MSLHSPW}$, respectively.

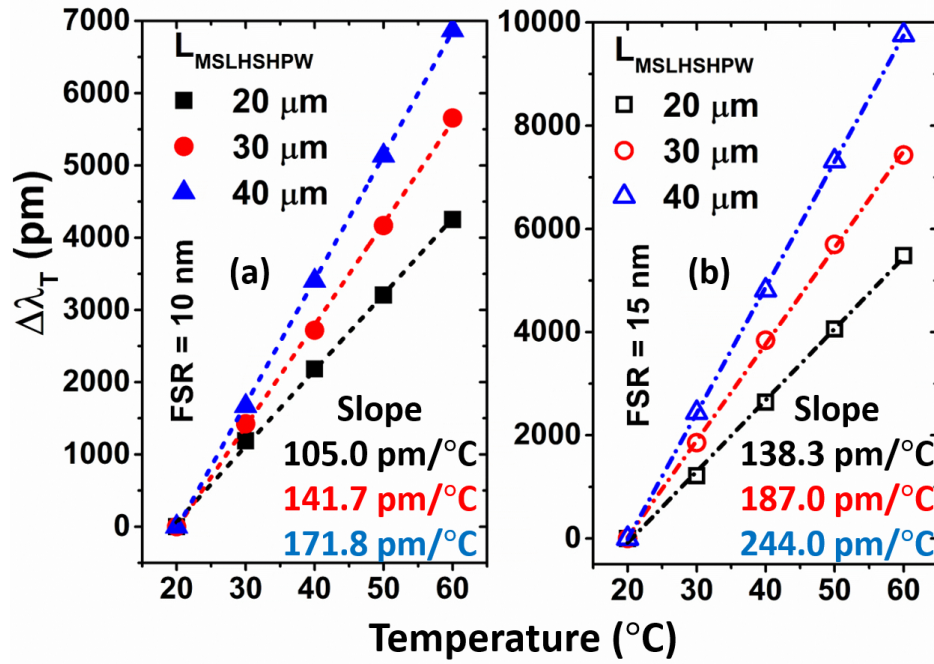


Figure 6.22: (a) and (b) represents the wavelength shift ($\Delta\lambda_T$) variations with the changing temperature of isopropanol for 10 and 15 nm FSR values, respectively. Slope of each curve represent the MZI sensitivity (S_T) as a temperature sensor.

Figures 6.22(a) and (b) illustrate a linear increasing relationship of $\Delta\lambda_T$ with the temperature (T) with 100% isopropanol concentration for 10 and 15 nm FSR , respectively. For the temperature ranging from 20 $^{\circ}\text{C}$ to 60 $^{\circ}\text{C}$, the $\Delta\lambda_T$ increases linearly with the increment of the T for all MZI designs with $L_{MSLHSPW} = 20, 30$, and 40 μm are shown by black, red, and blue lines, respectively. Changes for $FSR = 10$ nm are shown in Fig. 6.22(a) and for $FSR = 15$ nm in Fig. 6.22(b) by dashed and dashed-dotted lines, respectively. The device sensitivities (S_T) sensitivities can be evaluated from the slope of the fitted curves with the R^2 value of 0.999. Thus, for the MZI with $L_{MSLHSPW} = 20, 30$, and 40 μm has the temperature sensitivity (S_T) values of 105.2 pm/ $^{\circ}\text{C}$, 140.6 pm/ $^{\circ}\text{C}$, and 172 pm/ $^{\circ}\text{C}$ for $FSR = 10$ nm, respectively and 138.1 pm/ $^{\circ}\text{C}$, 187 pm/ $^{\circ}\text{C}$, and 243.9 pm/ $^{\circ}\text{C}$, respectively for $FSR = 15$ nm which indicate much higher and promising values compared to recent published results which are 172 pm/ $^{\circ}\text{C}$ in [Guan *et al.*, 2016] and 162.9 pm/ $^{\circ}\text{C}$ in [Zhang *et al.*, 2016]. Additionally, our proposed design is expected to work well in a wide temperature range from room temperature ($\sim 20^{\circ}\text{C}$) to the boiling point of isopropanol (82 $^{\circ}\text{C}$). Moreover, the sensing range (FSR/S_T) of the designed device with $L_{MSLHSPW} = 40 \mu\text{m}$ can be derived for 10 and 15 nm FSR as $\sim 58^{\circ}\text{C}$ and $\sim 61^{\circ}\text{C}$,

respectively. Detection limit (DL_T) is another important characteristic of a sensor that illustrate the efficiency to resolve a smallest refractometric change of the target and it can be defined as the ratio of resolution of the transmission spectra (λ_{Res}) to the device sensitivity (S_T). The λ_{Res} of a device depends not only on the resolution of the source and the measurement equipment (OSA) but also influenced by the extinction of the device and the noise present on the measured spectra. Thus, instead of using a specific λ_{Res} value for a laser source and OSA, we have considered the device λ_{Res} as 1 pm (approx.) for our theoretical investigations and as a result, our design with 40 μm MSLHSPW can have the temperature detection limit or resolution (DL_T) of 0.0058°C and 0.004°C for the 10 and 15 nm FSR , respectively.

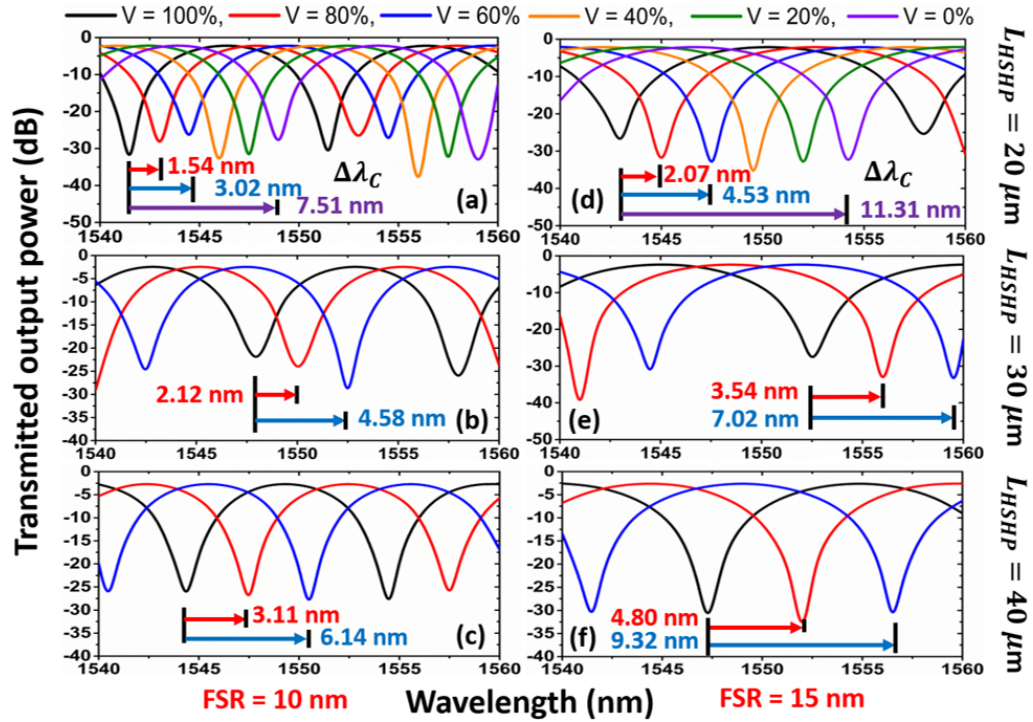


Figure 6.23: (a) - (f) indicate the MZI transmitted spectra for the volume concentration sensing of the isopropanol/water solution at a fixed temperature of 20°C. The figures (a), (b), and (c) on the left column indicate the output transmission spectra with the FSR value of 10 nm. The right-sided figures (d), (e), and (f) indicate the same with the $FSR = 15$ nm. Figures in each row (a, d), (b, e) and (c, f) depict the output responses of the MZI with 20, 30, and 40 μm long $L_{MSLHSPW}$, respectively.

6.4.2 Chemical Sensing

Next, feasibility of the same MZI sensor for the detection of volume concentration of isopropanol in the isopropanol/water solution at a constant temperature is also studied.

For this study, we kept the temperature fixed at the room temperature of 20°C. Figures 6.23 (a) - (c) show the MZI transmission responses of the 20, 30, and 40 μm long MSLHSHPW as a refractometric sensor with the FSR values of 10 nm and 6.23 (d), (e), and (f) for $FSR = 15$ nm. The black spectrum represents the transmission output for 100% isopropanol at $T = 20^\circ\text{C}$. Different colour spectra indicate different volume fraction of isopropanol and they also show a red shift of the wavelength with the isopropanol volume concentration ($\Delta\lambda_C$) which increase with the increment of both the $L_{MSLHSHPW}$ and FSR . The extinction ratios for the device have the values larger than 20 dB and the insertion losses were almost similar as those calculated with 100% isopropanol at $T = 20^\circ\text{C}$.

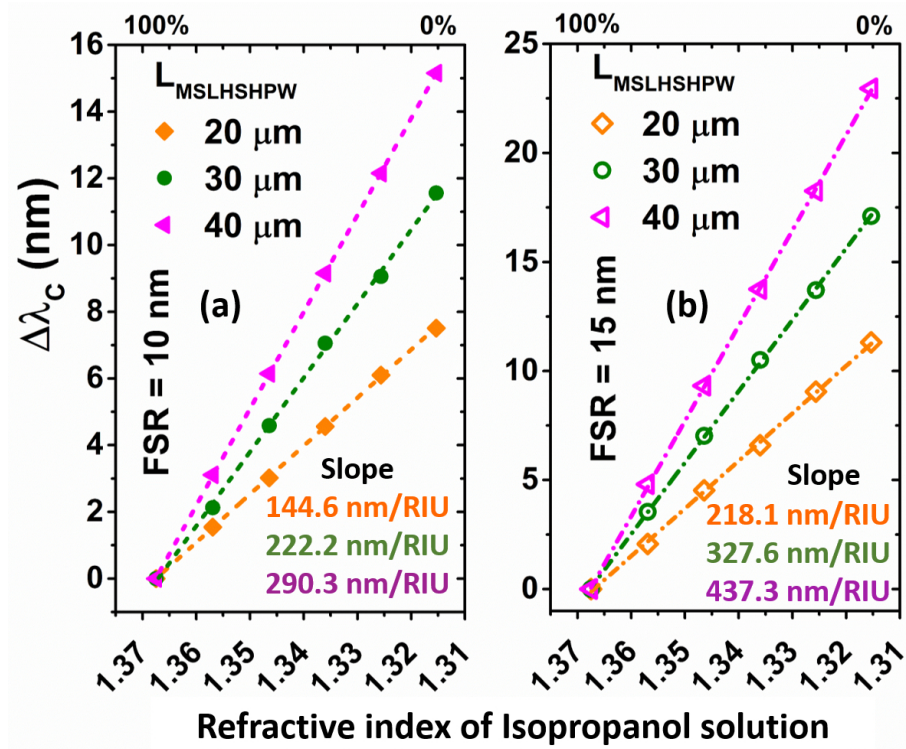


Figure 6.24: (a) and (b) represents the linear variations of wavelength shift ($\Delta\lambda_C$) with the volume concentration of isopropanol for 10 and 15 nm FSR values, respectively. Slope of each curve represent the MZI sensitivity (S_C) as a chemical concentration sensor.

The $\Delta\lambda_C$ s with the refractometric changes of the isopropanol solution are plotted in Figs. 6.24(a) and (b) for 10 and 15 nm FSR values, respectively. It can be observed that the $\Delta\lambda_C$ linearly increases with the reduction of isopropanol volume concentration. The horizontal x-axis indicates the refractive indices of isopropanol/water solution depending on the volume concentration (100% to 0%) of isopropanol. The corresponding concentration

sensitivities (S_C) can be read from the slope of the linearly fitted curves with $R^2 = 0.999$. Thus, for the detection of isopropanol volume concentration, the sensitivity (S_C) of the designed MZI with $L_{MSLHSHPW} = 20, 30$, and $40 \mu\text{m}$ reaches to 144.6 nm/RIU , 222.2 nm/RIU , and 290.3 nm/RIU , respectively for $FSR = 10 \text{ nm}$ and 218.1 nm/RIU , 327.6 nm/RIU , and 437.3 nm/RIU , respectively for $FSR = 15 \text{ nm}$. These results show a great improvement in liquid refractometric sensitivity compared to a recent published experimentally demonstrated hybrid plasmonic waveguide based sensor design with a sensitivity value of 160 nm/RIU [Sun *et al.*, 2017]. It can be noted that the sensitivity increases linearly with the FSR and sensor length, $L_{MSLHSHPW}$. For the same OSA wavelength resolution ($\lambda_{Res} = 1 \text{ pm}$), our MZI sensor with $40 \mu\text{m}$ long MSLHSHPW shows a considerable potential to measure the refractometric changes as small as 3.44×10^{-6} and $2.28 \times 10^{-6} \text{ RIU}$ for the 10 and 15 nm FSR , respectively. These results show an improved refractometric sensitivity compared to the hybrid plasmonic MZI design reported recently [Sun *et al.*, 2017].

6.5 Fabrication Tolerance

A detail study on fabrication tolerance of the proposed design is highly important in order to obtain a stable and robust sensing device. A best design of MSLHSHPW depends on optimisation of waveguide parameters such as Ag layer thickness (H_{Ag}), height (H_{Si}), and width (W_{Si}) of Si slab, and slot height (H_{slot}) to obtain a maximum power confinement in the horizontal slot section. Here, the optimised waveguide design offers 59.24% and 82.04% slot and sensing region (slot+clad) confinement, respectively with the waveguide design parameters such as $H_{Ag} = 150 \text{ nm}$, $W_{Si} = 740 \text{ nm}$, $H_{Si} = 150 \text{ nm}$, and $H_{slot} = 100 \text{ nm}$. Figure 6.11 indicates that the slot confinement (Γ_{slot}) and modal attenuation do not show any significant changes with $\pm 10\%$ of H_{Ag} variation. Although, W_{Si} and H_{Si} are optimised at 740 and 150 nm , respectively, however, it may differ during fabrication processes. Figure 6.13 and 6.14 indicate that the slot region is still capable to confine the light power of $>58\%$ within $\pm 10\%$ of W_{Si} and H_{Si} deviation from their best values. More than 58% of slot confinement results in $\sim 80\%$ power confinement in the sensing (slot+clad) region. It is worth to mention that the thickness of bottom Ag layer (H_{Ag}) and

top Si slab (H_{Si}) are chosen to have a same value of 150 nm to form a symmetric slot structure. One could easily obtain a slightly higher slot confinement (60%) by considering higher W_{Si} and lower H_{Si} . But in this configuration, other higher order modes appear at the close vicinity of the fundamental quasi-TM mode. It makes the device unstable for sensing applications due to its multimode operation. Figure 6.15(a) indicates that $\pm 10\%$ of H_{slot} variation from its optimised value is capable to maintain $>58\%$ quasi-TM slot power confinement. It can be noticed that only $\pm 1\%$ change in slot confinement is obtained with $\pm 10\%$ change in W_{Si} , H_{Si} , and H_{slot} . Therefore, this small change in slot power confinement does not make any significant change in waveguide performance as a sensing device. In this work, we considered three different lengths of the sensing arm such as $L_{MSLHSPW} = 20, 30$, and $40 \mu\text{m}$. The maximum temperature and refractometric sensitivities are obtained for $L_{MSLHSPW} = 40 \mu\text{m}$ which are shown in Fig. 6.22 and 6.24. It is worth noticing that the device sensitivity increases with $L_{MSLHSPW}$ in expenses of additional modal loss that arises due to extra length of the MSLHSPW. Therefore, a 10% increment and decrement in $L_{MSLHSPW}$ will increase and decrease, respectively the temperature and chemical concentration sensitivity by an amount of $\sim 9.34\%$ and $\sim 10.03\%$, respectively.

6.6 Summary

In conclusion, the design of a novel metal strip loaded MSLHSPW with its optimised designed parameters shows an enhanced power confinement of 59.24% and 82.04% in the low-index slot and possible total sensing region along with a low and acceptable loss. By integrating this MSLHSPW with the SiO_2 clad DHS waveguide results in a compact on-chip MZI sensing system, which not only shows a high sensitivity to the liquid temperature but also have a great potential in the detection of the liquid concentration. Waveguide optimisations, junction analyses and device performance have been studied theoretically with our in-house accurate FV-FEM and the LSBR methods. Our optimised MSLHSPW design shows a much higher refractometric sensitivity of 1.13. The MZI temperature sensitivity (S_T) are 105.2 $\text{pm}/^\circ\text{C}$ and 138.1 $\text{pm}/^\circ\text{C}$ for 20 μm long MSLHSPW in the sensing arm for the FSR values of 10 and 15 nm, respectively,

and it can be increased to 172 pm/°C and 243.9 pm/°C with the 40 μm L_{MSLHSHPW} . The same device is also sensitive to the changes of liquid volume concentrations. The device sensitivity (S_C) for concentration detection shows a high value of 144.6 nm/RIU and 218.1 nm/RIU for the 20 μm MSLHSHPW and it shows a significant enhancement to 290.3 nm/RIU and 437.3 nm/RIU for the higher value of MSLHSHPW length (40 μm). The effect of MSLHSHPW modal loss and the junction losses are mitigated by using unequal power splitting at the MZI input which results in very high interference fringe visibility i.e. $V' \simeq 1$. The low insertion loss, high fringe visibility, high extinction ratio and most importantly enhanced sensitivities make the design attractive for use in bio photonics and chemical analysis. Our proposal serves the successful demonstration of an on-chip compact MZI sensor that can be realised with the help of well-matured state-of-the-art CMOS fabrication technologies. Both temperature and concentration sensors can be integrated in an on-chip arrayed design for simultaneous detection of both. Based on the preliminary results this MZI sensor shows a great potential to be employed as an refractometric based temperature and liquid concentration sensor.

VERTICAL SLOTTED STRAIGHT RESONATOR AS A BIOCHEMICAL SENSOR

7.1 Introduction

Fabrication of silicon (Si) waveguides in a silicon-on-insulator (SOI) wafer within the telecommunication wavelength range of 1200 - 1600 nm was first proposed by Richard Soref [Soref and Larenzo, 1986], followed by the initial work of Graham Reed. The high-refractive-index contrast of SOI structures leads to the higher degree of light confinement and guidance through the silicon layer. This property can make the silicon waveguides and resonators to be the basic building blocks of compact photonic integrated circuits (PIC). Over the last two decades, silicon technology has attracted considerable attentions due to its potential low-cost by exploiting the CMOS fabrication technology, developed for electronics, which can also be used by the photonics industries. Light confinement in low-index slot section was first reported in 2004 by Almeida *et al.* [Almeida *et al.*, 2004] and since then SOI based slot waveguide became an intriguing area of research. The boundary condition of electromagnetic field demands normal component of electric flux density (\vec{D}) must be continuous at the dielectric interface, which forces normal component of \vec{E} -field to be discontinuous and very large in the low index region. These characteristics lead to a strong field enhancement in the low-index slot region. As

a result, the slot waveguides becoming an attractive choice as a refractive index (RI) based biological and chemical sensors. By combining the slot properties with resonating devices, an even higher sensitivity can be achieved. Combination of slot configuration with ring resonator was first investigated and proposed in [Barrios *et al.*, 2007a], [Barrios *et al.*, 2008] on a $Si_3N_4 - SiO_2$ platform with a maximum sensitivity of 212 nm/RIU. An improved sensitivity of 298 nm/RIU has also been reported by [Claes *et al.*, 2009] for the similar slot waveguide based ring resonator in SOI platform. These structural devices show significant improvement of refractive index sensitivity over the conventional strip waveguide based ring resonator, demonstrated by [De Vos *et al.*, 2007]. Integration of Bragg gratings on SOI platform with promising application in bio and chemical sensing has also been reported by [Fard *et al.*, 2013], [Jugessur *et al.*, 2009]. The conventional strip and rib waveguide based Bragg gratings use the evanescent field tails for the sensing, thus exhibiting a lower sensitivity with high quality (Q) factor. In 2013, [Wang *et al.*, 2013b] proposed an improved slot waveguide based Bragg sensors with sensitivity as high as 340 nm/RIU around 1550 nm wavelength with the help of enhanced light matter interaction into the slotted region. Next, in 2015, an improved bulk detection sensitivity (380 nm/RIU) of porous silicon ring resonator for biosensing applications has been reported by [Rodriguez *et al.*, 2015]. Other optical bio-chemical sensors have incorporated microdisk resonator [Lipka *et al.*, 2013], photonic crystal cavities [Caër *et al.*, 2014], [Yang *et al.*, 2016] and Mach-Zehnder interferometers [Luff *et al.*, 1998], [Misiakos *et al.*, 2014].

In this chapter, a detailed theoretical and numerical investigations of three dimensional single vertically-slotted resonator structure in a SOI platform are discussed. An in-house numerically efficient and rigorous three dimensional full-vectorial \vec{H} -field based finite element method (3D-FEM) is developed and used to obtain the modal solutions at the particular resonating wavelength. Initially, optimisations of design parameters, such as the width (W), height (H) and slot width (W_s) are carried out by a two dimensional full-vectorial \vec{H} -field based finite element method (2D FV-FEM). Only a cross-section of the device is considered for modal solutions. However, to investigate a resonating structure one need to simulate the complete three-dimensional structure as a whole. Thus, the optical resonating structure with isotropic and anisotropic media requires a new three-dimensional approach where the variational expression calculates the resonant

frequencies and associated vectorial mode profile of the cavity. The resonating modal fields, sensitivity (S) and detection limit (DL) of the proposed optimised device have been calculated by the full-vectorial 3D-FEM. Interestingly, we observed an effective change in sensitivity from 635 nm/RIU to 820 nm/RIU depending on the position of the perfect electric wall (PEW) in the device. As the detection limit (DL) of the sensor device is inversely related to the sensitivity (S), the changes in sensitivity due to metal boundary position also makes a noticeable change in the detection limit (DL). Such a high sensitivity and detection limit achieved by proposed device can be invaluablely important in the field of chemical sensing. We have validated this phenomenon with sucrose solution at ambient temperature (20°C). It has been noticed that bio-molecules become transparent in the near infra-red region (NIR). Hence the dominated optical absorption is governed by the water solvent which shows a dip in the absorption spectrum at 1550 nm wavelength. Hence we selected the operating wavelength of the device for bio-chemical sensing around 1550 nm, the standard telecommunication wavelength, which adds an extra advantage of availability of standardised resources of the telecommunication band to design the nano-structured sensing set-up.

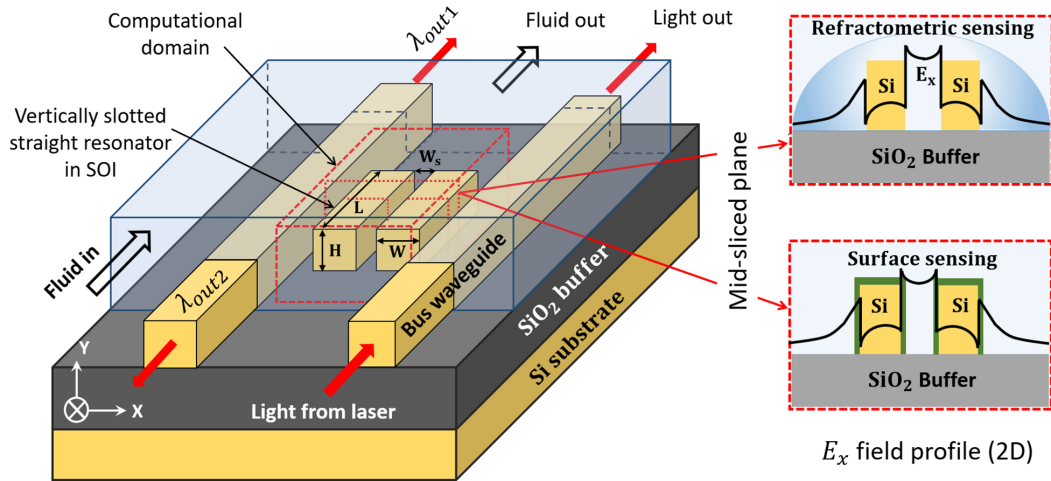


Figure 7.1: 3D schematic diagram of the single vertically-slotted straight SOI based resonator. Red dashed box is showing the computational domain. Insets are showing the mid-sliced plane with dominant E_x field profile along x-axis shown by black lines.

7.2 Vertical Slotted Straight Resonator

Figure 7.1 shows the 3D schematic diagram of our proposed device design. The main structure which is of our interest consists of two silicon cores separated by a narrow slot region shown by dashed red box. The compact vertically slotted straight resonating structure is coupled with two in and out integrated bus waveguides. Light from a tunable laser source travels through one bus waveguide and excites the slotted structure at a particular wavelength. Corresponding resonating wavelength (λ_{res}) can be picked by the three output facets of the in/out bus waveguides. During the resonance, electromagnetic energy builds up in the slot cavity and the resonance wavelength can be detected from the both facets of output bus waveguide (λ_{out1} and λ_{out2}) and also at the opposite end of the input bus waveguide. The response from the output integrated waveguide is detected by the photo-detectors. The silicon slot guide is separated by a silicon dioxide (SiO_2) buffer layer from the silicon substrate. The silicon and silicon dioxide refractive indices are taken as $n_{Si} = 3.476$ and $n_{SiO_2} = 1.44$, respectively at the 1550 nm operating wavelength. The key noticeable advantages of the proposed device can be explained in three steps. First, the compact design of the device due to nano-scale dimensions results high scale integration and ease of fabrication than other complex devices. Second, the slotted resonating structure has a significant advantage over the conventional rib and nano-wire structures. The dominant E_x field of the quasi-transverse-electric (TE) mode increases inside the slot region which allows a strong light-analyte interaction rather than to use only the evanescent field tail for sensing. Third, a much improved performance e.g. sensitivity (S) and detection limit (DL) can be achievable with the help of first two points. The slot and the surrounded region can be filled with any low-refractive-index, non-linear and organic material of one's interest. Here, the efficiency of the proposed device is presented by using the low-indexed sucrose solution in the slot and cover medium which represents the 3D slotted resonating structure as a bulk refractometric chemical sensor (upper inset of Fig. 7.1). We have also characterised the device as a bio-sensor dipped into water, where a 5 nm ultra-thin (T_s) bio-layer with refractive index 1.45 has been considered. Here the device performance has been analysed as a surface sensor (lower inset of Fig. 7.1)

The fabrication process of our CMOS compatible proposed straight device without a curved ring section can be simple compared to other alternative photonic sensing devices. Silicon vertically-slotted structure can easily be fabricated by etching two straight Si rails into a commercially available SOI wafer. Besides, if required further growth of top Si layer on SiO_2 buffer layer can be achieved by the plasma enhanced chemical vapour deposition (PECVD). The height of the Si layer can be adjusted by precise controlling the growing time or by reducing it. A photo-resist thin film can be deposited on the Si layer for patterning. Then reactive ion-etching (RIE) is used to make the both Si strips with a slot region in between them.

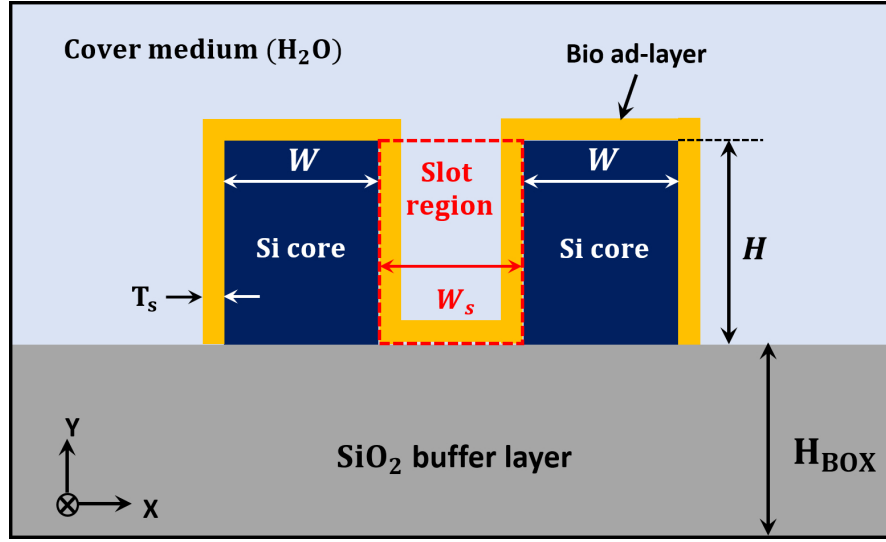


Figure 7.2: Cross-section of the 3D vertically slotted straight resonator. The x-y plane cross-sectional geometry of the device is similar to the vertically slotted waveguide.

7.2.1 Design and Optimisation of Device Parameters

The rigorous theoretical investigation of design parameters, calculation of dominant and non-dominant electric and magnetic field components and profiles for the fundamental quasi-TE and TM modes, due to the presence of sensing material with different refractive index values, are of great importance when designing a sensing device. Our in-house two dimensional (2D) (discussed in Section 3.3) and newly developed three dimensional (3D) finite element method (FEM) (discussed in 3.4) are used as numerical tools to obtain the modal solutions of the Si slotted resonator. The 3D slotted resonator is similar to a short length of straight vertical slot waveguide. Cross-section of the slotted resonator is shown

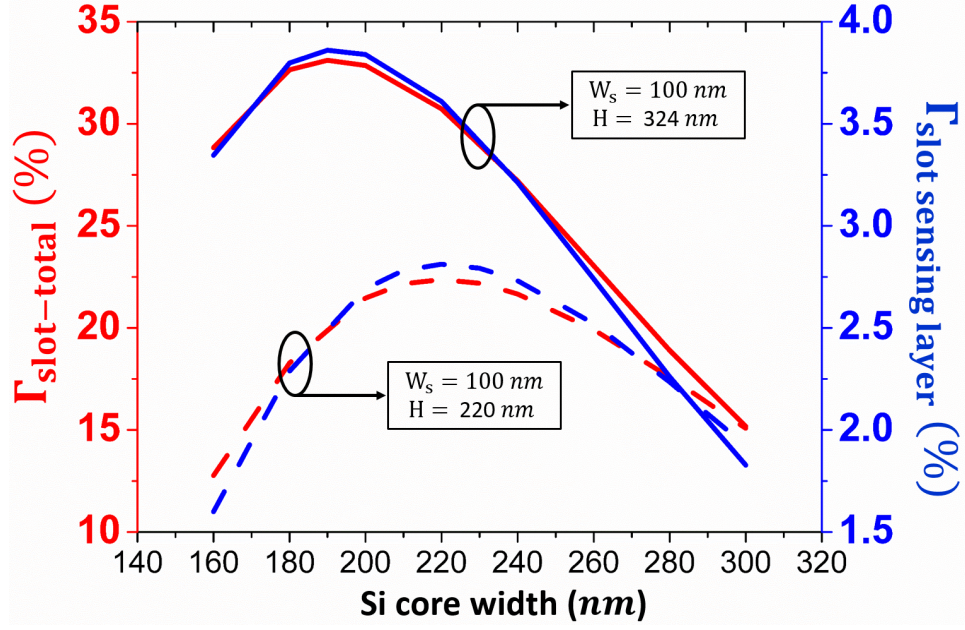


Figure 7.3: Optimisation of Si core width (W) depending on confinement factor (Γ). Total slot confinement ($\Gamma_{slot-total}$) and confinement of 5 nm sensing layer into slot versus Si core width (W) for a fixed Si core/slot height (H) of 220 and 324 nm. Slot width (W_s) is kept fixed at 100 nm. The cover medium, slot region, and sensing layer into slot are filled with water.

in Fig. 7.2. As a result, a part of the design parameters that lie on the x-y cross-sectional plane can be estimated by using the computationally efficient fully-vectorial rigorous 2D FV-FEM.

A 5 nm sensing layer (T_s) over the Si core and also inside the slot region is considered for bio-molecule detection, as shown in Fig. 7.2. The Si core width (W), slot height (H) and slot width (W_s) are optimised for different parameters, such as the power confinements into low-indexed slot and 5 nm sensing bio-layer into the slot region, normalised power density (NPD) and effective index (Δn_{eff}) change. The normalised power density (NPD) is defined as the power confinement per unit area of the waveguide. The Δn_{eff} is the change in the effective index (n_{eff}) due to the presence of 5 nm molecular bio ad-layer.

Figure 7.3 shows variation of the power confinement in the slot ($\Gamma_{slot-total}$) and 5 nm sensing layer ($\Gamma_{slot\ sensing\ layer}$) with the Si core width (W) by red and blue lines, respectively. The solid and dashed lines show the power confinement variations for two different sets of Si core heights, $H = 220$ and 324 nm, respectively. For both the cases, the slot width (W_s) is kept constant, $W_s = 100$ nm. When the core is wide enough,

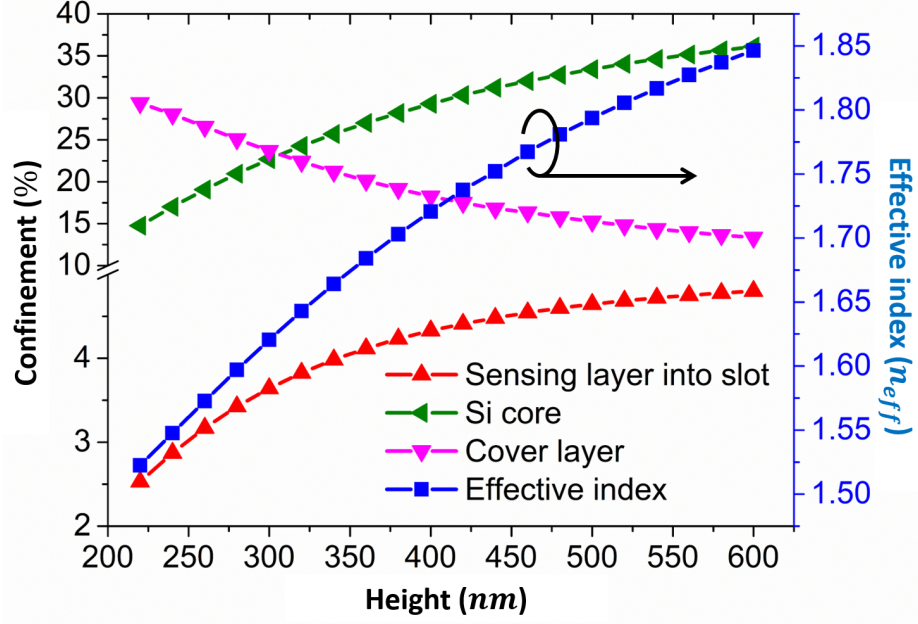


Figure 7.4: Left side scale shows the power confinement ($\Gamma\%$) variation of different regions, such as sensing layer into slot, Si core, and cover medium with Si core or slot height (H). Right side scale shows the effective index (n_{eff}) variation with H . The Si core width (W) and slot width (W_s) are fixed at 190 and 100 nm. A 5 nm ultra-thin bio-layer is considered for surface sensing.

the power confinement into Si core is large and this in turn results a low confinement into slot region. It can be observed that with the reduction of the core width (W), the confinements increase in the slot and reach their maximum values at $W = 190$ nm and $W = 220$ nm for $H = 324$ nm and $H = 220$ nm, respectively. Subsequently a rapid fall of confinement in slot region is also noticeable with further reduction of W as the guided slot mode approaches to the cut-off and power moves to substrate and cover layer. The power confinement of sensing layer into slot region ($\Gamma_{slot\ sensing\ layer}$) also shows similar trend as that of $\Gamma_{slot-total}$.

The effect of the Si core or slot height (H) variation has been studied and corresponding results are shown in Figs. 7.4 and 7.5. The effective index (n_{eff}) variation of the slot waveguide depending on H is shown blue curve with square markers in Fig. 7.4. As the Si core height increases the n_{eff} of the waveguide gradually increases for a fixed $W = 190$ nm and $W_s = 100$ nm. Increasing Si core height confines more light into high index dielectric medium, thus, power confinement of Si core, shown by the green line increases with increasing H . The magenta line depicts a decreasing nature of power confinement

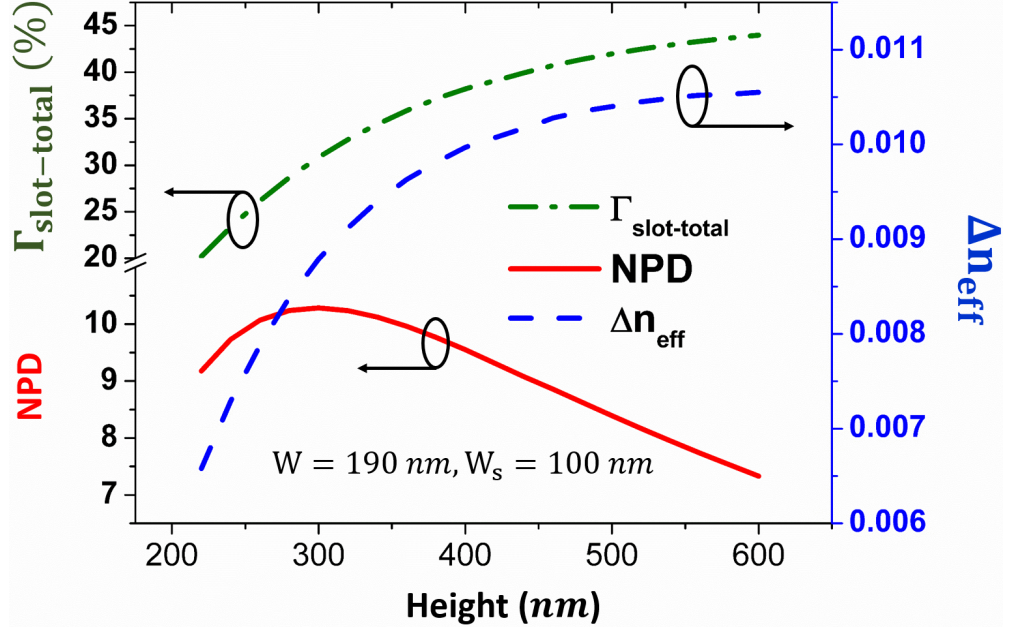


Figure 7.5: Si core or slot height (H) optimisation depending on confinement factor (Γ), normalised power density (NPD) and Δn_{eff} . The green dashed-dotted, blue dashed, and red solid lines depicts the variation of total slot confinement ($\Gamma_{slot-total}$), Δn_{eff} , and normalised power density (NPD), respectively with slot height (H). The Si core width (W) and slot width (W_s) are kept fixed at 190 and 100 nm, respectively. The cover medium, slot region, and the sensing layer into slot are filled with water.

in the cover medium with increasing H . Interestingly, light confinement in the sensing layer into slot region shows a rapid increment at lower values and almost saturates with higher values of Si core height (H).

To find out an optimised Si core or slot height (H), the variations of total slot confinement ($\Gamma_{slot-total}$), normalised power density (NPD) in the slot and change of waveguide effective index (Δn_{eff}) with H are of high important. These results are shown in Fig. 7.5. Partially optimised core width (W) is taken as 190 nm and slot width as 100 nm. The green dashed-dotted line shows the increment of total power confinement into slot region ($\Gamma_{slot-total}$) with H . Normalised power density (NPD) is another important design parameter in sensing device optimisation, when especially a localised high power confinement is exploited, such as an ultra-thin bio or chemical layer in the slot region. The variation of normalised power density (NPD), shown by a red solid curve, initially increases as slot height (H) increases and reaches a maximum value at $H = 300$ nm. But with the further increment of H , the normalised power density (NPD) decreases. On the other hand, variation of effective index shift (Δn_{eff}) due to the presence of a 5 nm

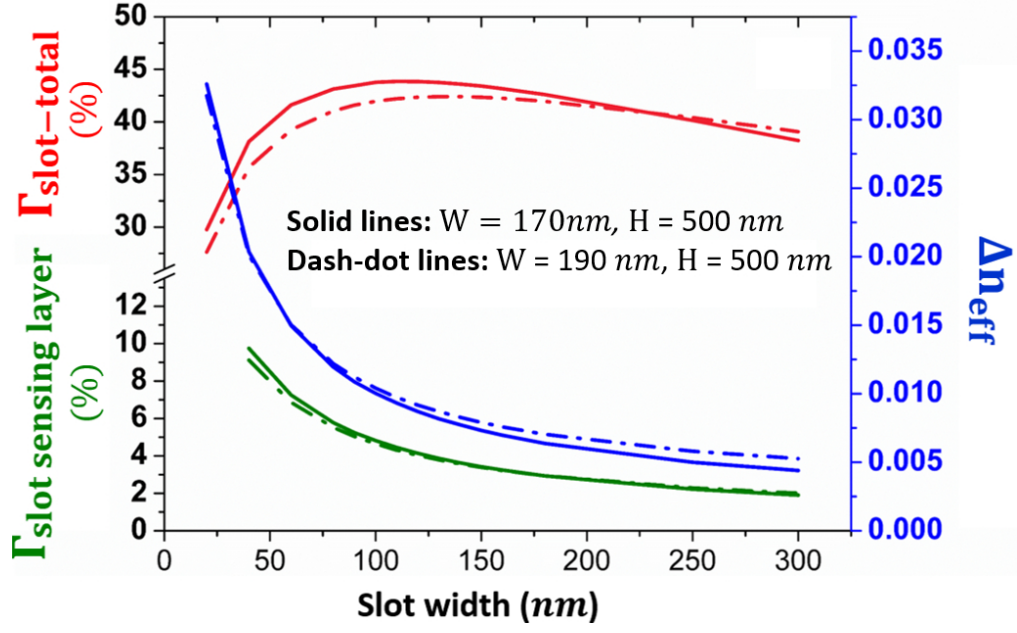


Figure 7.6: Optimisation of slot width (W_s). The solid lines (red, green, and blue) illustrates the variation of $\Gamma_{slot-total}$, $\Gamma_{slot\ sensing\ layer}$, and Δn_{eff} with W_s for $W = 170\text{ nm}$ and $H = 500\text{ nm}$ and the dashed-dotted lines (red, green, and blue) depicts the same for 190 nm Si strip width (W) and 500 nm height (H).

thick molecular bio-layer with H is a key design parameter for surface sensing, shown by a blue dashed line. The variation of Δn_{eff} with the H shows a strong correlation with the $\Gamma_{slot-total}$ variation. Both the parameters increase, as the slot height (H) increases. Although, generally SOI structures with $H = 220\text{ nm}$ is more widely used, however, as it is shown here that higher heights yield better sensors, so optimised slot height for our device is taken as 500 nm , which would be easy to fabricate [Yang *et al.*, 2008], yields $\Gamma_{slot-total} = 41.965\%$ and $\Delta n_{eff} = 0.0104$.

So far we kept the slot width (W_s) fixed at 100 nm , as it was theoretically optimised for slot waveguide based homogeneous sensor [Dell'Olio and Passaro, 2007] and also successfully used in label-free slot based ring resonator for bio sensing application [Claes *et al.*, 2009]. However, the slot width (W_s) variation with optimised W (190 nm) and H (500 nm) shows the maximum $\Gamma_{slot-total} = 42.405\%$ at a slightly wider slot width, $W_s = 130\text{ nm}$, shown by a red dashed-dotted line in Fig. 7.6. Here the confinement of sensing layer into slot ($\Gamma_{slot\ sensing\ layer}$) with green dashed-dotted line and effective index change (Δn_{eff}) with blue dashed-dotted line shows a strong correlation and both of them decrease with the increment of slot width (W_s). As a very small slot width may not easy to fabricate,

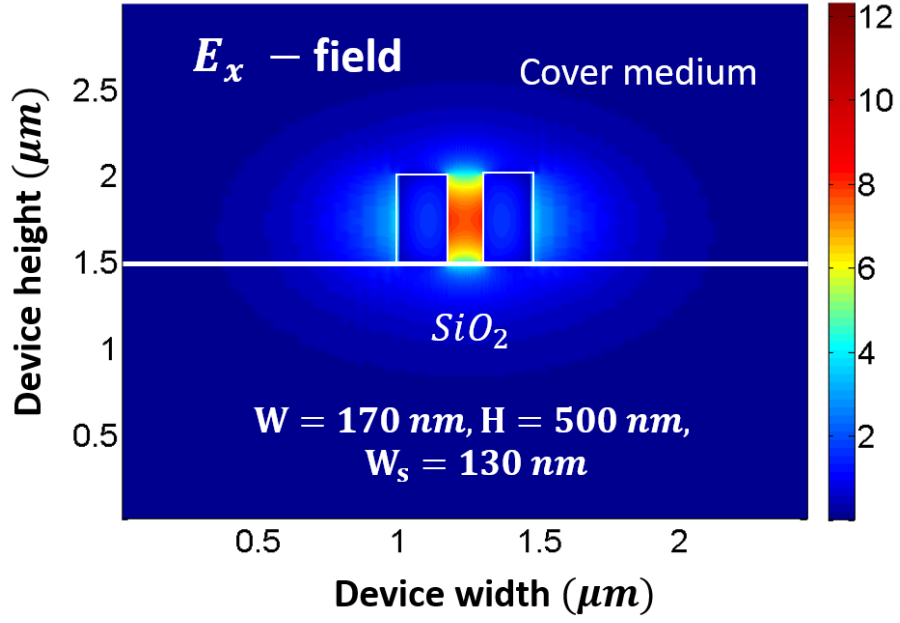


Figure 7.7: Enhanced E_x field into slot region for optimised structural dimensions: Si strip width (W) = 170 nm, height (H) = 500 nm, and slot width (W_s) = 130 nm. Full-vectorial 2D FV-FEM code is used for simulation.

hence total confinement into slot ($\Gamma_{slot-total}$) can be taken as a critical factor. A further investigation of $\Gamma_{slot-total}$ variation with W by keeping W_s and H fixed at 130 and 500 nm, respectively, gives only a small change in earlier optimised W and shows maximum confinement ($\Gamma_{slot-total} = 43.751\%$) at $W = 170$ nm. The red, green and blue solid lines in Fig. 7.6 shows the $\Gamma_{slot-total}$, $\Gamma_{slot\ sensing\ layer}$ and Δn_{eff} variations with the slot width (W_s), for $W = 170$ nm and this set suggests to a new value, $W_s = 110$ nm when $\Gamma_{slot-total}$ becomes maximum. As there was not much difference in $\Gamma_{slot-total}$ for $W = 170$ and 190 nm and a few nm extra slot width which may also be convenient for fabrication, we have finalised the optimised slot width as 130 nm. Hence all the optimised 2D design parameters of slot structure can be taken as, $W = 170$ nm, $H = 500$ nm, and $W_s = 130$ nm when the cover medium and the slot region is considered to be filled up with aqueous solution of refractive index 1.33. The full-vectorial 2D FV-FEM has again been applied to determine the effective index (n_{eff}) of the optimised structure and this value is 1.63827. The corresponding 2D E_x field profile is shown in Fig. 7.7. The 1D line plot of the normalised E_x and H_y field of the quasi-TE mode are shown in the Fig. 7.8(a) and (b), respectively. In the low index slot section, the normal component of the \vec{E} -field i.e. E_x component shows discontinuity at the high index contrast boundaries. Thus, a sharp peak

due to enhance light confinement can be observed in low indexed slot region, highlighted in violet in Fig. 7.8(a). However, the E_x field shows an uninterrupted continuous field distribution along y-axis with a peak inside the slot (Fig. 7.8(b)). Thus, the dominant E_x field of the quasi-TE mode of the vertical slot has an enhanced and very high field confinement in the low index slot region. Throughout these 2D FV-FEM simulations, the structure is discretised with 1,280,000 first order triangular elements.

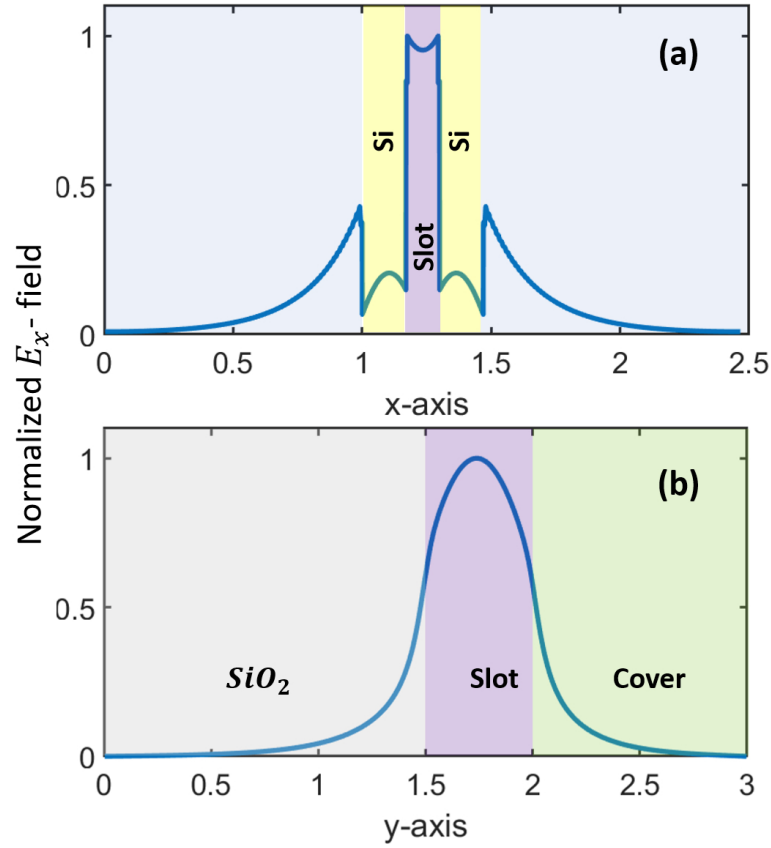


Figure 7.8: (a) and (b) illustrate the 1D line plot of the normalised E_x field of the vertically slotted quasi-TE mode along x and y-axes, respectively. Field plots are generated by 2D FV-FEM simulations.

Next, we design the vertically slotted resonating structure using the optimised W , H , and W_s (Fig. 7.1) discussed above. The slot supports longitudinal modes that resonance at a specific wavelength (λ_{res}) as,

$$\lambda_{res} = \frac{2 \cdot L \cdot n_{eff}}{m} \quad (7.1)$$

here m is the longitudinal mode order inside the cavity ($m = 1, 2, 3, \dots$) and $2L$ denotes

the round trip length of the electromagnetic wave in the resonator. As the fundamental mode is expected to be more stable and sensitive than other higher order modes, we calculate the length (L) of the slot resonator using Eq. 7.1 for the fundamental mode ($m = 1$). Finally, all the device dimensions have been considered can be summarised as, Si core width (W) = 170 nm, slot height (H) = 500 nm, slot width (W_s) = 130 nm and the device length (L) = 473.06 nm for the expected resonating wavelength (λ) of 1550 nm. Typical waveguide loss for vertical slots have been measured as < 20 dB/cm [Barrios *et al.*, 2007b]. However, water also absorbs light at 1550 nm and this value has been given as 47.5 dB/cm [Claes *et al.*, 2009]. In our design, nearly 20% of the power is confined in the water cladding, similar as reported in [Claes *et al.*, 2009]. So for the vertical slotted resonator shorter than 1 μ m, as reported here, the propagation loss of the slotted structure will be very small and neglected in our simulations.

In and out straight bus waveguides can be used to connect the resonator cavity with the light source and detectors. A phase matched Si strip waveguide of width 218 nm and height 500 nm can be used as bus, shown in Fig. 7.1. The gap between resonator and adjacent bus waveguide can be within the range of 250 nm to 400 nm to achieve a good coupling. Alternatively, to maintain the phase matched condition, a slot waveguide having the same dimensions: $W = 170$ nm, $H = 500$ nm, and $W_s = 130$ nm can also be used as bus waveguide. A rigorous least-squares boundary residual (LSBR) method is used to calculate the power transfer, the back reflection coefficient (ρ_r) and transmission loss of the butt coupled strip waveguide and slotted resonator for different gaps. For three different gaps 250, 300, and 400 nm, the power transfer from strip to slot resonator are 1.67%, 1.12%, and 0.512%, respectively. Some input signals also reflected from the junction between the input guide and the resonator section with slot guide and these reflection coefficients (ρ_r) have been calculated as 0.024, 0.020, and 0.012, for separations 250 nm, 300 nm, and 400 nm, respectively. On the other hand, the coupling losses at this junction are also calculated by using the LSBR method. These coupling losses are 0.2886 dB, 0.1956 dB, and 0.0833 dB for separations 250 nm, 300 nm, and 400 nm, respectively. It can be noted that 250 nm gap provides higher evanescent coupling to slot waveguides but with also higher butt-coupling loss from the input guide, whereas the 400 nm gap provides less evanescent coupling but with a higher butt-coupling efficiency. Thus a

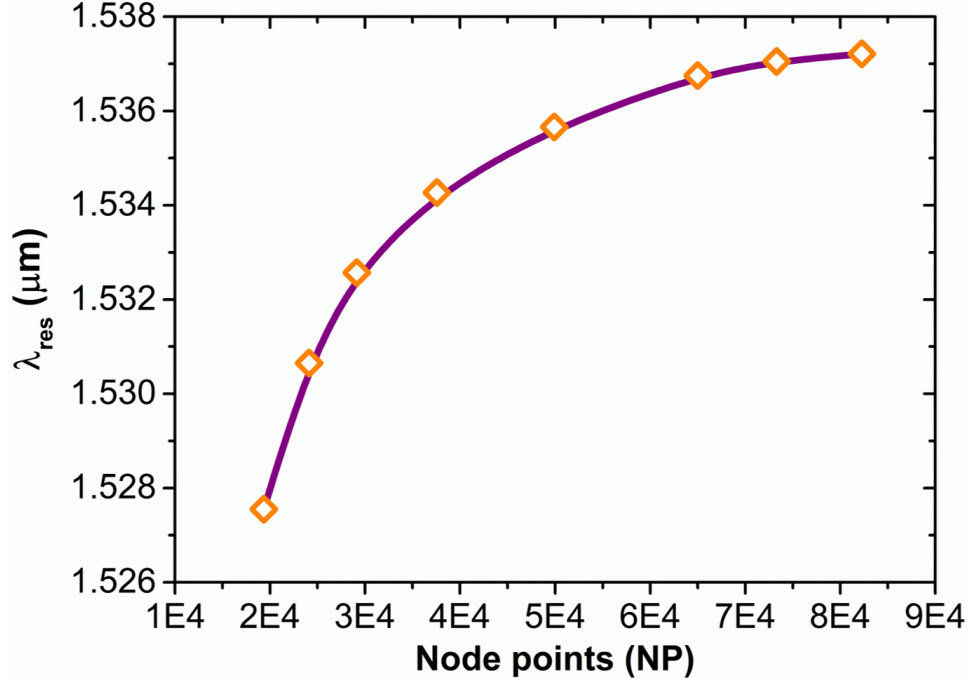


Figure 7.9: Resonating wavelength (λ_{res}) variation with the number of nodes in the three dimensional mesh distributions. A non-uniform, unstructured tetrahedral elements have been used for the 3D domain discretisation.

suitable separation could be in the range of 250 to 400 nm to couple light wave in between resonator and in/out bus waveguide.

7.3 Device Performance as a Sensor

In a resonating structure the self-consistent field gets confined and oscillates at a particular frequency, hence the basic performance investigation requires complete three dimensional field analysis of the quasi-TE and TM modes inside the resonating structure. For the present work, a dedicated rigorous and full-vectorial \vec{H} -field based three dimensional finite element (3D FV-FEM) code is developed to solve the problem. The 3D computational domain of the resonating structure is discretised with small tetrahedral elements. Instead of uniform meshing, a non-uniform, unstructured mesh distribution is considered for 3D FV-FEM, which results in an accurate and stable solution. Figure 7.9 shows the variation of the solution (here λ_{res}) with 3D mesh size. Node numbers (NP) increases with the numbers of tetrahedral elements i.e. the 3D mesh refinement. The 3D FV-FEM solution, λ_{res} shows a rapid increment in the beginning and then saturates with

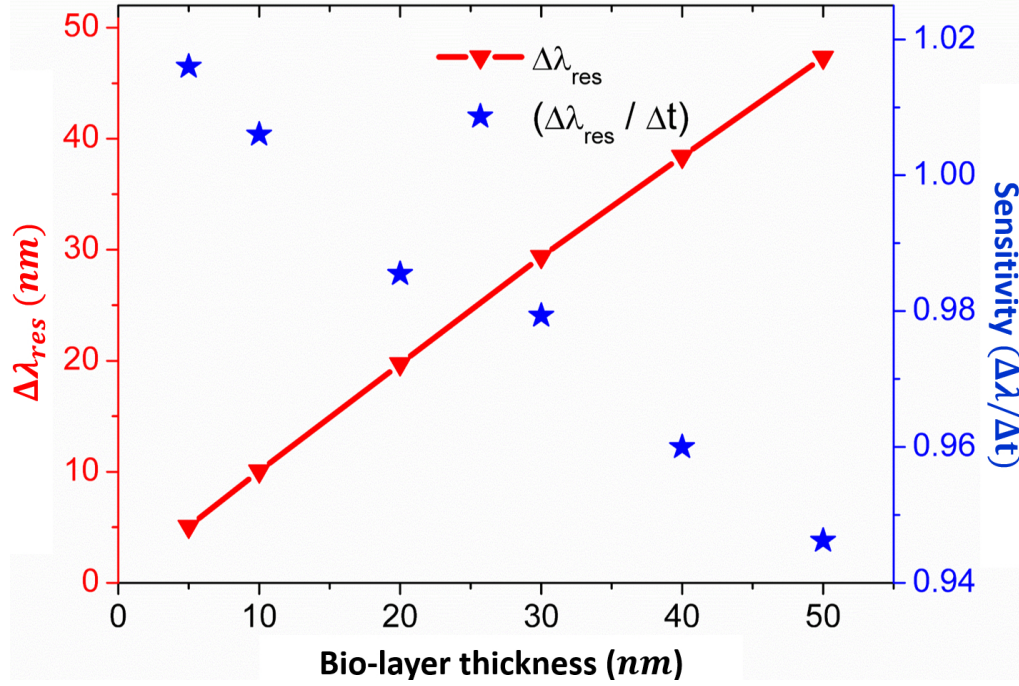


Figure 7.10: Surface sensing of the proposed device with optimised design parameters. The red line depicts a linear resonance wavelength shift ($\Delta\lambda_{res}$) for different bio-layer thickness of refractive index 1.45. The blue stars denote the surface sensitivity ($S_{surface}$) variation with bio-layer thickness ranging from 5 to 50 nm.

the increasing mesh size. Thus, a higher mesh with node numbers greater than 70,000 results in a much stable and accurate solution. Throughout the analyses, a 3D mesh with very high and sufficient number of tetrahedral elements ($NP = 82,273$) are considered to achieve a more stable and accurate resonating wavelength (λ_{res}) of the straight resonator.

We divided the performance analyses into two stages:

1. surface sensing with an ultra-thin bio-molecular layer covers the sensor surface (see Fig. 7.1, bottom inset)
2. homogeneous refractometric sensing (see Fig. 7.1, top inset), where sensitivity for bulk refractive index change in surrounding medium is considered.

7.3.1 Surface Sensing

The first stage of investigation is based on homogeneous bio-layer sensing where we considered a thick bio ad-layer of refractive index 1.45 on both the Si strips and inside the slot region. The cover medium is filled with aqueous solution ($n_{water} = 1.33$). For detail

analysis we have also considered different thickness of sensing layers ranging from 5 to 50 nm. During the 3D FV-FEM simulations, we have verified the numerical accuracy by considering over 4,56,817 first order tetrahedral elements in the computational domain of $1.47 \mu\text{m}$ (along x) \times $0.47306 \mu\text{m}$ (along y) \times $1.5 \mu\text{m}$ (along z). A resonating wavelength shift from 1537.21 nm to 1542.38 nm was observed due to the presence of ultra-thin 5 nm sensing layer with refractive index of 1.45. Hence, the refractive index change in the sensing layer causes a resonance shift ($\Delta\lambda_{res}$) of 5.2 nm for surface sensing. We have also studied the surface sensitivity ($S_{surface}$) for different bio-layer thickness. The $\Delta\lambda_{res}$ linearly increases with the thickness of sensing layer. This is shown by a red solid line in Fig. 7.10, depicts a strong linear resonance shift ($\Delta\lambda_{res}$) with bio-layer thickness change (Δt). The blue stars denote the variation of surface sensitivity,

$$S_{surface} = \frac{\Delta\lambda_{res}}{\Delta t} \quad (7.2)$$

against different bio-layer thickness, plotted in a high resolution scale. A small reduction of $S_{surface}$ can be observed with the increment bio-layer thickness. Our simulation shows almost similar sensitivity as reported in [Claes *et al.*, 2009] but in our case with a simpler straight structure.

7.3.2 Bulk Refractometric Sensing

The second stage of sensitivity investigation follows the detection of bulk refractive index change in the cover and slot region. Aqueous sucrose solutions with different concentrations are used over the sensing device. The refractive index of sucrose-water solution for different sucrose concentration at ambient temperature (20°C) are taken from [Sucrose Conversion Table, 1981]. Two different cases are considered during simulation process:

1. the slot region and cover medium are completely filled with the fluid, and
2. only cover medium is filled with sucrose solution and it is assumed that the narrow slot region is filled with air bubble.

In the present formulation, the natural boundary condition is that of a perfect electric wall (PEW). If the structure is enclosed inside a metal box, then we do not need to impose

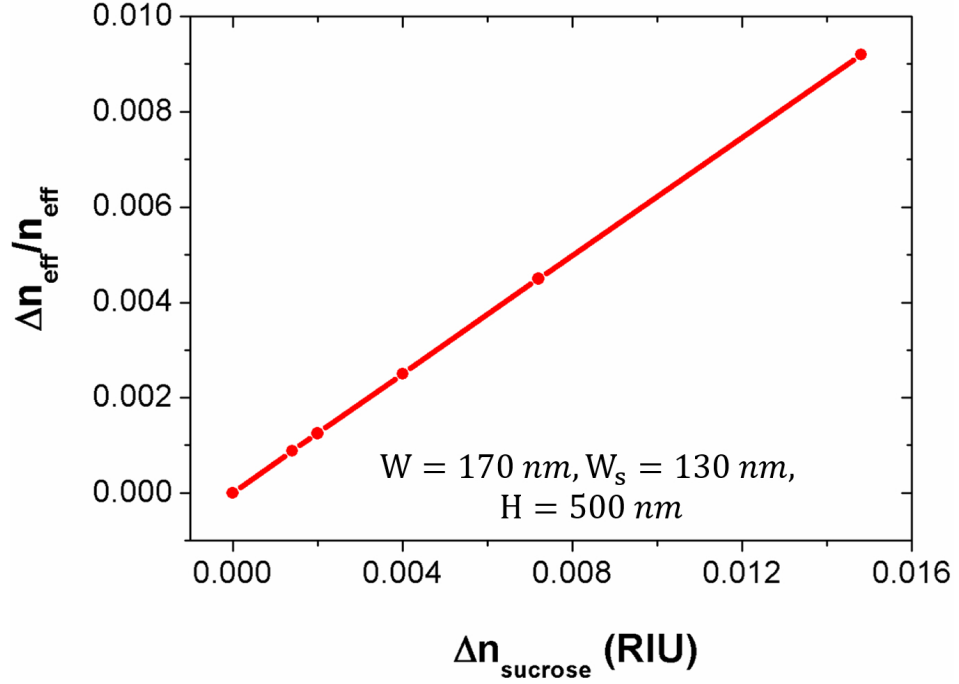


Figure 7.11: Bulk refractometric sensitivity (S) analysis of vertically single slotted waveguide with optimised design parameters at 1550 nm. The slope of the curve denotes the sensitivity of the slot waveguide while the cover medium is filled with sucrose solution.

the boundary condition. However, for an open type resonating structure, the computational boundary should be away from the resonating structure. The bulk sensitivity (S_{bulk}) also depends on the position of computational or physical electric wall. Figure 7.11 depicts the bulk refractive index sensitivity of the optimised single vertically-slotted waveguide simulated by 2D FV-FEM. The variation of normalised effective index change ($\Delta n_{\text{eff}}/n_{\text{eff}}$) with different refractive indices of sucrose solution is presented by the red solid line. The slope gives us the sensitivity $S_{\text{bulk}} = (\Delta n_{\text{eff}}/n_{\text{eff}})/\text{RIU}$ of 1.025 per RIU.

Figure 7.12 shows the resonance wavelength shift ($\Delta\lambda$) of the resonating structure as a function of refractive index of sucrose solution at 20°C. The solid line shows the variation of resonance wavelength shift ($\Delta\lambda$) with the change of refractive index of sucrose solution when the PEWs are placed at both end faces of Si strips. A strong linear shift is observed, and the slope of the lines i.e. sensitivity (S_{bulk}) shows the value of 635 nm/RIU and 335 nm/RIU for the fully filled and for the case of empty slot (a case arises when sensing liquid may not enter the narrow slot region due to presence of air bubble), respectively. A significant improvement can be observed of the proposed device sensitivity compared to the other devices reported earlier [Barrios *et al.*, 2007a, 2008; Claes *et al.*, 2009; De Vos

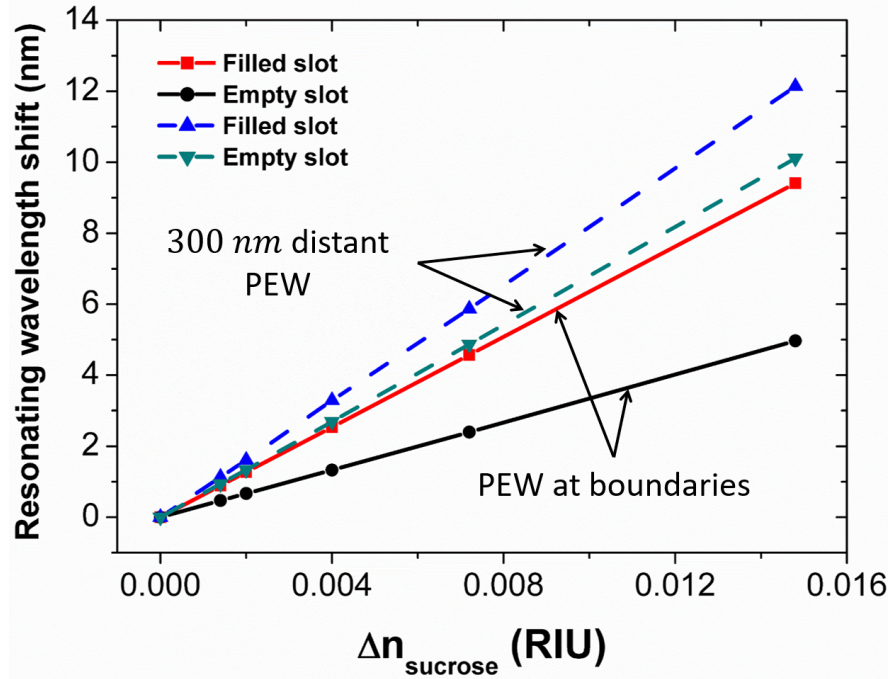


Figure 7.12: Bulk sensitivity (S_{bulk}) analysis of the proposed device. Resonating wavelength shift versus refractive index variation ($\Delta n_{sucrose}$) of sucrose solution at ambient temperature (20°C). The solid lines illustrate the resonating wavelength shift when the perfect electric walls (PEW) are touching the end faces of Si core. The dashed lines present the same when the PEWs are 300 nm away from both end faces of the Si core. The slope of each linear curve represents the sensitivity (S_{bulk}) for the filled and empty conditions.

et al., 2007; Fard *et al.*, 2013; Jugessur *et al.*, 2009; Rodriguez *et al.*, 2015]. The dashed line also shows a linear shift of resonance wavelength ($\Delta\lambda$) when the PEWs are positioned at 300 nm away from both the end faces of the Si core strips. Further distant PEWs do not show any significant improvement in the device sensitivity. Therefore, 300 nm distant PEWs are sufficient to obtain a high device sensitivity.

The 3D iso-surface profiles of confined E_x fields for both cases are shown in Fig. 7.13. The 3D iso-surface field profiles are generated by the post-processing of the eigenvectors obtained from complete device simulation by the developed 3D FV-FEM. Fluid-Si surface contact increases when the boundary walls are kept away from the Si strip's end faces. As a result, a greater sensitivity is observed, illustrated by the blue and green dashed lines with the slope of 820 nm/RIU and 683 nm/RIU for filled and empty slot conditions, respectively. These values are much higher and shows a considerable improvement over the theoretically and experimentally investigated sensing devices reported so far [Barrios *et al.*, 2007a, 2008; Claes *et al.*, 2009; De Vos *et al.*, 2007; Fard *et al.*, 2013; Jugessur

et al., 2009; Rodriguez *et al.*, 2015]. Besides the spectral shift i.e. sensitivity, detection limit (DL) is another important parameter to illustrate the efficiency of the sensor to detect and quantify the properties of the deposited sample of interest. The DL can be estimated from the sensitivity (S_{bulk}) and the sensor resolution (R) as, $DL = R/S_{bulk}$. The resolution of the device is controlled by the wavelength resolution ($\lambda_{resolution}$) of the light source and sensitivity (S_{bulk}) is the slope of the curves in Fig. 7.12. If we consider a laser source having wavelength resolution of 5 pm [De Vos *et al.*, 2007], a minimal detectable refractive index of 7.9×10^{-6} RIU and 6.1×10^{-6} RIU could be achieved for PEW touching the facets and 300 nm away from the Si strip facets, respectively.

7.4 Fabrication Tolerance

To achieve a robust device design, it is important to study the effect of fabrication tolerances. We have analysed three important design parameters such as, total slot confinement ($\Gamma_{slot-total}$), surface sensitivity ($S_{surface}$) and bulk sensitivity (S_{bulk}) with the device parameters by changing a few % of the optimised Si core width (W), slot height (H), and slot width (W_s). $S_{surface}$ and S_{bulk} are studied for 5 nm bio-ad layer and 5% sucrose solution over the device. We found $\Gamma_{slot-total} > 43\%$ for variation in W from -5% to +8% in the case of ideal situation (cover and slot region are filled with aqueous solution). During the growth of Si core, it may not always be possible to maintain the optimum slot height and slot width. Our study shows a considerable $\Gamma_{slot-total}$ variation from 40.96% to 45.91% with H variation within $\pm 10\%$. Besides, for the same variation of slot width (W_s), $\Gamma_{slot-total}$ remains $> 43\%$. In terms of sensitivity analysis, $S_{surface}$ varies from -5.39% to +3.92% for W variation within $\pm 6\%$. We also obtained -1.59% to +1.47% and +4.16% to -3.67% $S_{surface}$ variation for the change in H and W_s within $\pm 5\%$. On the other hand, bulk sensitivity (S_{bulk}) shows a much smaller -3.12% to 0.40% change for -10% to +5% variation of W . Similarly, the variation of H and W_s within $\pm 10\%$ results a small acceptable variation in S_{bulk} from -2.44% to +1.63% and +0.67% to -0.77%, respectively. These results indicate that the device can achieve over 43% total slot confinement and only smaller sensitivity change with $\pm 5\%$ fabrication imperfections. Thus, our proposed resonating structure is robust and possible to fabricate with the

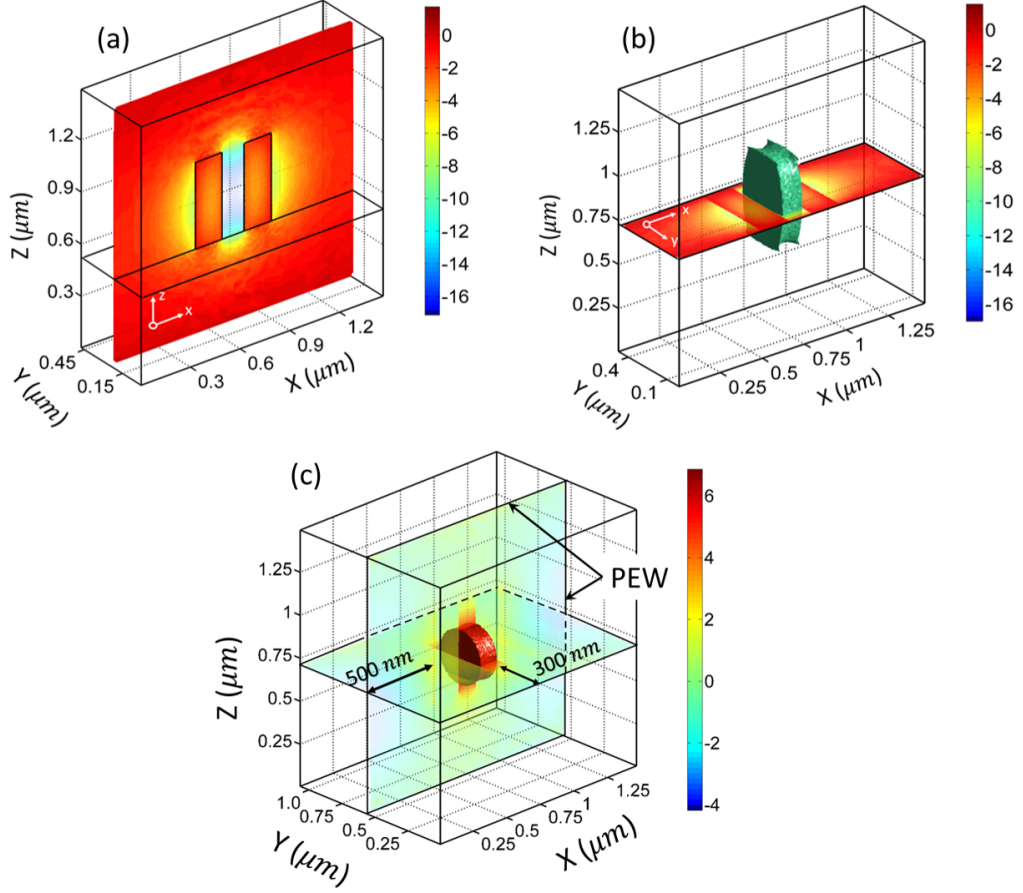


Figure 7.13: The dominant E_x field (2D and 3D) confined into straight single slotted resonator with optimised design parameters at the telecommunication wavelength. Field profiles are generated by post-processing of eigenvectors of resonating wavelength (λ_{res} being an eigenvalue), (a) shows the E_x field profile of slot resonator on an x-z sliced plane and (b) depicts the 3D iso-surface profile of E_x field. The PEWs are considered at both end faces of the Si cores. (c) 3D iso-surface profile of confined E_x field when the boundary PEWs are 300 and 500 nm away from both end faces and side faces of Si strips, respectively. A full-vectorial 3D FV-FEM code is used for complete resonating structure simulation.

available CMOS fabrication technology.

7.5 Summary

In this chapter, we report a SOI based vertically-slotted resonator as an efficient biochemical sensor, which is easy to fabricate. Device performance has been studied for surface sensing with a 5 nm bio-layer and bulk sensing where refractive index changes in the slot and cover region. A rigorous full-vectorial 3D FV-FEM is developed and used to simulate the device for different sensing applications. We obtained a considerably high 5.2 nm

resonance wavelength shift for surface sensing. On the other hand, an improved linear resonating wavelength shift of 635 nm/RIU and 820 nm/RIU have been achieved for homogeneous refractometric sensing when the boundaries are considered at the end faces and far away from the straight slot, respectively. The detection limit is obtained as low as 6.1×10^{-6} RIU. The proposed device serves the successful demonstration of label-free bio-chemical sensing applications of low-index confined electromagnetic field in a slotted resonating structure by using a full-vectorial 3D FV-FEM code. This nano-structural geometry is relatively simple and compact compared to other complex photonic devices, such as slotted ring resonator and nano-Bragg grating sensors. This can be realised in practice with the help of well-matured state-of-the-art fabrication technologies and surface chemistry [Yang *et al.*, 2008], [Barrios *et al.*, 2007b; Säynätjoki *et al.*, 2009]. Based on these preliminary results this slot resonator device shows a great potential to be employed as an effective bio-chemical sensor.

CONCLUSIONS AND FUTURE WORK

In this dissertation, consideration has been given to design, optimisation, and performance evolution of label-free, compact integrated slot waveguide based photonic sensors that will lead to precise and cost-effective detection of chemical concentration, DNA hybridisation, hazardous chemical vapour, and temperature. However, further investigations are required for improvement of hybrid plasmonic waveguide and resonator based sensor designs. In this chapter, we conclude our presented works which pave the platform for future research on integrated photonic based sensing devices.

8.1 Conclusions

The main objective of this research was to develop and modify the full-vectorial finite element method (FV-FEM) that provides a straightforward technique to solve the complex waveguide problems whose solutions are of practical interest. The finite element method is more advantageous than other numerical methods. It can consider any arbitrary shaped waveguide. Other established approaches such as finite difference method (FDM) and finite difference time domain (FDTD) method only consider waveguides with straight edges or a structure slightly perturbed from the regular shape. Unlike FDM and FDTD, the FV-FEM has provision to use regular or irregular distribution of mesh elements of different shapes such as triangles, rectangles, and quadrilaterals for two-dimensional (2D)

and tetrahedrons, bricks, prisms etc. for three-dimensional (3D) domain discretisation. If necessary, iso-parametric elements can also be used to define a structure with curved geometries such as optical fibre. Several alternative formulations can be considered to set-up a FEM code. The scalar formulation is a most simple approach however, it is inadequate for anisotropic problems. Besides, \vec{E} , \vec{H} , and $\vec{E}+\vec{H}$ field based vectorial formulations can also be followed. Among them the \vec{H} -field formulation has several advantages over others. It can be applied for general anisotropic problems and its natural boundary condition is the perfect electric wall, which can be left free for any arbitrary shaped boundary wall. Thus, compared to other numerical approaches, a full-vectorial \vec{H} -field based FV-FEM can solve a wide range of practical waveguide and resonator problems. The presence of non-physical modes amongst physical modes is quite unacceptable. The reason for the presence of non-physical or spurious modes is that the electromagnetic vector variational formulation only satisfy the Maxwell's two curl equations but not the two divergence equations. Rahman and Davies have proposed to eliminate those spurious modes by adopting the penalty method [Rahman and Davies, 1984b] in the vector variational formulation. It has demonstrated the usefulness to solve dielectric waveguide problems. However, it had limitations to eliminate the non-physical spurious modes while solving the metal based plasmonic and metal-dielectric based hybrid plasmonic waveguide problems. To overcome this limitation, I have developed a divergence modified 2D FV-FEM, which is presented in Chapter 3 and all its mathematical steps to set-up the code have been explained in detail. The 2D FV-FEM only considers a waveguide cross-section to simulate the propagating fundamental and associated higher order modes along the waveguide length. However, this approach is incapable to simulate a resonating structure. Modelling of a resonating structure needs to consider the structure as a whole. Thus, a three-dimensional approach was required to solve the problem. I have developed a new full-vectorial \vec{H} -field based 3D FV-FEM to simulate those complex resonating structures, discussed in detail in Chapter 3.

One of our main objectives was to develop novel hybrid plasmonic slot waveguide based photonic sensor devices. Before going into depth of those exotic waveguide designs with complex hybrid plasmonic modes, a simple metal nano-wire has been considered for a detail investigation of plasmonic mode evolutions and its characteristics. Unlike dielectric

waveguides, a rectangular shaped metal nano-wire guides four different fundamental modes form in combination of four individual surface plasmon modes supported by corners and edges of the metal nano-wire. This metal nano-wire design has been studied under identical and non-identical cladding conditions. Plasmonic modes exhibit higher effective indices than the surrounded cladding refractive index. As the modes approaches to cut-off, the mode field spreads into background region thus the plasmonic modes evolve into background quasi-TEM mode. A reduction of modal attenuation is observed in this situation. Depending on the mode propagation length, the ss^0 and as^0 are the long-range plasmonic modes for a metal nano-wire surrounded by an identical dielectric cladding. Additionally, for non-identical clad metal nano-wire a plasmonic supermode (PSM) forms due to coupling of different individual metal interface modes when they have similar propagation constant. This supermode exhibits modal evolutions with the nano-wire design parameters. New divergence modified 2D FV-FEM is used for these plasmonic modal analyses and this new modified approach has shown its efficiency in successful elimination of unwanted spurious modes. These rigorous study results are considered as basic building blocks to understand the modal behaviour of the hybrid plasmonic waveguides, discussed in the following chapters.

During plasmonic modal investigations, the mode effective area (*MEA*) is considered as an important parameter. It can be observed that several *MEA* formulations such as $A_{eff}^{H_t}$, $A_{eff}^{H_x}$, $A_{eff}^{H_y}$, $A_{eff}^{E_t}$, $A_{eff}^{E_x}$, $A_{eff}^{E_y}$, $A_{eff}^{S_z}$, $A_{eff}^{S_{z|max}}$, A_{eff}^U , and $A_{eff}^{U_{max}}$ (discussed in detail in Section 4.3) are already mentioned in many published literatures for waveguide analyses. However, there is an ambiguity about the appropriate mode effective area formula and its applicability for a wide range of low and high index contrast and hybrid plasmonic waveguides. Thus, an extensive comparative investigation has been carried out for effective area evaluation of those waveguides. For an circular optical fibre, a low index contrast waveguide, the $A_{eff}^{H_t}$, $A_{eff}^{E_t}$, $A_{eff}^{S_z}$, and A_{eff}^U have shown same effective area value and also matches with the spot-size (SPZ) value when the mode field profile follows its equivalent Gaussian profile at a particular fibre radius which is the radius value used for the commercial single mode fibre. Application of those mentioned *MEA* formulae on high index contrast SOI based ridge, vertical and horizontal slots, and hybrid plasmonic waveguides indicates that one should wisely choose the effective area formulation(s) that

is(are) based on the dominant field component(s) of the waveguide under consideration. The $A_{eff}^{S_{z|max}}$ and $A_{eff}^{U_{max}}$ formulae may be more suitable for localised mode field assessment such as sub-wavelength confinement in a plasmonic structure as they consider localised maximum value of the field.

In Chapter 5, we have designed a horizontal slotted composite plasmonic waveguide (HSCPW) and applied it for chemical vapour and bio-chemical surface sensing. A porous ZnO (P-ZnO) layer is considered as a horizontal slot to confine maximum light in between silver (Ag) and high index silicon (Si) layer. Due to its porosity, the P-ZnO layer can absorb ethanol vapour and then condense it as liquid ethanol due to capillary condensation. The refractive index of the P-ZnO layer varies depending on the absorbed ethanol percentage in the P-ZnO layer with different porosity. A Lorentz-Lorenz method has been followed for an accurate equivalent refractive index evaluation of the P-ZnO layer with absorbed ethanol. The HSCPW is optimised for 40% porous ZnO and it shows a high waveguide sensitivity of 0.7 per RIU. A compact Mach-Zehnder interferometer (MZI) is designed by incorporating HSCPW at both arms to determine the accurate refractive index change. The proposed device exhibits the maximum phase sensitivities of 0.30, 0.34, 0.38, and 0.40 for the 51.57%, 52.05%, 52.59%, and 53.16% volume fraction of ethanol vapour into slotted P-ZnO layer with 30%, 40%, 50%, and 60% porosities, respectively. Next, a horizontal slot is considered to be formed in between gold (Au) layer and silicon (Si), filled with liquid. It is designed for the detection of DNA hybridisation. A poly-L-lysine linker layer is considered for surface functionalisation in the slot region. The waveguide is optimised for maximum power confinement in the bio-layers at the slot surfaces. The refractive index change during conversion of ssDNA to dsDNA at the slot surface is successfully detected by the waveguide effective index change. The waveguide exhibits maximum sensitivity values of 0.0025 and 0.0019 RIU/nm for 80 and 100 nm slot height, respectively for the detection of DNA hybridisation, a surface sensing mechanism.

A novel design of metal strip loaded horizontal slot hybrid plasmonic waveguide (MSLHSPW) is designed and optimised for bulk sensing. The objective of this design was to obtain a lower mode attenuation with maximum light confinement in the slot region. The optimised waveguide design exhibits a considerably lower mode attenuation of 0.036 dB/ μ m and maximum quasi-TM field confinement of ~60% and ~82% in the slot and

sensing (slot+clad) region, respectively. This waveguide shows a much higher waveguide sensitivity of 1.13 for bulk sensing (isopropanol solution). For an accurate measurement, an asymmetrical MZI transducer has been designed by placing this waveguide in the sensing arm. The hybrid plasmonic waveguide loss has been compensated by applying asymmetrical power splitter which also helps to improve the interferometric fringe visibility to the ideal value (≈ 1). This single on-chip hybrid plasmonic MZI design is applied for simultaneous detection of temperature and concentration of a liquid chemical. The performance analyses of this sensing device exhibits a high temperature sensitivity of 244 pm/ $^{\circ}$ C and volume concentration sensitivity of 437.5 nm/RIU when isopropanol is considered as testing liquid. The compact foot-print of this sensor makes it affordable for on-chip mass production.

Besides, optical resonator has a crucial role in photonic sensing technology. A silicon-on-insulator based vertical slot straight resonator has been designed and optimised for bulk and surface sensing of liquid chemicals. A 2D FV-FEM is inadequate to model the resonating structure as a whole. Rather, a 3D numerical method is highly recommended to avoid any assumptions and approximations that are generally used in semi-3D or 2.5D approaches. We developed a new \vec{H} -field based full-vectorial 3D FV-FEM that can easily model a three-dimensional resonating structure. The proposed straight slot based resonator is first optimised for maximum slot confinement (43.75%) and then those optimised design parameters are used to calculate the effective length of the straight resonator to accommodate first order longitudinal mode. Finally, the sensitivity analyses of the resonating structure has been performed by using the 3D FV-FEM. We obtain a 5.2 nm resonance wavelength shift for the sensing of ultra-thin bio-layer on the device surface. It can also be used for bulk sensing and an improved linear resonating wavelength shift of 635 nm/RIU and 820 nm/RIU has been achieved for the conditions where the slot section is partially and completely filled with the liquid chemical, respectively. Its detection limit shows an attractive value of 6.1×10^{-6} RIU. This SOI based straight resonating structure is relatively simple and compact compared to other slotted ring resonators and Bragg grating based sensors. It can easily be fabricated by the current CMOS technology.

8.2 Future Work

All the results presented in this dissertation is considered as a small part of the on-going global research on integrated photonic sensing technology. Dielectric and hybrid plasmonic novel waveguides and resonator designs have been proposed and dedicated numerical modelling methods also have been developed for successful design, optimisation, and performance analyses. These initial results will lead us for further exploration of hybrid plasmonic waveguides and resonators for different photonic applications.

The 3D FV-FEM code has shown its ability to solve the 3D resonator problems with considerably less computational resources compared to the other time domain methods. However, there is a provision to enhance the 3D FV-FEM performance by using different strategies to handle large sparse matrices arising during global matrix formations. A cleaver memory allocation helps to reduce the computational costs which on the other hand could help to deal with complex electromagnetic problems. Therefore, modelling of three dimensional gratings and complex plasmonic cavity based resonators could be designed with the 3D FV-FEM code.

The enhanced power confinement in the slot section of the hybrid plasmonic waveguide can be exploited for low loss waveguide design, electro-optic modulators, and laser applications. Low-index gain mediums such as polymers and doped rare earth glass materials could be considered as slot materials for such applications.

Demonstration of electro-optic modulators and switches are also possible by using phase change materials. Phase changing materials (GST, GeTe etc.), nonlinear organic electro-optic materials, and graphene could be utilised in the hybrid plasmonic waveguide designs to realise such modulators and optical switches.

The 2D material like graphene and its oxides are promising in sensing applications due to its high surface-to-volume ratio with honeycomb carbon lattice exposed to the surroundings. Because of its selective absorbency for many bio-chemicals and gases, inclusion of the 2D graphene layer with integrated dielectric and hybrid plasmonic waveguides and resonators could lead us to enhance the sensor performance. Thus, the 2D material based integrated photonic sensors can also be investigated in future with our FV-FEM code.



2D FV-FEM: CALCULATIONS OF MATRIX ELEMENTS

A.1 Evaluation of $[Q]$ Matrix

Equation 3.28 shows that the $[Q]$ is a product of $[\vec{\nabla} \times]$ and the shape function $[N]$. Hence,

$$[Q] = \begin{bmatrix} 0 & -\frac{\partial}{\partial z} & \frac{\partial}{\partial y} \\ \frac{\partial}{\partial z} & 0 & -\frac{\partial}{\partial x} \\ -\frac{\partial}{\partial y} & \frac{\partial}{\partial x} & 0 \end{bmatrix} [N] \quad (\text{A.1})$$

where

$$[\vec{\nabla} \times] = \begin{bmatrix} 0 & -\frac{\partial}{\partial z} & \frac{\partial}{\partial y} \\ \frac{\partial}{\partial z} & 0 & -\frac{\partial}{\partial x} \\ -\frac{\partial}{\partial y} & \frac{\partial}{\partial x} & 0 \end{bmatrix} \quad (\text{A.2})$$

and, the shape function is

$$[N] = \begin{bmatrix} N_1 & N_2 & N_3 & 0 & 0 & 0 & 0 & 0 & 0 \\ 0 & 0 & 0 & N_1 & N_2 & N_3 & 0 & 0 & 0 \\ 0 & 0 & 0 & 0 & 0 & 0 & jN_1 & jN_2 & jN_3 \end{bmatrix} \quad (\text{A.3})$$

The j term in the shape function matrix is introduced for lossless cases where the H_z component is 90° out of phase with the transverse components. Equation A.1 then becomes

$$[Q] = \begin{bmatrix} 0 & -\frac{\partial}{\partial z} & \frac{\partial}{\partial y} \\ \frac{\partial}{\partial z} & 0 & -\frac{\partial}{\partial x} \\ -\frac{\partial}{\partial y} & \frac{\partial}{\partial x} & 0 \end{bmatrix}_{3 \times 3} \begin{bmatrix} N_1 & N_2 & N_3 & 0 & 0 & 0 & 0 & 0 & 0 \\ 0 & 0 & 0 & N_1 & N_2 & N_3 & 0 & 0 & 0 \\ 0 & 0 & 0 & 0 & 0 & 0 & jN_1 & jN_2 & jN_3 \end{bmatrix}_{3 \times 9} \quad (\text{A.4})$$

or,

$$[Q] = \begin{bmatrix} 0 & 0 & 0 & -\frac{\partial N_1}{\partial z} & -\frac{\partial N_2}{\partial z} & -\frac{\partial N_3}{\partial z} & j\frac{\partial N_1}{\partial y} & j\frac{\partial N_2}{\partial y} & j\frac{\partial N_3}{\partial y} \\ \frac{\partial N_1}{\partial z} & \frac{\partial N_2}{\partial z} & \frac{\partial N_3}{\partial z} & 0 & 0 & 0 & -j\frac{\partial N_1}{\partial x} & -j\frac{\partial N_2}{\partial x} & -j\frac{\partial N_3}{\partial x} \\ -\frac{\partial N_1}{\partial y} & -\frac{\partial N_2}{\partial y} & -\frac{\partial N_3}{\partial y} & \frac{\partial N_1}{\partial x} & \frac{\partial N_2}{\partial x} & \frac{\partial N_3}{\partial x} & 0 & 0 & 0 \end{bmatrix}_{3 \times 9} \quad (\text{A.5})$$

Assuming the wave propagation in z-direction, the operator $\frac{\partial}{\partial z}$ can be replaced by $-j\beta$ in Eq. A.5. Thus, the coefficients of $[Q]$ matrix can be obtained as follows

$$[Q] = \begin{bmatrix} 0 & 0 & 0 & j\beta N_1 & j\beta N_2 & j\beta N_3 & j\frac{\partial N_1}{\partial y} & j\frac{\partial N_2}{\partial y} & j\frac{\partial N_3}{\partial y} \\ -j\beta N_1 & -j\beta N_2 & -j\beta N_3 & 0 & 0 & 0 & -j\frac{\partial N_1}{\partial x} & -j\frac{\partial N_2}{\partial x} & -j\frac{\partial N_3}{\partial x} \\ -\frac{\partial N_1}{\partial y} & -\frac{\partial N_2}{\partial y} & -\frac{\partial N_3}{\partial y} & \frac{\partial N_1}{\partial x} & \frac{\partial N_2}{\partial x} & \frac{\partial N_3}{\partial x} & 0 & 0 & 0 \end{bmatrix}_{3 \times 9} \quad (\text{A.6})$$

Similarly, $[Q]^*$ can be obtained as:

$$[Q]^* = \begin{bmatrix} 0 & j\beta N_1 & -\frac{\partial N_1}{\partial y} \\ 0 & j\beta N_2 & -\frac{\partial N_2}{\partial y} \\ 0 & j\beta N_3 & -\frac{\partial N_3}{\partial y} \\ -j\beta N_1 & 0 & \frac{\partial N_1}{\partial x} \\ -j\beta N_2 & 0 & \frac{\partial N_2}{\partial x} \\ -j\beta N_3 & 0 & \frac{\partial N_3}{\partial x} \\ -j\frac{\partial N_1}{\partial y} & j\frac{\partial N_1}{\partial x} & 0 \\ -j\frac{\partial N_2}{\partial y} & j\frac{\partial N_2}{\partial x} & 0 \\ -j\frac{\partial N_3}{\partial y} & j\frac{\partial N_3}{\partial x} & 0 \end{bmatrix}_{9 \times 3} \quad (\text{A.7})$$

where

$$\frac{\partial[N]}{\partial x} = \begin{bmatrix} b_1 & b_2 & b_3 \end{bmatrix} \quad (\text{A.8})$$

and

$$\frac{\partial[N]}{\partial y} = \begin{bmatrix} c_1 & c_2 & c_3 \end{bmatrix} \quad (\text{A.9})$$

These partial differentiations have been evaluated from Eqs. 3.5 and 3.11.

A.2 Evaluation of $[A]_e$ and $[B]_e$ Matrix

$[A]_e$ element matrix from Eq. 3.37 can be evaluated based on $[Q]$ and $[Q]_e$ as

$$[A]_e = \hat{\epsilon}_r^{-1} \int_A [Q]^* \cdot [Q] dA \quad (\text{A.10})$$

$$= \hat{\epsilon}_r^{-1} \int_A \begin{bmatrix} \beta^2 [N]^T [N] + \frac{\partial [N]^T}{\partial y} \frac{\partial [N]}{\partial y} & -\frac{\partial [N]^T}{\partial y} \frac{\partial [N]}{\partial x} & \beta [N]^T \frac{\partial [N]}{\partial x} \\ -\frac{\partial [N]^T}{\partial x} \frac{\partial [N]}{\partial y} & \beta^2 [N]^T [N] + \frac{\partial [N]^T}{\partial x} \frac{\partial [N]}{\partial x} & \beta [N]^T \frac{\partial [N]}{\partial y} \\ \beta [N] \frac{\partial [N]^T}{\partial x} & \beta [N] \frac{\partial [N]^T}{\partial y} & \frac{\partial [N]^T}{\partial y} \frac{\partial [N]}{\partial y} + \frac{\partial [N]^T}{\partial x} \frac{\partial [N]}{\partial x} \end{bmatrix} dA \quad (\text{A.11})$$

here $dA = dxdy$ defines the area integration over the surface.

$[B]_e$ element matrix based on $[N]$ and $[N]^T$ (Eq. 3.38) can be obtained as

$$[B]_e = \hat{\mu}_r \int_A [N]^T \cdot [N] dA \quad (\text{A.12})$$

$$= \hat{\mu}_r \int_A \begin{bmatrix} [N]^T [N] & [0] & [0] \\ [0] & [N]^T [N] & [0] \\ [0] & [0] & [N]^T [N] \end{bmatrix} dA \quad (\text{A.13})$$

$$(\text{A.14})$$

or,

$$[B]_e = \hat{\mu}_r \int_A \begin{bmatrix} N_1^2 & N_1 N_2 & N_1 N_3 & 0 & 0 & 0 & 0 & 0 & 0 \\ N_2 N_1 & N_2^2 & N_2 N_3 & 0 & 0 & 0 & 0 & 0 & 0 \\ N_3 N_1 & N_3 N_2 & N_3^2 & 0 & 0 & 0 & 0 & 0 & 0 \\ 0 & 0 & 0 & N_1^2 & N_1 N_2 & N_1 N_3 & 0 & 0 & 0 \\ 0 & 0 & 0 & N_2 N_1 & N_2^2 & N_2 N_3 & 0 & 0 & 0 \\ 0 & 0 & 0 & N_3 N_1 & N_3 N_2 & N_3^2 & 0 & 0 & 0 \\ 0 & 0 & 0 & 0 & 0 & 0 & N_1^2 & N_1 N_2 & N_1 N_3 \\ 0 & 0 & 0 & 0 & 0 & 0 & N_2 N_1 & N_2^2 & N_2 N_3 \\ 0 & 0 & 0 & 0 & 0 & 0 & N_3 N_1 & N_3 N_2 & N_3^2 \end{bmatrix} dA \quad (\text{A.15})$$

As the linear triangular element has straight sides, a constant Jacobian, we can apply the numerical Gaussian quadrature integration. The exact expression of numerical

integration for linear triangular element is

$$\int_A N_1^i N_2^j N_3^k dA = \frac{i!j!k!2!}{(i+j+k+2)!} A_e \quad (\text{A.16})$$

here A_e signifies the area of the triangular element.

Therefore, the numerical integration of different forms can be obtained as

$$\int_A N_1^2 dA = \int_A N_2^2 dA = \int_A N_3^2 dA = \frac{A_e}{6} \quad (\text{A.17})$$

$$\int_A N_1 N_2 dA = \int_A N_2 N_3 dA = \int_A N_1 N_3 dA = \frac{A_e}{12} \quad (\text{A.18})$$

and

$$\int_A dA = A_e \quad (\text{A.19})$$

Therefore, with the help of Eqs. A.8 and A.9, some of the matrix elements of $[A]_e$ (Eq. A.11) matrix can be obtained as

$$[A_{1,1}]_e = \hat{\epsilon}^{-1} \int_A \left(\beta^2 N_1^2 + \left(\frac{\partial N_1}{\partial y} \right)^2 \right) dA = \frac{1}{\epsilon} \left[\frac{\beta^2 A_e}{6} + c_1^2 A_e \right] \quad (\text{A.20})$$

$$[A_{1,2}]_e = \hat{\epsilon}^{-1} \int_A \left(\beta^2 N_1 N_2 + \frac{\partial N_1}{\partial y} \frac{\partial N_2}{\partial y} \right) dA = \frac{1}{\epsilon} \left[\frac{\beta^2 A_e}{12} + c_1 c_2 A_e \right] \quad (\text{A.21})$$

$$[A_{1,3}]_e = \hat{\epsilon}^{-1} \int_A \left(\beta^2 N_1 N_3 + \frac{\partial N_1}{\partial y} \frac{\partial N_3}{\partial y} \right) dA = \frac{1}{\epsilon} \left[\frac{\beta^2 A_e}{12} + c_1 c_3 A_e \right] \quad (\text{A.22})$$

$$[A_{1,4}]_e = -\hat{\epsilon}^{-1} \int_A \left(\frac{\partial N_1}{\partial x} \frac{\partial N_1}{\partial y} \right) dA = -\frac{1}{\epsilon} b_1 c_1 A_e \quad (\text{A.23})$$

$$[A_{1,5}]_e = -\hat{\epsilon}^{-1} \int_A \left(\frac{\partial N_2}{\partial x} \frac{\partial N_1}{\partial y} \right) dA = -\frac{1}{\epsilon} b_2 c_1 A_e \quad (\text{A.24})$$

$$[A_{1,6}]_e = -\hat{\epsilon}^{-1} \int_A \left(\frac{\partial N_3}{\partial x} \frac{\partial N_1}{\partial y} \right) dA = -\frac{1}{\epsilon} b_3 c_1 A_e \quad (\text{A.25})$$

and so on.

In a similar fashion, the $[B]_e$ matrix shown in Eq. A.15 can be written as

$$[B]_e = \hat{\mu}_r \begin{bmatrix} \frac{A_e}{6} & \frac{A_e}{12} & \frac{A_e}{12} & 0 & 0 & 0 & 0 & 0 & 0 \\ \frac{A_e}{12} & \frac{A_e}{6} & \frac{A_e}{12} & 0 & 0 & 0 & 0 & 0 & 0 \\ \frac{A_e}{12} & \frac{A_e}{12} & \frac{A_e}{6} & 0 & 0 & 0 & 0 & 0 & 0 \\ 0 & 0 & 0 & \frac{A_e}{6} & \frac{A_e}{12} & \frac{A_e}{12} & 0 & 0 & 0 \\ 0 & 0 & 0 & \frac{A_e}{12} & \frac{A_e}{6} & \frac{A_e}{12} & 0 & 0 & 0 \\ 0 & 0 & 0 & \frac{A_e}{12} & \frac{A_e}{12} & \frac{A_e}{6} & 0 & 0 & 0 \\ 0 & 0 & 0 & 0 & 0 & 0 & \frac{A_e}{6} & \frac{A_e}{12} & \frac{A_e}{12} \\ 0 & 0 & 0 & 0 & 0 & 0 & \frac{A_e}{12} & \frac{A_e}{6} & \frac{A_e}{12} \\ 0 & 0 & 0 & 0 & 0 & 0 & \frac{A_e}{12} & \frac{A_e}{12} & \frac{A_e}{6} \end{bmatrix} \quad (\text{A.26})$$

3D FV-FEM: CALCULATIONS OF MATRIX ELEMENTS

B.1 Evaluation of $[A]_e$ and $[B]_e$ Matrices

The $[A]_e$ and $[B]_e$ element matrices from Eq. 3.77 and 3.78 are evaluated here.

The $[A]_e$ matrix can be defined as

$$\begin{aligned}
 [A]_e &= \hat{\epsilon}_r^{-1} \iiint [Q]_e [Q]_e^T dx dy dz \\
 &= \hat{\epsilon}_r^{-1} \int_V \begin{bmatrix} \{0\} & \frac{\partial \{N\}}{\partial z} & -\frac{\partial \{N\}}{\partial y} \\ -\frac{\partial \{N\}}{\partial z} & \{0\} & \frac{\partial \{N\}}{\partial x} \\ \frac{\partial \{N\}}{\partial y} & -\frac{\partial \{N\}}{\partial x} & \{0\} \end{bmatrix} \begin{bmatrix} \{0\}^T & -\frac{\partial \{N\}^T}{\partial z} & \frac{\partial \{N\}^T}{\partial y} \\ \frac{\partial \{N\}^T}{\partial z} & \{0\}^T & -\frac{\partial \{N\}^T}{\partial x} \\ -\frac{\partial \{N\}^T}{\partial y} & \frac{\partial \{N\}^T}{\partial x} & \{0\}^T \end{bmatrix} dV
 \end{aligned} \tag{B.1}$$

where

$$[Q]_e [Q]_e^T = \begin{bmatrix} \frac{\partial \{N\}}{\partial z} \frac{\partial \{N\}^T}{\partial z} + \frac{\partial \{N\}}{\partial y} \frac{\partial \{N\}^T}{\partial y} & -\frac{\partial \{N\}}{\partial y} \frac{\partial \{N\}^T}{\partial x} & -\frac{\partial \{N\}}{\partial z} \frac{\partial \{N\}^T}{\partial x} \\ -\frac{\partial \{N\}}{\partial x} \frac{\partial \{N\}^T}{\partial y} & \frac{\partial \{N\}}{\partial z} \frac{\partial \{N\}^T}{\partial z} + \frac{\partial \{N\}}{\partial x} \frac{\partial \{N\}^T}{\partial x} & -\frac{\partial \{N\}}{\partial z} \frac{\partial \{N\}^T}{\partial y} \\ -\frac{\partial \{N\}}{\partial x} \frac{\partial \{N\}^T}{\partial z} & -\frac{\partial \{N\}}{\partial y} \frac{\partial \{N\}^T}{\partial z} & \frac{\partial \{N\}}{\partial y} \frac{\partial \{N\}^T}{\partial y} + \frac{\partial \{N\}}{\partial x} \frac{\partial \{N\}^T}{\partial x} \end{bmatrix}_{12 \times 12} \tag{B.2}$$

On the other hand, the $[B]_e$ matrix can be written as

$$[B]_e = \hat{\mu}_r \int_v [N]_e [N]_e^T dV \quad (B.3)$$

$$= \hat{\mu}_r \int_v \begin{bmatrix} N_1 N_1 & N_1 N_2 & N_1 N_3 & N_1 N_4 & 0 & 0 & 0 & 0 & 0 & 0 & 0 & 0 \\ N_2 N_1 & N_2 N_2 & N_2 N_3 & N_2 N_4 & 0 & 0 & 0 & 0 & 0 & 0 & 0 & 0 \\ N_3 N_1 & N_3 N_2 & N_3 N_3 & N_3 N_4 & 0 & 0 & 0 & 0 & 0 & 0 & 0 & 0 \\ N_4 N_1 & N_4 N_2 & N_4 N_3 & N_4 N_4 & 0 & 0 & 0 & 0 & 0 & 0 & 0 & 0 \\ 0 & 0 & 0 & 0 & N_1 N_1 & N_1 N_2 & N_1 N_3 & N_1 N_4 & 0 & 0 & 0 & 0 \\ 0 & 0 & 0 & 0 & N_2 N_1 & N_2 N_2 & N_2 N_3 & N_2 N_4 & 0 & 0 & 0 & 0 \\ 0 & 0 & 0 & 0 & N_3 N_1 & N_3 N_2 & N_3 N_3 & N_3 N_4 & 0 & 0 & 0 & 0 \\ 0 & 0 & 0 & 0 & N_4 N_1 & N_4 N_2 & N_4 N_3 & N_4 N_4 & 0 & 0 & 0 & 0 \\ 0 & 0 & 0 & 0 & 0 & 0 & 0 & 0 & N_1 N_1 & N_1 N_2 & N_1 N_3 & N_1 N_4 \\ 0 & 0 & 0 & 0 & 0 & 0 & 0 & 0 & N_2 N_1 & N_2 N_2 & N_2 N_3 & N_2 N_4 \\ 0 & 0 & 0 & 0 & 0 & 0 & 0 & 0 & N_3 N_1 & N_3 N_2 & N_3 N_3 & N_3 N_4 \\ 0 & 0 & 0 & 0 & 0 & 0 & 0 & 0 & N_4 N_1 & N_4 N_2 & N_4 N_3 & N_4 N_4 \end{bmatrix} dV$$

$$= \hat{\mu}_r \int_v \begin{bmatrix} \{N\} \{N\}^T & \{0\} & \{0\} \\ \{0\} & \{N\} \{N\}^T & \{0\} \\ \{0\} & \{0\} & \{N\} \{N\}^T \end{bmatrix} dV \quad (B.4)$$

It is to be noted that both the matrices $[A]_e$ and $[B]_e$ are real symmetric. Investigating material is considered as loss less, this makes the elements of $[A]_e$ are either real or imaginary, existence of both the components are not possible. The subspace iterative matrix eigenvalue solver can only solve the real matrices and here the 3D FV-FEM produced real symmetric element matrix, hence it is beneficial that an additional element matrix conversion from complex to real is not needed.

Now to evaluate the element matrices the integration of quantities in terms of shape functions or volume coordinates need to be solved. As the tetrahedral element has straight sides and flat faces (constant Jacobian), we can use the numerical Gaussian quadrature integration. The exact expression of numerical integration for linear tetrahedral element is,

$$\int_v L_1^a L_2^b L_3^c L_4^d dV = \frac{a!b!c!d!}{(a+b+c+d+3)!} 6V \quad (B.5)$$

Therefore,

$$\int_v N_1^2 dV = \int_v N_2^2 dV = \int_v N_3^2 dV = \int_v N_4^2 dV = \frac{V}{10} \quad (B.6)$$

$$\begin{aligned} \int_v N_1 N_2 dV &= \int_v N_1 N_3 dV = \int_v N_1 N_4 dV = \\ \int_v N_2 N_3 dV &= \int_v N_2 N_4 dV = \int_v N_3 N_4 dV = \frac{V}{20} \end{aligned} \quad (B.7)$$

and

$$\int_v dV = V \quad (B.8)$$

Hence the calculations for the elements of matrix $[A]_e$ are

$$\begin{aligned}
 [A_{1,1}]_e &= \hat{\epsilon}^{-1} \int_v \frac{\partial \{N\}}{\partial z} \frac{\partial \{N\}^T}{\partial z} + \frac{\partial \{N\}}{\partial y} \frac{\partial \{N\}^T}{\partial y} dV \\
 &= \hat{\epsilon}^{-1} \int_v \left(\frac{\partial}{\partial z} \begin{Bmatrix} N_1 \\ N_2 \\ N_3 \\ N_4 \end{Bmatrix} \frac{\partial}{\partial z} \{N_1 \ N_2 \ N_3 \ N_4\} + \frac{\partial}{\partial y} \begin{Bmatrix} N_1 \\ N_2 \\ N_3 \\ N_4 \end{Bmatrix} \frac{\partial}{\partial y} \{N_1 \ N_2 \ N_3 \ N_4\} \right) dV \\
 &= \hat{\epsilon}^{-1} \begin{bmatrix} b_4 b_4 V + b_3 b_3 V & b_4 b_8 V + b_3 b_7 V & b_4 b_{12} V + b_3 b_{11} V & b_4 b_{16} V + b_3 b_{15} V \\ b_8 b_4 V + b_7 b_3 V & b_8 b_8 V + b_7 b_7 V & b_8 b_{12} V + b_7 b_{11} V & b_8 b_{16} V + b_7 b_{15} V \\ b_{12} b_4 V + b_{11} b_3 V & b_{12} b_8 V + b_{11} b_7 V & b_{12} b_{12} V + b_{11} b_{11} V & b_{12} b_{16} V + b_{11} b_{15} V \\ b_{16} b_4 V + b_{15} b_3 V & b_{16} b_8 V + b_{15} b_7 V & b_{16} b_{12} V + b_{15} b_{11} V & b_{16} b_{16} V + b_{15} b_{15} V \end{bmatrix} \quad (B.9)
 \end{aligned}$$

$$\begin{aligned}
 [A_{1,2}] &= -\hat{\epsilon}^{-1} \int_v \frac{\partial \{N\}}{\partial y} \frac{\partial \{N\}^T}{\partial x} dV \\
 &= -\hat{\epsilon}^{-1} \int_v \left[\begin{Bmatrix} N_1 \\ N_2 \\ N_3 \\ N_4 \end{Bmatrix} \frac{\partial}{\partial x} \{N_1 \ N_2 \ N_3 \ N_4\} \right] dV \\
 &= -\hat{\epsilon}^{-1} \begin{bmatrix} b_3 b_2 V & b_3 b_6 V & b_3 b_{10} V & b_3 b_{14} V \\ b_7 b_2 V & b_7 b_6 V & b_7 b_{10} V & b_7 b_{14} V \\ b_{11} b_2 V & b_{11} b_6 V & b_{11} b_{10} V & b_{11} b_{14} V \\ b_{15} b_2 V & b_{15} b_6 V & b_{15} b_{10} V & b_{15} b_{14} V \end{bmatrix} \quad (B.10)
 \end{aligned}$$

$$\begin{aligned}
 [A_{1,3}] &= -\hat{\epsilon}^{-1} \int_v \frac{\partial \{N\}}{\partial z} \frac{\partial \{N\}^T}{\partial x} dV \\
 &= -\hat{\epsilon}^{-1} \int_v \left[\begin{Bmatrix} N_1 \\ N_2 \\ N_3 \\ N_4 \end{Bmatrix} \frac{\partial}{\partial x} \{N_1 \ N_2 \ N_3 \ N_4\} \right] dV \\
 &= -\hat{\epsilon}^{-1} \begin{bmatrix} b_4 b_2 V & b_4 b_6 V & b_4 b_{10} V & b_4 b_{14} V \\ b_8 b_2 V & b_8 b_6 V & b_8 b_{10} V & b_8 b_{14} V \\ b_{12} b_2 V & b_{12} b_6 V & b_{12} b_{10} V & b_{12} b_{14} V \\ b_{16} b_2 V & b_{16} b_6 V & b_{16} b_{10} V & b_{16} b_{14} V \end{bmatrix} \quad (B.11)
 \end{aligned}$$

$$\begin{aligned}
 [A_{2,1}] &= -\hat{\epsilon}^{-1} \int_v \frac{\partial \{N\}}{\partial x} \frac{\partial \{N\}^T}{\partial y} dV \\
 &= -\hat{\epsilon}^{-1} \int_v \left[\begin{Bmatrix} N_1 \\ N_2 \\ N_3 \\ N_4 \end{Bmatrix} \frac{\partial}{\partial y} \{N_1 \ N_2 \ N_3 \ N_4\} \right] dV \\
 &= -\hat{\epsilon}^{-1} \begin{bmatrix} b_2 b_3 V & b_2 b_7 V & b_2 b_{11} V & b_2 b_{15} V \\ b_6 b_3 V & b_6 b_7 V & b_6 b_{11} V & b_6 b_{15} V \\ b_{10} b_3 V & b_{10} b_7 V & b_{10} b_{11} V & b_{10} b_{15} V \\ b_{14} b_3 V & b_{14} b_7 V & b_{14} b_{11} V & b_{14} b_{15} V \end{bmatrix} \quad (B.12)
 \end{aligned}$$

$$\begin{aligned}
 [A_{2,2}] &= \hat{\epsilon}^{-1} \int_v \left(\frac{\partial \{N\}}{\partial z} \frac{\partial \{N\}^T}{\partial z} + \frac{\partial \{N\}}{\partial x} \frac{\partial \{N\}^T}{\partial x} \right) dV \\
 &= \hat{\epsilon}^{-1} \int_v \left(\frac{\partial}{\partial z} \begin{Bmatrix} N_1 \\ N_2 \\ N_3 \\ N_4 \end{Bmatrix} \frac{\partial}{\partial z} \{N_1 \ N_2 \ N_3 \ N_4\} + \frac{\partial}{\partial x} \begin{Bmatrix} N_1 \\ N_2 \\ N_3 \\ N_4 \end{Bmatrix} \frac{\partial}{\partial x} \{N_1 \ N_2 \ N_3 \ N_4\} \right) dV \\
 &= \hat{\epsilon}^{-1} \begin{bmatrix} (b_4 b_4 + b_2 b_2) V & (b_4 b_8 + b_2 b_6) V & (b_4 b_{12} + b_2 b_{10}) V & (b_4 b_{16} + b_2 b_{14}) V \\ (b_8 b_4 + b_6 b_2) V & (b_8 b_8 + b_6 b_6) V & (b_8 b_{12} + b_6 b_{10}) V & (b_8 b_{16} + b_6 b_{14}) V \\ (b_{12} b_4 + b_{10} b_2) V & (b_{12} b_8 + b_{10} b_6) V & (b_{12} b_{12} + b_{10} b_{10}) V & (b_{12} b_{16} + b_{10} b_{14}) V \\ (b_{16} b_4 + b_{14} b_2) V & (b_{16} b_8 + b_{14} b_6) V & (b_{16} b_{12} + b_{14} b_{10}) V & (b_{16} b_{16} + b_{14} b_{14}) V \end{bmatrix} \quad (B.13)
 \end{aligned}$$

$$\begin{aligned}
 [A_{2,3}] &= -\hat{\epsilon}^{-1} \int_v \frac{\partial \{N\}}{\partial z} \frac{\partial \{N\}^T}{\partial y} dV \\
 &= -\hat{\epsilon}^{-1} \int_v \left[\frac{\partial}{\partial z} \begin{Bmatrix} N_1 \\ N_2 \\ N_3 \\ N_4 \end{Bmatrix} \frac{\partial}{\partial y} \{N_1 \ N_2 \ N_3 \ N_4\} \right] dV \\
 &= -\hat{\epsilon}^{-1} \begin{bmatrix} b_4 b_3 V & b_4 b_7 V & b_4 b_{11} V & b_4 b_{15} V \\ b_8 b_3 V & b_8 b_7 V & b_8 b_{11} V & b_8 b_{15} V \\ b_{12} b_3 V & b_{12} b_7 V & b_{12} b_{11} V & b_{12} b_{15} V \\ b_{16} b_3 V & b_{16} b_7 V & b_{16} b_{11} V & b_{16} b_{15} V \end{bmatrix}
 \end{aligned} \tag{B.14}$$

$$\begin{aligned}
 [A_{3,1}] &= -\hat{\epsilon}^{-1} \int_v \frac{\partial \{N\}}{\partial x} \frac{\partial \{N\}^T}{\partial z} dV \\
 &= -\hat{\epsilon}^{-1} \int_v \left[\frac{\partial}{\partial x} \begin{Bmatrix} N_1 \\ N_2 \\ N_3 \\ N_4 \end{Bmatrix} \frac{\partial}{\partial z} \{N_1 \ N_2 \ N_3 \ N_4\} \right] dV \\
 &= -\hat{\epsilon}^{-1} \begin{bmatrix} b_2 b_4 V & b_2 b_8 V & b_2 b_{12} V & b_2 b_{16} V \\ b_6 b_4 V & b_6 b_8 V & b_6 b_{12} V & b_6 b_{16} V \\ b_{10} b_4 V & b_{10} b_8 V & b_{10} b_{12} V & b_{10} b_{16} V \\ b_{14} b_4 V & b_{14} b_8 V & b_{14} b_{12} V & b_{14} b_{16} V \end{bmatrix}
 \end{aligned} \tag{B.15}$$

$$\begin{aligned}
 [A_{3,2}] &= -\hat{\epsilon}^{-1} \int_v \frac{\partial \{N\}}{\partial y} \frac{\partial \{N\}^T}{\partial z} dV \\
 &= -\hat{\epsilon}^{-1} \int_v \left[\frac{\partial}{\partial y} \begin{Bmatrix} N_1 \\ N_2 \\ N_3 \\ N_4 \end{Bmatrix} \frac{\partial}{\partial z} \{N_1 \ N_2 \ N_3 \ N_4\} \right] dV \\
 &= -\hat{\epsilon}^{-1} \begin{bmatrix} b_3 b_4 V & b_3 b_8 V & b_3 b_{12} V & b_3 b_{16} V \\ b_7 b_4 V & b_7 b_8 V & b_7 b_{12} V & b_7 b_{16} V \\ b_{11} b_4 V & b_{11} b_8 V & b_{11} b_{12} V & b_{11} b_{16} V \\ b_{15} b_4 V & b_{15} b_8 V & b_{15} b_{12} V & b_{15} b_{16} V \end{bmatrix}
 \end{aligned} \tag{B.16}$$

$$\begin{aligned}
 [A_{3,3}] &= \hat{\epsilon}^{-1} \int_v \left[\frac{\partial \{N\}}{\partial y} \frac{\partial \{N\}^T}{\partial y} + \frac{\partial \{N\}}{\partial x} \frac{\partial \{N\}^T}{\partial x} \right] dV \\
 &= \hat{\epsilon}^{-1} \int_v \left[\frac{\partial}{\partial y} \begin{Bmatrix} N_1 \\ N_2 \\ N_3 \\ N_4 \end{Bmatrix} \frac{\partial}{\partial y} \{N_1 \ N_2 \ N_3 \ N_4\} + \frac{\partial}{\partial x} \begin{Bmatrix} N_1 \\ N_2 \\ N_3 \\ N_4 \end{Bmatrix} \frac{\partial}{\partial x} \{N_1 \ N_2 \ N_3 \ N_4\} \right] dV \\
 &= \hat{\epsilon}^{-1} \begin{bmatrix} (b_3 b_3 + b_2 b_2) V & (b_3 b_7 + b_2 b_6) V & (b_3 b_{11} + b_2 b_{10}) V & (b_3 b_{15} + b_2 b_{14}) V \\ (b_7 b_3 + b_6 b_2) V & (b_7 b_7 + b_6 b_6) V & (b_7 b_{11} + b_6 b_{10}) V & (b_7 b_{15} + b_6 b_{14}) V \\ (b_{11} b_3 + b_{10} b_2) V & (b_{11} b_7 + b_{10} b_6) V & (b_{11} b_{11} + b_{10} b_{10}) V & (b_{11} b_{15} + b_{10} b_{14}) V \\ (b_{15} b_3 + b_{14} b_2) V & (b_{15} b_7 + b_{14} b_6) V & (b_{15} b_{11} + b_{14} b_{10}) V & (b_{15} b_{15} + b_{14} b_{14}) V \end{bmatrix}
 \end{aligned} \tag{B.17}$$

Similarly, the elements of matrix $[B]_e$ can also be evaluated by considering the numerical

Gaussian quadrature integration as

$$[B]_e = \hat{\mu} \begin{bmatrix} \frac{V}{10} & \frac{V}{20} & \frac{V}{20} & \frac{V}{20} & 0 & 0 & 0 & 0 & 0 & 0 & 0 & 0 \\ \frac{V}{20} & \frac{V}{10} & \frac{V}{20} & \frac{V}{20} & 0 & 0 & 0 & 0 & 0 & 0 & 0 & 0 \\ \frac{V}{20} & \frac{V}{20} & \frac{V}{10} & \frac{V}{20} & 0 & 0 & 0 & 0 & 0 & 0 & 0 & 0 \\ \frac{V}{20} & \frac{V}{20} & \frac{V}{20} & \frac{V}{10} & 0 & 0 & 0 & 0 & 0 & 0 & 0 & 0 \\ 0 & 0 & 0 & 0 & \frac{V}{10} & \frac{V}{20} & \frac{V}{20} & \frac{V}{20} & 0 & 0 & 0 & 0 \\ 0 & 0 & 0 & 0 & \frac{V}{20} & \frac{V}{10} & \frac{V}{20} & \frac{V}{20} & 0 & 0 & 0 & 0 \\ 0 & 0 & 0 & 0 & \frac{V}{20} & \frac{V}{20} & \frac{V}{10} & \frac{V}{20} & 0 & 0 & 0 & 0 \\ 0 & 0 & 0 & 0 & 0 & 0 & 0 & 0 & \frac{V}{10} & \frac{V}{20} & \frac{V}{20} & \frac{V}{20} \\ 0 & 0 & 0 & 0 & 0 & 0 & 0 & 0 & \frac{V}{20} & \frac{V}{10} & \frac{V}{20} & \frac{V}{20} \\ 0 & 0 & 0 & 0 & 0 & 0 & 0 & 0 & \frac{V}{20} & \frac{V}{20} & \frac{V}{10} & \frac{V}{20} \\ 0 & 0 & 0 & 0 & 0 & 0 & 0 & 0 & \frac{V}{20} & \frac{V}{20} & \frac{V}{20} & \frac{V}{10} \end{bmatrix} \tag{B.18}$$



VALIDATION OF 3D FV-FEM

C.1 Empty Rectangular Cavity: Analytical Solutions

Our in house \vec{H} -field based vectorial 3D FV-FEM is first applied to a simplest readily available problem that can be found in every electromagnetic text books. An empty air filled rectangular cavity with perfectly conducting walls is considered whose resonating frequencies and modes can be evaluated analytically. The perfectly conducting walls signify no dissipation of energy in the structure. We have taken the same problem to benchmark our 3D FV-FEM code.

The dimensions of the empty rectangular cavity (Fig. C.1) are taken from [Sadiku, 2014] as

$$a = 5 \text{ cm}; \quad b = 4 \text{ cm}; \quad c = 10 \text{ cm} \quad (\text{C.1})$$

Starting from the Maxwell's equations the \vec{H} field components of the resonating mode along x, y, and z directions can be expressed as

$$\begin{cases} H_x = H_{0x} \left[\sin\left(\frac{l\pi x}{a}\right) \cos\left(\frac{m\pi y}{b}\right) \cos\left(\frac{n\pi z}{c}\right) \right] \\ H_y = H_{0y} \left[\cos\left(\frac{l\pi x}{a}\right) \sin\left(\frac{m\pi y}{b}\right) \cos\left(\frac{n\pi z}{c}\right) \right] \\ H_z = H_{0z} \left[\cos\left(\frac{l\pi x}{a}\right) \cos\left(\frac{m\pi y}{b}\right) \sin\left(\frac{n\pi z}{c}\right) \right] \end{cases} \quad (\text{C.2})$$

where l , m , and n are positive integers signify resonant mode numbers.

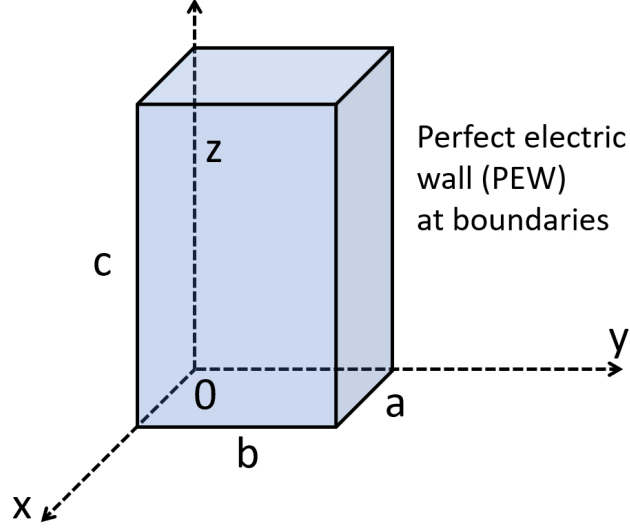


Figure C.1: Schematic diagram of a 3D air filled rectangular cavity with dimensions $a = 5$ cm, $b = 4$ cm, and $c = 10$ cm along x , y , and z directions. The cavity is considered to be enclosed with perfect electric walls (PEW).

The resonating wavelength (λ_{res}) and wavenumber (k_0) of the resonating modes can be obtained by using the following equation.

$$k_0^2 = \pi^2 \left[\left(\frac{l}{a} \right)^2 + \left(\frac{m}{b} \right)^2 + \left(\frac{n}{c} \right)^2 \right] \quad (C.3)$$

and

$$\lambda_{res} = \frac{2\pi}{k_0} \quad (C.4)$$

Resonating wavelengths and wavenumber of each resonating mode can be analytically determined by using Eqs. C.3 and C.4. The results are shown in Table C.1.

Table C.1: Analytical results of resonating wavelength (λ_{res}), wavenumber (k_0), and k_0a of different resonating modes of the empty rectangular cavity.

Modes	λ_{res}	k_0	k_0a
TE_{101}	8.9433	0.7025	3.5125
TE_{011}	7.4278	0.8459	4.2295
TE_{111}/TM_{111}	5.9628	1.0537	5.2685
TM_{110}	6.2470	1.0058	5.0290
TE_{102}	7.0711	0.8886	4.4429
TM_{210}	4.2400	1.4819	7.4094

C.2 Empty Rectangular Cavity: Numerical Computation by 3D FV-FEM

The same rectangular cavity is considered and its resonating modes and wavenumber are calculated using newly developed in-house 3D FV-FEM solver. As the 3D FEM formulation follows the same variational formulation which is derived from the Maxwell's two curl equations [Berk, 1956], the spurious non-physical solutions are present with the real solution. The effect of those spurious solutions can be minimised by introducing the divergence part with an extra weighting factor p (shown in Eq. 3.65). First, the numerical simulation has been done for the TE_{101} mode. Variation of real physical and non-physical wavenumbers (k_0) of the TE_{101} mode as a function of penalty term (p) is shown in Fig. C.2. The physical solution exhibits a very slow variation and it is shown by a black dashed line. Other scattered points represent the non-physical solutions. The H_x and H_z field distributions of the resonating TE_{101} mode for $p = 0, 0.1$, and 0.5 are shown in Fig. C.3. For $p = 0$, the non-physical solutions exist in a very close vicinity of the real physical solution thus result in distorted mode field distributions. Noisy H_x and H_z fields of TE_{101} for $p = 0$ are shown in Fig. C.3(a) and (d), respectively. As the penalty term is introduced ($p = 0.1, 0.2, \dots$ and so on) the fields became noise free as the k_0 values of the non-physical modes move away from the physical solution shown by the black dashed line in Fig. C.2. Figures C.3(b) and (e) show the H_x and H_z fields, respectively of the TE_{101} mode for $p = 0.1$. An improved but little noisy distribution can be seen here. Whereas, Figs. C.3(c) and (f) depict noise-free H_x and H_z fields, respectively when the penalty term (p) is considered as 0.5 .

The wavenumber (k_0) variations with penalty term (p) for different modes such as TE_{101} , TE_{011} , TE_{102} , TM_{110} , degenerated TE_{111} and TM_{111} , and TM_{210} are given in Fig. C.4(a). The percentage errors also have been evaluated as a function penalty term, shown in Fig. C.4(b). It can be noticeable that although the percentage error increases by a little amount, however, a noise-free field profile can also be obtained with the increment of penalty term. Hence it is important to choose an appropriate penalty term. We have considered $p = 0.5$ in order to give 50% weightage to the divergence part in vector variational formulation. It can be noticed that the percentage error also increase

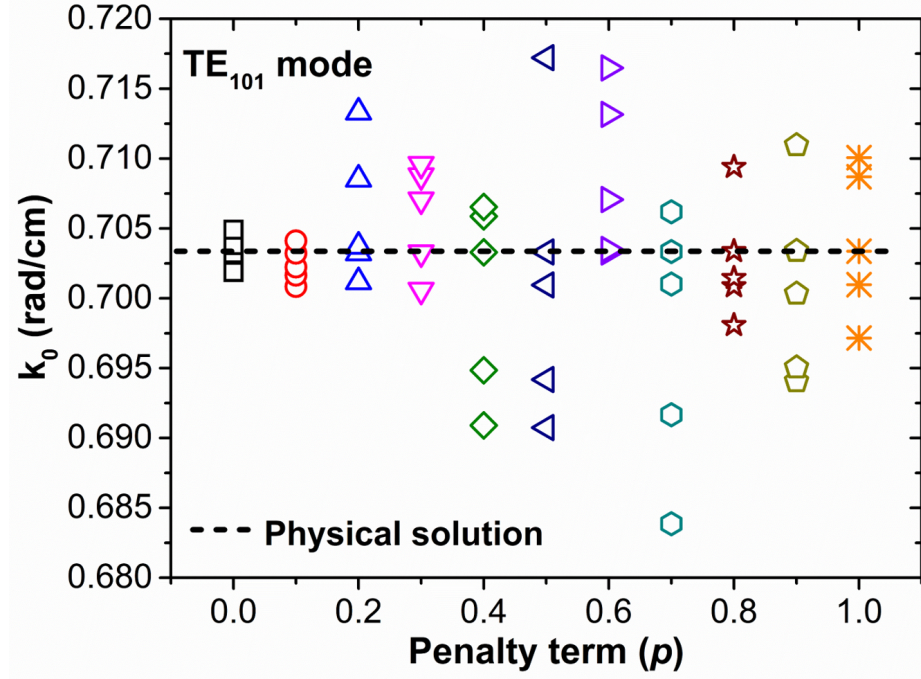


Figure C.2: Variation of computed TE_{101} wavenumber (k_0) of the empty rectangular cavity (Fig. C.1) against penalty term (p). The physical solution varies very slowly and its wavenumber(k_0) for each p are connected by a black dashed line. Other scattered points represent the non-physical spurious modes.

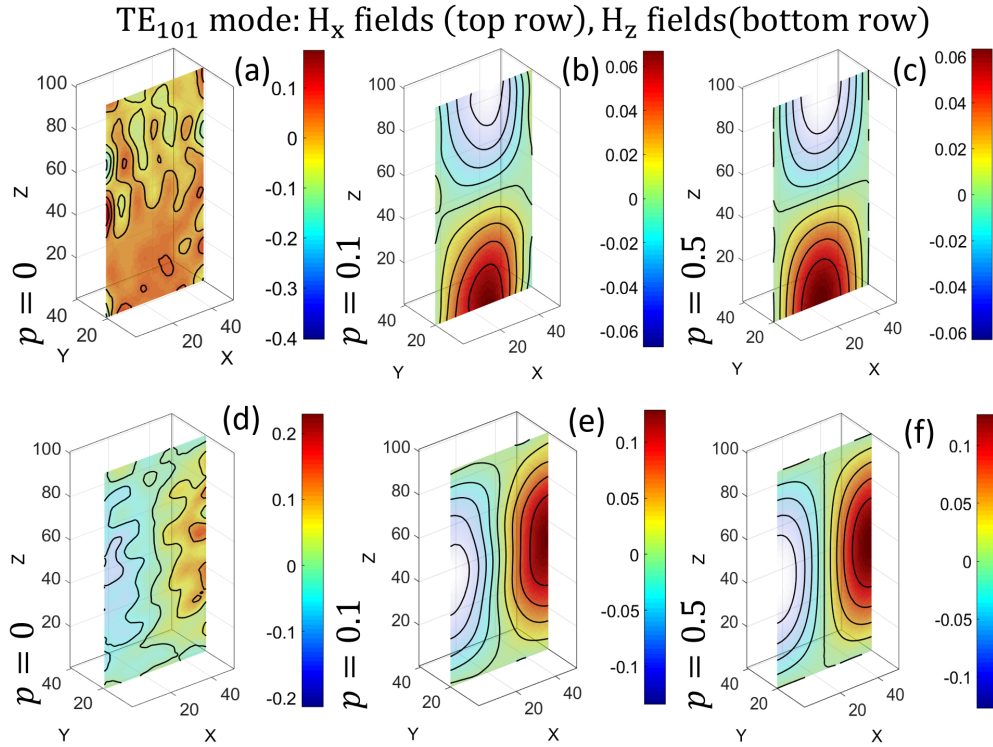


Figure C.3: H_x (top row) and H_z (bottom row) field distributions of TE_{101} mode with penalty term, $p = 0, 0.1$, and 0.5 .

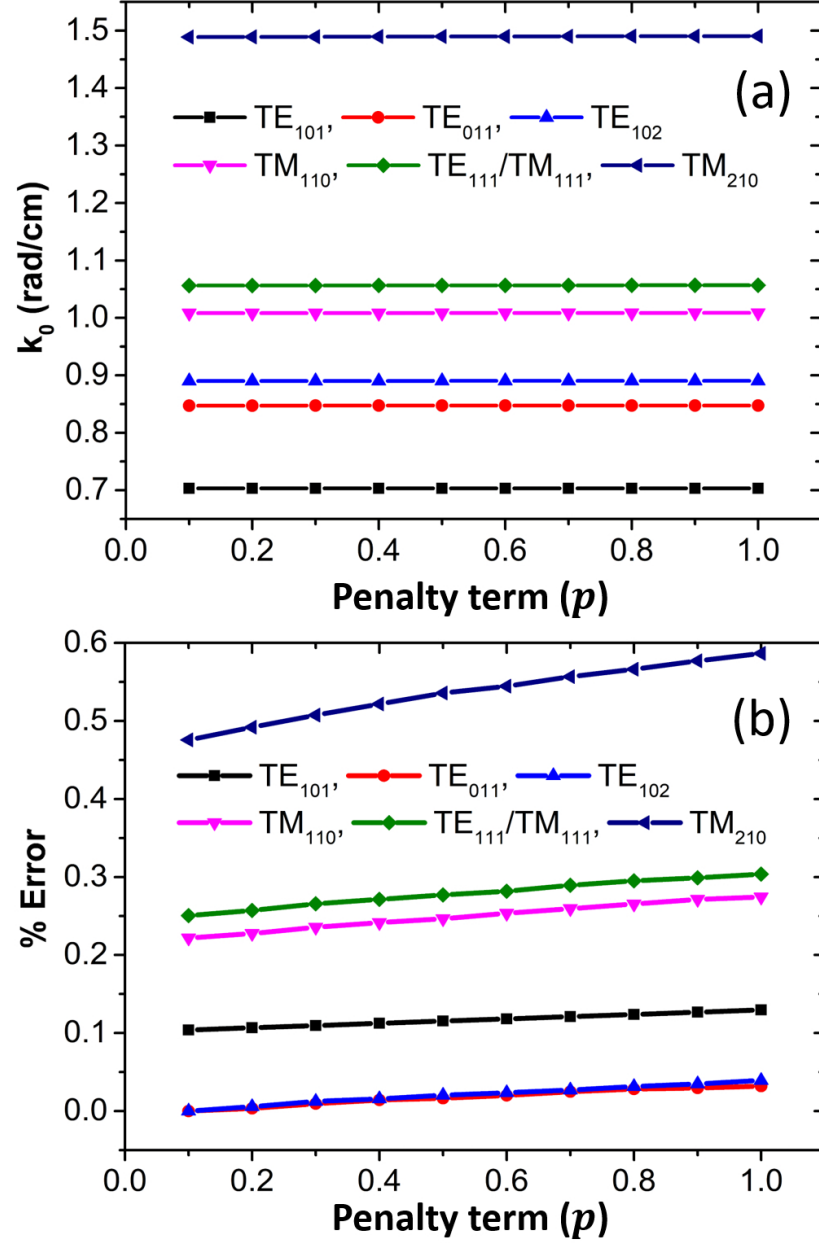


Figure C.4: (a) shows the wavenumber (k_0) variation of different modes such as TE_{101} , TE_{011} , TE_{102} , TM_{110} , degenerated TE_{111} and TM_{111} , and TM_{210} with penalty term (p); (b) illustrates the variation of numerical %error of those modes against penalty term. A 3D unstructured mesh with 18076 nodes is used for domain discretisation.

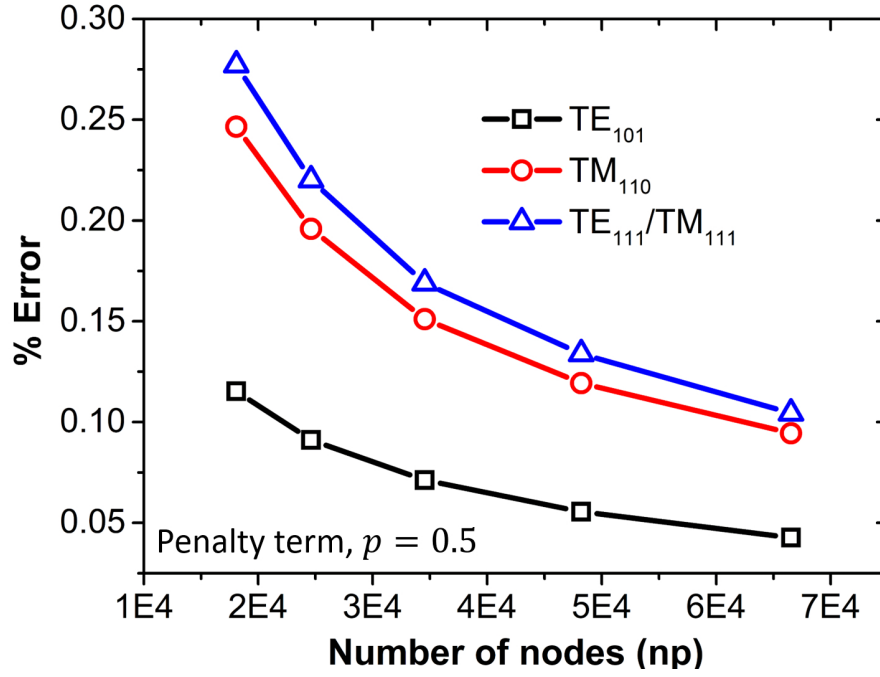


Figure C.5: Schematic diagram of a 3D air filled rectangular cavity of dimensions $a = 5$ cm, $b = 1$ cm, and $c = 10$ cm along x , y , and z directions. The cavity is considered to be enclosed with perfect electric walls (PEW).

for higher order modes. Inclusion of penalty term does not increase the matrix order and additional computational cost is almost negligible. For all these simulations, a 3D unstructured mesh distribution with node numbers (np) of 18076 has been considered for domain discretisation.

Next, the dependence of numerical accuracy on mesh size is studied for different TE and TM modes. TE_{101} , TM_{110} , and TE_{111} and TM_{111} degenerated modes are simulated with different mesh sizes keeping the penalty term fixed at 0.5. The mesh size is represented here in terms of node numbers (np). The simulation results are shown in the Tables C.2, C.3, and C.4. Figure C.5 reveals that the percentage error decreases and becomes almost stable with the incremental node numbers in a mesh which clearly indicates that a higher numerical accuracy could be obtained at higher mesh. It is also noticeable that the percentage error for higher order mode is higher for same mesh size. As the higher order mode field has faster spatial variation so they need a finer mesh to achieve same accuracy. These promising data and corresponding plots help to benchmark the 3D FV-FEM code. Figure C.6 (a), (b), and (c) show the analytically solved H_x field profiles of the degenerated TE_{111} and TM_{111} modes and Fig. C.6(d), (e), and (f) show the

FV-FEM simulated field profiles of the same mode for a detail comparison. The degenerated TE_{111} and TM_{111} field profiles from 3D FV-FEM are noise-free and also matching exactly with the analytical results. Eigenvalues (wavenumbers) are also matching well with the analytically obtained results. The percentage error for each and every mode has been calculated and their variations with penalty term and mesh size are shown in this section. All the graphs and field profiles are the solid evidence to assess the accuracy of the newly developed three dimensional \vec{H} -field based finite element program.

Table C.2: Analytical and 3D FV-FEM simulated wavenumber of the TE_{101} mode.

TE_{101} mode			
k_0 (analytical)	Node numbers (np)	k_0 (simulated)	%Error
0.70250	18076	0.70331	0.11530
	24611	0.70314	0.09110
	34542	0.70300	0.07117
	48218	0.70289	0.05552
	66543	0.70280	0.04727

Table C.3: Analytical and 3D FV-FEM simulated wavenumber of the TE_{110} mode.

TE_{110} mode			
k_0 (analytical)	Node numbers (np)	k_0 (simulated)	%Error
1.0058	18076	1.00828	0.24657
	24611	1.00777	0.19586
	34542	1.00732	0.15112
	48218	1.00700	0.11931
	66543	1.00675	0.09445

Table C.4: Analytical and 3D FV-FEM simulated wavenumber of degenerated TE_{111} and TM_{111} mode.

Degenerated TE_{111} and TM_{111} mode			
k_0 (analytical)	Node numbers (np)	k_0 (simulated)	%Error
1.05370	18076	1.05662	0.27712
	24611	1.05602	0.22018
	34542	1.05548	0.16893
	48218	1.05511	0.133814
	66543	1.0548	0.10439

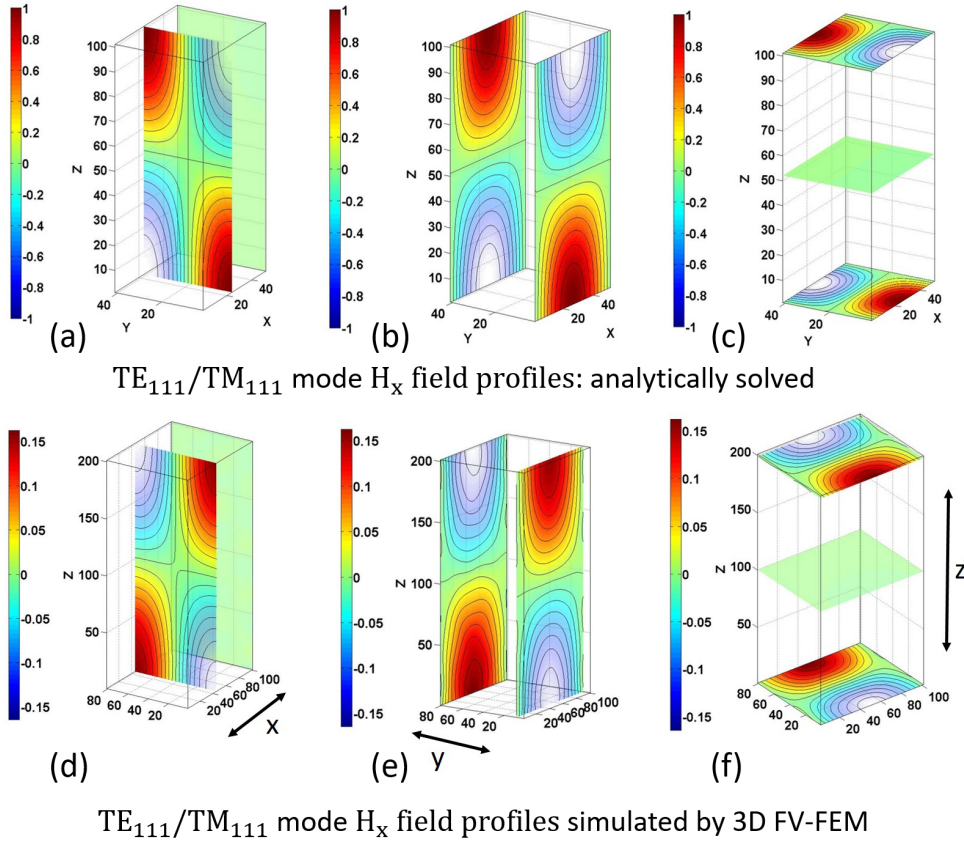


Figure C.6: Schematic diagram of a 3D air filled rectangular cavity of dimensions $a = 5$ cm, $b = 10$ cm, and $c = 10$ cm along x , y , and z directions, respectively. The cavity is considered to be enclosed with perfect electric walls (PEW).

BIBLIOGRAPHY

- Abraham, S. and Li, X. [2014], 'A cost-effective wireless sensor network system for indoor air quality monitoring applications', *Procedia Computer Science* **34**(0), 165–171.
- Agrawal, G. P. [2001], *Applications of Nonlinear Fiber Optics*, Academic press (San Diego, CA).
- Agrawal, G. P. [2012], *Fiber-Optic Communication Systems*, Vol. 222, John Wiley & Sons.
- Aguirre, A. D., Nishizawa, N., Fujimoto, J. G., Seitz, W., Lederer, M. and Kopf, D. [2006], 'Continuum generation in a novel photonic crystal fiber for ultrahigh resolution optical coherence tomography at 800 nm and 1300 nm', *Optics Express* **14**(3), 1145–1160.
- Alam, M., Aitchison, J. S. and Mojahedi, M. [2011], 'Compact hybrid TM-pass polarizer for silicon-on-insulator platform', *Applied Optics* **50**(15), 2294–2298.
- Alam, M., Bahrami, F., Aitchison, J. S. and Mojahedi, M. [2014], 'Analysis and optimization of hybrid plasmonic waveguide as a platform for biosensing', *IEEE Photonics Journal* **6**(4), 1–10.
- Almeida, V. R., Xu, Q., Barrios, C. A. and Lipson, M. [2004], 'Guiding and confining light in void nanostructure', *Optics Letters* **29**(11), 1209–1211.
- Andre, R. M., Marques, M. B., Roy, P. and Frazao, O. [2010], 'Fiber loop mirror using a small core microstructured fiber for strain and temperature discrimination', *IEEE Photonics Technology Letters* **22**(15), 1120–1122.
- Aref, S. H., Amezcua-Correa, R., Carvalho, J. P., Frazão, O., Caldas, P., Santos, J. L., Araújo, F. M., Latifi, H., Farahi, F., Ferreira, L. A. and Knight, J. C. [2009], 'Modal interferometer based on hollow-core photonic crystal fiber for strain and temperature measurement', *Optics Express* **17**(21), 18669–18675.

- Ashkin, A., Dziedzic, J. M. and Yamane, T. [1987], 'Optical trapping and manipulation of single cells using infrared laser beams', *Nature* **330**(6150), 769.
- Austin, E., van Brakel, A., Petrovich, M. N. and Richardson, D. J. [2009], 'Fibre optical sensor for C₂H₂ gas using gas-filled photonic bandgap fibre reference cell', *Sensors and Actuators B: Chemical* **139**(1), 30–34.
- Babar, S. and Weaver, J. [2015], 'Optical constants of Cu, Ag, and Au revisited', *Applied Optics* **54**(3), 477–481.
- Bajraszewski, T., Wojtkowski, M., Szkulmowski, M., Szkulmowska, A., Huber, R. and Kowalczyk, A. [2008], 'Improved spectral optical coherence tomography using optical frequency comb', *Optics Express* **16**(6), 4163–4176.
- Barrios, C. A., Banuls, M. J., Gonzalez-Pedro, V., Gylfason, K. B., Sanchez, B., Griol, A., Maquieira, A., Sohlström, H., Holgado, M. and Casquel, R. [2008], 'Label-free optical biosensing with slot-waveguides', *Optics Letters* **33**(7), 708–710.
- Barrios, C. A., Gylfason, K. B., Sánchez, B., Griol, A., Sohlström, H., Holgado, M. and Casquel, R. [2007a], 'Slot-waveguide biochemical sensor', *Optics Letters* **32**(21), 3080–3082.
- Barrios, C. A., Sánchez, B., Gylfason, K. B., Griol, A., Sohlström, H., Holgado, M. and Casquel, R. [2007b], 'Demonstration of slot-waveguide structures on silicon nitride/silicon oxide platform', *Optics Express* **15**(11), 6846–6856.
- Berini, P. [2000], 'Plasmon-polariton waves guided by thin lossy metal films of finite width: Bound modes of symmetric structures', *Physical Review B* **61**(15), 10484.
- Berini, P. [2001], 'Plasmon-polariton waves guided by thin lossy metal films of finite width: Bound modes of asymmetric structures', *Physical Review B* **63**(12), 125417.
- Berini, P. [2008], 'Bulk and surface sensitivities of surface plasmon waveguides', *New Journal of Physics* **10**(10), 105010.
- Berk, A. [1956], 'Variational principles for electromagnetic resonators and waveguides', *IRE Transactions on Antennas and Propagation* **4**(2), 104–111.

- Bernini, R., Campopiano, S. and Zeni, L. [2002], 'Silicon micromachined hollow optical waveguides for sensing applications', *IEEE Journal of Selected Topics in Quantum Electronics* **8**(1), 106–110.
- Bhatia, V. and Vengsarkar, A. M. [1996], 'Optical fiber long-period grating sensors', *Optics Letters* **21**(9), 692–694.
- Bierwirth, K., Schulz, N. and Arndt, F. [1986], 'Finite-difference analysis of rectangular dielectric waveguide structures', *IEEE Transactions on Microwave Theory and Techniques* **34**(11), 1104–1114.
- Birks, T. A., Roberts, P. J., Russell, P. S. J., Atkin, D. M. and Shepherd, T. J. [1995], 'Full 2-D photonic bandgaps in silica/air structures', *Electronics Letters* **31**(22), 1941–1943.
- Bock, W., Chen, J., Mikulic, P., Eftimov, T. and Korwin-Pawlowski, M. [2007], 'Pressure sensing using periodically tapered long-period gratings written in photonic crystal fibres', *Measurement Science and Technology* **18**(10), 3098.
- Bohren, C. F. and Huffman, D. R. [2008], *Absorption and Scattering of Light by Small Particles*, John Wiley & Sons, NY, USA.
- Bolívar, P. H., Nagel, M., Richter, F., Brucherseifer, M., Kurz, H., Bosserhoff, A. and Büttner, R. [2004], 'Label-free THz sensing of genetic sequences: towards THz biochips', *Philosophical Transactions of the Royal Society of London A: Mathematical, Physical and Engineering Sciences* **362**(1815), 323–335.
- Bond, W. [1965], 'Measurement of the refractive indices of several crystals', *Journal of Applied Physics* **36**(5), 1674–1677.
- Brucherseifer, M., Nagel, M., Haring Bolivar, P., Kurz, H., Bosserhoff, A. and Büttner, R. [2000], 'Label-free probing of the binding state of DNA by time-domain terahertz sensing', *Applied Physics Letters* **77**(24), 4049–4051.
- Bruel, M., Aspar, B. and Auberton-Hervé, A.-J. [1997], 'Smart-Cut: a new silicon on insulator material technology based on hydrogen implantation and wafer bonding', *Japanese Journal of Applied Physics* **36**(3S), 1636.

- Buric, M. P., Chen, K. P., Falk, J. and Woodruff, S. D. [2008], 'Enhanced spontaneous Raman scattering and gas composition analysis using a photonic crystal fiber', *Applied Optics* **47**(23), 4255–4261.
- Buric, M. P., Chen, K. P., Falk, J. and Woodruff, S. D. [2009], 'Improved sensitivity gas detection by spontaneous Raman scattering', *Applied Optics* **48**(22), 4424–4429.
- Burke, J., Stegeman, G. and Tamir, T. [1986], 'Surface-polariton-like waves guided by thin, lossy metal films', *Physical Review B* **33**(8), 5186.
- Bykov, D., Schmidt, O., Euser, T. and Russell, P. S. J. [2015], 'Flying particle sensors in hollow-core photonic crystal fibre', *Nature Photonics* **9**(7), 461.
- Caër, C., Serna-Otálvaro, S. F., Zhang, W., Le Roux, X. and Cassan, E. [2014], 'Liquid sensor based on high-Q slot photonic crystal cavity in silicon-on-insulator configuration', *Optics Letters* **39**(20), 5792–5794.
- Canet, D., Doering, K., Dobson, C. M. and Dupont, Y. [2001], 'High-sensitivity fluorescence anisotropy detection of protein-folding events: application to α -lactalbumin', *Biophysical Journal* **80**(4), 1996–2003.
- Castro-Camus, E., Palomar, M. and Covarrubias, A. A. [2013], 'Leaf water dynamics of *Arabidopsis thaliana* monitored in-vivo using terahertz time-domain spectroscopy', *Scientific Reports* **3**, 2910.
- Chamorovskiy, Y., Starostin, N., Ryabko, M., Sazonov, A., Morshnev, S., Gubin, V., Vorob'ev, I. and Nikitov, S. [2009], 'Miniature microstructured fiber coil with high magneto-optical sensitivity', *Optics Communications* **282**(23), 4618–4621.
- Chandran, S., Gupta, R. K. and Das, B. K. [2017], 'Dispersion enhanced critically coupled ring resonator for wide range refractive index sensing', *IEEE Journal of Selected Topics in Quantum Electronics* **23**(2), 424–432.
- Chang, C.-M. and Solgaard, O. [2013], 'Fano resonances in integrated silicon Bragg reflectors for sensing applications', *Optics Express* **21**(22), pp. 27209–27218.

- Chee, G.-J., Nomura, Y., Ikebukuro, K. and Karube, I. [2000], 'Optical fiber biosensor for the determination of low biochemical oxygen demand', *Biosensors and Bioelectronics* **15**(7-8), 371–376.
- Chen, C., Caucheteur, C., Voisin, V., Albert, J. and Berini, P. [2014], 'Long-range surface plasmons on gold-coated single-mode fibers', *Journal of the Optical Society of America B* **31**(10), 2354–2362.
- Chen, H., Ramachandra, M. and Padmanabhan, R. [1994], 'Biochemical characterization of a temperature-sensitive adenovirus DNA polymerase', *Virology* **205**(1), pp. 364–370.
- Chen, H., Rangasamy, M., Tan, S. Y., Wang, H. and Siegfried, B. D. [2010], 'Evaluation of five methods for total DNA extraction from western corn rootworm beetles', *PLoS one* **5**(8), pp. e11963.
- Chen, J., Xu, L., Li, W. and Gou, X. [2005], ' α -Fe₂O₃ nanotubes in gas sensor and lithium-ion battery applications', *Advanced Materials* **17**(5), 582–586.
- Cheung, K. and Auston, D. [1986], 'A novel technique for measuring far-infrared absorption and dispersion', *Infrared Physics* **26**(1), 23–27.
- Chiang, K. S. [1994], 'Review of numerical and approximate methods for the modal analysis of general optical dielectric waveguides', *Optical and Quantum Electronics* **26**(3), S113–S134.
- Claes, T., Molera, J. G., De Vos, K., Schacht, E., Baets, R. and Bienstman, P. [2009], 'Label-free biosensing with a slot-waveguide-based ring resonator in silicon on insulator', *IEEE Photonics Journal* **1**(3), 197–204.
- Cox, W. G. and Singer, V. L. [2004], 'Fluorescent DNA hybridization probe preparation using amine modification and reactive dye coupling', *Biotechniques* **36**(1), 114–123.
- Curtis, J. E., Koss, B. A. and Grier, D. G. [2002], 'Dynamic holographic optical tweezers', *Optics Communications* **207**(1-6), 169–175.
- Cusano, A., Pilla, P., Contessa, L., Iadicicco, A., Campopiano, S., Cutolo, A., Giordano, M. and Guerra, G. [2005], 'High-sensitivity optical chemosensor based on coated long-

- period gratings for sub-ppm chemical detection in water', *Applied Physics Letters* **87**(23), 234105.
- Dagli, N. and Fonstad, C. [1985], 'Analysis of rib dielectric waveguides', *IEEE Journal of Quantum Electronics* **21**(4), 315–321.
- Dar, T., Homola, J., Rahman, B. M. A. and Rajarajan, M. [2012], 'Label-free slot-waveguide biosensor for the detection of DNA hybridization', *Applied Optics* **51**(34), 8195–8202.
- Davies, J. B. [1973], 'A least-squares boundary residual method for the numerical solution of scattering problems', *IEEE Transactions on Microwave Theory and Techniques* **21**(2), 99–104.
- De Vos, K., Bartolozzi, I., Schacht, E., Bienstman, P. and Baets, R. [2007], 'Silicon-on-insulator microring resonator for sensitive and label-free biosensing', *Optics Express* **15**(12), 7610–7615.
- Dell'Olio, F. and Passaro, V. M. [2007], 'Optical sensing by optimized silicon slot waveguides', *Optics Express* **15**(8), 4977–4993.
- Deng, M., Liu, L., Zhao, Y., Yin, G. and Zhu, T. [2017], 'Highly sensitive temperature sensor based on an ultra-compact Mach–Zehnder interferometer with side-opened channels', *Optics Letters* **42**(18), 3549–3552.
- Ding, H., Li, X., Cui, J., Yang, L. and Dong, S. [2011], 'An all-fiber gas sensing system using hollow-core photonic bandgap fiber as gas cell', *Instrumentation Science and Technology* **39**(1), 78–87.
- Dobb, H., Kalli, K. and Webb, D. J. [2004], 'Temperature-insensitive long period grating sensors in photonic crystal fibre', *Electronics Letters* **40**(11), 657–658.
- Dudley, J. M. and Taylor, J. R. [2009], 'Ten years of nonlinear optics in photonic crystal fibre', *Nature Photonics* **3**(2), 85.
- Dutta, R., Bharadwaj, R., Mukherji, S. and Kundu, T. [2011], 'Study of localized surface-plasmon-resonance-based optical fiber sensor', *Applied Optics* **50**(25), E138–E144.

- Dwivedi, S., D’heer, H. and Bogaerts, W. [2013], ‘A compact all-silicon temperature insensitive filter for WDM and bio-sensing applications’, *IEEE Photonics Technology Letters* **25**(22), 2167–2170.
- Eggleton, B., Westbrook, P., Windeler, R., Spälter, S. and Strasser, T. [1999], ‘Grating resonances in air–silica microstructured optical fibers’, *Optics Letters* **24**(21), 1460–1462.
- Elhadj, S., Singh, G. and Saraf, R. F. [2004], ‘Optical properties of an immobilized DNA monolayer from 255 to 700 nm’, *Langmuir* **20**(13), 5539–5543.
- Falconer, R. J. and Markelz, A. G. [2012], ‘Terahertz spectroscopic analysis of peptides and proteins’, *Journal of Infrared, Millimeter, and Terahertz Waves* **33**(10), 973–988.
- Fard, S. T., Grist, S. M., Donzella, V., Schmidt, S. A., Flueckiger, J., Wang, X., Shi, W., Millspaugh, A., Webb, M., Ratner, D. M. *et al.* [2013], Label-free silicon photonic biosensors for use in clinical diagnostics, in ‘Silicon Photonics VIII’, Vol. 8629, International Society for Optics and Photonics, p. 862909.
- Favero, F. C., Pruneri, V. and Villatoro, J. [2012], ‘Microstructured optical fiber interferometric breathing sensor’, *Journal of Biomedical Optics* **17**(3), 037006.
- Federici, J. F., Schulkin, B., Huang, F., Gary, D., Barat, R., Oliveira, F. and Zimdars, D. [2005], ‘THz imaging and sensing for security applications – explosives, weapons and drugs’, *Semiconductor Science and Technology* **20**(7), S266.
- Ferreira, M. F., Castro-Camus, E., Ottaway, D. J., López-Higuera, J. M., Feng, X., Jin, W., Jeong, Y., Picqué, N., Tong, L., Reinhard, B. M., Pellegrino, P. M., Méndez, A., Diem, M., Vollmer, F. and Quan, Q. [2017], ‘Roadmap on optical sensors’, *Journal of Optics* **19**(8), 083001.
- Flueckiger, J., Schmidt, S., Donzella, V., Sherwali, A., Ratner, D. M., Chrostowski, L. and Cheung, K. C. [2016], ‘Sub-wavelength grating for enhanced ring resonator biosensor’, *Optics Express* **24**(14), 15672–15686.
- Foltynowicz, A., Masłowski, P., Ban, T., Adler, F., Cossel, K. C., Briles, T. C. and Ye, J. [2011], ‘Optical frequency comb spectroscopy’, *Faraday Discussions* **150**, 23–31.

- Frazao, O., Aref, S., Baptista, J. M., Santos, J. L., Latifi, H., Farahi, F., Kobelke, J. and Schuster, K. [2009], 'Fabry-Pérot cavity based on a suspended-core fiber for strain and temperature measurement', *IEEE Photonics Technology Letters* **21**(17), 1229–1231.
- Fu, H., Khijwania, S. K., Tam, H., Wai, P. and Lu, C. [2010], 'Polarization-maintaining photonic-crystal-fiber-based all-optical polarimetric torsion sensor', *Applied Optics* **49**(31), 5954–5958.
- Future, M. R. [2018], 'Global optical sensing market research report- forecast 2023'.
URL: <https://www.marketresearchfuture.com/reports/optical-sensing-market-3260>
- Garahan, A., Pilon, L., Yin, J. and Saxena, I. [2007], 'Effective optical properties of absorbing nanoporous and nanocomposite thin films', *Journal of Applied Physics* **101**(1), pp. 014320.
- Gas, L. [2013], 'Lower and upper explosive limits for flammable gases and vapors', *Mathereson Gas Products* p. 22.
- Gatti, D., Sala, T., Marangoni, M., Galzerano, G. and Gianfrani, L. [2012], 'Precision molecular spectroscopy with frequency combs', *Encyclopedia of Analytical Chemistry* pp. 1–20.
- Ghosh, S. and Rahman, B. M. A. [2016], Full vectorial finite element modelling: A composite plasmonic horizontal slot waveguide as a bio-sensor, in 'International Conference on Fibre Optics and Photonics', Optical Society of America, pp. Tu5C–3.
- Ghosh, S. and Rahman, B. M. A. [2017a], 'A compact Mach-Zehnder interferometer using composite plasmonic waveguide for ethanol vapor sensing', *Journal of Lightwave Technology* **35**(14), 3003–3011.
- Ghosh, S. and Rahman, B. M. A. [2017b], 'An innovative straight resonator incorporating a vertical slot as an efficient bio-chemical sensor', *IEEE Journal of Selected Topics in Quantum Electronics* **23**(2), 1–8.
- Giallorenzi, T. G., Bucaro, J. A., Dandridge, A., Sigel, G. H., Cole, J. H., Rashleigh, S. C. and Priest, R. G. [1982], 'Optical fiber sensor technology', *IEEE Transactions on Microwave Theory and Techniques* **30**(4), 472–511.

- Gibson, D. and MacGregor, C. [2013], 'A novel solid state non-dispersive infrared CO₂ gas sensor compatible with wireless and portable deployment', *Sensors* **13**(6), 7079–7103.
- Goell, J. [1969], 'A circular-harmonic computer analysis of rectangular dielectric waveguides', *Bell Labs Technical Journal* **48**(7), 2133–2160.
- Gong, H., Chan, C., Zu, P., Chen, L. and Dong, X. [2010], 'Curvature measurement by using low-birefringence photonic crystal fiber based Sagnac loop', *Optics Communications* **283**(16), 3142–3144.
- Graf, M., Scalari, G., Hofstetter, D., Faist, J., Beere, H., Linfield, E., Ritchie, D. and Davies, G. [2004], 'Terahertz range quantum well infrared photodetector', *Applied Physics Letters* **84**(4), 475–477.
- Grattan, K. T. V. and Sun, T. [2000], 'Fiber optic sensor technology: an overview', *Sensors and Actuators A: Physical* **82**(1-3), 40–61.
- Grubsky, V. and Feinberg, J. [2000], 'Long-period fiber gratings with variable coupling for real-time sensing applications', *Optics Letters* **25**(4), 203–205.
- Gu, Z., Xu, Y. and Gao, K. [2006], 'Optical fiber long-period grating with solgel coating for gas sensor', *Optics Letters* **31**(16), 2405–2407.
- Guan, X., Wang, X. and Frandsen, L. H. [2016], 'Optical temperature sensor with enhanced sensitivity by employing hybrid waveguides in a silicon Mach-Zehnder interferometer', *Optics Express* **24**(15), 16349–16356.
- Hameed, M. F. O., Saadeldin, A. S., Elkaramany, E. M. A. and Obayya, S. S. A. [2017], 'Label-free highly sensitive hybrid plasmonic biosensor for the detection of DNA hybridization', *Journal of Lightwave Technology* **35**(22), 4851–4858.
- Han, Y.-G., Chung, Y., Lee, S. B., Kim, C.-S., Jeong, M. Y. and Kim, M. K. [2009], 'Temperature and strain discrimination based on a temperature-insensitive birefringent interferometer incorporating an erbium-doped fiber', *Applied Optics* **48**(12), 2303–2307.

- Harms, P., Sipior, J., Ram, N., Carter, G. M. and Rao, G. [1999], 'Low cost phase-modulation measurements of nanosecond fluorescence lifetimes using a lock-in amplifier', *Review of Scientific Instruments* **70**(2), 1535–1539.
- Haron, S. and Ray, A. K. [2006], 'Optical biodetection of cadmium and lead ions in water', *Medical Engineering and Physics* **28**(10), 978–981.
- Hasegawa, T. and Sasada, H. [2017], 'Direct-comb molecular spectroscopy by heterodyne detection with continuous-wave laser for high sensitivity', *Optics Express* **25**(16), A680–A688.
- He, Z., Zhu, Y. and Du, H. [2008], 'Long-period gratings inscribed in air-and water-filled photonic crystal fiber for refractometric sensing of aqueous solution', *Applied Physics Letters* **92**(4), 044105.
- Heiblum, M. and Harris, J. [1975], 'Analysis of curved optical waveguides by conformal transformation', *IEEE Journal of Quantum Electronics* **11**(2), 75–83.
- Heinemann, L. and Schmelzeisen-Redeker, G. [1998], 'Non-invasive continuous glucose monitoring in Type I diabetic patients with optical glucose sensors', *Diabetologia* **41**(7), 848–854.
- Henningsen, J., Hald, J. and Petersen, J. C. [2005], 'Saturated absorption in acetylene and hydrogen cyanide in hollow-core photonic bandgap fibers', *Optics Express* **13**(26), 10475–10482.
- Hill, K. O. and Meltz, G. [1997], 'Fiber Bragg grating technology fundamentals and overview', *Journal of Lightwave Technology* **15**(8), 1263–1276.
- Hirayama, N. and Sano, Y. [2000], 'Fiber Bragg grating temperature sensor for practical use', *ISA Transactions* **39**(2), 169–173.
- Hocde, S., Loréal, O., Sire, O., Boussard-Pledel, C., Bureau, B., Turlin, B., Keirsse, J., Leroyer, P. and Lucas, J. [2004], 'Metabolic imaging of tissues by infrared fiber-optic spectroscopy: an efficient tool for medical diagnosis', *Journal of Biomedical Optics* **9**(2), 404–408.

- Homola, J. [2003], 'Present and future of surface plasmon resonance biosensors', *Analytical and Bioanalytical Chemistry* **377**(3), 528–539.
- Homola, J., Yee, S. S. and Gauglitz, G. [1999], 'Surface plasmon resonance sensors', *Sensors and Actuators B: Chemical* **54**(1), 3–15.
- Hoo, Y., Jin, W., Ho, H., Ju, J. and Wang, D. [2005], 'Gas diffusion measurement using hollow-core photonic bandgap fiber', *Sensors and Actuators B: Chemical* **105**(2), 183–186.
- Hoo, Y., Jin, W., Ho, H. L., Wang, D. and Windeler, R. S. [2002], 'Evanescent-wave gas sensing using microstructure fiber', *Optical Engineering* **41**(1), 8–10.
- Hu, D. J. J., Lim, J. L., Jiang, M., Wang, Y., Luan, F., Shum, P. P., Wei, H. and Tong, W. [2012], 'Long period grating cascaded to photonic crystal fiber modal interferometer for simultaneous measurement of temperature and refractive index', *Optics Letters* **37**(12), 2283–2285.
- Irace, A. and Breglio, G. [2003], 'All-silicon optical temperature sensor based on multi-mode interference', *Optics Express* **11**(22), 2807–2812.
- Iyer, S. S. [2002], 'Silicon Wafer Bonding Technology for VLSI and MEMS Applications (Emis Processing Series, 1)'.
- James, S. W. and Tatam, R. P. [2003], 'Optical fibre long-period grating sensors: characteristics and application', *Measurement Science and Technology* **14**(5), R49.
- Jing, Z. and Zhan, J. [2008], 'Fabrication and gas-sensing properties of porous ZnO nanoplates', *Advanced Materials* **20**(23), 4547–4551.
- Johnson, P. B. and Christy, R.-W. [1972], 'Optical constants of the noble metals', *Physical Review B* **6**(12), 4370.
- Jorgenson, R. C. and Yee, S. S. [1993], 'A fiber-optic chemical sensor based on surface plasmon resonance', *Sensors and Actuators B: Chemical* **12**(3), 213–220.

- Jugessur, A., Dou, J., Aitchison, J., De La Rue, R. and Gnan, M. [2009], 'A photonic nano-Bragg grating device integrated with microfluidic channels for bio-sensing applications', *Microelectronic Engineering* **86**(4-6), 1488–1490.
- Kakarantzas, G., Birks, T. and Russell, P. S. J. [2002], 'Structural long-period gratings in photonic crystal fibers', *Optics Letters* **27**(12), 1013–1015.
- Kaminow, I., Li, T. and Willner, A. E. [2010], *Optical Fiber Telecommunications VB: Systems and Networks*, Elsevier.
- Kano, H. and Hamaguchi, H. O. [2004], 'Femtosecond coherent anti-stokes Raman scattering spectroscopy using supercontinuum generated from a photonic crystal fiber', *Applied Physics Letters* **85**(19), 4298–4300.
- Kargar, A. and Chao, C.-Y. [2011], 'Design and optimization of waveguide sensitivity in slot microring sensors', *Journal of the Optical Society of America A* **28**(4), 596–603.
- Kawano, K., Kitoh, T., Kohtoku, M., Ito, T. and Hasumi, Y. [1998], 'Bidirectional finite-element method-of-line beam propagation method (FE-MoL-BPM) for analyzing optical waveguides with discontinuities', *IEEE Photonics Technology Letters* **10**(2), 244–245.
- Kedenburg, S., Vieweg, M., Gissibl, T. and Giessen, H. [2012], 'Linear refractive index and absorption measurements of nonlinear optical liquids in the visible and near-infrared spectral region', *Optical Materials Express* **2**(11), 1588–1611.
- Kejalakshmy, N., Agrawal, A., Aden, Y., Leung, D., Rahman, B. M. A. and Grattan, K. T. V. [2010], 'Characterization of silicon nanowire by use of full-vectorial finite element method', *Applied Optics* **49**(16), 3173–3181.
- Kersey, A. D., Berkoff, T. and Morey, W. [1993], 'Multiplexed fiber Bragg grating strain-sensor system with a fiber Fabry–Perot wavelength filter', *Optics Letters* **18**(16), 1370–1372.
- Khanna, A., Säynätjoki, A., Tervonen, A. and Honkanen, S. [2009], 'Control of optical mode properties in cross-slot waveguides', *Applied Optics* **48**(34), 6547–6552.

- Khodadad, I., Clarke, N., Khorasaninejad, M., Henneke, D. and Saini, S. S. [2014], 'Optimization of multiple-slot waveguides for biochemical sensing', *Applied Optics* **53**(23), 5169–5178.
- Kim, G., Cho, T., Hwang, K., Lee, K., Lee, K. S., Han, Y.-G. and Lee, S. B. [2009], 'Strain and temperature sensitivities of an elliptical hollow-core photonic bandgap fiber based on Sagnac interferometer', *Optics Express* **17**(4), 2481–2486.
- Kim, G.-D., Lee, H.-S., Park, C.-H., Lee, S.-S., Lim, B. T., Bae, H. K. and Lee, W.-G. [2010], 'Silicon photonic temperature sensor employing a ring resonator manufactured using a standard cmos process', *Optics Express* **18**(21), 22215–22221.
- Klimov, N., Berger, M. and Ahmed, Z. [2015], 'Towards reproducible ring resonator based temperature sensors', *Sensors & Transducers* **191**(8), 63.
- Klimov, N. N., Mittal, S., Berger, M. and Ahmed, Z. [2015], 'On-chip silicon waveguide Bragg grating photonic temperature sensor', *Optics Letters* **40**(17), 3934–3936.
- Klimov, N., Purdy, T. and Ahmed, Z. [2015], Fabry-Perot cavity-based silicon photonic thermometers with ultra-small footprint and high sensitivity, in 'Optical Sensors', Optical Society of America, pp. SeT4C–4.
- Knap, W., Dyakonov, M., Coquillat, D., Teppe, F., Dyakonova, N., Łusakowski, J., Karpierz, K., Sakowicz, M., Valusis, G., Seliuta, D., Kasalynas, I., El Fatimy, A., Meziani, Y. M. and Otsuji, T. [2009], 'Field effect transistors for terahertz detection: Physics and first imaging applications', *Journal of Infrared, Millimeter, and Terahertz Waves* **30**(12), 1319–1337.
- Knight, J. C., Birks, T. A., Atkin, D. M. and Russell, P. S. J. [1996], Pure silica single-mode fibre with hexagonal photonic crystal cladding, in 'Optical Fiber Communication Conference', Optical Society of America, p. PD3.
- Knight, J. C., Birks, T. A., Cregan, R. F., Russell, P. S. J. and De Sandro, P. D. [1998], 'Large mode area photonic crystal fibre', *Electronics Letters* **34**(13), 1347–1348.

- Knox, R. and Toullos, P. [1970], Integrated circuits for the millimeter through optical frequency range, in 'Proc. Symp. Submillimeter Waves', Vol. 20, Polytechnic Press of Polytechnic Institute of Brooklyn, pp. 497–515.
- Ko, S. and Grant, S. A. [2006], 'A novel FRET-based optical fiber biosensor for rapid detection of Salmonella Typhimurium', *Biosensors and Bioelectronics* **21**(7), 1283–1290.
- Kok, P., Munro, W. J., Nemoto, K., Ralph, T. C., Dowling, J. P. and Milburn, G. J. [2007], 'Linear optical quantum computing with photonic qubits', *Reviews of Modern Physics* **79**(1), 135.
- Konstantaki, M., Pissadakis, S., Pispas, S., Madamopoulos, N. and Vainos, N. A. [2006], 'Optical fiber long-period grating humidity sensor with poly (ethylene oxide)/cobalt chloride coating', *Applied Optics* **45**(19), 4567–4571.
- Kornaszewski, Ł., Gayraud, N., Stone, J. M., MacPherson, W. N., George, A. K., Knight, J. C., Hand, D. P. and Reid, D. T. [2007], 'Mid-infrared methane detection in a photonic bandgap fiber using a broadband optical parametric oscillator', *Optics Express* **15**(18), 11219–11224.
- Koshiba, M., Ooishi, K., Miki, T. and Suzuki, M. [1982], 'Finite-element analysis of the discontinuities in a dielectric slab waveguide bounded by parallel plates', *Electronics Letters* **18**(1), 33–34.
- Koshiba, M. and Saitoh, K. [2003], 'Structural dependence of effective area and mode field diameter for holey fibers', *Optics Express* **11**(15), 1746–1756.
- Kou, J.-l., Xu, F. and Lu, Y. Q. [2012], 'Loop-mirror-based slot waveguide refractive index sensor', *AIP Advances* **2**(4), 042142.
- Krasavin, A. V. and Zayats, A. V. [2010], 'Silicon-based plasmonic waveguides', *Optics Express* **18**(11), 11791–11799.
- Kress-Rogers, E. [1996], *Handbook of Biosensors and Electronic Noses: Medicine, Food, and the Environment*, CRC Press.

- Kretschmann, E. and Raether, H. [1968], 'Radiative decay of non radiative surface plasmons excited by light', *Zeitschrift für Naturforschung A* **23**(12), 2135–2136.
- Kronenberg, P., Rastogi, P. K., Giaccari, P. and Limberger, H. G. [2002], 'Relative humidity sensor with optical fiber Bragg gratings', *Optics Letters* **27**(16), 1385–1387.
- Kumari, B., Barh, A., Varshney, R. K. and Pal, B. P. [2016], 'Silicon-on-nitride slot waveguide: a promising platform as mid-IR trace gas sensor', *Sensors and Actuators B: Chemical* **236**, 759–764.
- Kumari, B., Varshney, R. K. and Pal, B. P. [2018], 'Design of chip scale silicon rib slot waveguide for sub-ppm detection of N₂O gas at mid-IR band', *Sensors and Actuators B: Chemical* **255**, 3409–3416.
- Kuze, A., Suto, H., Nakajima, M. and Hamazaki, T. [2009], 'Thermal and near infrared sensor for carbon observation fourier-transform spectrometer on the greenhouse gases observing satellite for greenhouse gases monitoring', *Applied Optics* **48**(35), 6716–6733.
- Lai, W.-C., Chakravarty, S., Wang, X., Lin, C. and Chen, R. T. [2011], 'On-chip methane sensing by near-IR absorption signatures in a photonic crystal slot waveguide', *Optics Letters* **36**(6), 984–986.
- Lakowicz, J. R., ed. [2006], *Fluorescence Sensing*, Springer US, Boston, MA, pp. 623–673.
- Lakowicz, J. R. and Maliwal, B. [1993], 'Optical sensing of glucose using phase-modulation fluorimetry', *Analytica Chimica Acta* **271**(1), 155–164.
- Lehmann, H., Bartelt, H., Willsch, R., Amezcua-Correa, R. and Knight, J. C. [2011], 'In-line gas sensor based on a photonic bandgap fiber with laser-drilled lateral microchannels', *IEEE Sensors Journal* **11**(11), 2926–2931.
- Li, H. [1980], 'Refractive index of silicon and germanium and its wavelength and temperature derivatives', *Journal of Physical and Chemical Reference Data* **9**(3), 561–658.
- Liang, W., Huang, Y., Xu, Y., Lee, R. K. and Yariv, A. [2005], 'Highly sensitive fiber Bragg grating refractive index sensors', *Applied Physics Letters* **86**(15), 151122.

- Liang, X., Morton, K. J., Austin, R. H. and Chou, S. Y. [2007], 'Single sub-20 nm wide, centimeter-long nanofluidic channel fabricated by novel nanoimprint mold fabrication and direct imprinting', *Nano Letters* **7**(12), 3774–3780.
- Lipka, T., Wahn, L., Trieu, H.-K., Hilterhaus, L. and Muller, J. [2013], 'Label-free photonic biosensors fabricated with low-loss hydrogenated amorphous silicon resonators', *Journal of Nanophotonics* **7**(1), 073793.
- Liu, Q., Kee, J. S. and Park, M. K. [2013a], 'A refractive index sensor design based on grating-assisted coupling between a strip waveguide and a slot waveguide', *Optics Express* **21**(5), 5897–5909.
- Liu, Q., Tu, X., Kim, K. W., Kee, J. S., Shin, Y., Han, K., Yoon, Y.-J., Lo, G.-Q. and Park, M. K. [2013b], 'Highly sensitive Mach–Zehnder interferometer biosensor based on silicon nitride slot waveguide', *Sensors and Actuators B: Chemical* **188**, 681–688.
- Lommens, P., Van Thourhout, D., Smet, P., Poelman, D. and Hens, Z. [2008], 'Electrophoretic deposition of ZnO nanoparticles, from micropatterns to substrate coverage', *Nanotechnology* **19**(24), 245301.
- Lu, F., Li, T., Xu, J., Xie, Z., Li, L., Zhu, S. and Zhu, Y. [2011], 'Surface plasmon polariton enhanced by optical parametric amplification in nonlinear hybrid waveguide', *Optics Express* **19**(4), 2858–2865.
- Luff, B., Wilkinson, J. S., Piehler, J., Hollenbach, U., Ingenhoff, J. and Fabricius, N. [1998], 'Integrated optical Mach-Zehnder biosensor', *Journal of Lightwave Technology* **16**(4), 583.
- Mahadevan-Jansen, A., Mitchell, M. F., Ramanujam, N., Utzinger, U. and Richards-Kortum, R. [1998], 'Development of a fiber optic probe to measure NIR Raman spectra of cervical tissue in vivo', *Photochemistry and Photobiology* **68**(3), 427–431.
- Maier, S. A. [2007], *Plasmonics: Fundamentals and Applications*, Springer Science & Business Media.
- Malitson, I. [1965], 'Interspecimen comparison of the refractive index of fused silica', *Journal of Optical Society of America A* **55**(10), 1205–1209.

- Mandon, J., Guelachvili, G. and Picqué, N. [2009], 'Fourier transform spectroscopy with a laser frequency comb', *Nature Photonics* **3**(2), 99.
- Marcatili, E. A. [1969], 'Dielectric rectangular waveguide and directional coupler for integrated optics', *Bell Labs Technical Journal* **48**(7), 2071–2102.
- Masson, J.-F., Obando, L., Beaudoin, S. and Booksh, K. [2004], 'Sensitive and real-time fiber-optic-based surface plasmon resonance sensors for myoglobin and cardiac troponin I', *Talanta* **62**(5), 865–870.
- Mathew, J., Semenova, Y., Rajan, G. and Farrell, G. [2010], 'Humidity sensor based on photonic crystal fibre interferometer', *Electronics Letters* **46**(19), 1341–1343.
- Mathews, S., Farrell, G. and Semenova, Y. [2011], 'Liquid crystal infiltrated photonic crystal fibers for electric field intensity measurements', *Applied Optics* **50**(17), 2628–2635.
- McCosker, R. J. and Town, G. E. [2010], Optical chemical sensor using a multi-channel directional coupler with slot waveguides, in 'International Conference on Photonics (ICP) 2010', IEEE, pp. 1–5.
- Mello, L. D. and Kubota, L. T. [2002], 'Review of the use of biosensors as analytical tools in the food and drink industries', *Food Chemistry* **77**(2), 237–256.
- Meltz, G., Morey, W. and Glenn, W. [1989], 'Formation of Bragg gratings in optical fibers by a transverse holographic method', *Optics Letters* **14**(15), 823–825.
- Minamikawa, T., Ogura, T., Nakajima, Y., Hase, E., Mizutani, Y., Yamamoto, H., Minoshima, K. and Yasui, T. [2018], 'Strain sensing based on strain to radio-frequency conversion of optical frequency comb', *Optics Express* **26**(8), 9484–9491.
- Minkovich, V. P., Monzón-Hernández, D., Villatoro, J. and Badenes, G. [2006], 'Microstructured optical fiber coated with thin films for gas and chemical sensing', *Optics Express* **14**(18), 8413–8418.

- Mirshekar-Syahkal, D. and Davies, J. B. [1982], 'Accurate analysis of coupled strip-finline structure for phase constant, characteristic impedance, dielectric and conductor losses', *IEEE Transactions on Microwave Theory and Techniques* **30**(6), 906–910.
- Misiakos, K., Raptis, I., Salapatas, A., Makarona, E., Botsialas, A., Hoekman, M., Stoffer, R. and Jobst, G. [2014], 'Broad-band Mach-Zehnder interferometers as high performance refractive index sensors: Theory and monolithic implementation', *Optics Express* **22**(8), 8856–8870.
- Monro, T. M., Warren-Smith, S., Schartner, E. P., François, A., Heng, S., Ebendorff-Heidepriem, H. and Afshar, S. [2010], 'Sensing with suspended-core optical fibers', *Optical Fiber Technology* **16**(6), 343–356.
- Nam, S. Y., Chun, H. J. and Lee, Y. M. [1999], 'Pervaporation separation of water–isopropanol mixture using carboxymethylated poly (vinyl alcohol) composite membranes', *Journal of Applied Polymer Science* **72**(2), 241–249.
- Narayanaswamy, R. and Wolfbeis, O. S. [2013], *Optical Sensors: Industrial Environmental and Diagnostic Applications*, Vol. 1, Springer Science & Business Media.
- Neuman, K. C. and Block, S. M. [2004], 'Optical trapping', *Review of Scientific Instruments* **75**(9), 2787–2809.
- Obayya, S. S. A., Rahman, B. M. A. and El-Mikati, H. A. [2000], 'New full-vectorial numerically efficient propagation algorithm based on the finite element method', *Journal of Lightwave Technology* **18**(3), 409.
- O'Brien, J. L. [2007], 'Optical quantum computing', *Science* **318**(5856), 1567–1570.
- Ogura, A. [1999], 'Method of fabricating SOI substrate'. US Patent 5,888,297.
- Okaba, S., Takano, T., Benabid, F., Bradley, T., Vincetti, L., Maizelis, Z., Yampol'skii, V., Nori, F. and Katori, H. [2014], 'Lamb-Dicke spectroscopy of atoms in a hollow-core photonic crystal fibre', *Nature Communications* **5**, 4096.

- Osowiecki, G. D., Barakat, E., Naqavi, A. and Herzig, H. P. [2014], 'Vertically coupled plasmonic slot waveguide cavity for localized biosensing applications', *Optics Express* **22**(17), 20871–20880.
- Otto, A. [1968], 'Excitation of nonradiative surface plasma waves in silver by the method of frustrated total reflection', *Zeitschrift für Physik A Hadrons and nuclei* **216**(4), 398–410.
- Oulton, R. F., Sorger, V. J., Genov, D., Pile, D. and Zhang, X. [2008], 'A hybrid plasmonic waveguide for subwavelength confinement and long-range propagation', *Nature Photonics* **2**(8), 496.
- Pan, C. and Rahman, B. M. A. [2017], 'High-sensitivity polarization-independent biochemical sensor based on silicon-on-insulator cross-slot waveguide', *IEEE Journal of Selected Topics in Quantum Electronics* **23**(2), 64–71.
- Pantic, Z. and Mittra, R. [1986], 'Quasi-TEM analysis of microwave transmission lines by the finite-element method', *IEEE Transactions on Microwave Theory and Techniques* **34**(11), 1096–1103.
- Passaro, V., Dell'Olio, F., Ciminelli, C. and Armenise, M. N. [2009], 'Efficient chemical sensing by coupled slot SOI waveguides', *Sensors* **9**(2), 1012–1032.
- Passaro, V. M., La Notte, M., Troia, B., Passaquindici, L., De Leonardis, F. and Giannoccaro, G. [2012], 'Photonic structures based on slot waveguides for nanosensors: State of the art and future developments', *Int. J. Res. Rev. Appl. Sci* **11**(3), 402–418.
- Passaro, V., Tullio, C., Troia, B., Notte, M. L., Giannoccaro, G. and Leonardis, F. D. [2012], 'Recent advances in integrated photonic sensors', *Sensors* **12**(11), 15558–15598.
- Patrick, H., Williams, G., Kersey, A., Pedrazzani, J. and Vengsarkar, A. [1996], 'Hybrid fiber Bragg grating/long period fiber grating sensor for strain/temperature discrimination', *IEEE Photonics Technology Letters* **8**(9), 1223–1225.
- Pickrell, G., Peng, W. and Wang, A. [2004], 'Random-hole optical fiber evanescent-wave gas sensing', *Optics Letters* **29**(13), 1476–1478.

- Piliarik, M., Homola, J., Maníková, Z. and Čtyroký, J. [2003], ‘Surface plasmon resonance sensor based on a single-mode polarization-maintaining optical fiber’, *Sensors and Actuators B: Chemical* **90**(1-3), 236–242.
- Qiu, S.-J., Chen, Y., Xu, F. and Lu, Y.-Q. [2012], ‘Temperature sensor based on an isopropanol-sealed photonic crystal fiber in-line interferometer with enhanced refractive index sensitivity’, *Optics Letters* **37**(5), 863–865.
- Rahman, B. M. A. and Agrawal, A. [2013], *Finite Element Modeling Methods for Photonics*, Artech House, USA.
- Rahman, B. M. A. and Davies, J. B. [1984a], ‘Finite-element solution of integrated optical waveguides’, *Journal of Lightwave Technology* **2**(5), 682–688.
- Rahman, B. M. A. and Davies, J. B. [1984b], ‘Penalty function improvement of waveguide solution by finite elements’, *IEEE Transactions on Microwave Theory and Techniques* **32**(8), 922–928.
- Rahman, B. M. A. and Davies, J. B. [1988], ‘Analysis of optical waveguide discontinuities’, *Journal of Lightwave Technology* **6**(1), 52–57.
- Rao, Y.-J., Webb, D. J., Jackson, D. A., Zhang, L. and Bennion, I. [1997], ‘In-fiber Bragg-grating temperature sensor system for medical applications’, *Journal of Lightwave Technology* **15**(5), 779–785.
- Reed, M., Benson, T. M., Kendall, P. C. and Sewell, P. [1996], ‘Antireflection-coated angled facet design’, *IEE Proceedings-Optoelectronics* **143**(4), 214–220.
- Rindorf, L., Jensen, J. B., Dufva, M., Pedersen, L. H., Høiby, P. E. and Bang, O. [2006], ‘Photonic crystal fiber long-period gratings for biochemical sensing’, *Optics Express* **14**(18), 8224–8231.
- Ritari, T., Tuominen, J., Ludvigsen, H., Petersen, J., Sørensen, T., Hansen, T. P. and Simonsen, H. R. [2004], ‘Gas sensing using air-guiding photonic bandgap fibers’, *Optics Express* **12**(17), 4080–4087.

- Robinson, J. T., Chen, L. and Lipson, M. [2008], ‘On-chip gas detection in silicon optical microcavities’, *Optics Express* **16**(6), 4296–4301.
- Rodriguez, G. A., Hu, S. and Weiss, S. M. [2015], ‘Porous silicon ring resonator for compact, high sensitivity biosensing applications’, *Optics Express* **23**(6), 7111–7119.
- Rogge, U. and Pregla, R. [1991], ‘Method of lines for the analysis of strip-loaded optical waveguides’, *Journal of the Optical Society of America B* **8**(2), 459–463.
- Ruan, Y., Foo, T. C., Warren-Smith, S., Hoffmann, P., Moore, R. C., Ebendorff-Heidepriem, H. and Monro, T. M. [2008], ‘Antibody immobilization within glass microstructured fibers: a route to sensitive and selective biosensors’, *Optics Express* **16**(22), 18514–18523.
- Russell, P. S. J. [2003], ‘Photonic crystal fibers’, *Science* **299**(5605), 358–362.
- Sadiku, M. N. [2014], *Elements of Electromagnetics*, Oxford University Press.
- Saito, Y., Kanaya, T., Nomura, A. and Kano, T. [1993], ‘Experimental trial of a hollow-core waveguide used as an absorption cell for concentration measurement of NH_3 gas with a CO_2 laser’, *Optics Letters* **18**(24), 2150–2152.
- Salvadé, Y., Schuhler, N., Lévêque, S. and Le Floch, S. [2008], ‘High-accuracy absolute distance measurement using frequency comb referenced multiwavelength source’, *Applied Optics* **47**(14), 2715–2720.
- Sani, E. and Dell’Oro, A. [2016], ‘Spectral optical constants of ethanol and isopropanol from ultraviolet to far infrared’, *Optical Materials* **60**, 137–141.
- Satija, J., Punjabi, N. S., Sai, V. and Mukherji, S. [2014], ‘Optimal design for U-bent fiber-optic LSPR sensor probes’, *Plasmonics* **9**(2), 251–260.
- Säynätjoki, A., Alasaarela, T., Khanna, A., Karvonen, L., Stenberg, P., Kuittinen, M., Tervonen, A. and Honkanen, S. [2009], ‘Angled sidewalls in silicon slot waveguides: conformal filling and mode properties’, *Optics Express* **17**(23), 21066–21076.

- Schuhler, N., Salvadé, Y., Lévêque, S., Dändliker, R. and Holzwarth, R. [2006], 'Frequency-comb-referenced two-wavelength source for absolute distance measurement', *Optics Letters* **31**(21), 3101–3103.
- Sharma, A. K. and Gupta, B. D. [2005], 'Fibre-optic sensor based on surface plasmon resonance with Ag–Au alloy nanoparticle films', *Nanotechnology* **17**(1), 124.
- Sharma, A. K., Jha, R. and Gupta, B. D. [2007], 'Fiber-optic sensors based on surface plasmon resonance: a comprehensive review', *IEEE Sensors Journal* **7**(8), 1118–1129.
- Sharma, E., Ghatak, A. and Goyal, I. [1983], 'Matrix method for determining propagation characteristics of optical waveguides', *IEEE Journal of Quantum Electronics* **19**(8), 1231–1233.
- Silvester, P. P. and Ferrari, R. L. [1996], *Finite Elements for Electrical Engineers*, Cambridge University Press, UK.
- Skorobogatiy, M. [2009], 'Microstructured and photonic bandgap fibers for applications in the resonant bio-and chemical sensors', *Journal of Sensors* **2009**(524237), 1–20.
- Slavík, R., Homola, J. and Čtyroký, J. [1999], 'Single-mode optical fiber surface plasmon resonance sensor', *Sensors and Actuators B: Chemical* **54**(1-2), 74–79.
- Solehmainen, K., Aalto, T., Dekker, J., Kapulainen, M., Harjanne, M., Kukli, K., Heimala, P., Kolari, K. and Leskelä, M. [2005], 'Dry-etched silicon-on-insulator waveguides with low propagation and fiber-coupling losses', *Journal of Lightwave Technology* **23**(11), 3875.
- Soref, R. and Lorenzo, J. [1986], 'All-silicon active and passive guided-wave components for $\lambda = 1.3$ and $1.6 \mu\text{m}$ ', *IEEE Journal of Quantum Electronics* **22**(6), 873–879.
- Statkiewicz-Barabach, G., Carvalho, J., Frazão, O., Olszewski, J., Mergo, P., Santos, J. and Urbanczyk, W. [2011], 'Intermodal interferometer for strain and temperature sensing fabricated in birefringent boron doped microstructured fiber', *Applied Optics* **50**(21), 3742–3749.

- Stern, M., Kendall, P. and McIlroy, P. [1990], 'Analysis of the spectral index method for vector modes of rib waveguides', *IEEE Proceedings J-Optoelectronics* **137**(1), 21–26.
- Sucrose Conversion Table* [1981], *United States Department of Agriculture (USDA)* **FILE CODE 135-A-50**.
- Sun, M., Xu, B., Dong, X. and Li, Y. [2012], 'Optical fiber strain and temperature sensor based on an in-line Mach–Zehnder interferometer using thin-core fiber', *Optics Communications* **285**(18), 3721–3725.
- Sun, Q., Sun, X., Jia, W., Xu, Z., Luo, H., Liu, D. and Zhang, L. [2016], 'Graphene-assisted microfiber for optical-power-based temperature sensor', *IEEE Photonics Technology Letters* **28**(4), 383–386.
- Sun, R., Dong, P., Feng, N.-N., Hong, C.-Y., Michel, J., Lipson, M. and Kimerling, L. [2007], 'Horizontal single and multiple slot waveguides: optical transmission at $\lambda = 1550$ nm', *Optics Express* **15**(26), 17967–17972.
- Sun, X., Dai, D., Thylén, L. and Wosinski, L. [2015a], 'High-sensitivity liquid refractive-index sensor based on a Mach-Zehnder interferometer with a double-slot hybrid plasmonic waveguide', *Optics Express* **23**(20), 25688–25699.
- Sun, X., Dai, D., Thylén, L. and Wosinski, L. [2015b], 'Double-slot hybrid plasmonic ring resonator used for optical sensors and modulators', *Photonics* **2**(4), 1116–1130.
- Sun, X., Thylén, L. and Wosinski, L. [2017], 'Hollow hybrid plasmonic Mach–Zehnder sensor', *Optics Letters* **42**(4), 807–810.
- Szmacinski, H. and Lakowicz, J. R. [1993], 'Optical measurements of pH using fluorescence lifetimes and phase-modulation fluorometry', *Analytical Chemistry* **65**(13), 1668–1674.
- Szmacinski, H. and Lakowicz, J. R. [1995], 'Fluorescence lifetime-based sensing and imaging', *Sensors and Actuators B: Chemical* **29**(1-3), 16–24.
- Szmacinski, H. and Lakowicz, J. R. [2002], Lifetime-based sensing, in 'Topics in Fluorescence Spectroscopy', Springer, pp. 295–334.

- Taflove, A. [1980], 'Application of the finite-difference time-domain method to sinusoidal steady-state electromagnetic-penetration problems', *IEEE Transactions on Electromagnetic Compatibility* **EMC-22**(3), 191–202.
- Tan, S. C. and Yiap, B. C. [2009], 'DNA, RNA, and protein extraction: the past and the present', *BioMed Research International* **2009**(574398), 1–10.
- Tao, J. F., Cai, H., Gu, Y. D., Wu, J. and Liu, A. Q. [2015], 'Demonstration of a photonic-based linear temperature sensor', *IEEE Photonics Technology Letters* **27**(7), 767–769.
- Teppe, F., Knap, W., Veksler, D., Shur, M., Dmitriev, A., Kachorovskii, V. Y. and Rumyantsev, S. [2005], 'Room-temperature plasma waves resonant detection of sub-terahertz radiation by nanometer field-effect transistor', *Applied Physics Letters* **87**(5), 052107.
- Thakur, H. V., Nalawade, S. M., Saxena, Y. and Grattan, K. T. V. [2011], 'All-fiber embedded PM-PCF vibration sensor for structural health monitoring of composite', *Sensors and Actuators A: Physical* **167**(2), 204–212.
- Themistos, C., Rahman, B. M. A. and Grattan, K. T. V. [1995], 'Finite-element analysis of surface-plasmon modes for lossy optical waveguides by the use of perturbation techniques', *Applied Optics* **34**(33), 7695–7701.
- Trouillet, A., Ronot-Trioli, C., Veillas, C. and Gagnaire, H. [1996], 'Chemical sensing by surface plasmon resonance in a multimode optical fibre', *Pure and Applied Optics: Journal of the European Optical Society Part A* **5**(2), 227.
- Tu, X., Song, J., Liow, T.-Y., Park, M. K., Yiyang, J. Q., Kee, J. S., Yu, M. and Lo, G.-Q. [2012], 'Thermal independent silicon-nitride slot waveguide biosensor with high sensitivity', *Optics Express* **20**(3), 2640–2648.
- Utzinger, U. and Richards-Kortum, R. R. [2003], 'Fiber optic probes for biomedical optical spectroscopy', *Journal of Biomedical Optics* **8**(1), 121–148.
- Verma, R. K. and Gupta, B. D. [2008], 'Theoretical modelling of a bi-dimensional U-shaped surface plasmon resonance based fibre optic sensor for sensitivity enhancement', *Journal of Physics D: Applied Physics* **41**(9), 095106.

- Verma, R. K., Sharma, A. K. and Gupta, B. D. [2007], 'Modeling of tapered fiber-optic surface plasmon resonance sensor with enhanced sensitivity', *IEEE Photonics Technology Letters* **19**(22), 1786–1788.
- Verma, R. K., Sharma, A. K. and Gupta, B. D. [2008], 'Surface plasmon resonance based tapered fiber optic sensor with different taper profiles', *Optics Communications* **281**(6), 1486–1491.
- Veronis, G. and Fan, S. [2005], 'Guided subwavelength plasmonic mode supported by a slot in a thin metal film', *Optics Letters* **30**(24), 3359–3361.
- Vicarelli, L., Vitiello, M., Coquillat, D., Lombardo, A., Ferrari, A., Knap, W., Polini, M., Pellegrini, V. and Tredicucci, A. [2012], 'Graphene field-effect transistors as room-temperature terahertz detectors', *Nature Materials* **11**(10), 865.
- Viphavakit, C., Komodromos, M., Themistos, C., Mohammed, W. S., Kalli, K. and Rahman, B. M. A. [2015], 'Optimization of a horizontal slot waveguide biosensor to detect DNA hybridization', *Applied Optics* **54**(15), 4881–4888.
- Vitiello, M. S., Coquillat, D., Viti, L., Ercolani, D., Teppe, F., Pitanti, A., Beltram, F., Sorba, L., Knap, W. and Tredicucci, A. [2011], 'Room-temperature terahertz detectors based on semiconductor nanowire field-effect transistors', *Nano Letters* **12**(1), 96–101.
- Vivien, L., Marris-Morini, D., Griol, A., Gylfason, K. B., Hill, D., Álvarez, J., Sohlström, H., Hurtado, J., Bouville, D. and Cassan, E. [2008], 'Vertical multiple-slot waveguide ring resonators in silicon nitride', *Optics Express* **16**(22), 17237–17242.
- Wadsworth, W. J., Ortigosa-Blanch, A., Knight, J. C., Birks, T. A., Man, T.-P. M. and Russell, P. S. J. [2002], 'Supercontinuum generation in photonic crystal fibers and optical fiber tapers: a novel light source', *Journal of the Optical Society of America B* **19**(9), 2148–2155.
- Wang, W., Tian, Y., Wang, X., He, H., Xu, Y., He, C. and Li, X. [2013], 'Ethanol sensing properties of porous ZnO spheres via hydrothermal route', *Journal of Materials Science* **48**(8), 3232–3238.

- Wang, X., Flueckiger, J., Schmidt, S., Grist, S., Fard, S. T., Kirk, J., Doerfler, M., Cheung, K. C., Ratner, D. M. and Chrostowski, L. [2013a], 'A silicon photonic biosensor using phase-shifted Bragg gratings in slot waveguide', *Journal of Biophotonics* **6**(10), 821–828.
- Wang, X., Grist, S., Flueckiger, J., Jaeger, N. A. and Chrostowski, L. [2013b], 'Silicon photonic slot waveguide Bragg gratings and resonators', *Optics Express* **21**(16), 19029–19039.
- Wang, X., Guan, X., Huang, Q., Zheng, J., Shi, Y. and Dai, D. [2013], 'Suspended ultra-small disk resonator on silicon for optical sensing', *Optics Letters* **38**(24), 5405–5408.
- Wang, X. and Madsen, C. K. [2014], 'Highly sensitive compact refractive index sensor based on phase-shifted sidewall Bragg gratings in slot waveguide', *Applied Optics* **53**(1), 96–103.
- Wang, Y., Zhao, Y., Nelson, J., Chen, Z. and Windeler, R. S. [2003], 'Ultrahigh-resolution optical coherence tomography by broadband continuum generation from a photonic crystal fiber', *Optics Letters* **28**(3), 182–184.
- Weng, S., Pei, L., Wang, J., Ning, T. and Li, J. [2017], 'High sensitivity D-shaped hole fiber temperature sensor based on surface plasmon resonance with liquid filling', *Photonics Research* **5**(2), 103–107.
- Yan, Z., Ying, Y., Zhang, H. and Yu, H. [2006], Research progress of terahertz wave technology in food inspection, in 'Terahertz Physics, Devices, and Systems', Vol. 6373, International Society for Optics and Photonics, p. 63730R.
- Yang, A. H. J., Lerdsuchatawanich, T. and Erickson, D. [2009], 'Forces and transport velocities for a particle in a slot waveguide', *Nano Letters* **9**(3), 1182–1188.
- Yang, A. H., Moore, S. D., Schmidt, B. S., Klug, M., Lipson, M. and Erickson, D. [2009], 'Optical manipulation of nanoparticles and biomolecules in sub-wavelength slot waveguides', *Nature* **457**(7225), 71.

- Yang, D., Wang, C. and Ji, Y. [2016], ‘Silicon on-chip 1D photonic crystal nanobeam bandstop filters for the parallel multiplexing of ultra-compact integrated sensor array’, *Optics Express* **24**(15), 16267–16279.
- Yang, S.-H., Cooper, M. L., Bandaru, P. R. and Mookherjea, S. [2008], ‘Giant birefringence in multi-slotted silicon nanophotonic waveguides’, *Optics Express* **16**(11), 8306–8316.
- Yebo, N. A., Lommens, P., Hens, Z. and Baets, R. [2010], ‘An integrated optic ethanol vapor sensor based on a silicon-on-insulator microring resonator coated with a porous ZnO film’, *Optics Express* **18**(11), 11859–11866.
- Yebo, N. A., Taillaert, D., Roels, J., Lahem, D., Debliquy, M., Van Thourhout, D. and Baets, R. [2009], ‘Silicon-on-insulator (SOI) ring resonator-based integrated optical hydrogen sensor’, *IEEE Photonics Technology Letters* **21**(14), 960–962.
- Yee, K. [1966], ‘Numerical solution of initial boundary value problems involving Maxwell’s equations in isotropic media’, *IEEE Transactions on Antennas and Propagation* **14**(3), 302–307.
- Yeo, T., Sun, T. and Grattan, K. T. V. [2008], ‘Fibre-optic sensor technologies for humidity and moisture measurement’, *Sensors and Actuators A: Physical* **144**(2), 280–295.
- Zhang, L., Lu, P., Chen, L., Huang, C., Liu, D. and Jiang, S. [2012], ‘Optical fiber strain sensor using fiber resonator based on frequency comb vernier spectroscopy’, *Optics Letters* **37**(13), 2622–2624.
- Zhang, L., Zhao, J., Lu, H., Li, L., Zheng, J., Li, H. and Zhu, Z. [2012], ‘Facile synthesis and ultrahigh ethanol response of hierarchically porous ZnO nanosheets’, *Sensors and Actuators B: Chemical* **161**(1), 209–215.
- Zhang, T., Nix, M. B., Yoo, B.-Y., Deshusses, M. A. and Myung, N. V. [2006], ‘Electrochemically functionalized single-walled carbon nanotube gas sensor’, *Electroanalysis* **18**(12), 1153–1158.
- Zhang, Y., Liu, P., Zhang, S., Liu, W., Chen, J. and Shi, Y. [2016], ‘High sensitivity temperature sensor based on cascaded silicon photonic crystal nanobeam cavities’, *Optics Express* **24**(20), 23037–23043.

- Zheng, S., Zhu, Y. and Krishnaswamy, S. [2013], 'Fiber humidity sensors with high sensitivity and selectivity based on interior nanofilm-coated photonic crystal fiber long-period gratings', *Sensors and Actuators B: Chemical* **176**, 264–274.
- Zhou, L., Sun, X., Li, X. and Chen, J. [2011], 'Miniature microring resonator sensor based on a hybrid plasmonic waveguide', *Sensors* **11**(7), 6856–6867.
- Zhou, T., Sang, Y., Wang, X., Wu, C., Zeng, D. and Xie, C. [2018], 'Pore size dependent gas-sensing selectivity based on ZnO@ZIF nanorod arrays', *Sensors and Actuators B: Chemical* **258**, 1099–1106.
- Zhou, W., Cheng, Z., Wu, X., Zhu, B., Sun, X. and Tsang, H. K. [2017], 'Fully suspended slot waveguides for high refractive index sensitivity', *Optics Letters* **42**(7), 1245–1248.
- Zhu, Z., Liu, L., Liu, Z., Zhang, Y. and Zhang, Y. [2017], 'Surface-plasmon-resonance-based optical-fiber temperature sensor with high sensitivity and high figure of merit', *Optics Letters* **42**(15), 2948–2951.
- Zia, R., Selker, M. D. and Brongersma, M. L. [2005], 'Leaky and bound modes of surface plasmon waveguides', *Physical Review B* **71**(16), 165431.
- Zia, R., Selker, M. D., Catrysse, P. B. and Brongersma, M. L. [2004], 'Geometries and materials for subwavelength surface plasmon modes', *Journal of the Optical Society of America A* **21**(12), 2442–2446.
- Zou, L., Bao, X., Afshar, S. and Chen, L. [2004], 'Dependence of the Brillouin frequency shift on strain and temperature in a photonic crystal fiber', *Optics Letters* **29**(13), 1485–1487.